On the deposition mechanism and irradiation behaviour of molecular plating thin films

Dissertation

zur Erlangung des Grades

„Doktor der Naturwissenschaften“

im Promotionsfach Chemie

am Fachbereich Chemie, Pharmazie und Geowissenschaften

der Johannes Gutenberg-Universität Mainz

von

Carl-Christian Bernhard Meyer

geb. in Idar-Oberstein

1. Gutachter: Univ.-Prof. Dr. Christoph E. Düllmann, JGU Mainz
2. Gutachter: Prof. Dr. Christina Trautmann, TU Darmstadt
3. Gutachter: Univ.-Prof. Dr. Michael Block, JGU Mainz

Tag der mündlichen Prüfung: 18.03.2025

Contributions

This thesis is based on three publications, which are listed below. The author is the main author of all three publications [I-III]. Furthermore, the order presented here is the one that makes more sense in terms of content and not order of chronological appearance. The publication IV with co-authorship of the author can be found in the appendix of the dissertation. It is to be regarded thematically as a preliminary publication to this work.

I. C.-C. Meyer, et al., Chemical conversions in lead thin films induced by heavy-ion beams at Coulomb barrier energies, Nuclear Instruments and Methods in Physics Research Section A: Accelerators, Spectrometers, Detectors and Associated Equipment 1028 (2022) 166365.

II. C.-C. Meyer, et al., Microscopic and spectroscopic analysis of ion-irradiated molecular-plated thin films for superheavy element production, Nuclear Instruments and Methods in Physics Research Section A: Accelerators, Spectrometers, Detectors and Associated Equipment, (2025) [submitted].

III. C.-C. Meyer, et al., Fabrication, swift heavy ion irradiation, and damage analysis of lanthanide targets, Radiochimica Acta 111 (11) (2023) 801-815.

IV. Haas, R., C.-C. Meyer, et al., ODIn—A setup for Off-line Deposit Irradiations of thin layers for nuclear physics applications. Nuclear Instruments and Methods in Physics Research Section A: Accelerators, Spectrometers, Detectors and Associated Equipment 957 (2020): 163366.

Declaration of academic integrity

I hereby declare that I have independently prepared the present dissertation entitled “On the deposition mechanism and irradiation behaviour of molecular plating thin films“. The thoughts and other aids taken directly or indirectly from external sources have been marked as such. The AI tool DeepL was used to improve the English texts.

Hiermit erkläre ich, dass ich die vorliegende Dissertation mit dem Titel “On the deposition mechanism and irradiation behaviour of molecular plating thin films“ selbständig angefertigt habe. Die aus fremden Quellen direkt oder indirekt übernommenen Gedanken und sonstigen Hilfsmittel sind als solche kenntlich gemacht. Zur Verbesserung der in englischer Sprache verfassten Texte wurde das KI-Tool DeepL verwendet.

Lemgo, den 18.01.2025

Abstract

Superheavy elements are produced by heavy ion fusion reactions using intense beams that irradiate suitable targets. For the heaviest elements, lead/bismuth and actinide targets are primarily used for this purpose. The production of actinide targets has been mainly based on the molecular plating (MP) method for decades.

The MP method is also widely used in the preparation of actinide and lanthanide samples for other research areas. The mechanism of the MP process has not yet been conclusively elucidated. The majority of work on the subject is limited to morphological studies. Spectroscopic studies have been limited to X-ray photoelectron spectroscopy (XPS) and energy dispersive X-ray spectroscopy (EDX). The reason for this limited spectroscopic data situation is to be found in the special challenges arising from the radioactivity of the actinide samples. Technical restrictions and legal requirements thus prevent access to modern methods, as the relevant laboratories lack the clearance to handle radioactive material. Besides radioactivity, high costs in acquisition and disposal prevent mass experiments, e.g. to optimise electrochemical parameters. Therefore, it is common to limit oneself to experiments on lanthanide samples. The present work was also limited to lanthanide samples, but radioactive tracers could be generated using the Mainz research reactor TRIGA Mark II. In this way, short-lived lanthanide isotopes were used to test working methods and analytical procedures that can also be transferred to future procedures with actinides. The electrochemical production of actinide targets is virtually limited worldwide to the MP process and some closely related methods. Developments in the technically more important field of lanthanide electrochemistry have not been transferred to target production. Thus, the established MP method is still limited by significant deposition of unwanted by-products and thus low maximum deposition rates of desired actinides.

When MP films are irradiated at the heavy ion accelerator, changes in the alpha spectra of the irradiated actinide thin films are a clear spectroscopic indication of chemical changes due to irradiation. Photographs taken before and after the accelerator experiments provide evidence of drastic morphological changes, which has been confirmed by some initial publications on lanthanide substitutes, using scanning electron microscopy (SEM). By understanding the chemical processes involved, it is hoped to improve the quality and stability of the MP targets used.

This dissertation presents two publications on mechanistic studies of lead and lathanide targets, presenting new insights into the MP process and the irradiation behaviour of the thin films. The third publication attempts to adapt established new methods for the electrochemical deposition of lanthanides to the needs of target production and to present the first irradiation tests with these thin films.

Zusammenfassung

Superschwere Elemente werden durch Schwerionen-Fusionsreaktionen unter Verwendung intensiver Strahlen, welche geeignete Targets bestrahlen, erzeugt. Bei den schwersten Elementen werden dazu vor allem Blei/Bismut und Actiniden-Targets eingesetzt. Die Produktion von Actiniden-Targets beruht seit Jahrzehnten hauptsächlich auf der Methode des Molecular Plating (MP).

Das MP Verfahren findet auch bei Präparation von Actiniden- und Lanthaniden-Proben für andere Forschungsgebiete breite Anwendung. Der Mechanismus des MP Verfahrens ist noch nicht abschließend aufgeklärt. Die Mehrheit der Arbeiten zum Thema beschränkt sich auf morphologische Studien. Spektroskopische Studien beschränkten sich bisher auf die Röntgenphotoelektronenspektroskopie (XPS) und die Energiedispersive Röntgenspektroskopie (EDX). Die Ursache für diese eingeschränkte spektroskopische Datenlage ist in den besonderen Herausforderungen zu suchen, die sich aus der Radioaktivität der Actiniden-Proben ergeben. Technische Einschränkungen und gesetzliche Vorgaben verhindern so den Zugriff auf moderne Methoden, da den entsprechenden Laboren die Freigabe für den Umgang mit radioaktivem Material fehlt. Neben der Radioaktivität verhindern hohe Kosten in der Anschaffung und Entsorgung Massenexperimente, um z.B. elektrochemische Parameter zu optimieren. Daher ist es üblich sich auf Experimente an Lanthaniden-Proben zu beschränken. Auch in der vorliegenden Arbeit wurde sich auf Lanthaniden-Proben beschränkt, jedoch konnten mittels des Mainzer Forschungsreaktors TRIGA Mark II radioaktiven Tracer erzeugt werden. So konnten anhand von kurzlebigen Lanthaniden-Isotopen Arbeitsweisen und Analyseverfahren erprobt werden, die sich auch auf zukünftige Verfahren mit Actiniden übertragen lassen. Die elektrochemische Herstellung von Actiniden-Targets ist weltweit quasi auf das MP Verfahren und einige engverwandte Methoden beschränkt. Entwicklungen auf dem technisch wichtigeren Gebiet der Elektrochemie der Lanthanide, wurden für die Target Herstellung nicht übertragen. So ist das etablierte MP Verfahren immer noch durch signifikante Abscheidungen von unerwünschten Nebenprodukten und damit geringen maximalen Abscheidemengen an gewünschten Actiniden eingeschränkt.

Bei der Bestrahlung von MP Filme am Schwerionenbeschleuniger, sind Veränderungen der alpha-Spektren der bestrahlten Actiniddünnfilme ein deutlicher spektroskopischer Hinweis auf chemische Veränderungen durch Bestrahlung. Fotos vor und nach den Beschleunigerexperimenten geben Hinweis auf drastische morphologische Veränderungen, was einige erste Publikationen an Lanthanidsubstituten, mittels Rasterelektronenmikroskopie (REM), bestätigt haben. Durch Verständnis der ablaufenden chemischen Prozesse, erhofft man sich Verbesserungen in der Qualität und Stabilität der verwendeten MP Targets.

Die vorliegende Arbeit präsentiert zwei Publikationen zu mechanistischen Studien an Blei- und Lathanidtargets, in denen neue Erkenntnisse zum MP Verfahren und zum Bestrahlungsverhalten der Dünnfilme präsentiert werden. Die dritte Publikation versucht etablierte neue Verfahren zur elektrochemischen Abscheidung von Lanthaniden, an die Bedürfnisse der Targetherstellung anzupassen, sowie erste Bestrahlungstests mit diesen Dünnfilmen zu präsentieren.

Contents

1. Introduction

The aim of this thesis is to gain new insights into the behaviour of molecular plating (MP) thin films when subjected to fast heavy ion (SHI) irradiation. The MP technique remains the principal means of producing actinide targets which are subsequently irradiated at the heavy ion accelerator to produce new superheavy elements.

The purpose of this chapter is to provide a brief overview of the scientific basis of superheavy elements, to elaborate on current target techniques, and to highlight the challenges of analysing thin films of such materials.

1.1. Scientific background of the superheavy elements

The swift detection of ten fresh transuranium elements soon after the Second World War's end and their categorisation in the recently concluded Actinide category increased understanding of the Periodic Table of Elements (PSE) and granted Nobel Prize in Chemistry (1951) to their inventors Glenn T. Seaborg (1912-1999) and Edwin McMillan (1907-1991) [144]. After this almost lightning expansion of the PSE, the question arose whether there could be even heavier elements, the so-called superheavy elements (SHE). After investigations of the fission properties and more precise measurements of the decay half-lives in particular had brought the macroscopic liquid drop model [15, 223] to its limits and more precise quantum mechanical descriptions, such as the nuclear shell model and later the Nilsson model [147], prevailed, as well as advances in computer technology made more extensive theoretical calculations possible, an island of stability (Fig. 1.1) was predicted [80, 185]. On this island of stability, new long-lived elements were suspected, and the first predictions of long half-lives led to extensive but unsuccessful attempts to detect SHE in nature [78].

The formation of SHE in neutron stars through the so-called r-process (rapid) is still assumed to be a possible source for the existence of SHE in the cosmos [165], but definitive spectroscopic evidence of SHE in stars is still pending. In the so-called r-process, elements heavier than iron are produced in the universe through neutron capture and subsequent beta decay (Fig. 1.1). Attempts to artificially generate such high neutron fluxes have also been made by detonating thermonuclear bombs [137]. However, this pathway reaches a natural limit at fermium (atomic number Z=100), as this element does not feature any

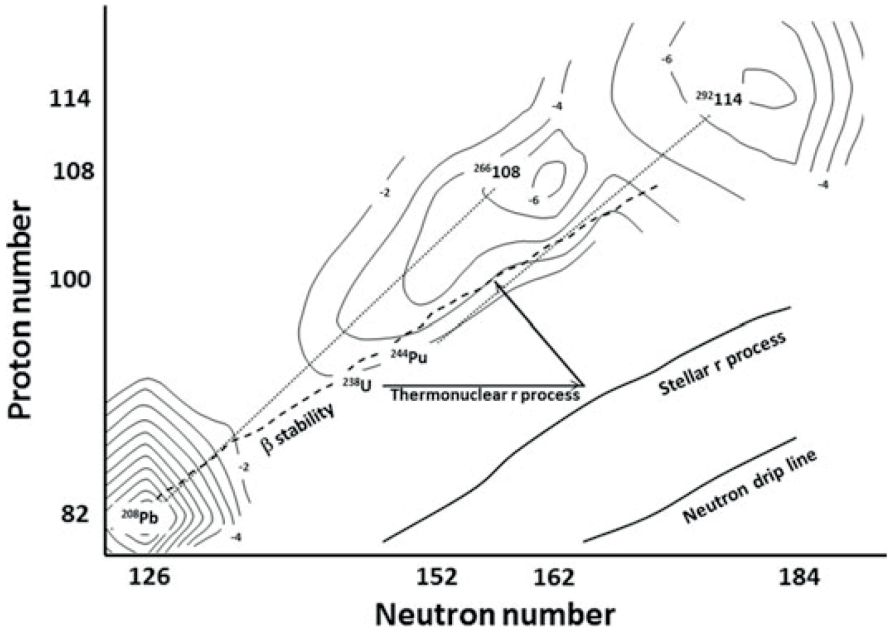

Figure 1.1.: The calculated microscopic corrections to liquid-drop masses for the heavy elements, showing a prediction of the location of the Island of Stability, centered at ^{298}114. Contours are labeled in MeV. The neutron-drip line is indicated, as are the pathways to the heavy elements followed by the stellar and thermonuclear r-processes. The compound nuclei produced in representative heavy-ion reactions are also shown, connected to the target nuclide by a dotted line. The heavy ion reaction of ^{108}Pb to ^{266}108 shows a cold fusion, the reaction of ^{244}Pu to ^{298}114 shows a hot fusion. From ref. [137]

β^--decaying isotope leading to the next heavier element (Fig. 1.2) [119]. Because of this, accelerator techniques were already developed for the discovery of the transfermium actinides, in which a heavier target material is bombarded with lighter charged particles or ions [144], to create a new atom through a fusion reaction.

The fundamental blueprint of the accelerator experiments, consisting of a lighter projectile and a heavier target, has endured to the present day. Notwithstanding, innovations in accelerator technology have enabled the usage of progressively heavier projectiles concentrated into more powerful beams [35, 148]. In target technology [36, 177], the heaviest actinides (Bk, Cf, Es) that can be produced in breeder reactors by neutron capture represent the heaviest target materials available. The experimental and organisational challenge now is to process these rare and short-lived actinides into targets in time for the accelerator experiment. Targets, in turn, that can withstand the new and intense accelerator beams [36].

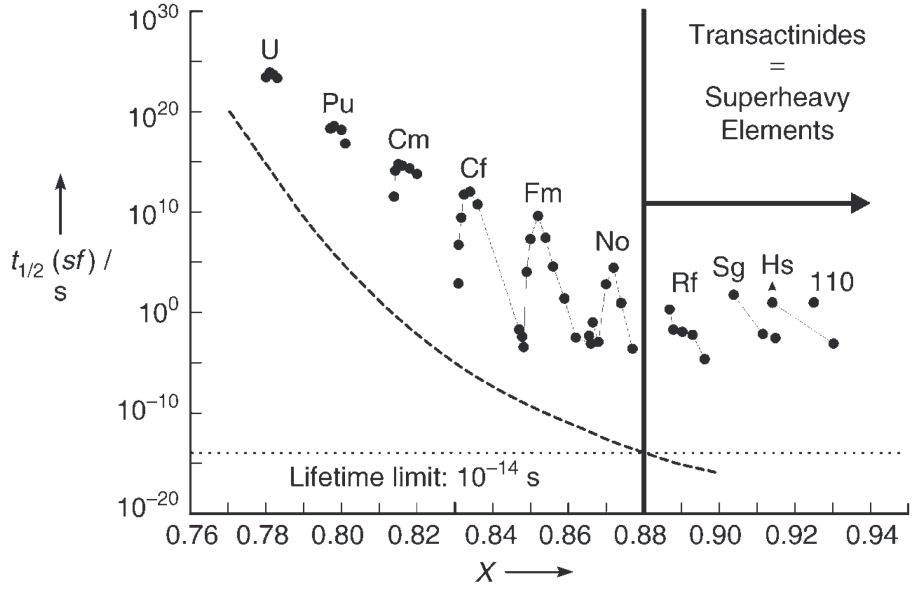

Figure 1.2.: Known spontaneous fission (sf) half-lives (t 1/2) of nuclides with even numbers of protons and neutrons (dots) and calculated hypothetical half-lives (dashed line) taking into account only the liquid-drop-model contribution plotted versus the fissility parameter X. The dotted line shows the lifetime-limit of 10×10^{-14}s for a chemical element. From ref. [185]

1.2. Nuclear reaction strategies

While transuranium elements up to and including ^{257}Fm can be bred in the breeder reactor by stepwise neutron capture, all heavier elements had to be produced by nuclear fusion reactions at the ion accelerator until now [185]. For this, the projectile must be accelerated fast enough to overcome the repulsive Coulomb forces between the two atomic nuclei. With impact parameters considerably smaller than the sum of both radii, the contact of both nuclei is deeper and the attractive nuclear forces come into play [208], the two nuclei fuse. Thus, a compound nucleus is formed, which contains all neutrons and protons of the initial nuclei [37]. In most cases, the formed compound nucleus disintegrates by fission. Only very rarely ($\approxeq 10^{-9}$) is the high excitation energy dissipated by the evaporation of particles, mostly neutrons, and by the emission of γ-rays. Each evaporated neutron removes $\approxeq 10$ MeV of excitation energy, but each neutron evaporation process is in competition with prompt fission. Production cross sections (Fig. 1.3 (a)) for transactinide nuclides range from nanobarns (10^{-33}cm^2) to picobarns (10^{-36}cm^2) [208]. Only after several neutron evaporation steps, typically four or five, the excitation energy is so low that the remaining energy is carried away by electromagnetic radiation (γ-rays), whose emission is a rather slow process and thus not competitive as long as fission or neutron evaporation are energetically possible. The final product at the end of the neutron evaporation cascade is a nucleus in its ground (or sometimes meta-stable) state, which is called the evaporation residue (EVR) [37].

Through the fusion reaction, the compound nucleus carries a certain excitation energy, depending on the selected target-projectile combination, a rough distinction is made between hot and cold fusion [185]. However, fusion depends decisively on the beam energy, which is converted into internal excitation energy. Lowering the beam energy to values that ensure the formation of an ideally "cold", i.e. non-excited compound nucleus in the ground state, is impossible because such beam energies are too small to overcome the Coulomb barrier, which is, however, a prerequisite for fusion [37].

The particularly low excitation energies in cold fusion result from the high binding energies per nucleon for both the semi-magic ion beam and the double-magic target nuclei [84], i.e. the use of more strongly bound shell-stabilised reaction partners enables the formation of the compound nucleus in a relatively cold state, i.e. at rather low excitation energy. Therefore, nuclei around the $Z = 82$ and $N = 126$ shell closures such as ^{208}Pb and ^{209}Bi were used as targets and allowed obtaining compound nuclei at about 10 to 20 MeV excitation energy [37]. These nuclei typically evaporate one to two neutrons from the compound nucleus (Fig. 1.3 (b)). The fusion reactions of targets composed of lead or bismuth were referred to as cold fusion due to their low excitation energies. Conversely, the fusion reactions involving actinide targets are termed hot fusion.

Hot fusion reactions are characterised by excitation energies of about 40 to 50 MeV when actinide target nuclei such as ^{238}U, ^{242,244}Pu, ^{243}Am, ^{248}Cm, ^{249}Bk, ^{249}Cf and ^{254}Es fuse with light ion beams, such as ^{18}O, ^{22}Ne and ^{26}Mg (Fig. 1.3 (c)). While cold fusion reactions typically only release one neutron, hot fusion reactions emit four or five neutrons before the compound nucleus cools down. Despite the emission of an additional three or four neutrons, these reactions are employed to synthesize the most neutron-rich and relatively long-lived isotopes used in the chemical research of superheavy elements, owing to the neutron-rich composition of the actinide targets [185]. The different cross sections are summarised in Fig. 1.3. The "abnormal" behaviour of ^{48}Ca-induced production cross sections, which remain fairly constant at the level of some pb, was associated with stabilising shell effects, i.e. increasing fission barrier heights, as one approaches the range of $Z = 114$. The fusion route via ^{48}Ca has been the dominant route to new SHE in recent years. Since the excitation energies are somewhat lower than for other hot fusion reactions and correspondingly fewer neurons have to evaporate, this fusion route is also referred [208] to as warm fusion (Fig. 1.3 (d)).

The study of hot fusion using a ^{48}Ca beam and actinide targets resulted in the discovery of five new elements. Another most important result is the change of the trend of cross sections measured in these reactions at element 112 (Fig. 1.3 (a)). Instead of continuously decreasing cross sections as indicated by the cross sections for production of elements 102, 103, and 108, the cross sections increase again and reach a maximum of about 10 pb for production of isotopes of elements 114 and 115. This result

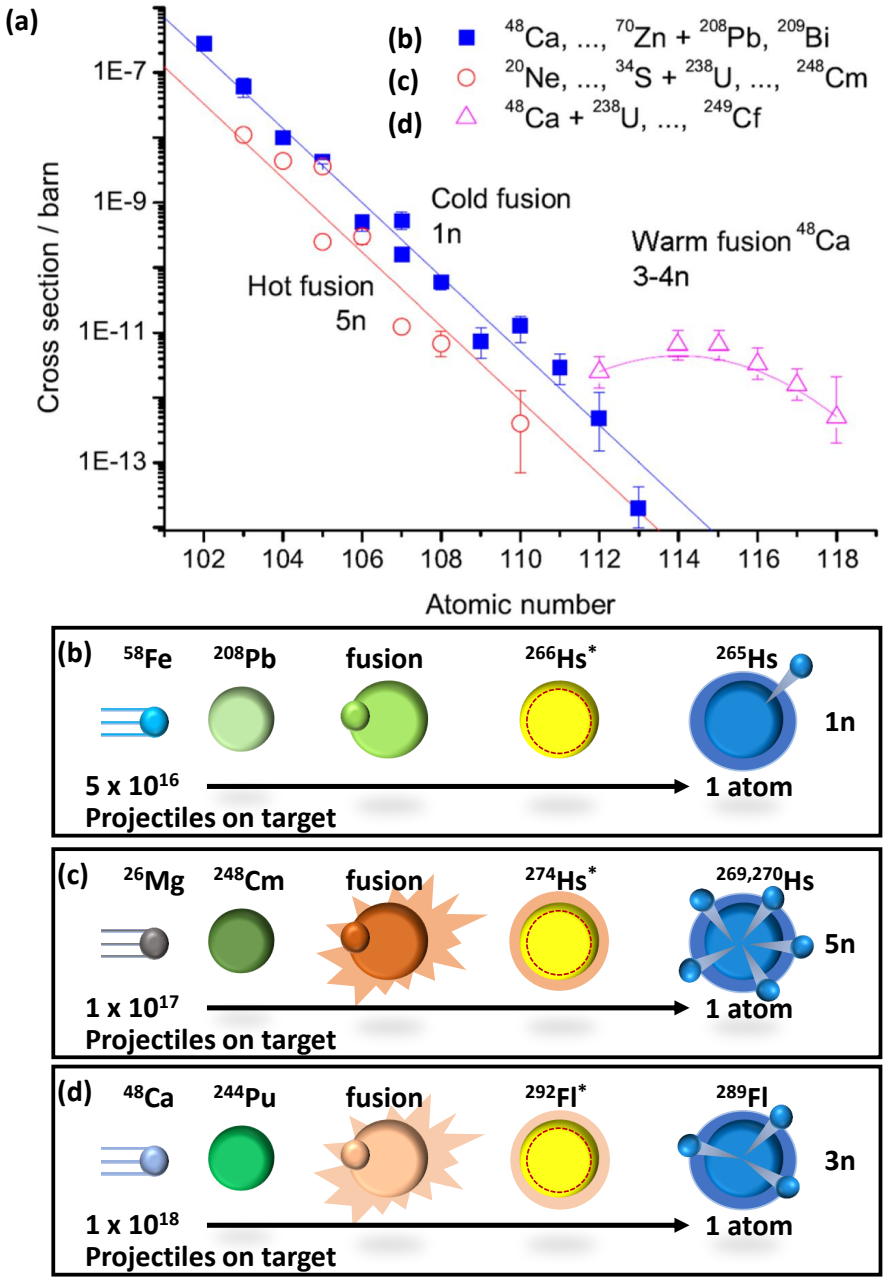

Figure 1.3.: (a) Experimental cross sections for the formation of nuclei with $Z \geqq 102$ in (■) the 1n evaporation channel of cold fusion reactions, (○) the 5n channel of hot fusion reactions, and (△) the 3-4n channel of warm fusion reactions with ^{48}Ca + actinide targets. The curves are drawn to guide the eye. From ref. [208] Schematic representation of: (b) a cold fusion reaction: ^{208}Pb(^{58}Fe,1n)^{265}Hs, and (c) a hot fusion reaction: ^{248}Cm(^{26}Mg,4-5n)^{269,270}Hs, and (d) an example of a warm fusion reaction ^{244}Cm(^{48}Ca,3n)^{289}Fl. scheme analogous to [185]

presents a convincing argument that the production mechanism of the identified isotopes of these elements must be determined by processes based on increased stability [84]. A complete comprehension of the root cause regarding this anomaly is yet to be achieved. Various theoretical approaches that mirror experimental cross sections offer distinct interpretations for this phenomenon. Certain models relate it to the proximity to the subsequent spherical shell closure, leading to significant fission barriers. Meanwhile, another approach anticipates the synthesis of nuclei to be oblate-shaped rather than spherical. The implication is that fission along the de-excitation cascade, which passes over a prolate saddle-point from the compound nucleus to the EVR, occurs with a lower probability. This is due to the significant rearrangement of the nucleus required along this route. All models, though, agree that probably exit channel phenomena are likely responsible for the surprisingly large cross sections to produce elements up to $Z = 118$ [37]. In general, it is also the bane of experimental studies of superheavy elements, as one has to try to create a nucleus with a very high ratio of neutrons to protons $N = Z$ from a reaction of lighter partners, which will have (much) smaller ratios of $N = Z$. Thus currently the study of superheavy elements is restricted to neutron deficient isotopes. In future radioactive beam facilities one can hope to use exotic beams with much higher $N = Z$ ratios to create more neutron rich superheavy elements [80].

1.3. Target techniques for SHE experiments

The generation of appropriate targets is a vital step in facilitating the success of SHE experiments. The continuous challenge for target technology is to maintain alignment with advancements in accelerator technology and evolving experimental parameters. When delineating the requisite target technology, it is also pertinent to differentiate between cold fusion and hot (warm) fusion.

An ideal target would be self-supporting, i.e. it would do without a supporting backing or substrate made of another material. It would be elementally pure and monoisotopic. Its thickness would correspond exactly to the excitation function for the desired fusion reaction resulting from the likewise ideally intense ion beam (Fig. 1.4 (a)).

In the real experiment (Fig. 1.4 (b)), the desired target nuclide must be supported on a backing or substrate. The introduction of new elements into the nuclear reactions, as induced by this substrate, results in the generation of unwanted radioactive by-products, which in turn can complicate the detection of new SHE. Additionally, beam energy is lost in the backing, causing it to heat up and thus reducing the lifetime of the target system or limiting the maximum possible beam intensity.Even if this energy loss and the resulting heating are brought under control, the smearing of beam energy still leads to a loss of efficiency in SHE production. It is important to note that both cold fusion and hot fusion experiments involve the use of real targets that are not elementally pure. Instead, these targets are composed of chem-

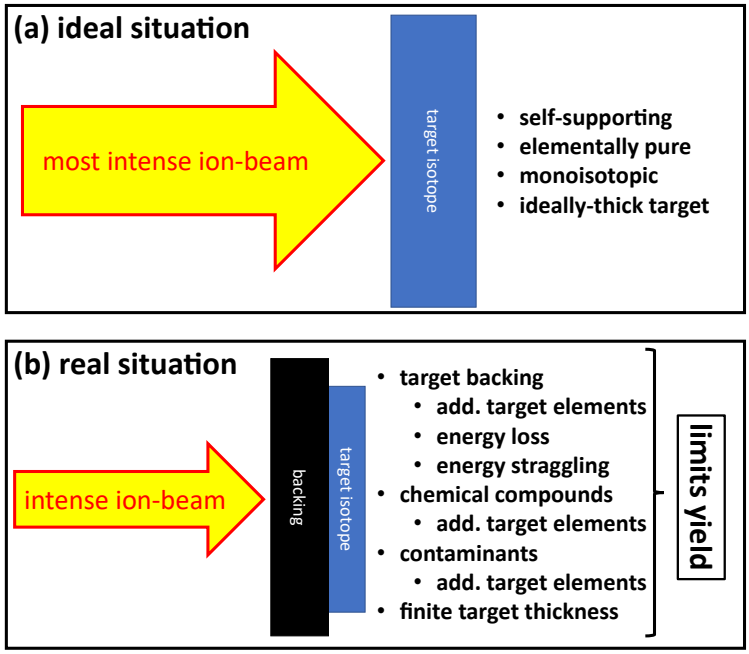

Figure 1.4.: Illustration of the basic structure of a target: (a) ideal target (b) real target.

ical compounds, which, as previously mentioned, introduce foreign elements into the nuclear reactions, thus leading to a series of subsequent issues. These issues are a result of the short-lived radioactive products that are produced.In addition to the aforementioned issues, most manufacturing methods are also plagued by contamination, which can only be limited in some manufacturing processes.It is evident that these real constraints limit the yields in SHE experiments.

1.3.1. Targets for cold fusion experiments

The nucleosynthesis of SHE via cold fusion routes is usually limited to targets made of the elements lead (Pb) and bismuth (Bi), but there are also cold fusion experiments with other target elements [54]. Suitable targets must have a uniform thickness compatible with the energy loss of heavy ions. While some metal foil targets can be self-supporting, most thin targets must be fabricated on a substrate, typically a substrate foil [118], which presents problems of adhesion and mechanical resistance to heating and cooling. In experiments that require high beam currents of heavy ions, heat dissipation becomes a problem. A beam with a current of 1 pμA ($6.2 \times 10^{13} \frac{\text{ions}}{\text{s}}$) deposits about 1 W of heat for each MeV of energy lost through the target. This usually favours the use of chemical compounds with high melting points as targets [137]. Since the melting points of metallic lead (327.5 °C) and bismuth (271.3 °C) cause problems under such conditions [17], metallic foils of these elements are no longer common targets; instead, high-melting compounds [99, 100] on substrate foils are used. The second important experimental method is

the use of target wheels [52, 62, 91, 127] (Fig. 1.7).

Figure 1.5.: ^{208}Pb-targets showing the backing side (1 and 3 from above) and the target side (2 and 4 from above), respectively, with an enlarged target area and improved backing quality (upper two) compared to the previous target version (lower two). From ref. [120] The targets illustrated show the development of target segments for the target wheel for SHIP experiment setup at the GSI Darmstadt. It shows the improvements on the way to the perfect PbS target.

Several compounds of lead and bismuth with higher melting temperatures have been tested as target materials for cold fusion reactions. Now, mostly PbS with a melting temperature of 1114 °C and Bi_2O_3 with a melting temperature of 817 °C are applied as target materials in case the expected beam intensities are too high for the metals [119]. The compounds have a well defined stoichiometry to guarantee a known and homogenous distribution of the target atoms across the target area. For intensity reasons the fraction of the target atoms in the compound is as high as possible and the mass of the other component as low as possible [99, 100]. These compound targets are prepared on thin carbon support foils (30 to 100 $\frac{\mu g}{cm^2}$) by chemical vapour deposition (CVD). Often, a thin carbon layer (5 to 10 $\frac{\mu g}{cm^2}$) is applied as a protective film after the actual target material deposition [119]. The carbon carrier foils are than clipped into curved titanium carrier segments (Fig. 1.5). Several segments form a target wheel (Fig. 1.7). Since stable non-radioactive elements are used for cold fusion reactions, the chemical and material science parameters are much better researched. The difficulties of producing actinide targets for hot fusion reactions will be

discussed in detail later. In the development of compound targets for cold fusion, not only the performance of metallic and compound targets was compared, but also the SHE production rates for different production paths [100]. Thanks to detailed studies, it was possible to produce customised targets that can optimally utilise the excitation energy of the 1n reaction (Fig. 1.6). It has not been possible to achieve an optimization in terms of thickness, backing, and chemical composition for actinide targets in hot fusion reactions, yet.

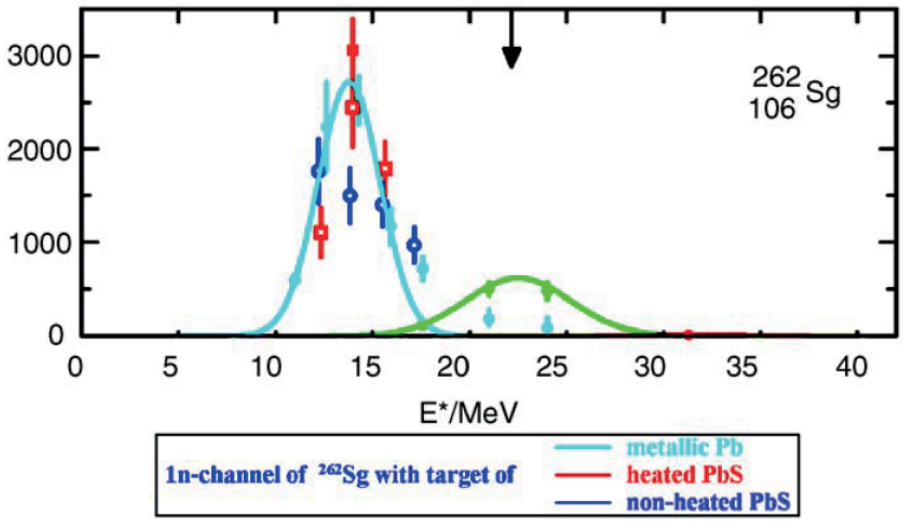

Figure 1.6.: Excitation energy E* of the compound nucleus versus the reaction cross-section in nb for the reaction ^{54}Cr+^{208}Pb $\rightarrow$ ^{262}Sg* for the 1n-channel with metallic lead (light blue points), heated PbS (red points), and black PbS (dark blue points). The continuous curves in light blue, green and red (one point on the X-axis) show the excitation function for metallic lead in the 1n- , 2n- , and 3n-channel, respectively. From ref. [100]

Target wheels [52, 62, 91, 127] are one of the most effective means of dissipating heat involves distributing the beam intensity over a large area. Rather than actually defocusing the beam, the usual method involves preparing targets in arc-shaped segments, distributed around the periphery of a wheel that is rotated at high velocity so that the areal density of target atoms through the beam spot is maximized (Fig. 1.7). Consequently, the number of ions depositing heat in a given beam-spot-sized target increment is minimized. Targets are rotated synchronously with the time macrostructure of the beam so that the supporting framework is not irradiated, which would impede conduction of heat from the foils [137]. Since, the most important parameter determining the limits of target stability under high beam intensity is the beam particle fluence per target area unit. The most obvious way for allowing higher beam intensities on the targets is therefore to enlarge the wheel diameter and the length of a single target segment, over which one beam pulse is distributed [91]. Aside from using a rotating target wheel, the energy deposited by the beam can be further distributed by defocusing the particle current in the vertical direction [62, 180]. Recent advances in ion optics have made it possible to achieve a more optimal distribution

of beam intensity on target segments. This not only prevents damage due to excessive beam focus, but also ensures that the target material receives optimal irradiation. However, despite these measures, it is still necessary to continuously remove power from the target, through processes such as black body radiation and heat conduction towards its frame. To avoid target melting and to increase the beam intensity, it was necessary to enhance the heat removal from the target. This was achieved by enhancing the two cooling processes, radiation and conduction, and by implementing a third cooling mode, which involves conduction and convection in a gas. It is worth noting that targets used in gas-filled recoil separators can withstand higher beam intensities than those used in vacuum, as evidenced by experiments [3, 180]. Technical measures to enhance the irradiation resistance, including target wheels, gas cooling, and improved beam guidance, were initially created for SHE experiments through the use of cold fusion and consequently modified to meet the unique needs of SHE experiments using hot fusion [91].

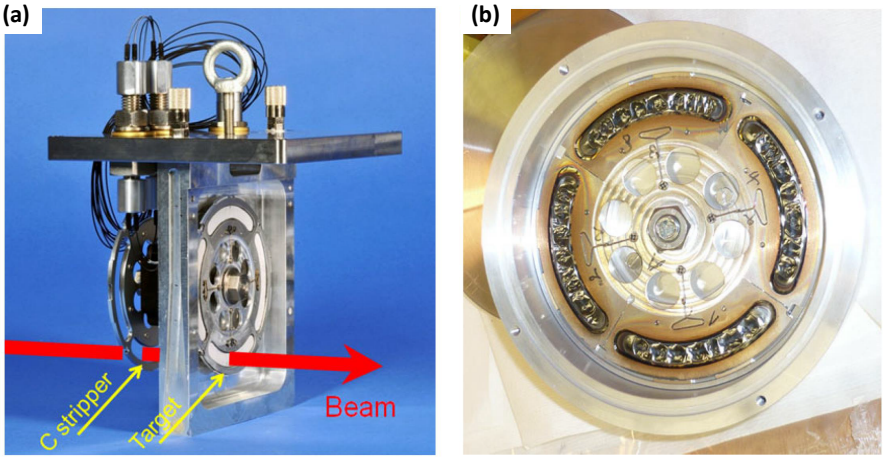

Figure 1.7.: (a) View of the open target cassette with the target wheel. Upstream, a wheel for carbon stripper foils is visible (no foils mounted in the picture) (b) The ^{249}Cf target wheel after the bombardment with the ^{50}Ti beam dose of 1×10^{19} ions. From ref. [91]

1.3.2. Targets for hot fusion experiments

Since 2000, six new superheavy elements with atomic numbers 113 to 118 have been synthesised in hot fusion reactions of ^{48}Ca beams on actinide targets. These target materials, including ^{242}Pu, ^{244}Pu, ^{243}Am, ^{245}Cm, ^{248}Cm, ^{249}Cf and ^{249}Bk, are available in very limited quantities and require specialised production and processing facilities located in only a few research centres worldwide [174]. High beam intensities and large beam doses make it necessary to use rotating target wheels also in these cases [84]. The use of a large area to maximize the intensity of the beam increases the amount of target material incorporated in the target by two orders of magnitude, to 10 mg. This not only increases the investment

in exotic enriched isotopes, but also increases the difficulty in handling high-dose actinide targets like those fabricated from ^{243}Am, ^{249}Bk, and ^{249}Cf [137]. The generally used production is by molecular plating (MP) [162] of the material from an organic solvent, the MP procedure will be discussed in more detail later. The MP process demands a relatively thick and stable backing foil, e.g. a titanium foil of $1\frac{\text{mg}}{\text{cm}^2}$ specific thickness [84].

The high radioactivity, the low availability and the associated low technical application mean that the actinide materials used are much less well researched than the target materials for cold fusion. Nuclides heavier than ^{239}Pu are actually only available from high-flux research reactors such as the American Oak Ridge National Laboratory (ORNL) and the Russian Research Institute for Advanced Reactors (RIAR) in Dmitrovgrad [174]. Samples of heavy actinides obtained typically have to be purified by chromatographic methods [177]. Following the purification processes, the samples are typically introduced into the MP process in dilute aqueous nitric acid.However, analysis of whether non-radioactive by-products from the purification process, such as ion exchange resins and their decomposition products, as well as other organic molecules and foreign ions from solvents or acids, have been inadvertently carried along is generally not performed. The high radioactivity inherent in the process necessitates a restriction to radiochemical characterisation, with the focus being directed towards the separation of other radioactive nuclides.The MP process remains inadequately comprehended, thereby impeding the establishment of satisfactory process control measures.Consequently, the target films exhibit diminished definition and reproducibility with regard to consistent thickness and quality, analogous to target thin films composed of stable nuclides for cold fusion.

1.3.3. Change under irradiation

The irradiation behaviour of targets for SHE experiments has rarely been investigated spectroscopically, typically limited to imaging methods such as atomic force microscopy (AFM) and scanning electron microscopy (SEM). During irradiation, targets are monitored by measuring projectiles that are elastically scattered from the target nuclei. In none of the experiments with PbS compound targets was a significant reduction in the rate of scattered projectiles observed, which would indicate a loss of material or a change in the target material. This was affirmed by weighing and x-ray analysis (energy dispersive X-ray spectroscopy, EDX) of irradiated targets in comparison with non irradiated targets as a standard. Yet, in regions where the beam hit the target intensively the deep velvet black color of the surface gets a slight metallic glint [99]. Irradiation with SHI thus induces changes that can already be detected with the naked eye. As can be seen in Fig. 1.8 (a1-a2), PbS forms an almost sponge-like structure with walls roughly aligned in one direction that, upon irradiation, does not change in principle. Only the walls seem to fold up and criss-cross more randomly, after irradiation [100]. For Bi_2O_3 targets, the target sur-

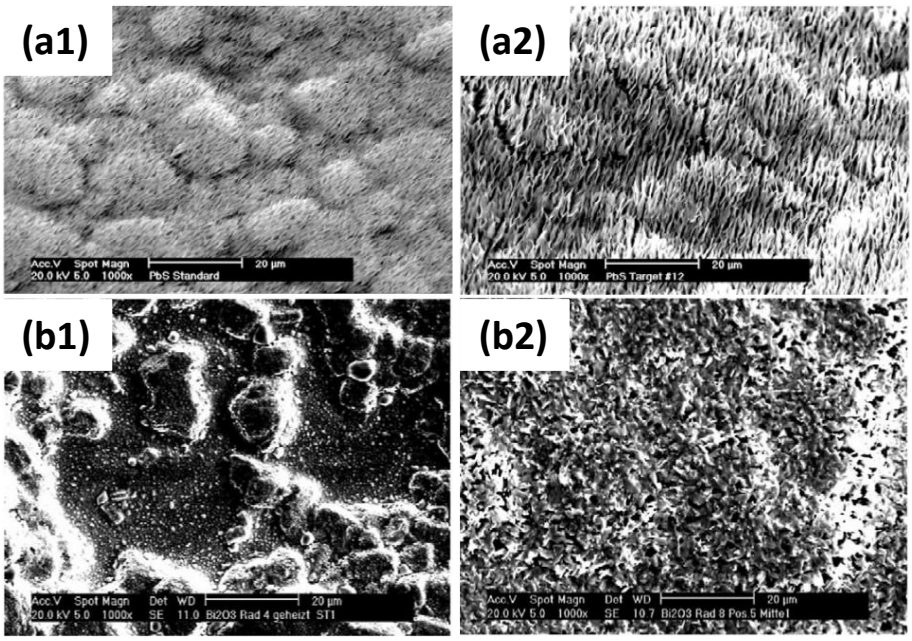

Figure 1.8.: Pictures of a Scanning Electron Microscope (SEM) of a PbS-layer as evaporated (a1) and irradiated with a beam dose of 3.5×10^{17} ^{40}Ar-particles (a2). From ref. [99] SEM pictures of unirradiated Bi_2O_3 targets (b1) and of Bi_2O_3 targets after irradiation with a beam dose of 7.4×10^{18} ^{70}Sn-particles (b2) From ref. [100]

face already has some defined structure and a surface roughness before irradiation (Fig. 1.8 (b1)). After irradiation an important structural change is obvious. The surface is no longer a continuous layer but more sponge-like. This is even more obvious at the higher magnification. What really happens during bombardment and how this resulting structure affects the yield in heavy element synthesis was not elucidated [100]. Changes in the chemical composition of the target layers, like loss of volatile compounds like oxygen and sulphur is not reported in literature. Online measurements of Bi_2O_3 targets by electron beam confirm that continued irradiation leads to a reduced coverage of the carbon baking with bismuth compounds [94, 124].

The targets required for hot and warm fusion are produced from actinides using the MP process. The incomplete understanding of the MP process results in poor process control, i.e. the films produced can only be stored to a limited extent or cannot be used directly in the SHE experiment. Over the years, conditioning at the heavy ion accelerator has established itself as a viable process [20, 85, 129]. For this purpose, the MP thin films are exposed to successively higher ion currents at the accelerator. Since the actinides used are α-emitters, changes can be observed through irradiation (Fig. 1.9). The broader distribution of α-energies measured before conditioning, gradually narrowed and reached saturation after irradiation with a radiation dose of 1×10^{18} ions. Further irradiation did not induce any further changes in the α-spectra. From the relatively sharp low-energy edge, the authors concluded that a homogeneous

layer developed, that a not well-defined structure, even containing residues of the solvent, transformed into a homogeneous transparent glassy layer during irradiation. This layer is said to be very resistant to increasing radiation doses. An optical inspection of the targets after the experiment supported this conclusion [85]. Further examination methods of the targets after irradiation were announced in both publications [20, 85], but have not been published so far.

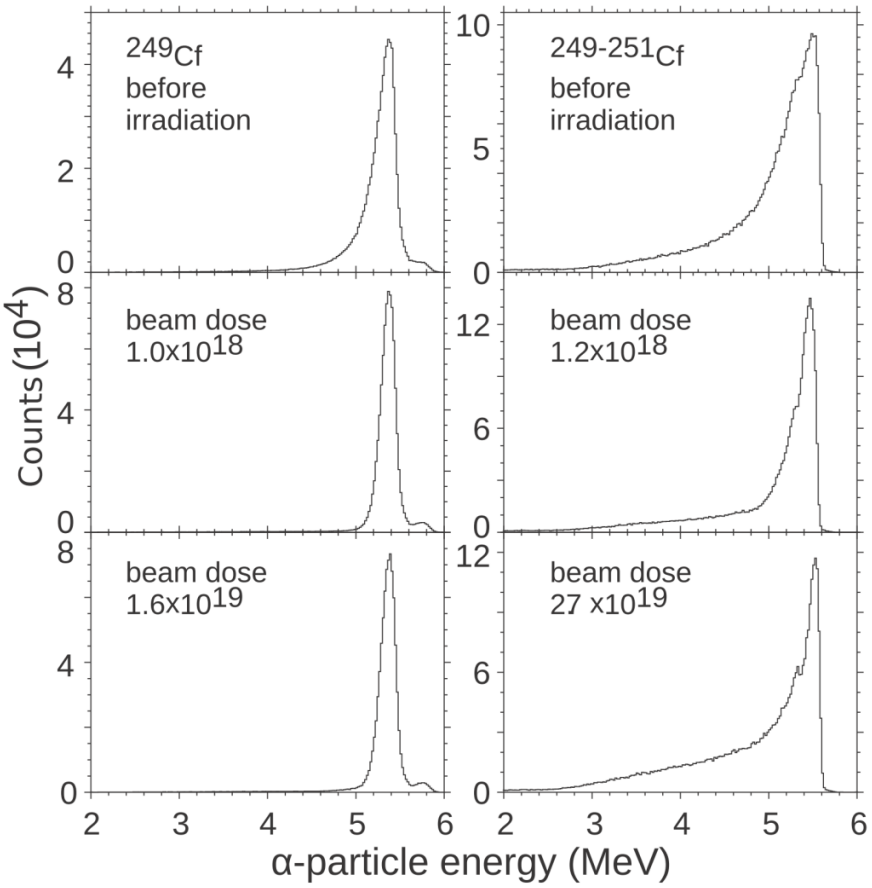

Figure 1.9.: Spectra of α energies measured from the ^{249}Cf (left panel) and mixed-Cf (right panel) rotating targets with the detector system in the focal plane of DGFRS (**D**ubna **G**as-**F**illed **R**ecoil **S**eparator) before irradiations and after given beam doses of ^{48}Ca projectiles passing through the targets. From ref. [20]

Changes in surface morphology have been described in work with lanthanide substitutes (Fig. 1.10) [129]. If fresh MP films are characterised by a cracked morphology, irradiation seems to melt these cracked surfaces into a closed film. Attempts to visualise changes in the chemical composition of MP films by irradiation using energy dispersive X-ray spectroscopy have not yielded clear results. X-ray diffraction methods were characterised by a poor signal-to-noise ratio. The investigations on lanthanide

substitutes thus confirmed the change in thin film morphology assumed from the altered α-spectra. They also underlined the analytical challenge of clearly characterising cracked thin films spectroscopically on comparably thicker titanium foils. The known problems in the instrumental analysis of MP films will be discussed in detail later. For comparable analyses on irradiated actinide targets [85], further radiation protection and legal requirements would have to be met, which further complicates work in this area.

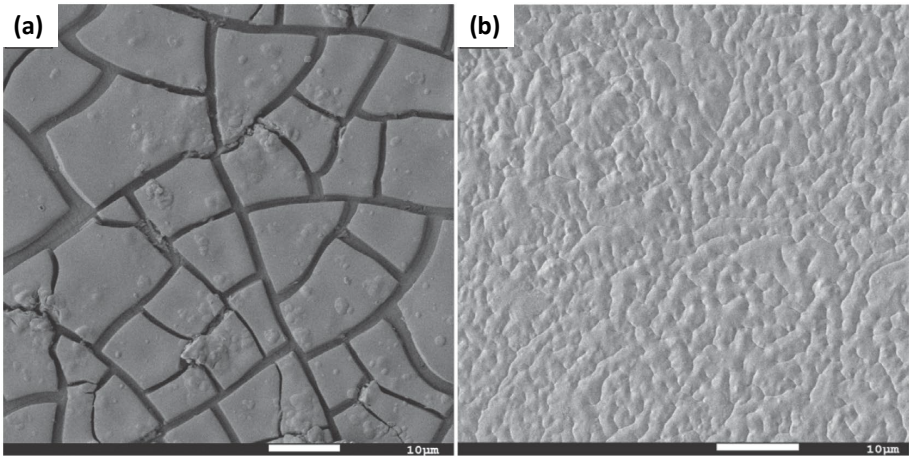

Figure 1.10.: SEM images of an irradiated ^{160}Gd target, in separate experiments, with ^{45}Sc and ^{50}Ti beams. The left panel shows the edge of the target, i.e., area outside the beam path and the right panel shows the irradiated area of the target. The images were taken with a 1400 to 1600 magnification. The total target ion exposure to ^{45}Sc and ^{50}Ti beams, center-of-target energies of of 3.8 to 4.7 $\frac{\text{MeV}}{\text{u}}$, was 3.2×10^{14} ions. From ref. [129]

1.3.4. Backing or substrate

The choice of a proper backing material is a crucial point in many SHE studies. Very often a material with a low Z-number is used in order to prevent the production of interfering transfer products obtained in reactions with the beam. In general, backing foils should only be made of materials with Z<55 (Cs), since heavy elements produce α-active nuclei with the common projectiles and thus increase the background in α-spectroscopy (Fig. 1.11). High α-background radiation makes the detection of new SHE more difficult in experiments. In addition to a low atomic number, the backing materials should be easy to process into mechanically stable films, as well as being sufficiently chemically stable for the most common manufacturing process, molecular plating. The six most common elements for backing films are highlighted in yellow (Fig. 1.11). Normally, deposition is performed on commercially available self-supporting foils with thicknesses ranging from 5 µm up to 50 µm. The baking foils should always be as thin as technically possible, with a reproducible consistent thickness and of course no pinholes [46]. Thinner foils made from backing material are often not commercially available and have to be produced

at great expense in specialised laboratories [118, 119].

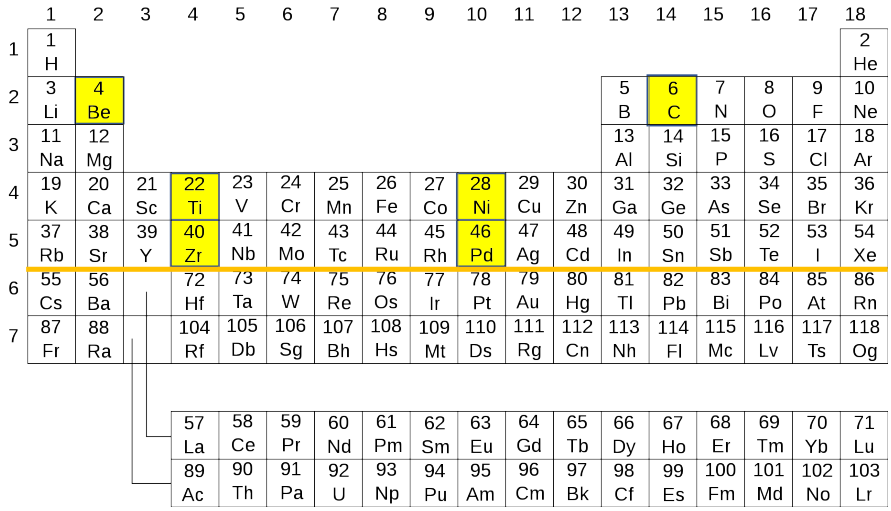

Figure 1.11.: PSE with the classic materials for target backings highlighted in yellow. All elements below the orange line are not suitable as backing materials because they form α-emitters with the usual projectiles, which would drastically complicate detection in SHE experiments.

In summary, baking materials must meet the following criteria, according to [119]:

Low Z - Material with a low Z is preferable, to minimize the production of α-emitting isotopes in the interaction between projectile and the backing material that would contribute to unwanted background. These experiments often rely on the unambiguous identification of single nuclei of the heaviest elements via detection of their radioactive decay, mostly α-decay.

Mechanical and thermal stability - Mechanical and thermal stability is needed for an acceptable handling and good durability in the beam. This is especially important for rare and highly radioactive actinides.

Good adhesion - To guarantee a good adhesion of the target material to the backing, the thermal expansion coefficient of the backing material should be as similar as possible to that of the target material.

Chemical stability - There must not be any chemical reaction between target material and backing material.

Thickness - To minimize the straggling and the energy loss in the backing the backing layer should be as thin as possible without losing too much in mechanical stability.

	LINAC-S^3	
Beam	^{48}Ca	^{70}Zn
E [MeV/u]; I [pμA]	5;1	5;1
$\sigma_\theta \times \sigma_r$ [mm²]	0.5×2.5	0.5×2.5
$\varnothing_{wheel}$ [mm]	160	670
Targets	$Ti + Cm_2O_3$	$C + Bi_2O_3$
Thickness [μg/cm²]	900 + 450	40 + 226
dE [MeV]	12.3 + 4.0	1.4+3.5
dP/S_{circ} [mW/mm²]	3.33 + 1.08	0.09+0.23

Figure 1.12.: Parameters and power density in targets and backings according to the conditions at the LINAC-S3 setup at the GANIL research facility in France. From ref. [94]

The thickness of the backing films has a decisive influence on the performance of a target system in an SHE experiment. The aim is to deposit the target nuclides on the thinnest possible backing, since the ion beam loses a lot of energy in the backing, in order to come as close as possible to the ideal target system (Fig. 1.4), i.e. a self-supporting target system. The usual loss of ion beam energy is shown here [94] for hot and cold fusion (Fig. 1.12). With the same energy per nucleon and the same particle flux, two typical technically up-to-date target systems for the two types of fusion reaction are shown here. The target system on the left for hot resp. warm fusion with ^{48}Ca consists of a titanium backing (900 $\frac{\mu g}{cm^2}$ corresponding to 2.0 μm thickness) on which curium has been deposited by molecular plating. The complex composition of the MP thin films is approximated with curium sesquioxide in this publication [94]. The target system on the right (Fig. 1.12) for cold fusion shows a compound target where bismuth oxide has been deposited on a very thin carbon film (40 $\frac{\mu g}{cm^2}$ corresponding to 0.2 μm thickness). In this case, the representation of the bismuth thin film as sesquioxide is not an approximation, but the result of precise reaction control in the production of these targets. Precise reaction control, which the molecular plating procedure for actinide targets for hot fusion experiments does not allow, yet. The thicker titanium backing thus absorbs about ten times more beam energy than the thinner carbon backing (dE in MeV). The differences in the deposited energy per area (dP/S_{circ} in $\frac{mW}{mm^2}$) are even greater, i.e. the thicker titanium foil heats up much less than the thinner carbon foil with the same irradiation, because a beam with a current of 1 pμA deposits approximately 1 W of heat for every MeV of energy loss through the target [137]. Since heat generation during irradiation, as described in the previous sections, must be dissipated with great effort, thinner carbon foils are actually the better backing material. However, although the production of molecular plating targets on carbon foils for accelerator experiments is described in the

literature [63], in practice highly radioactive rare actinides are shied away from being deposited on such a fragile backing. In order to ensure the safety of the production and installation of the finished target wheels in the experiment, even the most recent SHE experiments are still predominantly carried out with titanium backings [182].

1.4. Ideal target thickness

Besides the issue of thermalized energy, there are two factors that limit the optimum thickness of a target used in a superheavy element experiment. The first of these is the range of projectile energies over which evaporation residues are produced. The second factor limiting target thickness is the recoil range of the evaporation residues. In the cold-fusion reaction, energy loss of the beam is the factor limiting target thickness, while in the hot-fusion reaction the low recoil velocity of the evaporation residues is the limiting factor [137].

The transmission decreases due to scattering as the target thickness increases, but the *yield = (target thickness · transmission)* growth reaching the saturation. Targets must be optimized while maximizing the yield. The optimal target thickness is typically in the range 0.3 to 0.5 $\frac{\text{mg}}{\text{cm}^2}$ and depends on reacting partners, reaction characteristics, the energy of bombarding particles, composition of the target, and the acceptance of the used separator. The highest yields were achieved with metallic targets; the second best were oxides, followed by flourides. The stoichiometric ratio between Actinides and oxygen, (e.g. U_3O_8 and UO_2 , CmO_2 and Cm_2O_3 oxide are known) plays a minor role. For "very thick" targets, used in "chemical" experiments without pre-separation, the optimal thickness depends mainly on the width of the excitation function. These functions for the complete fusion reactions are approximated with the Gaussian and for ^{48}Ca + Actinide reactions, they have FWHM of about 10 MeV (Fig. 1.13). Using the specific energy loss, this value will be recalculated with regard to the target thickness, which gives the dispersion of ≈ 0.5 $\frac{\text{mg}}{\text{cm}^2}$ for oxide targets. Thus, the target having the thickness (1.5 $\frac{\text{mg}}{\text{cm}^2}$) can be considered as infinitely thick [36].

Regardless of the asymmetry of the reaction, production of superheavy recoils is not significantly increased by increasing the target thickness beyond 2.0 $\frac{\text{mg}}{\text{cm}^2}$. In practice, the momentum acceptance criteria of on-line separators are significantly more strict. The areal densities of lead and bismuth targets in online cold-fusion physics experiments are usually on the order of 0.5 to 1.0 $\frac{\text{mg}}{\text{cm}^2}$, while the actinide targets in ^{48}Ca irradiations rarely exceed 0.5 $\frac{\text{mg}}{\text{cm}^2}$ [137], mostly to the inherent limitations of the molecular plating process. Thus, actinide targets for hot fusion reactions, whether the favourable thickness limit is 1.5 [36] or 2.0 [137] $\frac{\text{mg}}{\text{cm}^2}$, fall well short of these thicknesses. Previous manufacturing methods for actinide targets, especially molecular plating, fall well short of 1.0 $\frac{\text{mg}}{\text{cm}^2}$ for the production of actinide

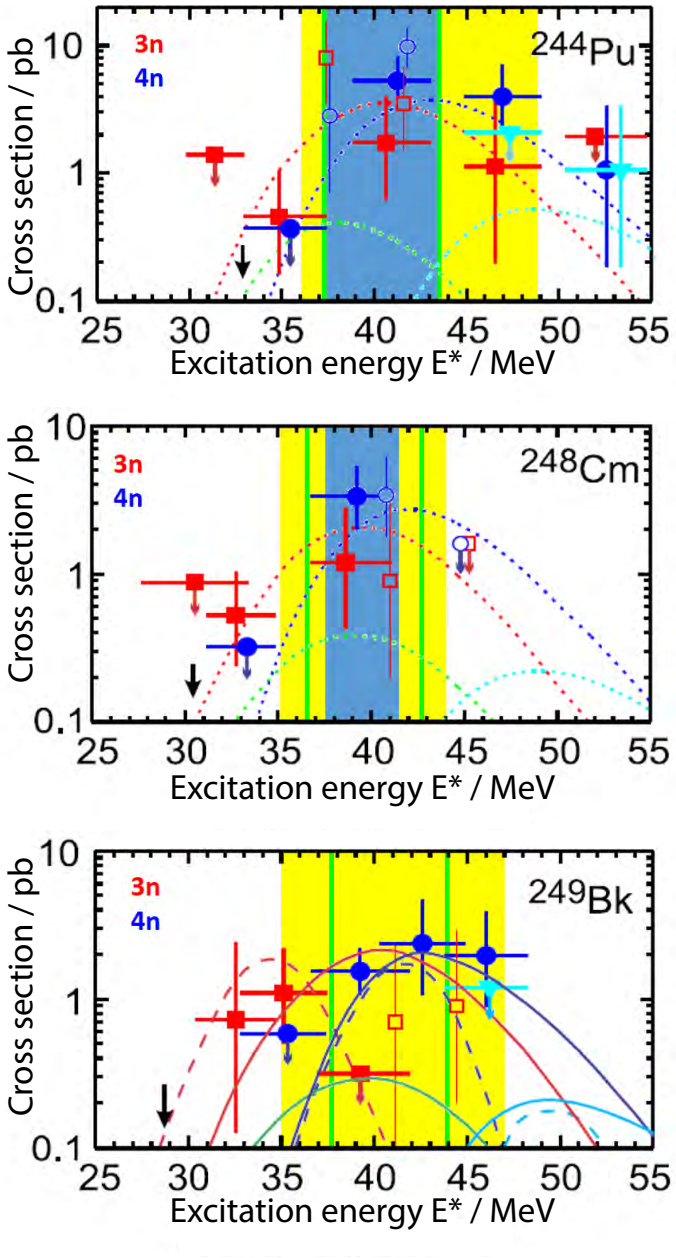

Figure 1.13.: Excitation functions for production of elements 114, 116 and 117 (from *Oganessian et al. 2015*, [152] where all other excitation functions with actinide targets are also included). Filled data points: from FLNR Dubna (cf. from *Oganessian et al. 2015*, [152]), open ones from TASCA (^{244}Pu, [40] ^{249}Bk [97]) and SHIP (^{248}Cm [85]). Lines are theoretical models (references mentioned in from *Oganessian et al. 2015*, [152]). Blue: Energy range that is swept in the existing TASCA targets (810 $\frac{\mu g}{cm^2}$ ^{244}Pu and 530 $\frac{\mu g}{cm^2}$ ^{248}Cm). Green lines: Energy range within 800 $\frac{\mu g}{cm^2}$ thick targets. Yellow: From a nuclear physics point of view, this is a useful range of the excitation function.

target wheels [39]. Thus, the experimentally possible target thickness and thus the theoretical maximum production rate for SHE is not achieved. Furthermore, the discussion of stoichiometric ratios of oxides or other counter anions in the actinide thin films is futile if one cannot control the chemical composition of the actinide thin films in the MP process. Nor have the necessary analytical equipment to control this. Missing from the discussion of optimal target thickness in the literature is the fact that the density of actinides in metallic form changes drastically to their compounds. The effect is much larger than for the classical target elements, lead and bismuth, for cold fusion. These detailed chemical questions have so far been largely ignored in the calculations for optimal target systems for actinides, although, for example, the density mentioned is an important quantity in the widely used software for such calculations [232]. The incomplete understanding and thus the incomplete control of the molecular plating process can be named as the main cause here.

1.5. Molecular Plating

Molecular plating (MP) represents one of the most commonly employed techniques for target preparation. The MP method was developed in the 1960s by *Parker and Falk* [162], extensively characterised with the methods of the time [157, 160, 159] and then directly applied for target production for basic fundamental research [163, 161]. In molecular plating, the desired lanthanides or actinides in their nitrate or chloride form are dissolved in dilute nitric acid [177] or hydrochloric acid [96] and as such added to an organic solution (isobutanol/isopropanol [177], N,N-dimethylformamide [142] or pyridine [216]). Electrochemical deposition occurs at high voltages (up to $\frac{\mathrm{kV}}{\mathrm{cm}^2}$) and low current densities ($\frac{\mathrm{mA}}{\mathrm{cm}^2}$) compared to other electrochemical processes used for f-block metals [107], i.e., lanthanides and actinides. While constant voltage is usually preferred in conventional electrochemical depositions [90, 217], MP is done at constant current [177, 107]. It is typically conducted in a cell comprising two electrodes, with the cations being deposited on the working electrode, that is to say the cathode (see Fig. 1.14). The most frequently used approach in molecular plating is deposition from isobutanol/isopropanol (9:1) to which the actinide element is added in a small volume of dilute nitric acid solutions [177, 206]. More recent approaches also studied N,N-dimethylformamide (DMF) as a solvent [142]. The MP method also connects well to established separation and purification methods for rare actinide isotopes, e.g. [177], which is why it has proven itself for numerous experiments in basic research [42, 43]. Precursor syntheses are not required and the undried nitrates and chlorides obtained from the purification steps can be directly used in their aqueous acids for the MP process. Non-deposited material can be extracted from the supernatant solutions with reasonable effort, and the deposited thin films can also be detached from the support material rather easily without having to dissolve large amounts of support material, thus making the reprocessing of rare actinides accessible [177, 206]. The reproducibility of the yields is less satisfactory [177] leading to rather large fluctuations, as is obvious from the original publications [157, 160, 159]. Another limita-

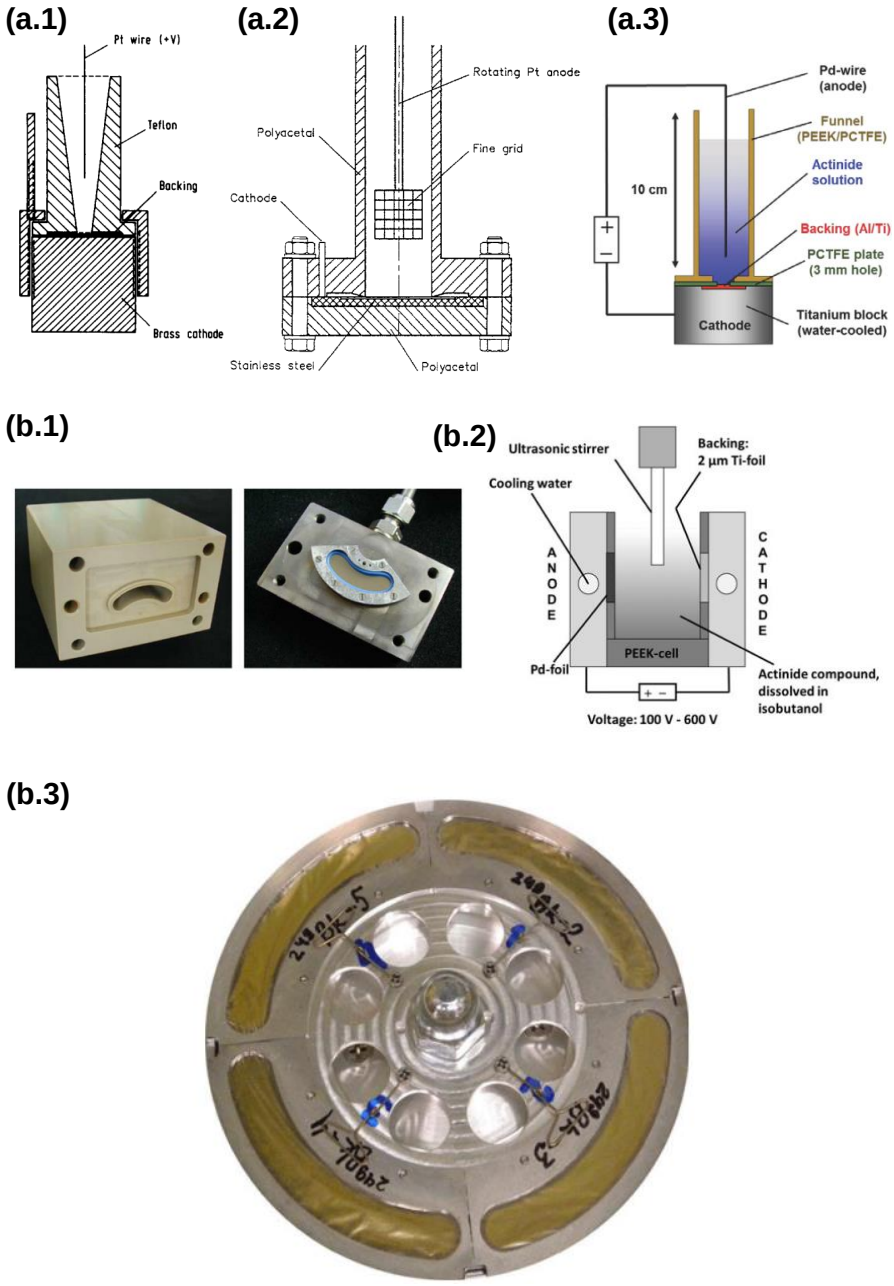

Figure 1.14.: MP construction for small round targets in the shape of a chimney over the decades (a.1) *Trautmann and Folger 1989* [206], (a.2) *Ingelbrecht 1997* [89], (a.3) *Eberhardt 2018* [43]. When producing banana-shaped segments for target wheels (b.2 and b.3), [177], a different set-up has proved successful: the segments, which are covered with foil, are installed at the side of the MP cell (b.1 [45]).

tion of the MP method is the achievable areal density. More than 800 $\frac{\mu g}{cm^2}$ are typically not deposited in one step [51, 89, 1], at least not in complex geometries as they are used at many SHE laboratories [91]. To achieve thicker targets, several modifications of the MP process were adopted, including multiple calcination and repetition of the MP process [231], double-sided targets [19] and reduction of the deposited thin film in a hydrogen atmosphere to then produce intermetallic layers [210] with the metallic substrate. In recent years, new electrochemical approaches [107, 117], or approaches outside electrochemistry [70], provided access to thicker targets.

1.5.1. History

Even in the original publication [162] the essential aspects of the process are clearly stated: Firstly, there is no electrolytic dissociation, i.e. the deposited metals are not reduced; secondly, very high voltages and very low electrical currents are used, whereas the opposite is the case with conventional electrochemical deposition; thirdly, the method is easy to use; and fourthly, the material is deposited in high yield. The high yield, the fact that the target material used is very rare, and the simplicity of the application, which often requires deposition behind thick shielding against radioactivity, explain the lasting success of the method [175]. The low current densities of the MP process, mA/cm^2 instead of A/cm^2, prevent excessive production of hydrogen gas at the cathode, gas bubbles that would interfere with the formation of a thin film [89, 214]. *Parker and Falk* extended the method to many metals [157, 159, 160, 163] and used it to produce targets for fundamental nuclear physics research [161].

Over the decades, the MP method has been established for a wide variety of targets for a wide variety of experiments in basic research [206]. The ease of use and relative robustness of the method allowed targets to be produced in a wide variety of shapes, so that requirements from ongoing experiments, such as conversion to target wheels, could be easily implemented. This has resulted in a large number of different cell designs over the decades and for different applications, see Fig. 1.14. To date, a chimney-shaped structure has been established for the production of simple round targets. The coated foil is installed at the bottom of the structure, modern approaches vary the anode shape [101], for example, or actively cool the cathode [43] for a better result. The basic advantage of this design is that only one seal has to prevent the volatile solvents from leaking out, and the structure also allows the seal to be pressed on without having to exert pressure on the target foil. The frequently small volumes often make stirring of the electrolyte solution unnecessary.

In order to coat the individual segments of target wheels using molecular plating, new set-ups had to be developed; the main problem here was and is the sealing of the cell against the solvents used. The larger

volumes required necessitated the use of stirrers [43, 45, 46].

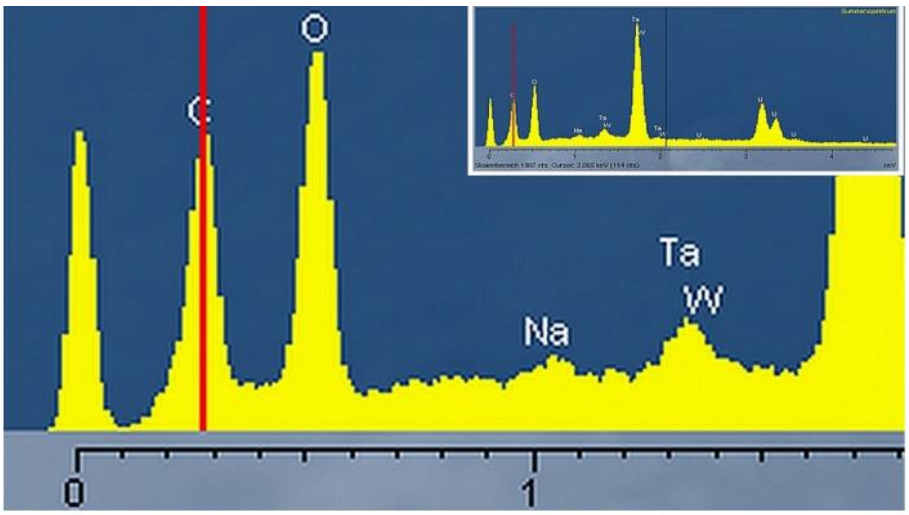

Figure 1.15.: Close up of an energy dispersive spectrum of uranium on a tantalum backing. Nitrogen is not detectable in the spectrum. The small picture shows a larger energy range. From ref. [113]

1.5.2. State of knowledge about the composition of MP thin films and the mechanism of deposition

The simultaneous establishment [6, 58, 59, 175] of the term 'molecular plating' established certain mechanistic ideas, which were often only proved or disproved by analytical methods decades later. Prior to the publication of the molecular plating process, *Hansen 1959* [76] published an attempt to mechanistically explain the deposition of lanthanides and actinides from aqueous mixtures with organic solvents. As no publication on molecular plating contains any references to solvent drying processes and the desired actinides are introduced in the form of aqueous acids, *Hansen's* approaches have long been used for the mechanistic explanation of the MP method [206, 212]. As has been previously stated, the deposits on the cathode are not composed of the metals through the direct reduction of ions in solution; rather, they are comprised of insoluble compounds, which are most commonly hydroxides. The electrodeposition of uranium and other actinides from aqueous media occurs via a precipitation reaction within a hydroxyl ions layer that forms at the cathode surface. Indeed, if the direct reduction of the elements of interest is excluded, cathodic deposition will occur as a result of a reduction in the hydrogen ion concentration at the cathode, accompanied by a corresponding increase in the hydroxyl ion concentration at the cathode surface. This forced increase makes the precipitation of oxy-hydroxide compounds possible, which could not be precipitated under common conditions since its solubility product could not be reached. Considerable effort has been made to study the theoretical and experimental conditions for this process

and to optimise electrodeposition setups and electrodeposition parameters affecting deposition yield and energy resolution of the sources [34].

As *Parker and Falk 1962* [162] observed, the most notable distinction between the method to be delineated and the conventional electrodeposition process is the absence of comparable electrolytic dissociation during the passage of current. Additionally, in the present case, the same chemical compound, chloride or nitrate depending on the circumstances, is deposited at the cathode as the original substance dissolved in the electrolyte. It was therefore assumed that the lanthanides or actinides were incorporated into the thin film in their used form, i.e. as chlorides or nitrates.

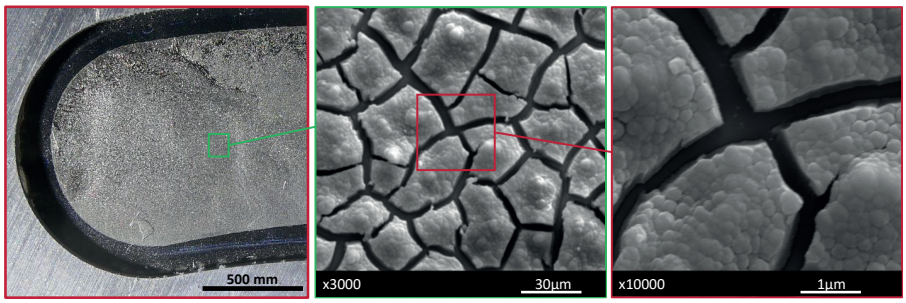

Figure 1.16.: (Left) Photography of a segment of the TASCA (**T**rans**A**ctinide **S**eparator and **C**hemistry **A**pparatus) target wheel [91, 118]. The thin lanthanum film (thickness 500 $\frac{\mu g}{cm^2}$) deposited on a 2.1 µm thick titanium substrate is glued to the frame of the target wheel. (Middle and right) Scanning electron microscope images showing the typical cracked surface morphology of targets produced by molecular plating.

Thermogravimetric, EDS and IR analyses conducted by *Ramaniah et al. 1975* [169] revealed the absence of nitrates in MP films. In particular, the IR analyses of uranium films demonstrated a U-O stretching vibration of UO_2^{2+}, which led to the assumption that uranium was deposited as an oxide or hydroxide. Furthermore, the addition of phenolphthalein revealed the presence of water in the isopropyl alcoholic solution, and a hydroxide-rich layer was observed at the cathode. Consequently, the hypothesis proposed by Parker regarding the deposition of nitrates as a chemically unchanged molecular species was refuted. Later work confirmed the formation of complex hydroxide films [155, 179]. Nevertheless, the distinctive characteristics of uranium (U) and plutonium (Pu), with their higher oxidation states (+6 and +4, respectively, being the most stable), differ from those of the lanthanides and post-plutonium actinides (+3). This could potentially lead to the formation of MPs with a completely distinct electrochemistry [214]. Consequently, the analytical outcomes of MP studies on uranium films may not be directly applicable to these target materials.

Liebe et al. 2008 [113] attempted to elucidate the mechanism of the MP process using spatially resolved X-ray microanalysis (EDX) and neutron activation analysis at the TRIGA research reactor in Mainz [44].

Their work confirmed the absence of nitrates in the thin films for both uranium and lanthanide depositions. Based on the strong oxygen signals in the EDX spectrum, they described the MP thin films as oxides, see Fig. 1.15, despite the presence of an equally robust carbon signal. However, the authors also point out the problems of thin film analysis of MP films on titanium substrates, e.g. the natural oxide layer of titanium and the LM transition lines interfere with analysis by X-ray methods such as X-ray microanalysis or X-ray photoelectron spectroscopy (XPS). XPS is usually less affected due to its better spectroscopic resolution. The authors also used tantalum backings, which would of course be completely unsuitable for SHE target fabrication, see Fig. 1.11. Another important finding of the authors was that spatially resolved methods bypass the challenging morphology of MP films (see Fig. 1.17 and 1.16).

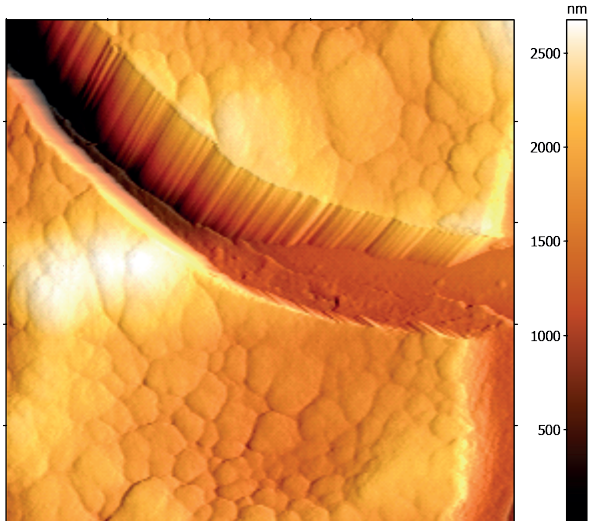

Figure 1.17.: Atomic force microscopy image ($2.5 \times 2.5\,\mu m$) of an unirradiated La MP thin film (thickness $500\ \frac{\mu g}{cm^2}$), deposited on a thin titanium foil ($2.1\,\mu m$).

Vascon's [214] extensive work on the molecular plating process focused mainly on the morphology of the thin films, but also on their modification, which will be discussed in more detail in the following section. His studies using XPS provided valuable information on the chemical composition of MP thin films. The XPS studies also demonstrated that in lanthanide MP thin films, the nitrate or chloride precursors are not incorporated into the thin film. However, as observed by *Liebe et al. (2008)* [113], carbon is the predominant element in the atomic composition of the MP films, accompanied by oxygen. The use of sputtering methods demonstrated that this carbon species is not a surface impurity, but rather, it is present throughout the entire thin film. The carbon species was identified as a carboxylate, and the electrochemical decomposition or oxidation of the alcoholic solvents used was assumed to be the cause, see Fig. 1.18. However, *Vascon et al. 2012* [217] highlighted the inherent challenges of XPS analysis of MP thin films, including the challenging morphology and the tendency of non-conductive thin films

to become electrically charged, which can impede the clear identification of measured chemical shifts. *Vascon et al. 2013* [216] also showed that the carbon species is incorporated into the film itself during molecular plating and is not carried into the film by processes in the ambient air; thin films were produced under an inert gas atmosphere for this purpose. It was also shown that these carbon species are not only formed in the frequently used alcoholic solvents, i.e. mixtures of isopropanol and isobutanol, but also in dimethylformamide (DMF).

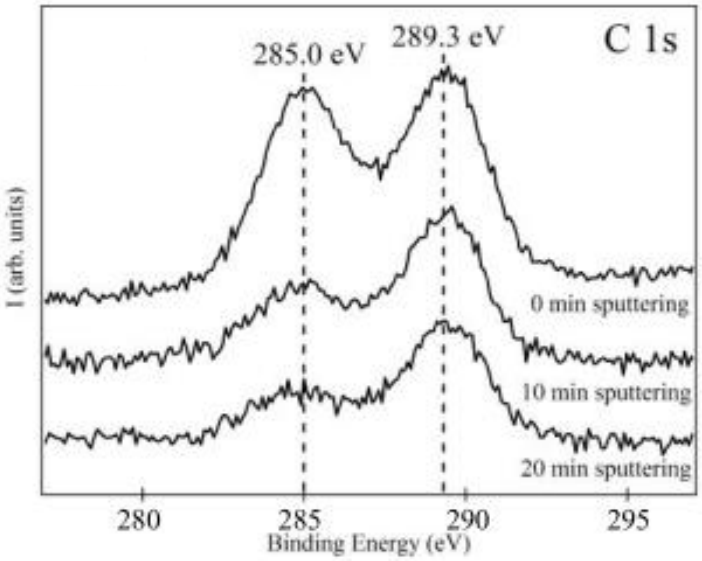

Figure 1.18.: The C1s spectra show the presence of two components: the C 1s peak at 285.0 eV is aliphatic carbon of the mixed isopropanol/isobutanol solvent. The peak at 289.3 eV can be attributed to COOM -metal carboxylate-groups formed during the plating process by solvent electrolysis. From ref. [217]

More recent work gave first insights into the chemical composition by means of X-ray photoelectron spectroscopy (XPS) [142, 217, 28, 189]. These studies clearly showed that no reduction of the metals takes place, which is in line with common models for the electrochemistry of the f-block metals. Furthermore, oxygen and carbon are co-deposited in larger quantities. Carbon was detected as a carbonate-like and an aliphatic species [142]. For oxygen, a clear differentiation between an oxidic, hydroxydic or carbonyl species was not possible with XPS. Diffraction methods were unsuccessful on fresh MP films, while oxycarbonates, a known thermal degradation product of carbonates and carboxylates of f-metals, were detected on annealed MP films [28, 29]. Quantification attempts by conventional energy dispersive X-ray spectroscopy (EDX) in the course of scanning electron microscopy (SEM) were unsuccessful due to the difficult morphology [129] of the samples. Conducting classical electrochemical investigations of the MP process pose challenges due to the high voltage densities needed [107], which render off-the-shelf potentiostats ineffective. Custom-made potentiostat setups are, therefore, necessary to conduct such investigations. Thus, the nature, origin and content of the observed carbon species, as well as the

exact electrochemical mechanism [189, 122], remain open questions of the MP process. In their 2016 publication, *Choi and Chung* [28] investigate the production of lanthanum thin films and their subsequent calcination at temperatures of 700K and 900K, respectively, the authors employ X-ray diffraction (XRD) for the analysis of their MP thin films. The use of XPS enabled the authors to demonstrate that untreated MP films contain a carbon species. The publication does not include comprehensive XPS spectra of carbon. XRD analysis revealed the absence of any chemical species in non-calcined MP films, which were found to be too amorphous. Following heating, the formation of oxycarbonates ($La_2O_2CO_3$) and, with increasing proportion, sesquioxides (La_2O_3) was observed,see Fig. 1.19. Oxycarbonates are recognised as thermal degradation products of lanthanide or actinide carboxylates, as well as their carbonates [108, 195, 196].

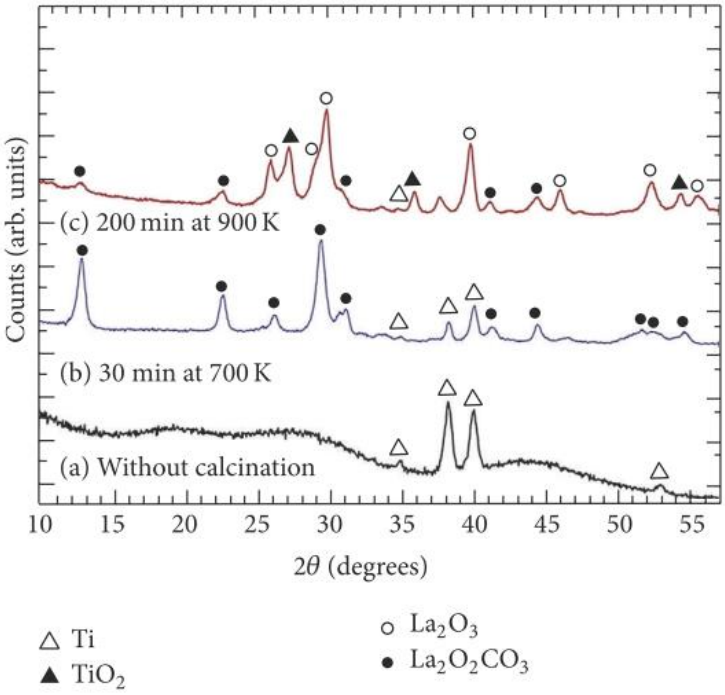

Figure 1.19.: X-ray diffraction patterns of three layers on Ti electrodeposited at 400 V: (a) without calcination and with calcination (b) at 700 K for 30 min and (c) at 900 K for 200 min. Without calcination (a), only the reflexes of the titanium backing are visible. From ref. [28]

In conclusion, the current state of knowledge regarding the composition of MP films and the mechanism of deposition, as it existed prior to the present work, can be summarised as follows: The residual moisture in the otherwise organic electrolyte is split electrochemically, resulting in the generation of a basic environment at the cathode. This environment facilitates the precipitation of lanthanides or actinides as hydroxides. The films contain a carbon species, identified as a carboxylate by XPS and interpreted as a decomposed solvent. Diffraction methods such as XRD are unable to provide usable results for un-

treated MP thin films, see Fig. 1.19. The hypothesis that the precursors, i.e. chlorides or nitrates, are incorporated into the film has been refuted. Calcination of the thin films leads via the oxycarbonates to the sesquioxides.

1.5.3. About the morphology of MP thin films

In addition to the intricate chemical processes involved in the molecular plating process, the formation of a stable, closed thin film with robust substrate adhesion is of significant scientific and technological importance. The microstructure of MP films is characterised by a surface that is broken and resembles dried mud, see Fig. 1.16 1.17 and 1.20. This surface structure is frequently referred to as "mudcracking." A more recent paper by *Kurth et al. 2016* [107], corroborates this observation of a broken surface, but attributes it to the oxidation behaviour of the neodymium (Nd) used in the MP process. Vascon's comprehensive research [214] on the surface morphology of MP thin films was also primarily conducted with neodymium as a non-radioactive alternative, yet yielded more precise insights into the various influencing factors.

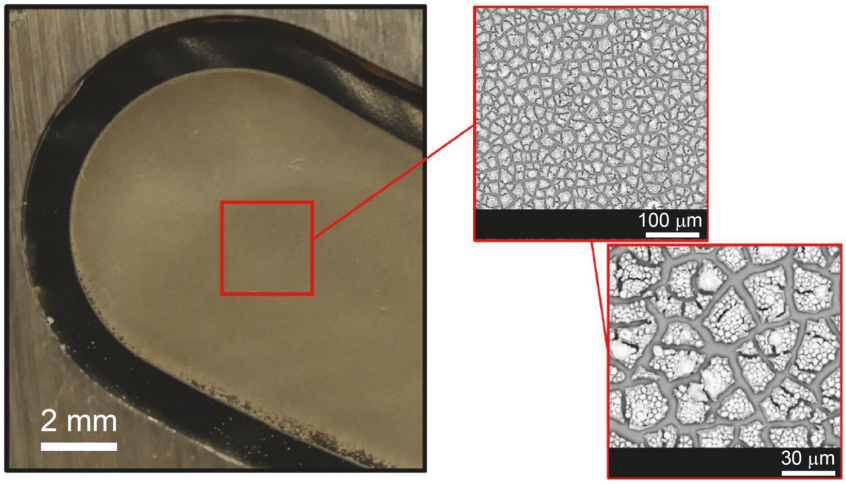

Figure 1.20.: Photograph (left) and SEM pictures (centre and right) of a 500 $\frac{\mu g}{cm^2}$ ^{147}Sm target on a TASCA segment. From ref. [119]

In order to optimise the production of smooth and crack-free layers for use as nuclear targets, a series of constant current density measurements were conducted using neodymium (Nd) as a model element.The variables selected for investigation were the plating solvent, electrolyte concentration, applied current

density and surface roughness of the deposition substrate.Additionally, the samples were subjected to drying in a variety of environments. The resulting deposits were then analysed using a range of techniques, including X-ray Photoelectron Spectroscopy (XPS), radiographic imaging (RI), atomic force microscopy (AFM), and scanning electron microscopy (SEM).The results obtained from the characterisation were employed to identify the principal parameters that regulate the molecular plating of smooth and crack-free layers. The investigation revealed that the roughness of the deposition substrate and the solvent utilised for plating emerged as two pivotal factors influencing the quality of the layers produced.It was observed that surface cracking occurred during the drying process when volatile solvents and deposition substrates with inadequate smoothness were employed.The utilisation of different drying environments, such as air and Ar, did not result in any discernible impact on the deposited layers.

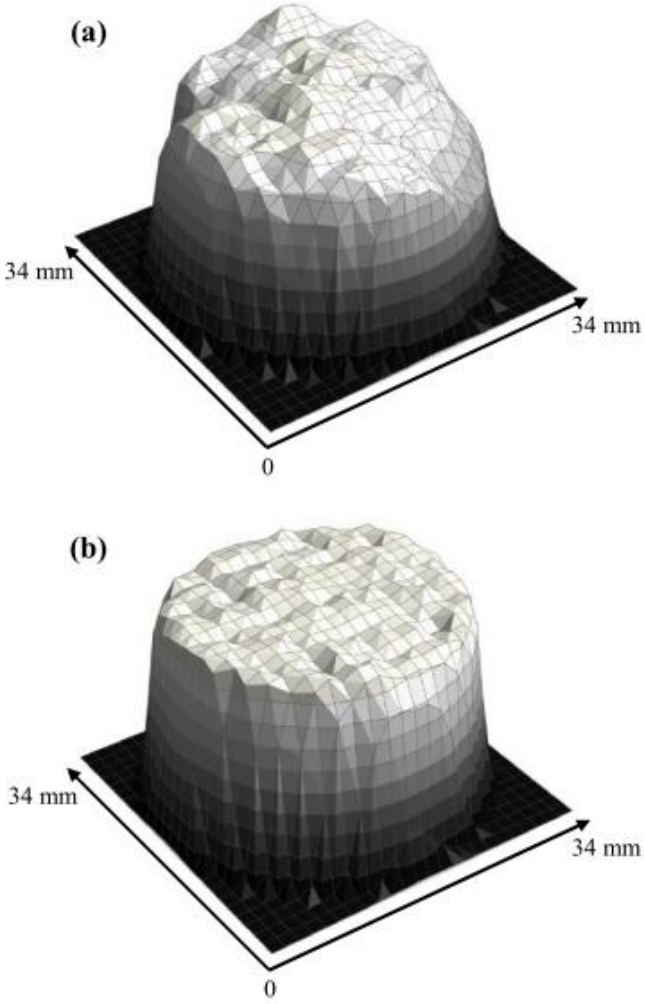

Figure 1.21.: Influence of substrate surface roughness and plating solvent. 3D graphs of radiographic imaging (RI), samples produced using molecular plating and the following substrate/solvent systems: (a) Ti and the “classic“ isopropanol and isobutanol mixture, (b) Ti and N,N-Dimethylformamide (DMF). From ref. [216]

The potential avenues for enhancing the surface structure are depicted in Fig. 1.21. While a comprehensive transition to the established target system of SHE basic research, namely thin titanium foils adhered to wheel segments, has not yet materialised, it exemplifies the hitherto untapped or unexplored prospects in the electrochemical deposition of lanthanides or actinides.

1.6. Modern electrochemistry

The work of *Vascon* and others demonstrates the continued fundamental possibilities of the molecular plating process, which can be enhanced through a deeper understanding and the resulting possibilities for modification and improvement. With a few exceptions, the molecular plating process is limited to target production, i.e. basic research in nuclear physics. It has no industrial significance. The electrochemical processing of lanthanides, indeed some of the actinides, but also other metals with similarly challenging electrochemical properties is of the utmost importance for the global economy. It is therefore important to remind ourselves once again of the basic electrochemical properties of these elements.

The metallic f-elements (lanthanides and actinides) react with water to form hydrogen and metal hydroxides or oxides. Therefore, the pure metallic f-elements cannot be deposited electrochemically from an aqueous solution [16, 107]. One approach to electroplating metallic f-elements is the use of ionic liquids [16, 60]. A more favourable alternative is deposition from anhydrous organic solvents [107, 117]. For this purpose f-element precursors have to be found, which can be easily synthesized and dried. The preparation should be simple and quantitative to allow a safe production from heavy actinides for target production. The chlorides and nitrates used for molecular plating are not suitable for this purpose, as they are poorly soluble in many organic solvents and difficult to dry [133]. The established drying methods for chlorides and nitrates are not suitable for the typical microgram approaches of target production. Nevertheless, the anhydrous chlorides enable the deposition of metallic lanthanides and actinides from dry N,N-dimethylformamide (DMF) [126]. In order to produce thick metallic targets, a suitable precursor must therefore fulfil the following conditions:

Synthesizability - it must be possible to perform the synthesis by simple means, quickly and quantitatively. Large preparative effort is not tolerable if losses of valuable actinides and exposure of humans and material to radioactive radiation are to be avoided. The direct production of the water-free form or the drying of the hydrate must be easy and completely possible.

Solubility - the water-free precursors must be completely soluble in the target solvent.

Stability - the counter-anion must be sufficiently electrochemically stable for successful electrodeposition. The resiliency against e.g. alpha radiation should be sufficiently high that the precursor survives the time between synthesis and galavinic deposition.

Separability - The counter anion must be easily separable from the desired f-element cation, therefore only weakly coordinating anions are suitable for precursor synthesis [154, 186, 106]. Too strong coordination of the anions in the complex also reduces the deposition efficiency [187].

The negative standard reduction potentials of lanthanides and actinides (f-elements) are higher than those of aluminium and are comparable to those of magnesium [31, 16]. The electrochemical deposition of magnesium and aluminium is only successful if the metal salts are present in a non-aqueous solution, e.g. an anhydrous organic solvent or ionic liquids. The salts used for this purpose must be easily synthesisable without any residual water content. Currently, the deposition of aluminium and aluminium-magnesium alloys for special requirements on small parts is carried out on a laboratory scale, where layer thicknesses of up to 50 µm are achievable [73], which corresponds to in 13.5 mg/cm^2. With modern electrochemical methods, it is therefore possible to produce significantly thicker layers of electronegative metals. A comparable electrochemical process for f-metals is not yet known for target-making.

1.7. Outline of the work

From this superficial introduction to the subject, it is clear that there are three fundamental issues to be addressed in this thesis:

Firstly, the molecular plating process needs to be better understood analytically, in particular the carbon species formed need to be identified.

Secondly, the MP thin film changes during irradiation with fast heavy ions (SHI). Again, the chemical processes involved are still completely unclear.

Third, as briefly mentioned in the penultimate section, modern electrochemistry allows chemically well-defined thin films of unprecedented thickness. This could achieve the chemical precision that allowed the cold fusion target technology to make the most of the experimental setups. This would make it possible to circumvent the limitations of the MP process and still get by with the smallest amounts of the heaviest actinides available, if modern methods of lathanide electrochemistry can be successfully applied to the traditional target techniques.

2. Publication I: Chemical conversions in lead thin films induced by heavy-ion beams

The following article was published as full article in *Nuclear Instruments and Methods in Physics Research Section A: Accelerators, Spectrometers, Detectors and Associated Equipment*, volume 1028, pages 166365 in 2022. It describes first irradiation experiments on different lead target systems.

2.1. Own contributions

The experiments presented were planned and carried out independently. The samples were prepared independently. The Raman measurements were carried out in the Materials Research Department, and were carried out after instruction on the measuring device. The evaluation of the data and the writing of the article were done completely independently.

Chemical conversions in lead thin films induced by heavy-ion beams at Coulomb barrier energies

C.-C. Meyer[1,2], A. Dragoun[1,2], Ch. E. Düllmann[1,2,3], R. Haas[1,2,3], E. Jäger[3], B. Kindler[3], B. Lommel[3], A. Prosvetov[3,4], M. Rapps[1,†], D. Renisch[1,2], P. Simon[3,4], M. Tomut[3,5], C. Trautmann[3,4], A. Yakushev[3]

2.2. Abstract

Superheavy elements are produced via fusion reactions, by bombarding thin target foils with intense beams of energetic ions with energies around the Coulomb barrier. Currently, production of rare isotopes relies mainly on the molecular plating (MP) method, which yields thin films of the desired target material on a backing foil. Intense heavy-ion beams are known to modify the film structure, which leads to deterioration of the targets over irradiation time. To gain a better understanding of the processes at a microsopic scale, comparative tests were carried out using Coulomb barrier heavy-ion beams provided from the UNILAC accelerator at GSI Darmstadt, Germany. For this purpose, targets of lead were prepared using MP and Drop-on-Demand inkjet-printing. Lead targets were baked-in and analysed by digital optical microscopy, scanning electron microscopy and confocal Raman spectroscopy.

2.3. Introduction

With ever increasing beam intensities of new accelerator facilities, the durability of nuclear targets under beam influence becomes more essential. Recent reviews [36, 148] have emphasized the need for a new generation of actinide targets for the synthesis of new super heavy elements. With the completion of new and more powerful accelerators being installed at major superheavy element labs [35, 199, 72] and R&D work towards a high-intensity linear accelerator ongoing at GSI Darmstadt and Helmholtz Institute Mainz, Germany [9], current target technology is reaching severe limitations [148]. Synthesis of the heaviest known elements was achieved using actinide targets [42]. These are frequently produced using the molecular plating (MP) technique [158, 206, 116, 217], in which the f-elements are electrochemically deposited from an organic solution at low current densities [114]. The use of organic solvents leads to high voltages during electrochemical deposition [90]. Since the f-elements are added in aqueous solutions, a metallic deposition of the f-elements is impossible [16]; reduction of the f-metal cations to the elemental state could not be observed under these conditions [216, 143, 218]. The advantage of the

[1]Department Chemie, Johannes Gutenberg-Universität Mainz, 55128 Mainz, Germany
[2]Helmholtz-Institut Mainz, 55128 Mainz, Germany
[3]GSI Helmholtzzentrum für Schwerionenforschung GmbH, 64291 Darmstadt, Germany
[4]Technische Universität Darmstadt - Materialwissenschaft, 64287 Darmstadt, Germany
[5]Institut für Materialphysik, Westfälische Wilhelms-Universität Münster, 48149, Münster, Germany

MP method is the high yield; disadvantages include the co-deposition of undesired by-products. There is also still no complete and uniform explanation of the chemical processes involved in the MP procedure [216, 28, 141]. Freshly produced target layers are quite sensitive to humidity and oxidation in air and often deteriorate during long storage times. To prevent these aging processes, freshly produced targets are usually converted into a long-term stable form. For this, the state-of-the-art relies on a reliable on-line conditioning procedure with heavy-ion beams at Coulomb barrier energies [9, 85, 20, 198], where the beam intensity is initially kept very low and is then stepwise increased to levels used in long production runs (order of 10^{12}-10^{13} ions s^{-1}). After this conditioning procedure MP targets can be successfully stored over decades and used in subsequent experiments. The exact nature of the processes on a microscopic scale has not been fully elucidated to date, though.

So, despite their decade long use, neither the MP process itself, nor the performance of MP targets in accelerator beams are fully understood. The main limitation in the past was access to state-of-the-art analytical facilities, due to the high radioactivity of the used actinides. This is why it is important to test new analytical approaches with non-radioactive substitutes first and then, if successful, to apply for access to the few laboratories that can examine highly radioactive actinide samples with modern analytical methods. A comprehensive systematic study of the beam performance of MP targets can be expected to give valuable insight into the chemical processes, and therefore aid the development of new target systems. In order to explore whether target conditioning is also possible without accelerator access, the ODIn [71] test setup was realised. This provides electron beams (up to 1.5 keV) and ions of gaseous elements (up to 5.0 keV).

The conditioning procedure [9, 85, 20, 198], leads to physical and chemical transformations, which have previously been described by studies using microscopic methods, like atomic force microscopy [216, 129, 220] and scanning electron microscopy [217, 129, 219]. During the conditioning process, however, a change in the alpha spectra of the actinide thin films is observed, i.e, the peaks become narrower and the prominent low-energy tailing, which is present in spectra of freshly produced MP layers, disappears. The phenomenon is explained by the evaporation of unwanted volatile components [20, 198] present in the fresh thin films, though, spectroscopic proof has not yet been provided. However, the loss of tailing in the alpha spectra indeed supports compacting and the loss of unwanted minor components.

Most f-element films are deposited on a thin foil, typically titanium or carbon foil of a few micrometer thickness [118]. To minimize the energy loss, which leads to unwanted target heating, these backing foils are kept as thin as possible. The current typical thickness (2.3 µm) is a compromise between mechanical stability, in order to be able to apply the target material safely, and the performance in the heavy ion beam. X-ray diffraction (XRD) studies of the deposited thin films proved to be challenging, due to the

amorphousness of uncalcined f-metal thin films produced by MP [28, 129] and because the metal foils used as substrate are always significantly thicker than the deposited f-metal thin films. Additional X-ray photoelectron spectroscopy (XPS) studies could neither clarify the MP process [216, 143, 218] nor the conditioning process [25]. Alpha-particle spectroscopy of alpha-emitting target isotopes indicates changes in the thin films after irradiation [85, 129]. Attempts to induce effects similar to those from heavy-ion beams by thermal heating to 700 °C in oxidizing and reducing atmosphere were unsuccessful [141, 25]. Thermal stability [129, 118] of thin metal foils, which are often used as backing material, is limited. This greatly limits thermal-based attempts to mimic conditioning tests in oven systems, since conversion temperatures into the oxides are comparatively high for most f-metal compounds. More detailed spectroscopic investigations of the irradiation effects are still pending, so that there is still no full understanding of the processes in target layers during irradiation [129]. Confocal Raman spectroscopy has been successfully applied in the material sciences in studies of ion-beam modified materials [204]. It has not been applied yet to study the properties of MP target layers and their changes under heavy-ion irradiation [198].

The goals of this study are: (i) to prove that it is possible to investigate the radiation induced chemical reactions in target materials without beamtime at particle accelerators and to supplement the accelerator based conditioning procedure, by using the recently commissioned ODIn-setup [71] at the Helmholtz-Institute Mainz; (ii) the comparison of established and newly developed [70] methods of target production, regarding their beam performance; (iii) the establishment of new analytical approaches of target characterization, in order to reveal changes in the structure and chemical composition of target materials [198].
In the following, the performance of different methods of target fabrication in the heavy ion beam will be compared. For first experiments ^{nat}Pb-targets are used [83]. In addition, lead oxide compounds show a characteristic colour variety depending on their oxidation state, which is well documented in literature [164]. By analysing the resulting lead compounds, we hope to gain new insights into the MP method and the conditioning process. There are numerous examples of Raman analyses of lead thin films from the applied sciences (geology, materials science, petrology and archaeology), e.g. [192, 213]. There are also systematic studies on the stability and reproducibility of Raman measurements [24] on lead thin films, for which sufficiently reliable reference spectra are available [23]. First studies on the chemical stability of lead compounds under irradiation were undertaken already in the 1930s [82]. In comparison to f-element chemistry, the chemistry of lead is much better understood and more extensively documented in literature, which makes lead an ideal test element for a first systematic investigation, before venturing into studies with lanthanides and actinides. In addition to the established MP method, the Drop-on-Demand (DoD) [70] method was investigated with confocal Raman spectroscopy. The DoD technique [70] has been used to produce samples for a wide variety of experiments [222, 43, 109, 170, 68],

but applications in superheavy element research have so far been lacking. The suitability as a target technique for ion accelerators is to be determined in initial experiments. Furthermore, the possibility of replacing the previously necessary conditioning procedure at the accelerator with an offline [71] method was explored.

2.4. Experimental Methods

2.4.1. Target production

All targets were prepared using lead(II) nitrate in analytical quality (CAS: 10099-74-8). The used solvents acetone (CAS: 67-64-1, propan-2-on), isobutanol (IB, CAS: 78-83-1, 2-methylpropan-1-ol) and isopropanol (IP, CAS: 67-63-0, propan-2-ol) were of technical quality. The nitric acid (CAS: 7697-37-2) and the hydrochloric acid (CAS: 7647-01-0) were of analytical quality. All chemicals were purchased from Merck KGaA, Darmstadt, Germany. All used water was purified by a Milli-Q™Direct Water Purification System.

2.4.1.1. Molecular plating

For the irradiation test at the UNILAC accelerator at GSI Darmstadt, targets were prepared in a geometry to fit the four-segment target wheel [91] of the **T**rans**A**ctinide **S**eparator and **C**hemistry **A**pparatus (**TASCA**). A 2.3 µm titanium foil was glued (E-Solder 3021, EPOXY Produkte GmbH) to the curved aluminium frames [118] and served as target backing. Before the MP process, the titanium foil was for 1 min immersed in hydrochloric acid, then degreased and dried with acetone. Special care had to be taken to protect the sensitive adhesive layer, so that the glued titanium foil does not peel off the aluminium frame. For the plating process we used a stock solution consisting of lead(II) nitrate dissolved in diluted nitric acid (0.1 $\frac{\text{mol}}{\text{L}}$). Aliquots of 100 µL were mixed with isobutanol/isopropanol (9:1). The mixture was placed in the TASCA plating cell [42], with the target backing serving as cathode. The targets were plated at 1200 V with a current of 0.5 $\frac{\text{mA}}{\text{cm}^2}$ for 3 h. This yielded targets of 600(54) $\frac{\mu\text{g}}{\text{cm}^2}$ thickness (surface weight (SW), i.e. areal density), which displayed a thin film of homogenous appearance (Fig. 2.1 (a)). The target production process is described in detail in the literature given [42, 177]. The MP process works on thin metal foils (a few µm thick) as well as thin carbon foils. It does not work on non-conductive backings, such as polymer films.

For the irradiation tests at the ODIn setup, a different target geometry was employed, therefore a different plating cell was used [43]. The Titanium backing foil was thicker (25 µm) and the molecular plating

processes yielded circular (d = 8 mm) thin films (Fig. 2.2 (a)).

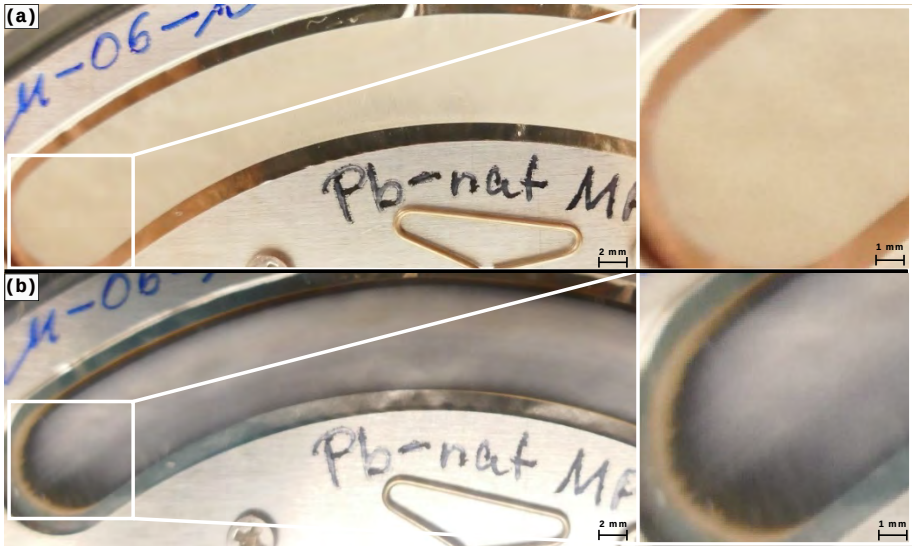

Figure 2.1.: A segment of a target wheel for the TASCA experiment [91], coated with lead via molecular plating (SW = 600(54) $\frac{\mu g}{cm^2}$), before (a) and after (b) irradiation with 5.90 $\frac{MeV}{u}$ ^{48}Ca-beam, accumulated fluence 6.5×10^{13} $\frac{ions}{cm^2}$.

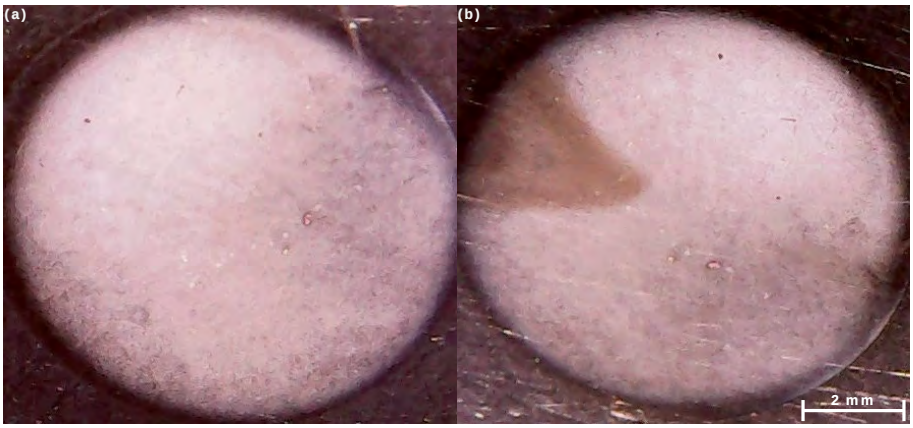

Figure 2.2.: Examples of MP lead targets (SW = 100(10) $\frac{\mu g}{cm^2}$) for irradiation by the ODIn-setup (a) unirradiated, (b) irradiated with 1.5 keV e^--beam, $I = 3.2 \times 10^{19}$ $\frac{ions}{cm^2}$. A triangular discolouration on the edge of the target is clearly visible after irradiation.

2.4.1.2. Target printing by Drop-on-Demand

In the Drop-on-Demand technique, a solution of the desired element is precisely distributed on the target [222, 43, 109, 170, 68] substrate in an inkjet printing process. By choosing an optional thermal

post-treatment, the exact speciation of the target material can be adjusted. In the present case, the temperature range was chosen that the deposited lead(II) nitrate should completely transform into lead(II) oxide. In contrast to the MP process for the same elements, one has full control over the speciation of the target material and is not hindered by poorly controllable by-products. One disadvantage is the thermal sensitivity of the thin titanium foils (2.3 µm) and the adhesive binding (E-Solder 3021, EPOXY Produkte GmbH) used in the TASCA target frames, which greatly limits the useable temperature range.

For the target fabrication by printing, the DoD printer [70] was filled with the lead nitrate stock solution (40 $\frac{\text{mg}}{\text{mL}}$). A drop pattern (Fig. 2.3) was chosen for the curved TASCA target frames, in order to visualise local target stability and performance more easily. The pattern [70, 68] resulted in an average surface weight of $2.1(2)\ \frac{\text{mg}}{\text{cm}^2}$ over the whole TASCA segment, at a coverage of 35 %. However, this means that a single printed drop has a theoretical surface weight of $6.0(6)\ \frac{\text{mg}}{\text{cm}^2}$, which is once again significantly higher than the surface weight of the TASCA MP targets used ($\text{SW} = 600(54)\ \frac{\mu\text{g}}{\text{cm}^2}$). So a significant amount of desired target material is concentrated within the drops. After printing, the target was heat treated in a muffle furnace at T = 500 °C for 1 h. Printing and heat treatment yielded circular drops of 350 µm diameter on average.(Fig. 2.4 (a) and Fig. 2.8).

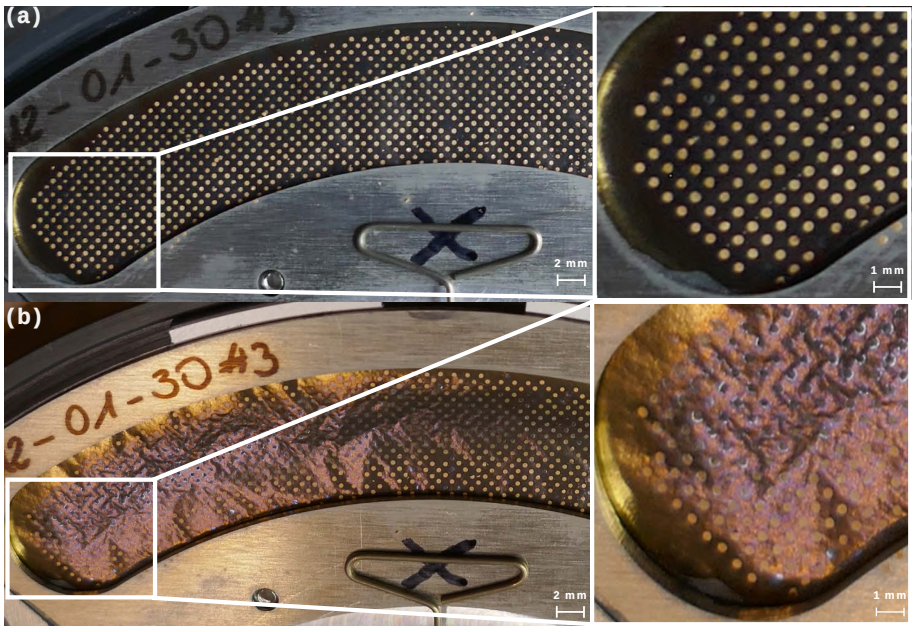

Figure 2.3.: TASCA-Segments coated via DoD ($\text{SW} = 2.1(2)\ \frac{\text{mg}}{\text{cm}^2}$). (a) after tempering in a muffle furnace (T= 500 °C, 1 h) and (b) after irradiation with a ^{50}Ti-beam, $4.85\ \frac{\text{MeV}}{\text{u}}$, $3.3 \times 10^{13}\ \frac{\text{ions}}{\text{cm}^2}$

.

2.4.2. Ion irradiation of targets

2.4.2.1. TASCA

The irradiation of the targets was performed in two consecutive campaigns. A first MP target was irradiated at the TASCA beamline of the GSI UNILAC with $5.90\,\frac{\mathrm{MeV}}{\mathrm{u}}$ ^{48}Ca-beam ($6.5 \times 10^{13}\,\frac{\mathrm{ions}}{\mathrm{cm}^2}$, Fig. 2.1 (b)). A second MP target and a DoD target were irradiated at TASCA with $4.85\,\frac{\mathrm{MeV}}{\mathrm{u}}$ (^{50}Ti-beam, $3.3 \times 10^{13}\,\frac{\mathrm{ions}}{\mathrm{cm}^2}$, Fig. 2.3 (b)). Ion flux was increased stepwise 2.2×10^{9} **to** $4.0 \times 10^{10}\,\frac{\mathrm{ions\,s}}{\mathrm{cm}^2}$ for both irradiations. At this ion flux bulk heating of the sampls can not be excluded [204].

2.4.2.2. Irradiation of MP lead targets at the ODIn setup

To yet broaden our studies, the ODIn setup [71] delivering low-energy ions and electrons from an ion gun and an electron gun, was also employed. The sample was fixed with conductive adhesive tape on the sample holder in ODIn. The thin films were irradiated with an electron beam of 1.5 keV and a beam current of $6.2 \times 10^{14}\,\frac{\mathrm{e}^-}{\mathrm{s}}$. The electron gun optics focuses the electron beam into an isosceles triangle (Fig. 2.2 (b)) with an edge length of 3 mm, cf. [71] for the technical details. In the irradiation experiments shown here, the electron beam was not scanned over the sample surface, but was only focused on a constant point in order to better indicate the dose per area. The irradiated part of the thin films immediately turned dark. The entire irradiation lasted about one hour with approximately $5.0 \times 10^{19}\,\frac{\mathrm{e}^-}{\mathrm{cm}^2}$.

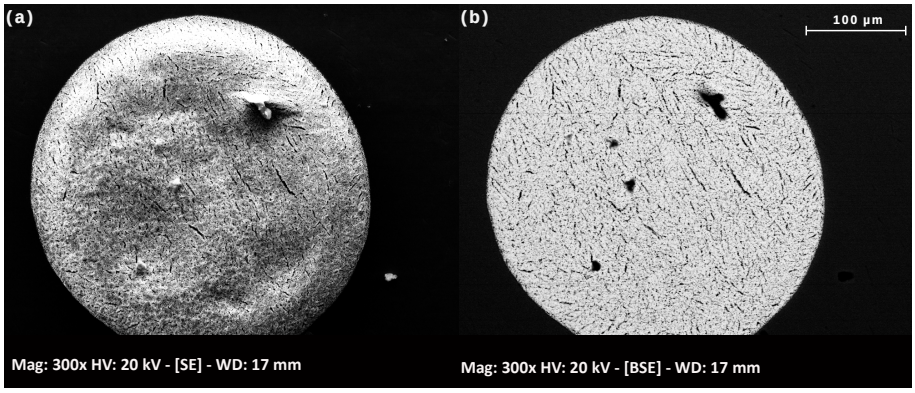

Figure 2.4.: SEM images of one DoD printed drop of lead nitrate after tempering in a muffle furnace (T = 500 °C, 1.0 h) and after irradiation with a ^{50}Ti-beam, $4.85\,\frac{\mathrm{MeV}}{\mathrm{u}}$, $3.3 \times 10^{13}\,\frac{\mathrm{ions}}{\mathrm{cm}^2}$. The drop is in the middle of the irradiated DoD TASCA segment and has therefore been fully irradiated. (a) is a SE recording. (b) is a BSE recording.

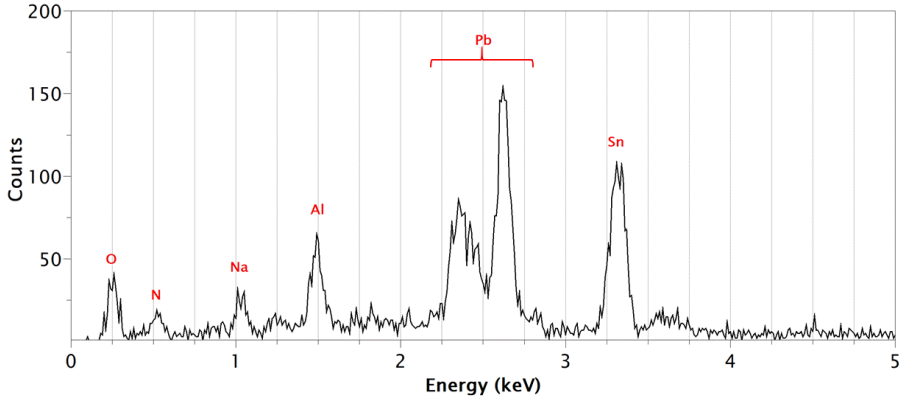

Figure 2.5.: EDX point spectrum of one of the black crystallites on the surface of the printed drops. (cf. Fig. 2.4)

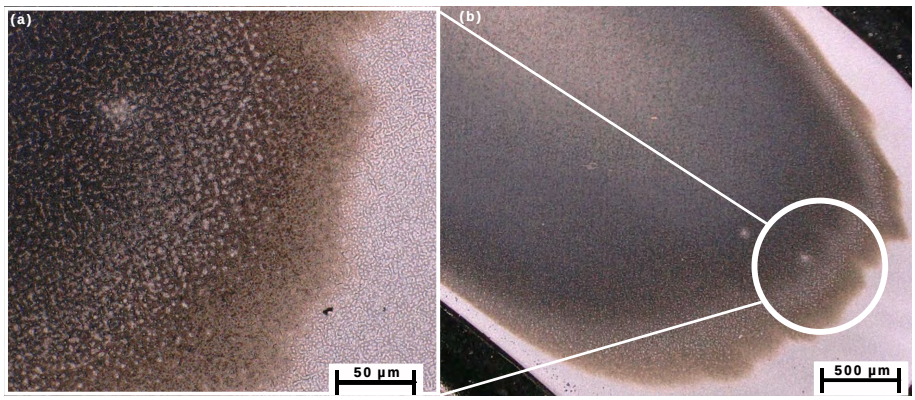

Figure 2.6.: TASCA segments coated with lead via MP (SW = 600(54) $\frac{\mu g}{cm^2}$), after irradiation with 5.90 $\frac{MeV}{u}$ ^{48}Ca-beam (6.5×10^{13} $\frac{ions}{cm^2}$). The recordings were made with a KEYENCE VHX-6000 digital optical microscope at the GSI target lab. (a) shows an enlargement of the transition between irradiated and non-irradiated area. (b) is a less magnified overview image for orientation.

2.4.3. Target analysis

2.4.3.1. Scanning electron microscopy

In order to evaluate the ion beam-induced surface modifications, scanning electron microscopy (SEM, Philips XL30, Amsterdam, The Netherlands) with an acceleration voltage of 20 kV was carried out in combination with detectors for secondary (SE) and backscattered electrons (BSE).

In addition, energy-dispersive X-ray spectroscopy (EDX) was used to investigate the changes in elemental composition of the thin films. The EDX spectra were evaluated with the NIST DTSA-II Lorentz software package [146]. The detector (SphinX 133 XL40 by eumeX Instrumentebau GmbH) used was equipped with an ultra-thin window (UTW). Thus, the detection of elements lighter than sodium (Na)

is theoretically possible. To exclude chemical manipulations by the electron beam, the SEM/EDX measurements were performed after the confocal Raman spectroscopy and light microscopy measurements.

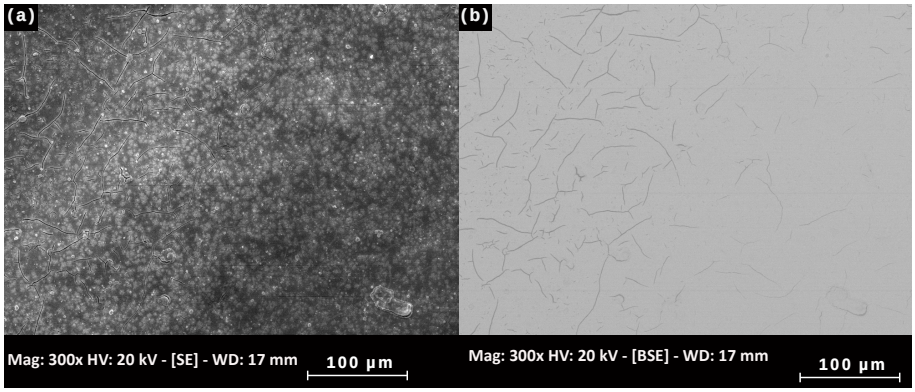

Figure 2.7.: SEM images of MP TASCA segment after irradiation with 5.90 $\frac{\text{MeV}}{\text{u}}$ ^{48}Ca-beam (6.5×10^{13} $\frac{\text{ions}}{\text{cm}^2}$). The images show the border between the irradiated and unirradiated part of the thin film. (a) is a SE recording. (b) is a BSE recording.

2.4.3.2. Digital optical microscopy

The digital microscopy images of the samples were taken with a KEYENCE VHX-6000 in the Target Laboratory at GSI. Digital microscopy allows the differentiation of different lead species by their specific color.

2.4.3.3. Confocal Raman spectroscopy

For a first screening, a single test measurement was performed at the the Institute of Geosciences of the Johannes Gutenberg University Mainz, Germany. Raman spectra from 100 cm^{-1} to 600 cm^{-1} were collected with a Jobin Yvon (Horiba) LabRam HR 800 spectrometer equipped with an Olympus BX41 optical microscope and a Si-based charge-coupled device (CCD) detector. The instrumentation used an Ar^{+} ion laser (514 nm emission), a grating with 1800 $\frac{\text{grooves}}{\text{mm}}$, and a slit width of 100 mm. These parameters, and the optical path length of the spectrometer led to a spectral resolution of 0.8 cm^{-1} . The spectral acquisition time was set to 240 s for all measurements [87]. For the initial proof-of-concept the drop pattern of the DoD target was utilised (Fig. 2.3). One drop at the unirradiated rim of the segment and one drop in the fully irradiated segment centre were analysed (Fig. 2.8).

The majority of the targets was analysed by confocal Raman spectroscopy (HR800 system, Horiba Jobin Yvon) at the Materials Research Department of GSI with 633 nm excitation wavelength, other settings

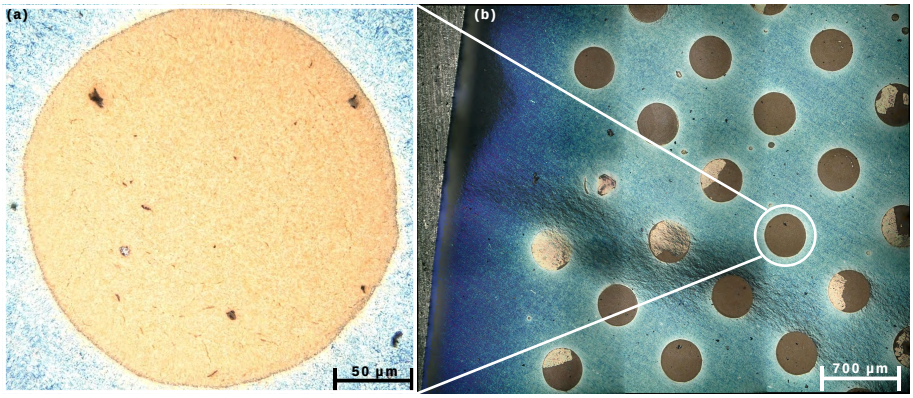

Figure 2.8.: Digital optical microscope images of (a) one printed drop of lead nitrate after tempering in a muffle furnace (T = 500 °C). (b) macroscopic damage after irradiation with 4.85 $\frac{\text{MeV}}{\text{u}}$ (^{50}Ti-beam, 3.3×10^{13} $\frac{\text{ions}}{\text{cm}^2}$). The recordings were made with a KEYENCE VHX-6000.

were identical to those given above. Raman spectra from 100 cm^{-1} to 4000 cm^{-1} were collected [167]. First, automatic line scans were carried out over the entire sample diameter. This ensured repeatability of the measurements, and a distinction between irradiated and non-irradiated areas of the sample surface was immediately possible. Since the thin target foils of the TASCA segments were sagging after irradiation, the automatic scan routine failed, so that selected areas were manually scanned, by optically selecting areas of characteristic colour changes. In order to study potential effects due to laser-induced material modification [24], the laser was focused on a point of the thin film at maximum power and consecutive measurements were recorded. Even several minutes of laser bombardment did not induce changes in the Raman spectra. We thus exclude sample modifications due to the analysing laser beam. From tabulated refractive indices of the lead compounds to be presumed, it can be deduced that for both wavelengths the laser light of the Raman microscopes only penetrates approximately the first 25 nm of the thin films. Therefore, an influence of the titanium substrate on the spectra can be excluded.

2.5. Results

2.5.1. Irradiation with swift heavy ions

2.5.1.1. DoD TASCA-targets

As can be seen from both microscopy methods, the unirradiated and also the irradiated printed drops consist of aggrates of finest crystals. During the crystallization process, microcracks have formed. Both in the BSE part of the SEM images (Fig. 2.4) as well as in the light microscopy image (Fig. 2.8), crystals of different colour and contrast are visible. In EDX point scans (Fig. 2.5) lead, tin, aluminium and sodium are clearly detectable. Sodium is a common contaminant, probably introduced during handling

of the samples. The aluminium signal comes from the sample holder. The strong lead signal comes from the underlying lead dot. Lead and aluminium are both visible in the EDX spectrum, because the technique has an inherent penetration depth of about 2 µm to 3 µm. Confocal Raman (Fig. 2.3) measurements [171] were able to identify the black crystallites as tin(IV) oxide. Although lead(II) nitrate was used in analytical quality for target production, our samples obviously contain microscopic contamination of tin compounds.

Table 2.1.: Raman spectroscopy for printed lead(II) nitrate drops recorded at 514 nm. From a printed drop at the rim and in the centre of the target, several Raman spectra were recorded at different locations. The averaged FWHMs of the significant peaks are shown here.

	$148\,\mathrm{cm}^{-1}$	$341\,\mathrm{cm}^{-1}$
rim	$3.33 \pm 0.04\,\mathrm{cm}^{-1}$	$15.68 \pm 0.65\,\mathrm{cm}^{-1}$
centre	$3.73 \pm 0.05\,\mathrm{cm}^{-1}$	$16.21 \pm 0.78\,\mathrm{cm}^{-1}$

Macroscopic changes induced by the ion irradiation are clearly visible (Fig. 2.3). Several printed drops are partially or completely chipped off by irradiation; irradiated areas turn dark, changing the colour to almost black. The Raman spectra (Fig. 2.9) show narrow bands without significant background. According to literature, the two prominent bands at $148\,\mathrm{cm}^{-1}$ and $341\,\mathrm{cm}^{-1}$ are ascribed to tetragonal lead(II) oxide (litharge) [24]. The position of the bands remained the same. However, the irradiation leads to a significant broadening of the peaks. The corresponding full width at half maximum (FWHM) values are presented in Tab. 2.1. At $488\,\mathrm{cm}^{-1}$ the mentioned contamination with tin(IV) oxide [171] is weakly visible (Fig. 2.9).

2.5.1.2. MP TASCA-targets

The ion irradiation has a much stronger effect on the MP thin films. From the unirradiated edge of the segment to the irradiated centre, numerous colour shades are visible (Fig. 2.6), which might indicate chemical transformations. At the transition zone between the irradiated and the unirradiated area, a disappearance of microcracks in the thin film is observed with the SEM images (Fig. 2.7). In the irradiated area of the thin film, microcracks are no longer visible. The irradiation has melted the thin film together into a homogeneous surface, which corresponds well to the literature [129]. The Raman spectra of the target before and after irradiation are shown in Fig. 2.10 (a). In unirradiated thin films only basic lead(II) carbonate ($(PbCO_3)_2$ x $Pb(OH)_2$) can be detected by characteristic bands at $110\,\mathrm{cm}^{-1}$, $1051\,\mathrm{cm}^{-1}$ and $1055\,\mathrm{cm}^{-1}$ [24, 23]. The spectra have a comparatively high background and poor signal-to-noise ratio, suggesting an amorphous state. The observed peaks at $110\,\mathrm{cm}^{-1}$, $1051\,\mathrm{cm}^{-1}$ and $1055\,\mathrm{cm}^{-1}$ agree well with the literature values; the intense band at $1051\,\mathrm{cm}^{-1}$ is attributed to the CO stretching vibration

of the carbonate anion [21, 30, 53, 183, 47]. Solvent degradation products [143], specifically carboxylates [217, 216, 219], as described to be present in MP films in the literature were not detected. Raman bands significant for carboxylate compounds, such as the symmetrical C-C stretching vibration at about 940 cm^{-1}, could not be observed in any sample [229]. In general, no Raman signals attributed to aliphatic organic carbon compounds could be detected.

After bombardment with swift heavy ions with 5.0 $\frac{MeV}{u}$ ^{48}Ca-beam, $I = 6.5 \times 10^{13}$ $\frac{ions}{cm^2}$, orthorhombic lead(II) oxide (massicot) was detected as the dominant chemical species in the thin films (Fig. 2.10 (b)). The peaks at 142 cm^{-1} and 285 cm^{-1} correspond to the relevant literature. Minimal peak shifts and broadening, as well as characteristic grey colouring in the colour image (Fig. 2.6), point to the presence of additional lead suboxides. Reference spectra of the suboxides in satisfactory form are missing in the literature. Lead(II) carbonates were no longer detectable after bombardment, and there are no indications for the presence of lead(IV) compounds (Fig. 2.10). At the transition between the irradiated and non-irradiated region there were spectra (Fig. 2.11) indicating intermediate reaction steps in the conversion of lead(II) carbonate into orthorhombic lead(II) oxide as described in [30] and [183]. After irradiation, the thin films show a significantly stronger Raman signal with significantly narrower bands, which could indicate recrystallization. On the other hand, lead(II) oxides are significantly better Raman scatterers than the lead(II) carbonates [183].

2.5.2. Electron irradiation with ODIn

On the targets irradiated at ODIn the changes caused by the triangular electron beam are clearly visible (Fig. 2.2). The conversion from lead(II) carbonate to orthorhombic lead(II) oxide (massicot) can also be observed here, but the transformation is less complete, as carbonates remain detectable (1051 cm^{-1}, Fig. 2.12). No other lead(II) oxide modifications than massicot can be identified. The Raman spectra after the irradiation with a 1.5 keV e^--beam largely correspond to the spectra of ion beam exposed samples. In the case of targets irradiated with ODIn, the triangular discolourations of the thin films could be seen with the naked eye, but changes in the morphology, such as the fusion of microcracks in the case of targets irradiated with TASCA, could not be observed via SEM. With SEM, the irradiated part of the surface could hardly be distinguished from the non-irradiated part.

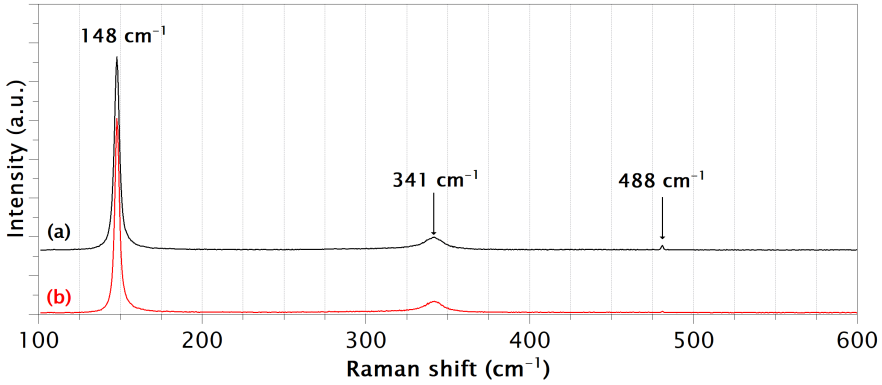

Figure 2.9.: Raman spectra of a DoD lead target after irradiation by TASCA with 4.85 $\frac{\text{MeV}}{\text{u}}$ (^{50}Ti-beam, 3.3×10^{13} $\frac{\text{ions}}{\text{cm}^2}$), (a) unirradiated rim, (b) irradiated centre of the target. Recorded at $\lambda_0 = 514$ nm, 15 mW.

2.6. Discussion

2.6.1. Molecular plating

The slight quality differences in the Raman spectra of the unirradiated thin films can be explained by the different target geometries and thereby plating cells used. The biggest distinction between the two electrochemical setups is the different thicknesses of the titanium carrier foils (2.3 µm and 25 µm). Nevertheless, both set-ups produce the same chemical species in the MP thin films.

The interpretation of our Raman spectra can only be partially reconciled with the results of older work on the subject [216, 129]. No evidence of cracked solvents or the formation of carboxylates could be found. Despite the high electrical voltages and the resulting waste heat, a quasi-quantitative formation of carboxylates from isopropanol and isobutanol seems insufficient as an explanation for the carbon content of the MP thin films described in literature [216, 129]. Oxidation to the carboxylic acids taking place in a reducing cathodic environment would anyway have been unexpected. Furthermore, in other studies of molecular plating in dimethylformamide (DMF) [143] and isobutanol (IB) [28] the possible formation of carbonates has been mentioned. Most organic solvents can dissolve much more carbon dioxide than water can [90]. Therefore, sufficiently high carbon dioxide partial pressures could be expected even under normal conditions. In combination with the high local pH values, which have also been known [76, 10] for a long time and are induced by electrolysis of residual water in organic solvents, precipitation as basic carbonates seems to be the most plausible explanation for our results on the layer composition of MP produced targets [86]. The process could therefore be described as electrophoresis rather than electrodeposition. This model would also explain the lack of reduction of metal cations, which is described in all publications on the subject. The occurrence of carbonate-like C-bonds in films

produced from DMF [143] and IB/IP [28] as seen via XPS correlates well with the solubility of carbon dioxide in these solvents [90]. Since no drying and degassing procedures for the solvents used are described in the aforementioned publication on molecular plating, the content of water and air described in textbooks [90] for untreated solvents can be assumed. Therefore, the carbon dioxide of the ambient air is the obvious explanation for the observed carbonates [143] and their degradation [28] products in MP thin films. Understanding the processes governing molecular plating and the composition of the produced layers are a prerequisite for elucidating the processes [9, 85, 20, 198] occurring under heavy-ion beam irradiation.

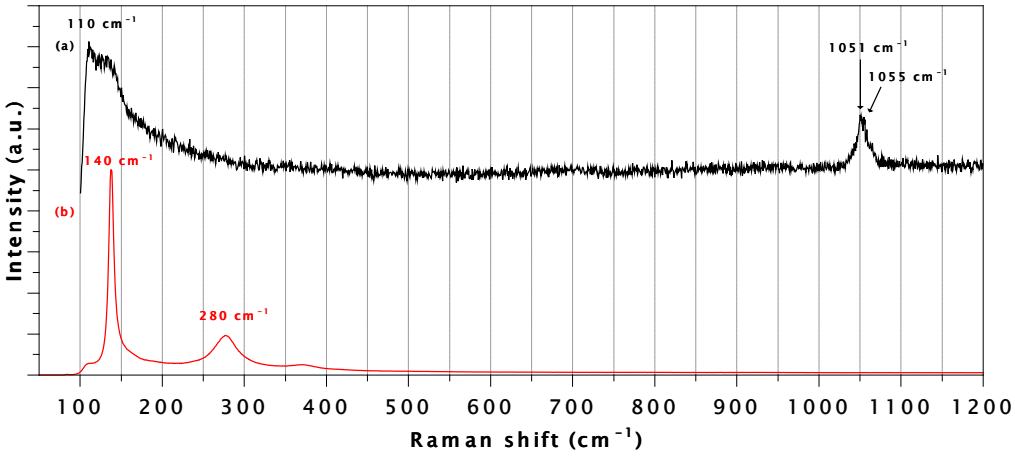

Figure 2.10.: Raman spectra of a MP lead target after irradiation by TASCA with 5.90 $\frac{\text{MeV}}{\text{u}}$ ^{48}Ca-beam (6.5×10^{13} $\frac{\text{ions}}{\text{cm}^2}$), (a) unirradiated rim, (b) irradiated centre of the target. Recorded at $\lambda_0 = 633$ nm, 16 mW.

2.6.2. Radiation-induced reactions

Using the Raman spectra, a radiation-induced conversion of basic carbonates to oxides was observed (Fig. 2.10). No series of different fluences was available, we thus could not identify details of this transition and no intermediate stages could be identified. Known oxide-carbonate intermediates [30] could be identified (Fig. 2.11) but could not be assigned to any specific fluence. The thermal transformation of the lead(II) carbonates into the two polymorphous lead(II) oxides, litharge and massicot, is precisely reported in the literature [30, 183], but the necessary transformation temperatures described were not reached macroscopically in any of the irradiation experiments. The observed process can therefore not be exclusively temperature induced. However, the ion flux (4.0×10^{10} $\frac{\text{ions}}{\text{s cm}^2}$) at TASCA is high so microscopic local heating cannot be excluded. However, irradiation at ODIn, which does not lead to substantial sample heating, induces equivalent transformations (Fig. 2.12), so the influence of temperature can be

assumed to be small.

For the case of the bombardment with swift heavy ions, the primary effect can be attributed to ion irradiation-induced electronic excitation in the crystal lattice of a material after relaxation, which results from a state of warm dense matter by the creation of structural defects due to the displacement of atoms [204]. Due to the presence of carbonate species and the high vacuum applied in both types of irradiation, the system can simply relax to the oxide by releasing gaseous decomposition products.
Irradiation with electrons leads to the same chemical transformation, but due to the significantly lower energies, a different mechanism can be assumed. The electron beam is strong enough to break chemical bonds, and a relaxation of the system by evaporation of carbon dioxide is also likely. Here, too, the high-vacuum conditions are conducive to pulling the reaction to the side of the products. Thus, if lead(II) carbonate is irradiated in a vacuum, the thermodynamically stable lead(II) oxide modification - litharge - is formed (Fig. 2.10).

In the DoD printing process, due to the low temperature chosen for calcination, the metastable lead(II) oxide - massicot - is formed (Fig. 2.6). The temperatures had to be so low to protect the thin titanium foil and the bonding with the target frame. The observed massicot shows no transformation into litharge, although litharge is the thermodynamically more stable modification. The change in the DoD spectra due to irradiation are very small, a change in the chemical species cannot be observed.

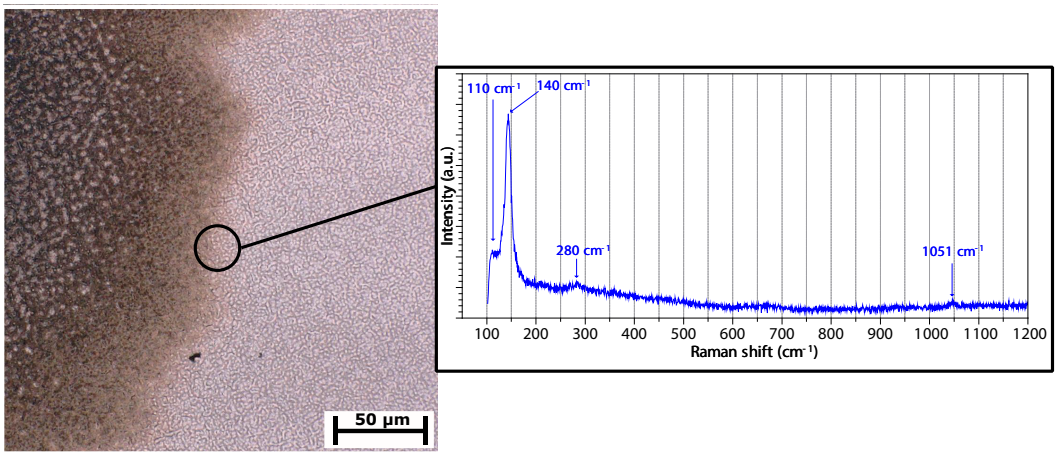

Figure 2.11.: Raman spectra of a MP lead target after irradiation by TASCA with 5.90 $\frac{\text{MeV}}{\text{u}}$ ^{48}Ca-beam (6.5×10^{13} $\frac{\text{ions}}{\text{cm}^2}$). The spectrum was recorded at the transition between the irradiated and non-irradiated part of the MP lead target (Fig. 2.6). For technical reasons of the TASCA setup, this boundary is not sharply defined. The Raman spectrum shows the transition between basic carbonate and the oxide. Comparable spectra were also recorded at the boundaries of the irradiated triangle in the ODIn setup. Recorded at $\lambda_0 = 633$ nm, 16 mW.

2.7. Conclusion and Outlook

The MP process is dominated by the formation of basic carbonates; cracked solvent residues could not be observed by Raman spectroscopy. Future experiments still need to clarify the cause of the observed carbonates, the natural carbon dioxide concentration in moist non-degassed solvents seems to be the most obvious explanation. These carbonates rapidly convert to their oxides when irradiated with ions at the TASCA setup, with the applied amount of radiation corresponding to the first few minutes of a superheavy elements experiment.

(i) We could show, that the ODIn setup induces equivalent chemical transformations in MP thin films. This could be a first step towards studies of chemical changes in MP thin films without beam time on accelerators. In this way, innovations in target technology, such as DoD, could be screened for potential suitability. The problem remains, of course, that targets of the same thickness as those at the particle accelerator cannot be conditioned at the ODIn setup, since the projectiles produced have a lower penetration depth [71].
(ii) Recently, numerous physical experiments have been made possible using the Drop-on-Demand [222, 43, 109, 69] method, but a performance test in the heavy ion beam has not yet been described. The chosen droplet pattern (Fig. 2.8) had clear advantages for observing spatially resolved changes, but it also induced a locally very high surface weight ($SW = 6.0(6)\ \frac{mg}{cm^2}$), which could be an explanation for the macroscopic instability that needs improvement. DoD thin films printed as closed thin films show significantly better macroscopic stability. On the microscopic level, the strengths (Fig. 2.9) of the method become apparent. Through DoD printing, chemically narrowly defined and cleanly crystallized thin films can be produced. Here, established synthesis methods such as sol-gel synthesis [207] and polymer-assisted deposition [56, 55] still have great potential, through modification for the DoD method. Such a combination of established target techniques may provide a solution to the problems observed for DoD targets and thus enable printable targets that better withstand heavy ion beams.
(iii) By means of confocal Raman spectroscopy new insights into molecular plating and the heavy-ion conditioning process could be gained. The MP process seems to work differently than previously thought. The formation of carbonates by electrochemically induced precipitation seems to be an obvious explanation of our measurement results as well as complementary studies reposted in literature and is also applied outside heavy ion research [28]. The heavy ion bombardment induces a chemical transformation, which has not been described in the literature so far to our knowledge. Especially in combination with other analytical methods, further insights seem to be possible in order to clarify the complex chemical processes in the interaction of intense heavy ion beams with targets. A challenge in transferring the approach to lanthanides and actinides is the lack of reference, e.g. Raman spectra, in literature, so that users have to synthesize and characterize their own standard compounds or use meth-

ods of theoretical chemistry. Confocal Raman spectroscopy is therefore a useful supplement to target analysis, but in principle several different spectroscopic methods should always be used to avoid misinterpretations. It would be beneficial to supplement the Raman results with infrared spectroscopy studies. Methods of X-ray diffraction (XRD) could allow a more precise assignment to individual modifications, which might allow identifying irradiation-induced intermediates, thus helping to elucidate the pathway of beam-induced transformations. Especially vibrational spectroscopic methods fail here when it comes to precise assignment. However, better crystallization [28] sites in the thin films would be necessary to carry out such diffraction studies with benchtop devices. Of course, X-ray photoelectron spectroscopy (XPS) and wavelength dispersive X-ray spectroscopy (WDX) would also be desirable to investigate the elemental composition [143, 28] and its change after irradiation in the thin films. The most efficient would be to combine all methods. For the general experimental setup, fluence series [204] would be desirable for future studies, so that the intermediate products of the conversion processes could also be precisely recorded spectroscopically.

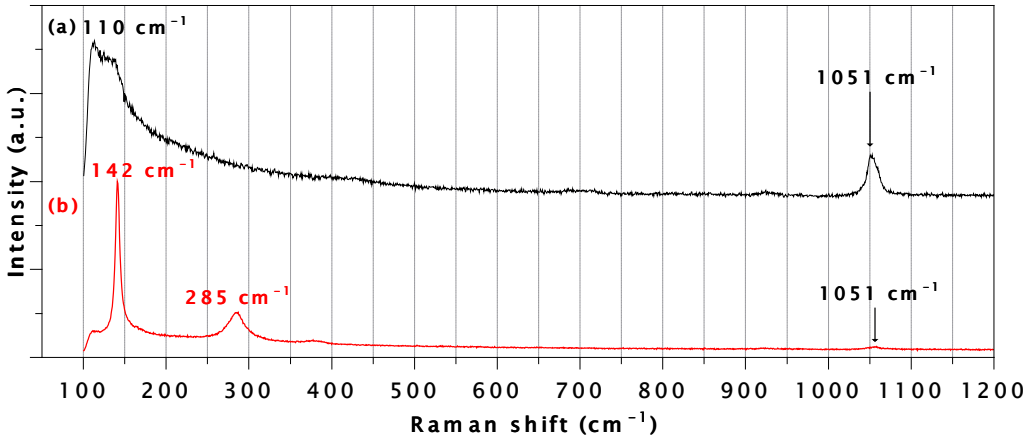

Figure 2.12.: Raman spectra of a MP lead target after irradiation by the ODIn-setup with 1.5 keV e^--beam, $I = 5.0 \times 10^{19} \frac{e^-}{cm^2}$ (a) non-irradiated part of the thin film, (b) irradiated triangular discolouration on the edge of the target. Recorded at $\lambda_0 = 633$ nm, 16 mW.

The comparison with the DoD targets also shows that the development of alternative methods to the MP process is advantageous. Ideally, the target material should be in a chemically stable form that is not directly converted to another compound under irradiation, thus ensuring tighter control and prediction of the target properties in the experiment. Future studies must show, if the MP process deposits the lanthanides and actinides as basic carbonates. Unlike their oxides [204], the carbonates [28, 93, 196] and hydroxycarbonates [98] of f-metals have not yet been systematically tested concerning their radiation stability, since the formation of carbonates and basic carbonates in the MP process had not been described before. Unlike the oxides of the actinides and lanthanides, the carbonates have hardly any tech-

nical significance, so that little is known about their behaviour under irradiation. However, interest in the f-metal carbonates has increased recently [93], which gives hope for results from other research areas.

2.8. Acknowledgements

Our sincere thanks go to Tobias Häger from the Institute of Geosciences of the Johannes Gutenberg University Mainz for the introductory access to a confocal Raman microscope, so we were able to prove the feasibility of the analytical methods. The results presented here are based on the experiment U308, which was performed at the beam line X8/TASCA at the GSI Helmholtzzentrum für Schwerionenforschung, Darmstadt (Germany) in the frame of FAIR Phase-0. We also acknowledge the local support of the mechanical workshop at the research reactor TRIGA Mainz and the financial support from the Helmholtz Institute Mainz.

3. Publication II: Microscopic and spectroscopic analysis of ion-irradiated molecular-plated thin films

The following article has been accepted for publication in the peer-reviewed journal 'Nuclear Instruments and Methods in Physics Research Section A: Accelerators, Spectrometers, Detectors and Associated Equipment' in 2025. The article describes the analysis of MP thin films. As well as their chemical modification under irradiation.

3.1. Own contributions

The publication was conceived and drafted independently. The experiments and analyses were designed and executed independently. The diffraction experiments were outsourced, and the contributions are presented in the publication. The analyses at the Ion Beam Center of the Helmholtz-Zentrum Dresden-Rossendorf and at the Joint Research Centre (JRC) - Karlsruhe were devised by me and actively supervised on-site. The raw data was analysed in close collaboration with the scientists at the respective institutions. The final evaluation of all data and their integration into the extended context of the publication was carried out exclusively by myself.

Microscopic and spectroscopic analysis of ion-irradiated molecular-plated thin films for superheavy element production

C.-C. Meyer[1,2], E. Artes[1,2,3], M. Bender[3,4], J. Brötz[5], Ch. E. Düllmann[1,2,3], T. Gouder[6], E. Jäger[3], B. Kindler[3], S. Herz[1], B. Lommel[3], M. Major[5], C. Mokry[1], F. Munnik[7], M. Rapps[1,†], D. Renisch[1,2], J. Runke[1], A. Seibert[6], C. Trautmann[3,5], N. Trautmann[1], O. Walter[6], A. Yakushev[3]

3.2. Abstract

The heaviest known elements are produced via fusion reactions by bombarding actinide targets with intense heavy ion beams. The production of actinide targets relies mainly on the molecular plating (MP) technique. Long-term stability of MP produced targets is typically achieved by a conditioning procedure, in which fresh targets are exposed to successively increasing beam intensities. This leads to non-trivial physical and chemical transformations, which are presently poorly understood. To shed light on processes in the initial irradiation stage, we irradiated thin Tm MP films with Cl and Au ions of different fluences, with the latter ranging from 10^{10} $\frac{\text{ions}}{\text{cm}^2}$ to 10^{14} $\frac{\text{ions}}{\text{cm}^2}$, and analyzed their morphology and composition by a variety of microscopic, spectroscopic and ion beam techniques. The study was conducted on lanthanide targets, which serve as non-radioactive analogues for heavy actinide targets. Combining the results of several methods, we conclude that the MP thin films consist of a mixture of carbonates and formates. Under irradiation, these films transform into amorphous oxides with embedded carbon clusters.

3.3. Introduction

In recent decades, remarkable progress has been made in the production of superheavy elements (SHE) [84, 36, 148, 193]. For this purpose, targets of the heaviest actinides, such as ^{242}Pu [182], ^{243}Am [176, 226] and ^{249}Bk [150], were irradiated with ^{48}Ca ions at heavy-ion accelerators. Actinide targets are typically produced by molecular plating (MP), where the desired actinides are electrochemically deposited as thin films ($\frac{\mu\text{g}}{\text{cm}^2}$) on very thin Ti foils (1.5 µm to 2.3 µm) [119]. The MP method presents a critical limitation to experimental progress in the field [198, 197, 38], as it is unable to produce targets of sufficient

[1]Department Chemie, Johannes Gutenberg-Universität Mainz, 55128 Mainz, Germany
[2]Helmholtz-Institut Mainz, 55128 Mainz, Germany
[3]GSI Helmholtzzentrum für Schwerionenforschung GmbH, 64291 Darmstadt, Germany
[4]Hochschule RheinMain, 65428 Rüsselsheim, Germany
[5]Technische Universität Darmstadt – Materialwissenschaft, 64287 Darmstadt, Germany
[6]European Commission, Joint Research Centre (JRC) - Karlsruhe, 76344 Eggenstein-Leopoldshafen, Germany
[7]Helmholtz-Zentrum Dresden-Rossendorf, Ion Beam Center, 01328 Dresden, Germany

thickness to cover the full useful width of the excitation functions [38, 131]. Given the large solid angle acceptances of current recoil separators and the overall detection efficiency of current experimental setups, production rates can almost exclusively be increased by using more intense ion beams and/or thicker targets. [138, 199, 35, 72, 39]. Both options require the development of actinide targets with improved stability. At present, the MP method is unable to take full advantage of the higher beam intensities that are now available [36, 198, 197]. A prerequisite for new target developments is a profound understanding of the existing MP method and the behaviour of MP targets in the ion beam. Despite numerous publications on the MP method, the exact process of molecular plating and thus the properties of the MP thin films remain rather unknown. A brief current literature overview can be found in [6].

MP targets have sometimes limited stability after production and are usually conditioned on-line [85, 20] using progressively increasing heavy-ion beam intensities over the course of a few hours. Bake-in procedures at GSI are done at earliest available beamtimes after target fabrication or alternatively directly at the beginning of a SHE production run, e.g., during adjustments of the experimental setup. Examples for this are ^{243}Am targets used at TASCA (**T**rans**A**ctinide **S**eparator and **C**hemistry **A**pparatus) in 2012 for spectroscopy experiments on Mc ($Z = 115$) decay chains [176], and later Nh ($Z = 113$) and Mc ($Z = 115$) chemistry studies [226]. Or ^{244}Pu targets produced in 2014 for chemical studies of Fl ($Z = 114$) [225, 227] as well as for Fl nuclear spectroscopy studies [182, 33, 32]. Without conditioning, the actinide thin films may experience limited adherence to their backing. After bake-in, though, even storage for months or years under normal conditions in air has no effect on the performance of such baked-in targets. The chemical processes involved in different conditioning procedures are still unknown, but attempts have already been made to develop offline equipment in order to make progress in this field without irradiation time [71, 132].

For SHE production experiments, special MP targets are fabricated from actinide isotopes, which usually are α emitters [43]. α-Spectroscopic studies of the target layer show that the width of the α-lines undergoes a change [85, 20] as the beam fluence increases, indicating a radiation-induced alteration in the material. These modifications are initiated by a relatively low ion dose and then remain constant throughout the entire SHE production experiment. Changes in the morphology of actinide thin films were also documented by photographic images [85, 20], atomic force microscopy (AFM) [129] and scanning electron microscopy (SEM) [129]. Analytical methods have so far been limited to energy dispersive X-ray spectroscopy (EDX) [129] and conventional X-ray diffraction (XRD) [129]. Both methods are challenged by the peculiarities of the current MP target technology and characterised by a poor signal-to-noise ratio. Initial research using Raman spectroscopy on thin ion-irradiated lead films [71, 132] as a model system for accelerator targets has demonstrated the conversion of carbonates into oxides.

A more detailed examination of MP-produced films and research into the conditioning process would benefit from access to state-of-the-art analytical techniques. Furthermore, the analysis of actinide films necessitates the use of licensed laboratories with the corresponding handling permits. To circumvent this issue, we thus replaced the actinides with lanthanide targets. Actinides elements with $Z \geq 95$ are chemically very similar to lanthanides [31], rendering the latter ideal for initial studies and for the development of novel protocols for actinide target production [119, 38, 6]. The irradiation of lanthanide thin films serves as a preliminary stage for irradiation experiments on actinide thin films. Analyzing these films poses specific challenges due to their intricate morphology. Similar demands are present for both irradiated and non-irradiated films. The MP thin films produced and irradiated in this study were characterised using the following analytical methods:

i) SEM to examine morphological alterations.

ii) Various ion beam analysis (IBA) techniques for elemental analysis, including elastic recoil detection analysis (ERDA), Rutherford backscattering spectrometry (RBS) and particle-induced X-ray emission (PIXE).

iii) Raman and infrared (IR) spectroscopy to identify changes of functional groups.

iv) X-ray photoelectron spectroscopy (XPS) for identification of elements and their chemical state.

v) Grazing incidence X-ray diffraction (GIXD) to identify beam-induced structural changes of the MP films.

3.4. Experimental

3.4.1. Target production

The targets were prepared from analytical grade lanthanide nitrates (Merck KGaA Darmstadt). The used solvents, isopropanol and isobutanol, and the nitric acid were also of analytical quality (Merck KGaA Darmstadt). The Ti backings had 99.9 % purity (Goodfellow). A solution comprising a 9:1 ratio of isobutanol to isopropanol was employed for the deposition process. This ratio is the most commonly utilised solvent mixture for MP target production within our laboratory [43]. The lanthanides were then electrochemically deposited from this solution onto a 25 µm-thick Ti foil. The deposited area was circular with a diameter of 0.6 cm (area: 0.28 cm^2). The depositions were carried out galvanostatically at a constant current of 0.28 µA and for 1 h. The exact production method and the electrochemical cell construction are described in [43, 217].

3.4.2. Target irradiation

Irradiations were performed at the materials research beamline M3 at the UNILAC accelerator at the GSI Helmholtz Centre for Heavy Ion Research in Darmstadt, Germany, using 8.3 $\frac{\text{MeV}}{\text{u}}$ Au^{26+} ions. Homogeneous exposure of samples was achieved by using a slightly defocussed beam. To prevent heating of the samples, the ion flux was kept below approximately $2.0(2) \times 10^9$ $\frac{\text{ions}}{\text{cm}^2\,\text{s}}$. The applied fluence ranged from 3.0×10^{11} to 1.0×10^{13} $\frac{\text{ions}}{\text{cm}^2}$ with an estimated uncertainty of about 10%. This accumulated fluence corresponds to the first few minutes of the target irradiation in a superheavy element production campaign and thus provides insight about the effects during the target conditioning process.

The parameters for the irradiations with Cl and Au ions are given in Table 3.3 together with comparative data of Ca ions applied earlier during bake-in procedures [132]. For the density of the MP films, we presume 2.73 $\frac{\text{g}}{\text{cm}^3}$ [26] which is the density of a thulium carbonate and as such notably lower than that of thulium hydroxide and oxide.

The calculated ranges of the three different ion species exceed by far the thickness of 0.7 to 1.4 µm [129] or the achievable area density (about 500 $\frac{\mu\text{g}}{\text{cm}^2}$) of the MP films, as shown in Table 3.3. In contrast to the typical SHE experiments [197, 38], where the beam first penetrates the backing and then enters the target thin film, our samples were positioned with the thin film facing the ion beam. This was also considered in the calculations presented. The total absorbed dose in Gray was calculated by multiplying the electronic energy loss per unit pathlength (dE/dx)e with the fluence.

content...

3.4.3. Target characterization

3.4.3.1. Scanning electron microscopy and energy dispersive X-ray spectroscopy

In order to evaluate the ion beam-induced surface modifications, scanning electron microscopy (Philips XL30) with an acceleration voltage of 20 kV was carried out in combination with detectors for secondary (SE) and backscattered electrons (BSE). In some cases, the samples were sputter-coated by a thin silver layer to avoid charging effects during imaging. The elemental composition of the thin films was investigated by energy-dispersive X-ray spectroscopy (EDX) and analyzed with the NIST DTSA-II Lorentz software package [146].

Table 3.1.: List of studied samples and analytical methods applied. The uncertainty of the areal density is assumed to be 10% based on an average of the density values given in the literature [177].

sample name	element	area density $\frac{\mu g}{cm^2}$	SEM	Raman	IR	IBA	GIXD	XPS
Tb-50	Tb	50	x	x	-	-	-	-
Er-50	Er	50	x	x	-	-	-	-
Tm-50	Tm	50	x	x	-	-	-	-
Tm-500	Tm	500	-	x	x	-	x	x
Tm target-1	Tm	500	-	x	-	-	-	-
Tm target-2	Tm	500	-	x	-	x	-	-
Tm target-3	Tm	500	x	x	-	x	x	-
Tm target-4	Tm	500	x	x	-	x	x	-
Tm target-5	Tm	500	x	x	-	-	x	x
Tm target-6	Tm	500	-	x	x	-	-	x
HDZR-500	Tm	500	x	-	-	x	-	-

Table 3.2.: List of irradiations. The first irradiation used 8.3 $\frac{MeV}{u}$ Au^{26+} ions at the M3 beamline of the GSI Darmstadt. For damage characterization of the Au-irradiated samples by means of ion beam analysis (IBA), we used a 1.2 $\frac{MeV}{u}$ Cl^{7+} beam at the HZDR. All samples have an area density of 500 $\frac{\mu g}{cm^2}$. The uncertainty of the area density and of ion irradiations are estimated to be 10%.

sample name	element	1st irradiation $\frac{Au\,ions}{cm^2}$	IBA	2nd irradiation $\frac{Cl\,ions}{cm^2}$
Tm target-1	Tm	3.0×10^{11}	-	-
Tm target-2	Tm	5.0×10^{11}	x	2.0×10^{14}
Tm target-3	Tm	1.0×10^{12}	x	2.4×10^{14}
Tm target-4	Tm	3.0×10^{12}	x	2.4×10^{14}
Tm target-5	Tm	5.0×10^{12}	-	-
Tm target-6	Tm	1.0×10^{13}	-	-
HDZR-500	Tm	-	x	8.7×10^{13}

Table 3.3.: Beam parameters for the different irradiations of Tm targets including the total kinetic energy in MeV per nucleon (MeV/u), the electronic and nuclear stopping power, the applied fluence as well as the projected ion range as calculated with the SRIM-2013.00 code, assuming a thulium carbonate target density of 2.73 g cm^{-3} [26]. The dose D is the product of the energy loss and the accumulated fluence.

ion	energy [$\frac{\text{MeV}}{\text{u}}$]	(dE/dx)e [$\frac{\text{keV}}{\text{nm}}$]	(dE/dx)n [$\frac{\text{keV}}{\text{nm}}$]	fluence [$\frac{\text{ions}}{\text{cm}^2}$]	range [µm]	range [$\frac{\mu\text{g}}{\text{cm}^2}$]	D [MGy]
^{35}**Cl**	1.2	3.3	6.1×10^{-3}	20×10^{13}	16	4452	388.94
^{48}**Ca**	5.9	2.8	1.8×10^{-3}	7×10^{13}	85	23 160	106.50
^{197}**Au**	8.3	17.9	2.2×10^{-2}	1×10^{13}	109	29 769	105.07

3.4.3.2. Elastic Recoil Detection Analysis

Some of the Tm targets were analyzed with Elastic Recoil Detection Analysis (ERDA) at the Ion Beam Center of the Helmholtz-Zentrum Dresden-Rossendorf (HZDR) using a 1.2 $\frac{\text{MeV}}{\text{u}}$ Cl ion beam. The angle between the sample normal and the incoming beam was 75°, the scattering angle was 30°. The analyzed area was about $2 \times 2\,\text{mm}^2$. The recoil atoms and scattered ions were detected with a Bragg Ionisation Chamber (BIC), which enables energy measurements and Z identification of the particles. H recoils were detected with a separate solid state detector at a scattering angle of 40°. The beam fluence is monitored using a gold plated rotating vane (1 Hz) and a solid state detector, which detects Cl backscattering from Au. This system is calibrated against the ion beam current measured with a Faraday cup. The resulting fluences per sample are given in in Table 3.2.

3.4.3.3. μ-beam - spatially resolved RBS and PIXE

Some of the Tm targets were analyzed with Rutherford Backscattering Spectrometry (RBS) and Particle Induced X-ray Emission (PIXE) at HZDR using a 3 MeV proton beam. The beam was focused to about $7 \times 5\,\mu\text{m}^2$. The backscattered protons were detected at a scattering angle of 174° with a silicon strip detector. A Ketek silicon drift detector collimated to 80 mm^2 was used to detect the X-rays emitted from the sample. The detector was placed outside the sample chamber. In addition, a 65 µm aluminium absorber was used to further reduce the contribution of the X-rays from the Ti substrate and stop backscattered protons from entering the detector. RBS was used to obtain depth profiles of the main elements except H, which cannot be detected by RBS. For C, N, and O evaluated cross-sections from SigmaCalc

are used [66]. For Ti, there exist no accurate data in the relevant energy range and for the used scattering angle. Therefore a measurement on the Ti backing foil was performed to obtain non-Rutherford cross-sections, which was possible using the program NDF [8]. AFM measurements across the pristine Ti foil showed a substantial roughness of rms = 39(8) nm. Thus the deduced cross-section might not be of universal validity.

In the case of the Tm thin films, a preliminary large-scale PIXE scan was conducted, after which individual areas of the thin film were selected for point measurements. All large PIXE scans contain 128×128 points or 128×100 points and have a size of $260 \times 260\,\mu m^2$ or $260 \times 205\,\mu m^2$, respectively.

3.4.3.4. Raman spectroscopy

Raman spectra from $50\,cm^{-1}$ to $4000\,cm^{-1}$ were collected with a Jobin Yvon (Horiba) LabRam HR 800 spectrometer equipped with an Olympus BX41 optical microscope and a Si-based charge-coupled device (CCD) detector. The instrumentation used a grating with 1800 $\frac{\text{grooves}}{\text{mm}}$ and a slit width of 100 mm. Excitation wavelengths of 633 nm and 488 nm were used. These parameters, and the optical path length of the spectrometer led to a spectral resolution of $0.8\ cm^{-1}$. The spectral acquisition time was set to 40 s for all measurements. In order to exclude modifications due to laser irradiation, long-term measurements were carried out analogous to [23]. The Raman spectra were assessed using the Fityk software [224].

3.4.3.5. Infrared spectroscopy

Infrared (IR) spectra were recorded with a Bruker Alpha Platinum-ATR. For this purpose, the Bruker Platinum ATR monolithic diamond crystal was pressed onto the MP thin films and the spectra were recorded in the attenuated total reflection setup. The IR spectra were recorded after all other analytical work was completed, as the ATR mode may mechanically damage the surfaces. The spectra were recorded using Bruker OPUS software and analyzed by the Spectragryph software package [130].

3.4.3.6. X-ray photoelectron spectroscopy

For elemental analysis, several selected samples were investigated by XPS, some time (days up to months) after their preparation. Irradiated samples were stored under ambient air for even longer times and underwent several other characterisation methods beforehand. During the measuring campaign the samples were stored in a UHV-chamber (base pressure about 2.0×10^{-8} mbar) neighbouring the XPS analysis chamber. The base pressure in the XPS chamber was kept below 5.0×10^{-10} mbar. XPS

measurements were conducted using a monochromatic Al K_α X-ray source and a hemispherical analyzer Phoibos 150 with HAS 3500 plus controller (all from Specs, Berlin). The microfocus high performance X-ray source XRC-1000 MF was equipped with a μ-FOCUS 500 monochromator (all from Specs, Berlin). XPS analysis and peak fitting were performed with CasaXPS [48] (Ver. 2.3.24 PR 1.0).

Generally, charging effects lead to a slight broadening of the full width half maximum (FWHM) of XPS peaks. Such charge shifts can be corrected using a flood gun, which flushes the sample surface with low-energy electrons in order to compensate for the charge. At the same time, the electron beam emitted by the flood gun can modify surface species [7, 41]. Therefore, care has to be taken in the interpretation of the data.

3.4.3.7. Grazing incidence X-ray diffraction

In grazing incidence X-ray diffraction(GIXD), a very small angle of incidence (ω) was chosen to limit the penetration depth of the photons to a thin surface layer of the film. The X-ray beam and sample were fixed to ensure a small angle of incidence ($\omega \approx 0.1$ - 5°) while the detector moves at an angle of 2Θ to collect diffraction signals. The structural information thus originates predominantly from the near-surface region (<400 nm). For the GIXD measurements, a SmartLab device from the Rigaku company with a rotating anode was used with CuK_α radiation (λ = 1.5406 Å).

3.5. Results and Discussion

3.5.1. Morphology of MP films

3.5.1.1. Non-irradiated samples

The molecular plating method produces thin films with a characteristic morphology consisting of individual tiles separated from neighboring tiles by deep cracks down to the substrate as shown in a representative SEM image (Fig. 3.1 right). This morphology is extensively described for the MP process [107, 113] and is also referred to as mudcracking [6, 202] or mud-caking [25, 141]. Each material produces a different mudcracking pattern and minute changes in MP parameters can have a large impact on the morphologies [107, 216]. Other methods of electrochemical deposition of lanthanides and actinides also describe a cracked surface structure [202, 117, 12, 184]. Vascon et al. showed that the cracks form after plating during drying and that the individual tiles of the thin film are not smooth, but have a rough substructure [216]. The formation of surface cracks depends mainly on the chosen solvent (isobutanol:isopropanol, 9:1). It should be noted that the solvent was kept constant throughout our ex-

periment series.

Our scanning electron microscopy images clearly show (Fig. 3.1 right), that mudcracking leads to a significant portion of the surface of MP targets becoming uncovered. This effect should be taken into account during irradiation experiments and when utilising analysis methods without a micrometre spatial resolution such as ERDA, GIXD and IR spectroscopy, etc.

3.5.1.2. Irradiated samples

First we discuss morphological changes of a fresh Tm MP film caused by the irradiation with 1.2 $\frac{\text{MeV}}{\text{u}}$ Cl ions (beam applied for ERDA). For an accumulated fluence of 2×10^{14} $\frac{\text{ions}}{\text{cm}^2}$, the changes in the irradiated area ($2 \times 2\,\text{mm}^2$) can easily be identified by the naked eye (Fig. 3.1 left). The sharp focus of the ion beam allows the interface between irradiated and non-irradiated area of the target to be displayed in one SEM image (Fig. 3.1 right) at high magnification. The SEM images of the two areas underline the difference; the characteristic tiles due to mudcracking are clearly visible in the non-irradiated area (Fig. 3.1 right). After the irradiation with 1.2 $\frac{\text{MeV}}{\text{u}}$ Cl ions, the tiles barely cover the Ti backing, they shrank in size and are strongly deformed (Fig. 3.1 right).

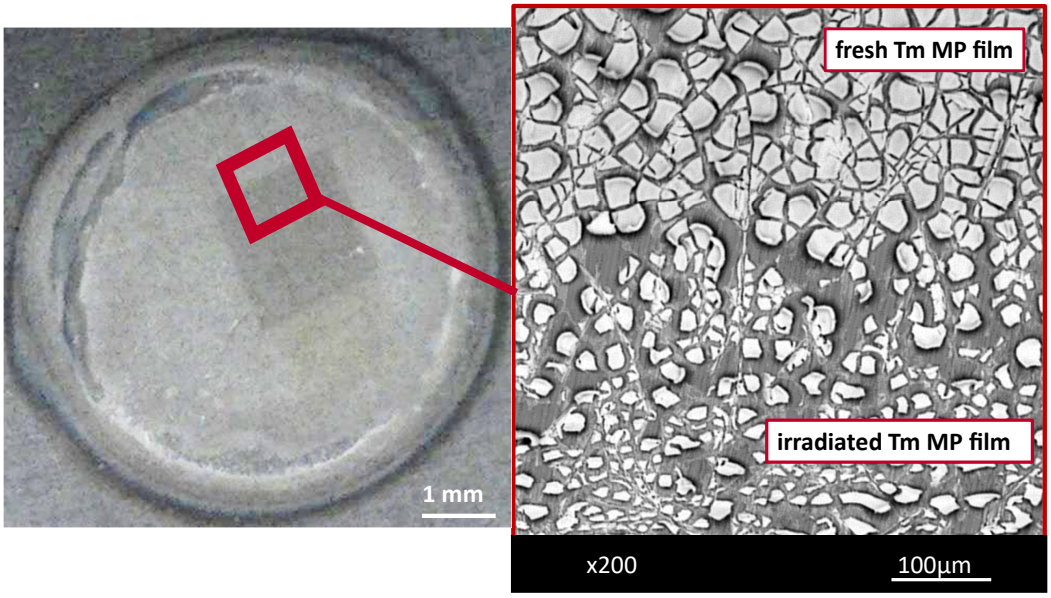

Figure 3.1.: Photography (left) and SEM image (right) of a 500 $\frac{\mu\text{g}}{\text{cm}^2}$ thick Tm target (sample: HZDR-500) after irradiation with 1.2 $\frac{\text{MeV}}{\text{u}}$ Cl ions (2.0×10^{14} $\frac{\text{ions}}{\text{cm}^2}$). On the photography, the irradiated area is clearly visible as dark square. On the SEM image, the upper part is the non-irradiated area and the lower part shows the irradiated area.

We also inspected the morphological changes of samples exposed to a fluence series with 8.3 $\frac{\text{MeV}}{\text{u}}$ Au^{26+} ions (Fig. 3.2, 1a-1c) and subsequently analyzed the films by ERDA with 1.2 $\frac{\text{MeV}}{\text{u}}$ Cl^{7+} ions (Fig. 3.2, 2a-2c). Up to the maximum applied Au ion fluence, the size of the tiles does not seem to change, but the uncovered area in between individual tiles becomes smaller. At the highest fluence (3.0×10^{12} $\frac{\text{ions}}{\text{cm}^2}$), Tm covers the Ti backing almost without cracks. Comparable observations have been described for MP gadolinium films [129].

Samples that were irradiated with Au ions and then ERDA-analyzed with the high-intensity Cl beam are shown in Fig. 3.2, 2a-2c . Morphological changes were also observed in samples irradiated with Cl ions only. Individual tiles exhibit deformation and shrinkage, but the overall effects appeared to be less pronounced the larger the fluence of the preceding Au irradiation.

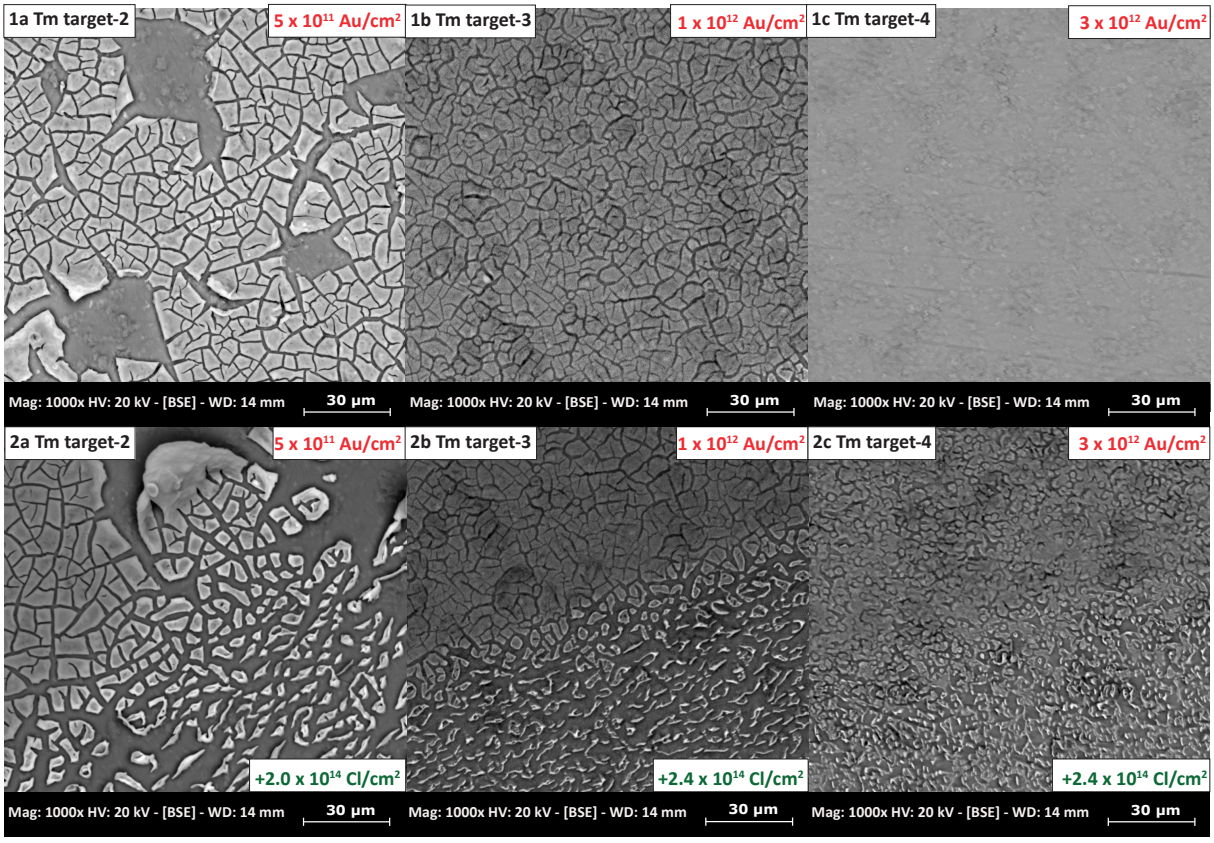

Figure 3.2.: SEM images of MP Tm thin films (thickness 500 $\frac{\mu\text{g}}{\text{cm}^2}$, samples: Tm target-2 to Tm target-4) irradiated with different fluences. Top row (1a-1c): Tm films irradiated with 8.3 $\frac{\text{MeV}}{\text{u}}$ Au ions at increasing fluence. Bottom row (2a-2c): same sample series after ERDA analysis using 1.2 $\frac{\text{MeV}}{\text{u}}$ Cl ions of fluence 2.0×10^{14} $\frac{\text{ions}}{\text{cm}^2}$ to 2.4×10^{14} $\frac{\text{ions}}{\text{cm}^2}$. The lower series shows exactly the transition area of the ERDA analysis beam spot. Note that the SEM image 1c is slightly defocused, making the surface appear smoother than it really is.

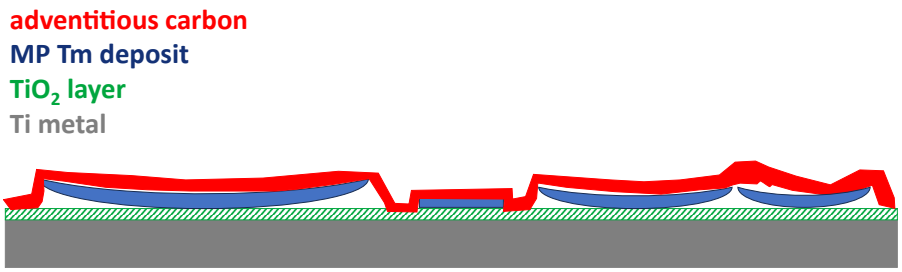

Figure 3.3.: Sketch of cross-section through the MP Tm film, to illustrate the difficulties of XPS, RBS and ERDA measurements due to tile formation, cracks and adventitious carbon contamination.

3.5.2. Ion beam analysis

Damage effects in samples exposed to 1.2 $\frac{\text{MeV}}{\text{u}}$ Cl ions for ERDA were analyzed with a μ-beam. The border area between ERDA-irradiated and non-irradiated sample surface was examined, so that the influence of irradiation on the thin films could be studied (Fig. 3.4 (a)). A sketch (Fig. 3.3) of the cross-section of the non-irradiated MP thin films, as derived from our microscopy images and the existing literature [217, 28, 140], illustrates the challenges in the application of ion beam methods in materials analysis.

3.5.2.1. Non-irradiated samples

The analysis of RBS and PIXE with a μ-beam made it possible to spectroscopically investigate individual tiles on the mudcracked surface. The element concentrations calculated from the RBS depth profiles for individual tiles of non-irradiated MP thin film (thickness 500 $\frac{\mu\text{g}}{\text{cm}^2}$) are dominated by the elements C and O (Fig. 3.4 (c)). Tm is only a minor component in atomic percent of the thin films. The N signal is characterised by a poor signal-to-noise ratio, therefore nitrogen is just barely detectable by RBS. Still, the weakness of the N signal suggests that we can exclude a significant deposition of nitrate species, which is consistent with other spectroscopic studies [216, 28]. The Ti signal from the backing foil varies between individual tiles, which indicates that the tiles are of different thicknesses. The signal strength remained consistent across all tiles for the other elements. The depth profiles are obtained after analysis using the NDF-code [8] and conversion from the spectrum recorded during the RBS measurement. The film thicknesses obtained from the analysis are given in units of at/cm^2. A conversion into a length unit is problematic as the mass density of the film is not precisely known. A length estimate based on the weighted average of the atomic densities gives a film thickness of about 2 µm for the μ-beam measurements (Fig. 3.4 (c,d)), which is consistent with our AFM and 3D laser scanning microscope measurements (not shown).

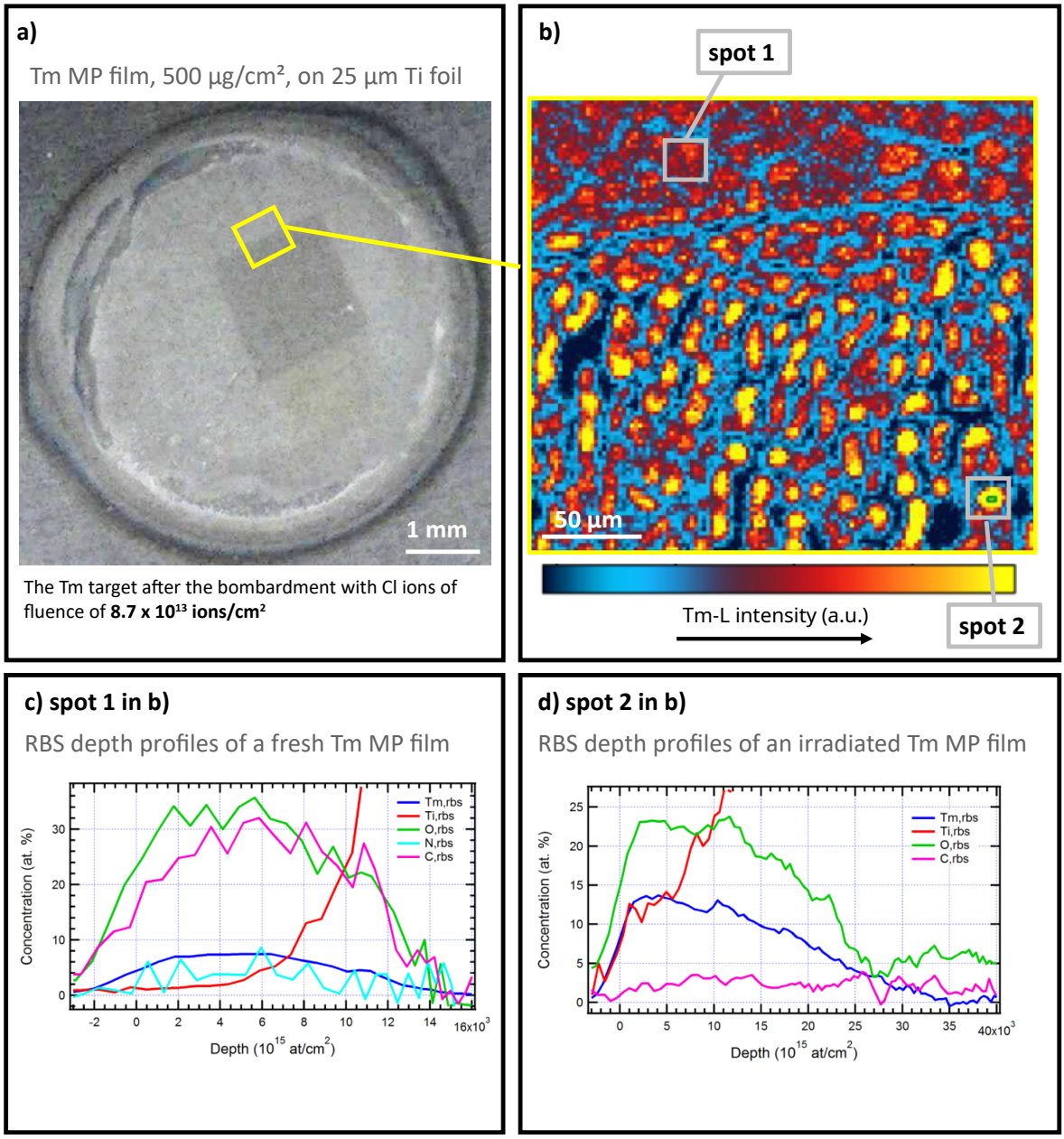

Figure 3.4.: (a) Photography of MP Tm thin film (sample: HZDR-500) with yellow frame indicating the PIXE analyzed area performed after ERDA analysis with 8.7×10^{13} $\frac{\text{ions}}{\text{cm}^2}$ of 1.2 $\frac{\text{MeV}}{\text{u}}$ Cl ions. (b) PIXE map of non-irradiated (top area) and Cl-ion exposed area (bottom). The color code corresponds to high (yellow) and low (blue) Tm concentrations. Spot 1 and 2 indicate spots analyzed by μ-beam RBS analysis. (c) and (d) RBS data for various elements from spot 1 (non-irradiated) and spot 2 (Cl ion irradiated), respectively.

3.5.2.2. Irradiated samples

Comparing the PIXE data at the transition between non-irradiated and irradiated (Fig. 3.4 (b)), we first see that the elemental distribution of the PIXE map reproduces quite well the morphology of the MP thin films, as observed by SEM (Fig. 3.1 right). The higher intensity of the Tm-L signal is the result of Tm being accumulated in a smaller area. Furthermore, the distances between the Tm island or MP tiles are larger than in the non-irradiated area.

The RBS element analysis of the non-irradiated area (Fig. 3.4 (c)) is dominated by C and O. Irradiation leads to the loss of most of the carbon. Due to the irradiation, the relative proportion of Tm increases, oxygen and Tm become the dominant components, C is detectable just above the signal noise and nitrogen is below the detection limit (Fig. 3.4 (d)).

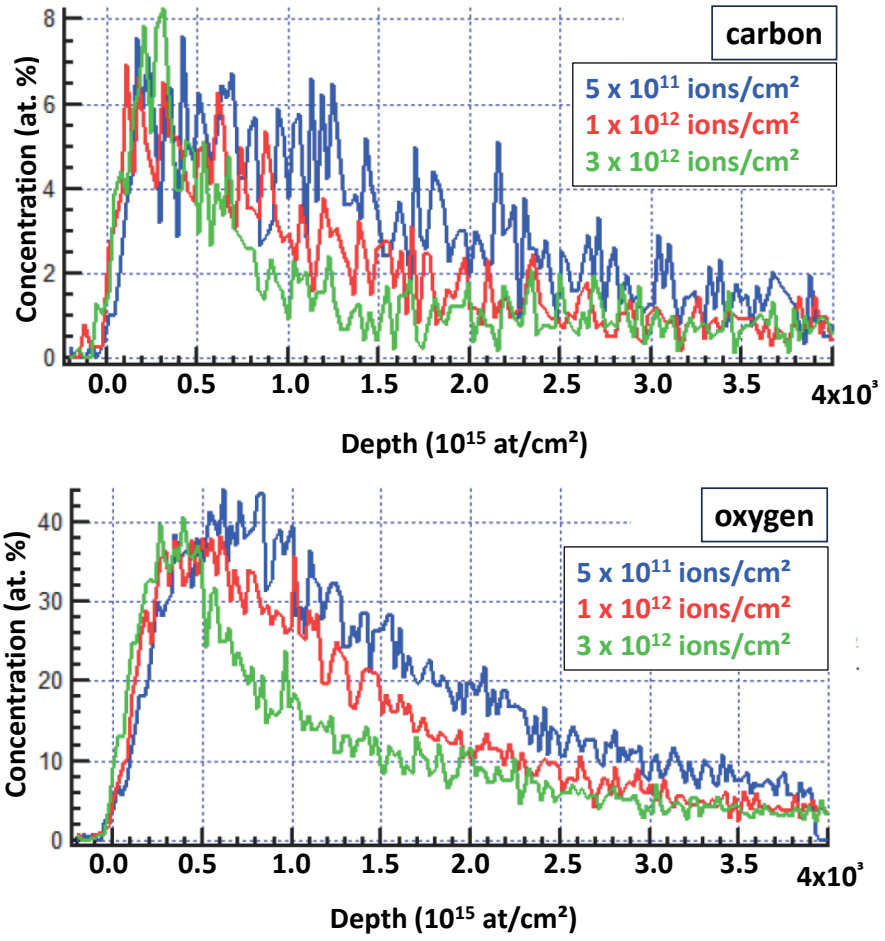

Figure 3.5.: C and O concentration as a function of depth deduced from ERDA spectra for MP Tm thin films (sample series Tm target-2 to Tm target-4). The contribution of both elements decreases with depth and with increasing fluence.

The ERDA investigation of the fluence series of Au-ion irradiated Tm samples (Fig. 3.5) confirms the decrease of the overall carbon and oxygen concentration as a function of fluence. The depth profile of the oxygen concentration fits well with the oxygen contents that were detected in the irradiated thin films by means of RBS. The carbon content determined by ERDA is higher than what was determined by the RBS measurements of irradiated thin films. The irradiation-induced alterations of the thin films, namely compaction and the loss of light elements, rendered the evaluation of the ERDA data a challenging endeavour. The ERDA measurements were further complicated by the morphology of the samples, a problem that is circumvented in RBS/PIXE measurements due to their superior spatial resolution. Collectively, the ERDA measurements align with the hypothesis that the irradiation with energetic heavy ions results in a depletion of C and O in MP thin films. Based on the results obtained from the ion beam methods, no significant beam-induced loss of Tm was observed. The combined PIXE/RBS/ERDA data suggest that the MP film tiles lose volatile components containing O and C, as a consequence of irradiation. This may result in chemical transformations that could potentially lead to the formation of a compound with a higher density, which in turn would result in a reduction of the area covered by the MP thin film.

We conclude from our data, that the determination of the elemental composition by the applied ion beam analysis was clearly at the limit of statistical significance for both non-irradiated and irradiated thin films. Techniques with high spatial resolution (e.g. using a μ-beam) are particularly suitable for overcoming challenges associated with the morphology of the MP films.

3.5.3. Vibrational spectroscopy

3.5.3.1. Non-irradiated samples

After achieving promising results using confocal Raman spectroscopy on lead model systems [71, 132], we applied the method on a series of thin MP-produced lanthanide films including Tb, Er, and Tm (Fig. 3.6). The exceptional spatial resolution of this method enabled us to spectroscopically examine individual tiles, ensuring that the complex morphology and the presence of a Ti backing did not affect the accuracy of the measurements. Despite the thin Tb films exhibiting more pronounced mudcracking compared to Er and Tm, their Raman spectra are remarkably similar (Fig. 3.6). Furthermore, none of the samples exhibit any orientation-dependent behavior in their Raman spectra, indicating that they are in an amorphous or microcrystalline state composed of randomly oriented microcrystals [195].

The Raman spectra were recorded using two different lasers of wavelengths, 473 nm and 633 nm, of the confocal Raman microscope. Several different tiles were examined per sample in order to produce representative results for each sample. The spectra were identical for both excitation wavelengths and

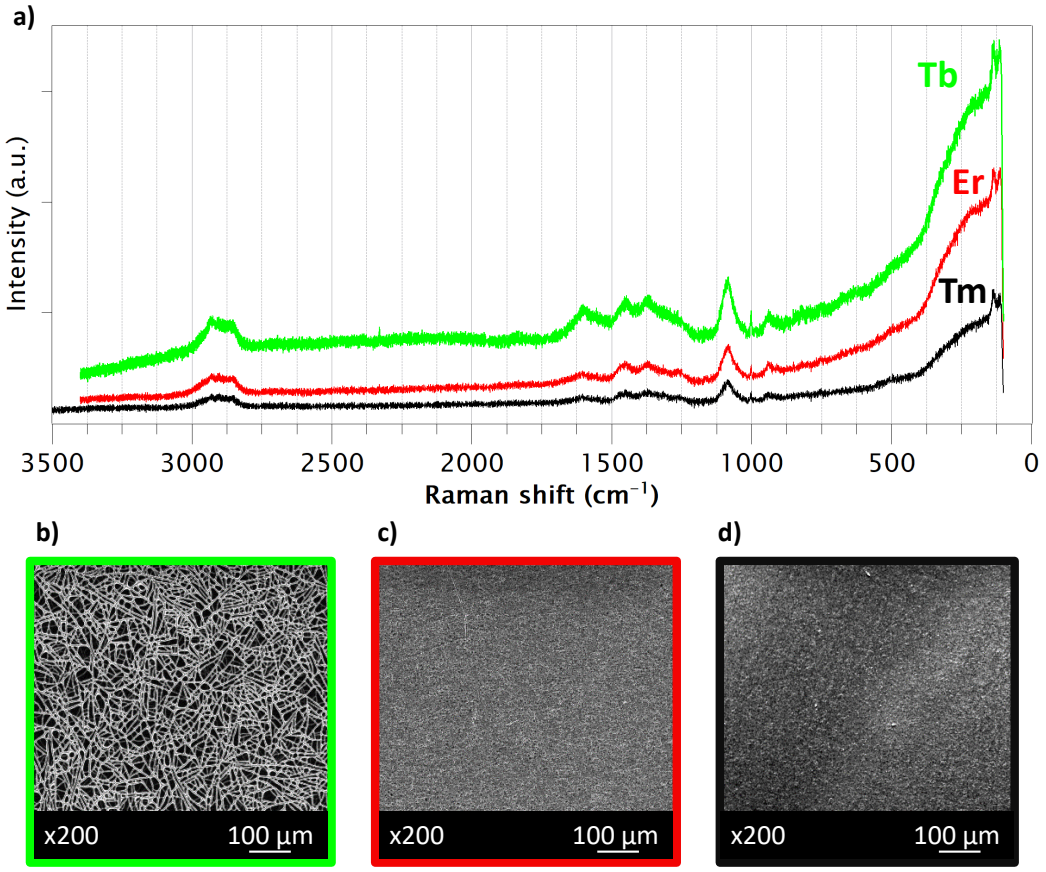

Figure 3.6.: (a) Raman spectra of Tb (sample Tb-50), Er (sample Er-50) and Tm (sample Tm-50) films of thickness: 50 $\frac{\mu g}{cm^2}$ and (b)-(d) respective SEM images. Despite different morphologies, MP thin films of different lanthanides show the same Raman spectrum.

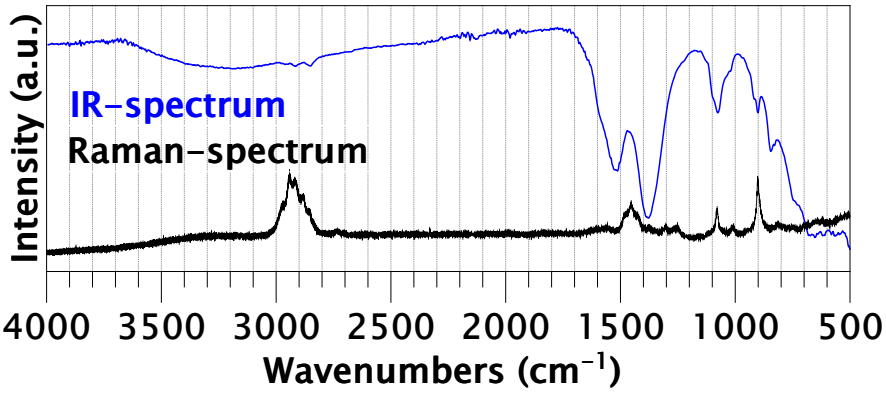

Figure 3.7.: Raman and IR spectrum of MP Tm thin film (thickness 500 $\frac{\mu g}{cm^2}$, sample: Tm-500).

exhibited identical peak intensities. The ratio of the peak positions also remained constant, but the peak positions themselves fluctuated by about 3 cm^{-1} from measuring point to measuring point. According to [28], MP films are armorphous material, while the reference literature cited below refers exclusively to monocrystalline materials. For the final fit of the bands and the assignment to literature values, the spectrum with the lowest background was selected (Fig. 3.7).

In the Raman spectra of our Tb, Er and Tm films, carbonate [195, 2, 221, 75] and formate [95, 139, 190] could be identified. Some Raman modes of the chemically closely-related anions overlap (Fig. 3.7). The identified bands are given in Table 3.4 and assigned to Raman modes where possible. Herzberg [79] nomenclature was used.

The wavenumber range from 50 to 700 cm^{-1} is characterised by a high background and a poor signal-to-noise ratio, we thus ignored this wave number regime for the analysis (Fig. 3.6). At larger wavenumbers, the spectrum is dominated by two bands, a sharp narrow peak (902 cm^{-1}), which can be assigned to the out-of-plane bend (ν_2) of the carbonate ion, as well as a multiplet (2733 to 3066 cm^{-1}), which is assigned to the C-H stretching vibration of the formate. Most of the other peaks in the spectrum can be assigned to either anion.

The free carbonate anion belongs to the point group D_{3h} and therefore has four vibrational transitions [2]. We assign the bands between 1560 to 600 cm^{-1} (Tab. 3.4) to coordinated carbonate. The four normal vibrational transitions are expected in a range from 1090 to 1070 cm^{-1} (ν_1), 930 to 850 cm^{-1} (ν_2), 1560 to 1420 cm^{-1} (ν_3) and 820 to 750 cm^{-1} (ν_4). The splitting of the degenerate modes ν_3 and ν_4 may be caused by the symmetry reduction from D_{3h} to C_{2v} or C_s from the free to the coordinated carbonate anion [75]. In an amorphous phase all four vibrational transitions of the carbonate ions are expected to

Table 3.4.: Assignment of bands in the Raman and IR spectra of the non-irradiated MP Tm films, as designated by Herzberg [79].

Wavenumber	Method	Carbonate	Formate	References
401	IR	unknown		
563	IR	unknown		
619	IR	ν_{4a}	-	[194]
653	IR	ν_{4b}	-	[194]
673	IR	ν_{4c}	-	[194]
754	Raman	ν_{4a}	ν_{3a}	[2, 221, 75, 95, 190]
813	Raman	ν_{4b}	ν_{3b}	[2, 221, 75, 95, 190]
846	IR	ν_{2a}	-	[194]
901	IR	ν_{2b}	-	[194]
902	Raman	ν_2	-	[2, 221, 75]
1008	Raman	-	ν_{6a}	[190]
1076	IR	ν_1	-	[2, 221, 75]
1079	Raman	ν_1	ν_{6b}	[2, 221, 75, 190]
1252	Raman	unknown		
1302	Raman	unknown		
1374	Raman	-	ν_{2a}	[95, 190]
1379	IR	ν_{3a}	ν_{2a}	[194, 95, 190]
1423	Raman	ν_{3a}	ν_{5a}	[2, 221, 75, 95, 190]
1453	Raman	ν_{3b}	-	[2, 221, 75]
1476	Raman	ν_{3c}	-	[2, 221, 75]
1514	IR	ν_{3b}	-	[194]
1557	Raman	ν_{3d}	-	[2, 221, 75]
1583	Raman	-	ν_{4a}	[139, 190]
1605	Raman	-	ν_{4b}	[139, 190]
2733	Raman	-	ν_{1a}	[95, 139, 190]
2770	Raman	-	ν_{1b}	[95, 139, 190]
2882	Raman	-	ν_{1c}	[95, 139, 190]
2915	IR	-	ν_{4a}	[95]
2918	Raman	-	ν_{1d}	[95, 139, 190]
2942	Raman	-	ν_{1e}	[95, 139, 190]
2960	IR	-	ν_{4b}	[95]
3066	Raman	-	ν_{1f}	[95, 139, 190]

be both infrared and Raman active. Furthermore, one would expect that the degenerancy of the ν_3 and ν_4 modes for the free carbonate ions is lifted [2]. Detailed correlation schemes and group theory discussion of the spectroscopy of carbonate in solid phases can be found in [2, 221, 75]. The observed Raman spectra (Fig. 3.7) can therefore be partly explained by bound carbonate in an amorphous phase.

The free formate anion has the point group C_{2v}, thus six vibrational transitions can be derived from group theory [95, 139, 190]: The C-H stretch in the range from 3070 to 2730 cm^{-1} (ν_1), the O-C-O symmetric stretch from 1380 to 1360 cm^{-1} (ν_2), the O-C-O symmetric deformation from 820 to 750 cm^{-1} (ν_3), the O-C-O asymmetric stretch from 1610 to 1580 cm^{-1} (ν_4), the C-H in-plane bend from 1430 to 1420 cm^{-1} (ν_5) and the out-of-plane bend from 1080 to 1005 cm^{-1} (ν_6) [190]. Only the most intense bands at 2918 cm^{-1} and 2942 cm^{-1} can be unambiguously assigned to the C-H stretch (ν_1) of the formate [139] in good agreement with the reported literature values of 2920 cm^{-1} and 2949 cm^{-1} [95]. For the other modes, no exact measured or calculated values are given for thulium formates, but they are available for homologues from the lanthanide series. As in the case of carbonate, symmetry reduction in amorphous materials would be an explanation for the occurrence of bands that are in principle symmetry-forbidden bands in the Raman spectrum. The C-H stretching vibration (ν_1) is of particular importance in formates, thus its variation within the lanthanide series has been systematically studied [95, 190].

It should be mentioned that the nitrate anion also has a D_{3h} symmetry and should thus produce Raman bands similar to those of carbonates, which is how Raman spectra of uranium MP films were interpreted [92]. However, due to the very different chemistry of uranium compared to lanthanides and heavy actinides, this interpretation of the Raman spectra cannot be applied. Other studies on uranium MP targets could not detect any nitrate in the thin films by Raman and IR [179] or XPS [189, 155], and the thin films were reported to be nitrogen-free.

We also recorded IR spectra for a fresh MP Tm film and compare the respective IR and Raman spectrum in Fig. 3.7. Comparison with the literature shows that carbonates [194] and formates [95] also contribute to the IR spectrum. Large differences are present only in the OH-bands. The bands were again assigned using Herzberg nomenclature (Tab. 3.4).

3.5.3.2. Irradiated samples

Figure 3.8 shows spectra from a series of 8.3 $\frac{\mathrm{MeV}}{\mathrm{u}}$ Au ion irradiations. With increasing fluence, the two most prominent Raman bands (at 1079 cm^{-1} (a) and at 2942 cm^{-1} (c)) disappear and two new bands (b) gradually emerge around 1590 cm^{-1} (1650 to 1480 cm^{-1}) and 1360 cm^{-1} (1440 to 1290 cm^{-1}).

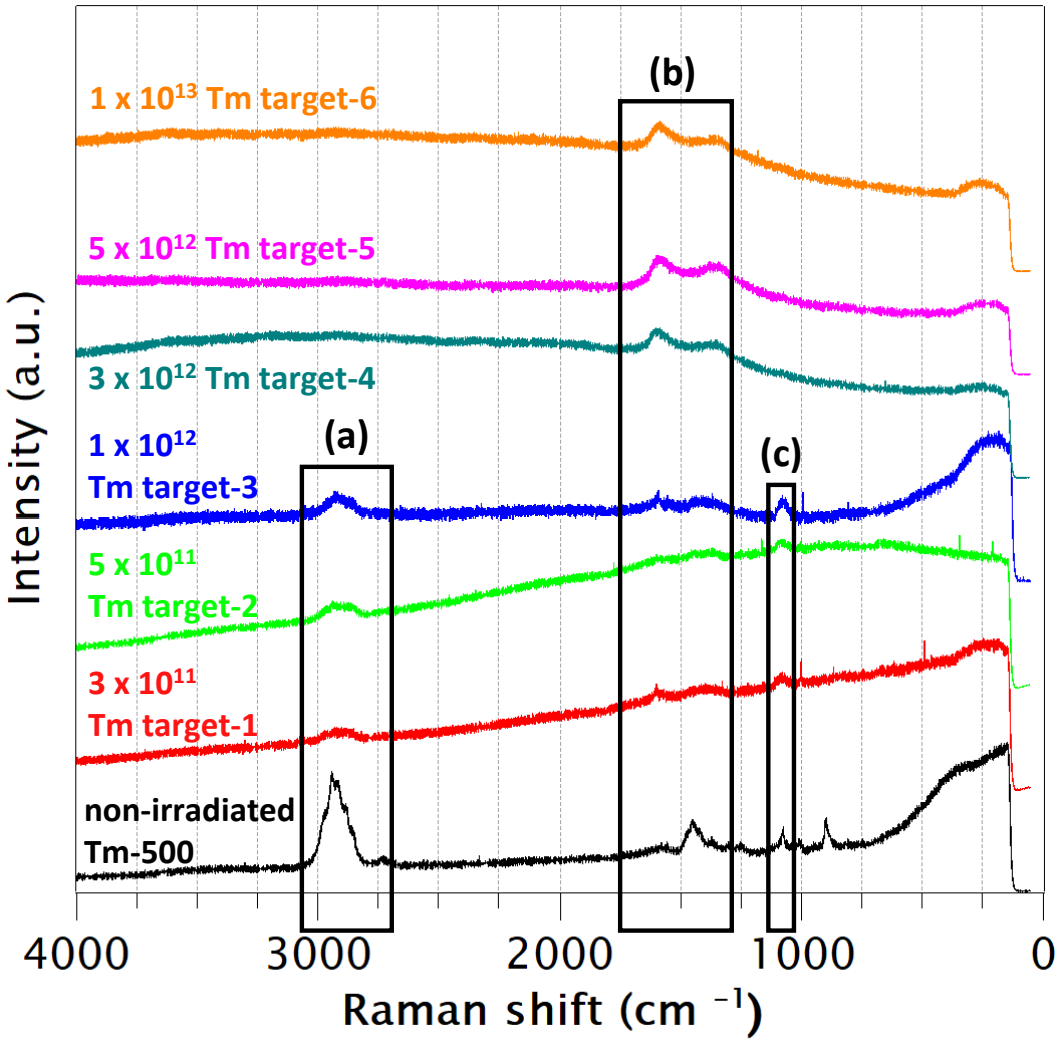

Figure 3.8.: Raman spectra of a Tm sample series (Table 3.2) irradiated with 8.3 $\frac{\text{MeV}}{\text{u}}$ Au ions of different fluences. The boxes indicate the position of bands assigned to formate (a), graphite (D and G band) (b) and carbonate (c). The fluence is given in units of $\frac{\text{ions}}{\text{cm}^2}$

The two new bands can be assigned to the D (1440 to 1290 cm^{-1}) and G (1650 to 1480 cm^{-1}) peaks, which are characteristic for graphite-like structures embedded into an oxide structure [191, 49, 11]. The G-band is the primary mode in graphene and graphite. It represents the planar configuration sp^2-bonded carbon that constitutes graphene. The band is resonant, which means that it is much more intense than would be expected otherwise. The D-band is known as the disorder band or the defect band. It represents a ring breathing mode from sp^2 carbon rings, though to be active the ring must be adjacent to a graphene edge or a defect. A significant D-band indicates defects to be present in the material. The intensity of the D-band is directly proportional to the level of defects in the sample [81]. In light of the aforementioned findings, it can be posited that the irradiated MP thin films can be characterised as amorphous oxides with embedded carbon clusters, as evidenced by the results of our Raman spectroscopy analysis [11].

The IR spectrum of the sample with the highest fluence is plotted together with the Raman spectrum of the same sample in Fig. 3.9. In the region of high wavenumbers, there is also activity that could be assigned to OH-oscillations. The hygroscopicity of the samples may be a potential explanation for the origin of this OH-oscillation. Otherwise, the IR spectrum of the irradiated samples does not permit further identification of chemical species. Yet, the appearance of oxycarbonates has been inferred from earlier GIXD and XPS studies [28], for lanthanum MP thin films that were heated to 700 K. However, Raman and IR spectra of these oxycarbonates [64] could not be identified in our films. Therefore, ion irradiation obviously induces a different form of transformation rather than pure heating [129].

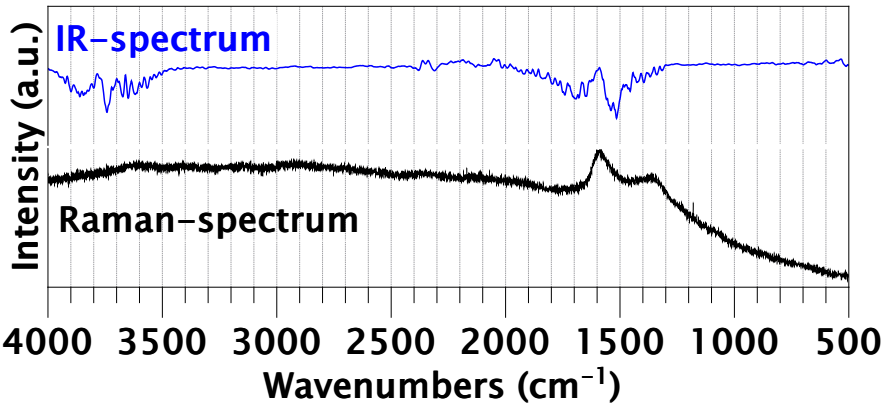

Figure 3.9.: IR and Raman spectra of MP Tm thin film (thickness 500 $\frac{\mu g}{cm^2}$, sample: Tm target-6) after irradiation with 8.3 $\frac{MeV}{u}$ Au ions of fluence 10^{13} $\frac{ions}{cm^2}$.

3.5.4. X-ray photoelectron spectroscopy (XPS)

In the XPS overview spectra (not shown) of the MP Tm thin films the expected characteristic Tm, O, and C peaks as well as the peaks of Ti are visible. The Ti signal originates from the Ti backing due to the mudcracking morphology as illustrated in Fig. 3.1 and 3.3. The tiles do not completely cover the surface and the Ti backing (together with its oxide layer) is exposed to the analyzing beam.

The electrical conductivity of the MP films is rather poor, which favours charging effects [110, 27] during the XPS measurement. As is typical for air-exposed samples, they are covered with so-called "adventitious carbon", a layer of short-chain oxygen-containing organic carbon compounds. Together with charging effects, this makes the direct interpretation of the C1s spectra difficult [7, 61]. Further, it is important to note that numerous authors report charge-corrected measured binding energies. Often, the dominant C1s peak is attributed to adventitious carbon and placed in a range of 284.5 to 285.5 eV. This approach leads to inconsistencies in the energy positions among different reports as the final charge-corrected binding energy is not necessarily accounting for the nature of different organic species [7, 61]. Therefore in this experimental series we tried to avoid relying on the absolute, charge-corrected BE values but tried to use peak differences for our interpretations [41].

Despite the problems described in the previous paragraphs, we discuss in the following the change in C1s spectra under irradiation. The C1s region (Fig. 3.10) for the irradiated samples is less complex than that of the fresh MP samples. The number of carbon species needed to develop a peak model is reduced for the irradiated samples and the peak observed above 292 eV is absent after irradiation. Table 3.5 summarises the assigned chemical species. Carbon species containing C-Cl and C-N bonds were excluded from consideration as no indications for the presence of Cl and N were obtained in XPS overview spectra, nor with other analytical methods like RBS or ERDA. Fluorine was observed only for the irradiated films (samples Tm target-5 and Tm target-6) and is assumed to be due to surface contamination during sample handling or storage in a UHV-chamber. We ascribe the peaks in the C1s XPS spectra to the following three carbon species: (i) a thin layer of adventitious carbon-containing material on the conductive Ti [61], (ii) the same layer on the MP thin film and (iii) the confirmed carbon species in the MP thin film itself.

The C1 peak is interpreted to represent the C-C/C-H contribution of the adventitious carbon on the Ti backing (Fig. 3.10). This is supported by the absence of the peak when no Ti is detected in overviews and Ti2p detail spectra. The binding energy (BE) corresponds to the value measured on a blank Ti reference backing (not shown) without deposited film. The superposition of the peaks in the irradiated samples (Fig. 3.10 (b) and (c)) illustrates a major problem of interpretation. The main peak can be fitted with variable proportions of adventitious carbon contributions, i.e. both C1 and C2 species in variable

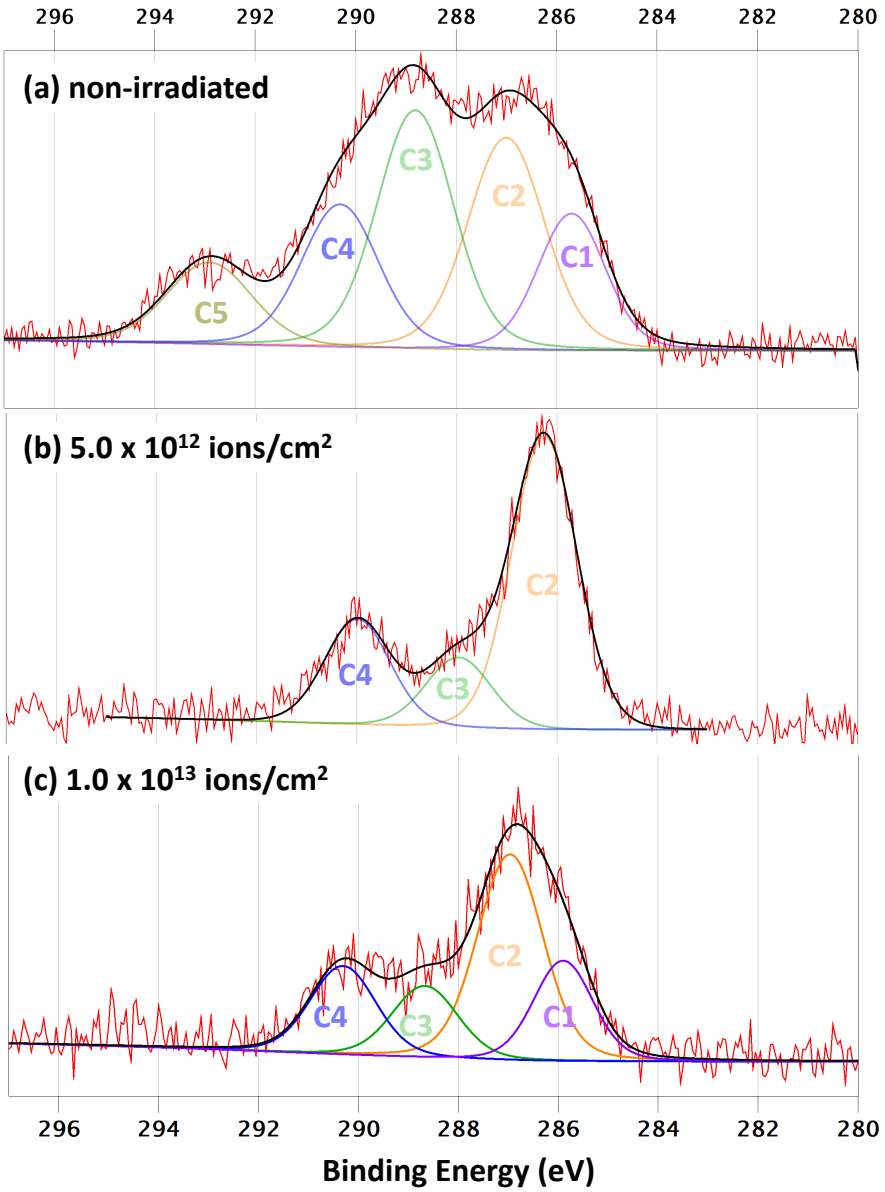

Figure 3.10.: C1s XPS spectra of MP Tm samples together with fits of individual carbon species for non-irradiated sample (top) and two samples irradiated with 8.3 $\frac{\text{MeV}}{\text{u}}$ Au ions of different fluence. The samples shown are Tm-500 (a), Tm target-5 (b) and Tm target-6 (b).

Table 3.5.: Measured binding energy (BE) and chemical shift (CS) of different carbon species.

Peak	**BE** eV	**CS** eV	**Possible species**
C1	285.7		C-C/C-H contrib. of advent. carbon on Ti backing [61]
C2	286.3 - 287.0		C-C/C-H contrib. of advent. carbon on MP Tm film [61]
C3	287.9 - 288.8	1.5 - 1.8	C-O-C, C-OH, C*-O-C=O [48]
C4	290.0 - 290.4	3.3 - 3.7	C-O-C*=O HCOO [48]
C5	292.8 - 292.9	5.9	O=C(-O-)2 [48]

proportions. This discrepancy is likely due to the challenging morphology of the samples, in addition to the limitations of the XPS method, such as charging effects.

Given the intricate surface morphology of the samples and the ion-beam-induced inconsistency in the XPS spectra, a quantification of the Tm-C ratio was deemed to be unreliable and unsound. Additionally, the issue of adventitious carbon (Table 3.5) on the Ti backing alone would have rendered further calculations even more arbitrary.

However, the clear change in the C1s spectra induced by the ion irradiation can be reconciled with the results of Raman spectroscopy and ion beam analysis, which suggest that the freshly deposited formates, (hydroxo)carbonates, hydroxides change under irradiation to a more oxidic species with intercalated carbon clusters.

Also in the O1s region distinct differences between the freshly deposited and the irradiated samples are observed (Fig. 3.11 (a)). Again, a BE component at 532 eV is observed that correlates with the presence of Ti in the spectra. This is likely due to an oxidised Ti surface (TiO_2). For the blank Ti reference sample, an oxidised layer was observed as well. Another assignment possibility for the 532 eV peak would be a thulium oxide component. In principle, the O1s peaks of metal oxides are characterized by a narrow peak shape, while the peaks of carbonates or formates should be broader. The shoulder at 529 eV in the non-irradiated samples could be explained by carbonate or formate based on the other analysis results, but this is not certain due to the inconclusive energy calibration. Furthermore, metal carbonates would be expected at higher BE than metal oxides, not lower. Thus, no clear, unambiguous conclusion can be drawn from the O1s spectra alone.

In the Tm4d region differences are observed between non-irradiated and irradiated samples (Fig. 3.11 (b)). While the fresh samples display a double peak structure for the 4d maximum, this is not distinctly seen for the irradiated samples. The double-peak structure in the Tm4d spectrum of the non-irradiated MP samples may be due to a differential charge shift effect that is not fully compensated by the flood gun, the intrinsic shape of the deposited material, or a superposition of different chemical species.

3.5.5. X-ray diffraction

For structural analysis of our thin films, X-ray diffraction under grazing incidence was performed (Fig. 3.12). Non-irradiated MP thin films yield only three broad and weak reflections, which can be best fitted with thulium formate [95, 18, 230]. Based on the half-width of the reflexes, the size of the crystallites in the sample that contribute to the reflex can be deduced. The diffraction pattern of our samples is thus indica-

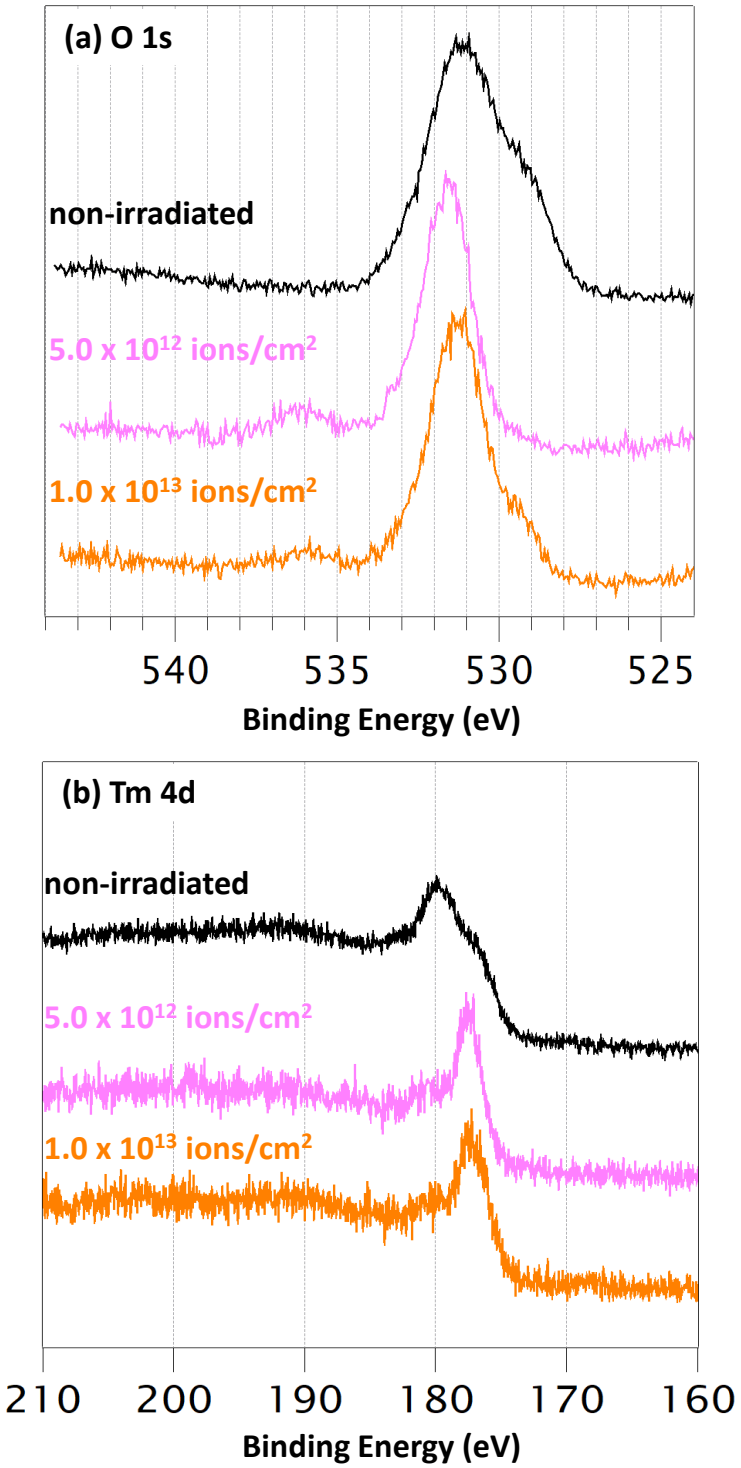

Figure 3.11.: (a) O1s and (b) Tm4d XPS spectra of MP Tm samples for a non-irradiated sample (top) and two samples irradiated with 8.3 $\frac{\text{MeV}}{\text{u}}$ Au ions of different fluence. The samples shown are Tm-500 (black), Tm target-5 (pink) and Tm target-6 (orange).

tive of the amorphicity of the phases and is consistent with the literature for diffraction experiments on untreated lanthanum MP films on Ti foils [28]. The roughness of the Ti substrate [118, 178] used also made the diffraction measurements more difficult and certainly contributes to the dominance of the Ti reflections. The characterisation of irradiated MP films was unsuccessful. We assume that the diffraction pattern did not show any structure probably due to further amorphization and could not be analyzed. Yet, future diffraction experiments with even smaller angles of incidence together with synchrotron X-ray diffraction (SXRD) could enable a reliable identification of the different crystallites in the MP thin films.

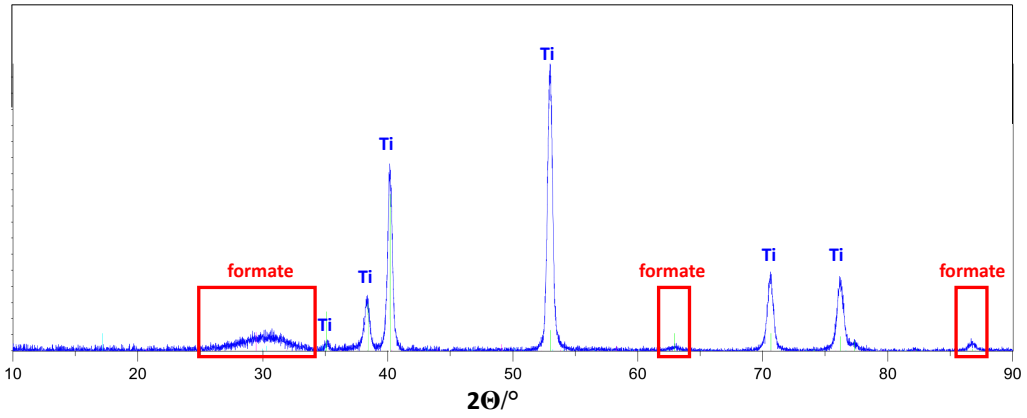

Figure 3.12.: GIXD diffractogram of non-irradiated MP Tm sample (sample: Tm-500), the red boxes show the reflections that can be assigned to thulium formate, while the sharp reflections originate from the Ti backing.

3.6. Summary

3.6.1. Characterisation of fresh films prepared by Molecular Plating

Microscopic methods confirm that of thin Tm films produced by molecular plating on a Ti backing are fractured, exhibiting a mudcracking morphology (Fig. 3.1 right). The films are composed of individual tiles, which significantly impacts the applicability of various analysis methods (Fig. 3.3). The most accurate results were obtained using high spatial resolution analytical methods such as Raman and RBS/PIXE, which allowed us to analyze individual tiles.

Our XPS characterization showed that the fresh films do not contain significant amounts of N, although Tm was added as nitrates in diluted nitric acid in the MP process. This result for N agrees well with the literature for the MP process from alcoholic solvents [28, 216]. Studies on the MP process with aqueous nitrates from DMF [142] also showed no significant N in the XPS spectra, which in this particular case, also excludes the intercalation of nitrogen-based solvent degradation products. Thus, nitrogen

compounds, such as nitrates and their degradation products, can be excluded as a constituent component of MP thin films.

The C1s XPS spectra of non-irradiated MP films showed a whole range of different carbon species. Unambiguous chemical identification by XPS alone is not possible, but in accordance with literature [216, 28, 142] the assignment of the dominant carbon compound in the MP thin film to the carbonates and a carboxylic acid-like species (Tab. 3.5) is apparent. The formation of carbonates right after electroplating can be excluded, because the phase diagrams in the literature [108] clearly show that at room temperature and under ambient concentration of carbon dioxide (about 600 ppm) in the laboratory air, the formation of lanthanide carbonates is negligible [13, 156]. Therefore, it can be concluded that the formation of carbonates through the weathering of hydroxides and oxides is an unlikely mechanism. A similar behaviour is to be expected for the production process of heavy actinide targets, but literature data are scarce. Experiments reported in [217, 216] clearly showed that the C1s species are formed during the MP process and not by drying the thin films in laboratory air. In addition, several XPS studies [142, 216, 189] have demonstrated that the carbon species in MP thin films is not a surface phenomenon, but is intrinsic to the entire thin film.

The XPS oxygen spectra did not permit a clear identification of the chemical species of the MP thin films and could not be reconciled with the assignments of the C peaks. This is because different binding energies would be expected for carbonates or carboxylic acid-like species, but from our XPS analysis, which is afflicted by differential charging, a reliable determination of binding energies is not possible. Publications on XPS studies of MP thin films often neglect discussion of the oxygen spectra. However, in one XPS study [142] on samarium MP films, the O1s spectra were discussed, and the observed O1s binding energy could be attributed to carbonates based on the observed C1s spectra.

Our ion beam analysis experiments also showed that C and O are the dominant species in fresh MP thin films. In both the ERDA (Fig. 3.5) and RBS (Fig. 3.4 (c,d)) depth profiles, O and C predominate over the intended lanthanides in atomic percent. Again, a conclusive quantification of the MP film constituents was not possible, i.e., no sum formula of the MP thin films could be determined.

From GIXD measurements, we conclude that the MP films are amorphous and that Tm exists in the formate phase (Fig. 3.12). Due to the amorphous structure [28] of the MP thin films, as well as the roughness of the Ti backings, the results are not very clear. Moreover, the challenging morphology makes it difficult to interpret the GIXD data. By means of vibrational spectroscopy, carbonates and formates were identified as components of the fresh films (Fig. 3.7).

3.6.2. Chemical changes induced by heavy-ion irradiation

The irradiation of Tm MP thin films with 8.3 $\frac{\text{MeV}}{\text{u}}$ Au ions induces drastic changes in morphology (Fig. 3.2). With increasing fluence, the cracks disappear and Tm becomes more and more homegeneously distributed across the entire surface. This effect has also been reported for MP plated Gd films [129]. Upon further irradiation with Cl ions of 1.2 $\frac{\text{MeV}}{\text{u}}$, (characterized by a lower energy loss than the 8.3 $\frac{\text{MeV}}{\text{u}}$ Au ions), films pre-irradiated with Au ions exhibit fewer morphological changes than non-irradiated films (Fig. 3.2).

Analysis by RBS revealed that the ion irradiation drastically reduces the C content of the MP thin films (Fig. 3.4). The RBS spectra of the irradiated films are dominated by O and Tm. Overall, the relative proportion of the target element is greater after irradiation, probably because a large fraction of volatile by-products from the MP process outgassed. This loss of unwanted material through the first irradiation could be an explanation for the beneficial effect of the conditioning process [85, 20]. Our ERDA investigation (Fig. 3.5) showed that the loss of O and C increases with fluence (Fig. 3.5).

The XPS measurements of the irradiated MP films underline beam-effects on the C component (Fig. 3.10). No clear chemical species can be assigned. However, within the C1s peak, the loss of carbon species with higher binding energies, e.g. carbonates and formates, is obvious. The carbon species (Tab. 3.5) with the highest relative binding energy (C5, carbonate-like) disappears completely through irradiation. In contrast, an aliphatic carbon species (C2) is the dominant component of the MP thin films following irradiation. We were not able to identify by XPS compounds with higher binding energies as seen by Raman spectroscopy. Our XPS data clearly demonstrate the loss of carbon species and the disappearance of carbonates.

IR and Raman spectroscopy (Fig. 3.9) provide evidence for newly formed chemical species. Two characteristic Raman bands are visible over a very high background, which fit an assignment to C nanoparticles [191, 11]. In the IR spectra hydroxide bands were identified. Based on the overall spectroscopic findings, the irradiated MP thin films can be best described as amorphous oxide with embedded C nanoparticles.

3.7. Conclusion

The established models for the MP process assumed the formation of hydroxyl ions during deposition according to Hansen's theory [76, 169, 34, 77]. Due to the non-reduction of the lanthanide or actinide cations [28, 142, 216, 189], basic precipitation is assumed to occur by a combination of electrophoresis

and electroplating [107]. The observed C content was explained by intercalated solvents and products of solvent decomposition. The analytical methods used in this study could not detect any decomposition products from the solvents used. The origin of observed C content is not clear, but organic solvents can dissolve much more carbon dioxide than, e.g., water can. At room temperature and normal pressure, the solubility of carbon dioxide in water is 0.033 $\frac{\text{mol}}{\text{L}}$, 0.15 $\frac{\text{mol}}{\text{L}}$ to 0.17 $\frac{\text{mol}}{\text{L}}$ for short-chain alcohols and 0.18 $\frac{\text{mol}}{\text{L}}$ for DMF [90]. Therefore, it can be assumed that moist and non-degassed organic solvents contain enough carbon dioxide to explain the formation of the carbonates that we observed. Another source for the input of carbon dioxide and thus carbonates could also be the used acids [57, 211]. If we look at the Pourbaix diagram [86, 105] of carbon dioxide, we see that formate can be formed from carbonates under the parameters described for the MP process, i.e., standard room temperature and partial pressure for carbon dioxide in ambient air. Due to the reductive basic conditions at the cathode, the carbonates are partially reduced to formates. It is precisely under these conditions that the oxidation of solvents, such as isopropanol and isobutanol, to carboxylic acid-like species seems very unlikely to occur as an explanatory model for the observed C1s XPS (Fig. 3.10) and Raman spectra (Fig. 3.7). However, should the solvents used be oxidized anodically and reach the cathode by diffusion, we or comparable studies [28, 142, 216, 189] should have been able to detect these decomposition products. Neither studies in DMF [142] found nitrogen signals in the thin film, nor did we find the typical rotational spectra of short-chain alcohols. As with the carbonates, no conclusive mechanism is described in the literature for the formation of thulium formates by weathering of hydroxides and oxides that may have formed in humid laboratory air. Formate formation during the molecular plating process is the most obvious explanation, while a formation after plating seems to be unlikely. The resulting thin films can therefore be described as a mixture of armorphous basic carbonates and formates.

The chemical conversion of our samples differs significantly from the heat-induced conversion of MP thin films described in literature [28, 25]. The oxycarbonate agglomerates reported are known thermal degradation products of carbonates [108] and formates [139]. Thermogravimetric investigations of related carboxylic acid-lanthanide compounds also indicate oxycarbonates as the final product before the heat-induced transformation into the sesquioxides [64, 88]. The chemical transformations we identified after the irradiation with heavy ions cannot be explained by a purely thermal process [129, 180], since none of the known decomposition products were detected. Radiation-induced amorphousness could also be a reason for the lack of spectroscopic evidence. The response of the oxides of the lanthanides [204] and actinides [205] to irradiation with swift heavy ions has been extensively investigated for pure crystalline samples. Ion irradiation induces defect formation in the crystal and the loss of O. It would therefore be logical to attribute the chemical transformation of our MP films to a comparable mechanism [200]. This also includes the loss of light volatile elements, like C and O, so that the lanthanide oxide with embedded carbon clusters remain [11]. The relatively strong Raman-signal of the carbon clusters does not yield any

information regarding their quantitative contribution to the MP thin film following irradiation. Based on the ion beam analyses, it can be inferred that irradiated thin films exhibit a significantly higher O than C content. Despite extensive research, we were unable to identify a satisfactory explanation for the observation that thin films previously irradiated with Au ions exhibit a reduced degree of morphological change when irradiated with Cl ions, in comparison to those that have not been irradiated.

Future studies would benefit from complementary microscopic techniques that offer sufficient spatial resolution enabling effective analysis despite the challenging morphology of the MP thin films. As the production of superheavy elements relies on actinide, and not on lanthanide targets, the presented studies will ideally also be performed with actinide targets. Such studies, though, require access to modern analytical methods in appropriate licensed nuclear analytical laboratories. These studies will ideally be complemented with irradiations applying higher fluences.

3.8. Acknowledgements

We would like to thank our colleagues from the research reactor TRIGA Mainz for carrying out the neutron activation of the lanthanide standards. We also acknowledge the local support of the mechanical workshop at the TRIGA reactor site Mainz and the financial support from the Helmholtz Institute Mainz. We would like to thank our colleagues from the Department of Materials Science at the Technical University of Darmstadt for their helpful cooperation. The results presented here are based on experiments, which were performed at the beam lines X0 and X8 at the GSI Helmholtzzentrum für Schwerionenforschung, Darmstadt (Germany) in the frame of FAIR Phase-0. This project received funding from the German BMBF (project 05P21UMFN2). We express our gratitude to the Ion Beam Centre of the Helmholtz-Zentrum Dresden-Rossendorf for conducting the ion beam analysis of our samples. Access to the ActUsLab/PAMEC and ActUsLab/FMR facilities was granted under the Framework of access to the Joint Research Centre Physical Research Infrastructures of the European Commission (Research Infrastructure Access Agreement N° 2020-1-RD-ActUsLab-FMR Targets-SHE1 (AUL-233) and 2020-1-RD-ActUsLab-PAMEC Targets-SHE2 (AUL-228)). Any opinions, findings and conclusions or recommendations expressed in this paper are those of the authors and do not necessarily reflect those of the European Commission.

3.9. Declaration of generative AI and AI-assisted technologies in the writing process

In the course of preparing this work, the authors employed the deepL tool to enhance the readability and linguistic quality of the text. Following the utilization of this tool, the authors conducted a thorough review and editing of the content, assuming full responsibility for the content of the published article.

4. Publication III: Fabrication, swift heavy ion irradiation, and damage analysis of lanthanide targets

The following article was published as full article in *Radiochimica Acta*, volume 111, pages 801-815 in 2023. It describes the initial approaches to alternative production methods for targets in heavy ion research, with the objective of complementing or even replacing the established molecular plating. To this end, modern electrochemical methods for target production were adapted, and preliminary irradiation experiments were conducted.

4.1. Own contributions

The experiments presented were planned and carried out independently. The spectroscopic methods shown were carried out and analysed independently, while the diffraction methods were carried out externally. The contribution of each method is listed in the publication. The production of the radioactive tracers at the Mainz research reactor (FRMZ) was carried out with the active support of the reactor team and the radiation protection team. The radioactive tracers were again handled completely independently, naturally with the required legal and technical support from the FRMZ radiation protection team.

Fabrication, swift heavy ion irradiation, and damage analysis of lanthanide targets

C.-C. Meyer[1,2], E. Artes[1,2,3],M. Bender[3,4], J. Brötz[5], Ch. E. Düllmann[1,2,3], C. Haese[6], E. Jäger[3], B. Kindler[3], B. Lommel[3], M. Major[5], M. Rapps[1,†], D. Renisch[1,2], C. Trautmann[3,5], A. Yakushev[3]

4.2. Abstract

One limiting factor in progress in the discovery and study of new superheavy elements (SHE) is the maximum achievable thickness and irradiation stability of current generation actinide targets. The desired thickness of targets, using full excitation function widths, cannot be achieved with current target technology, especially the widely used molecular plating (MP). The aim of this study was to transfer progress in the electrochemistry of lanthanides and actinides to the production of targets. Here, we report on the production of lanthanide targets using anhydrous electrochemical routes. In a first irradiation series, thulium thin films with areal densities up to $1800\,\mu g/cm^2$ were produced using anhydrous triflate compounds and subjected to irradiation tests, using $6.0\,MeV/u$ ^{48}Ca ions at a fluence of 3.9×10^{14} ions$/cm^2$ and $8.6\,MeV/u$ ^{197}Au ions at fluences in the range of 3.0×10^{11} to 1.0×10^{13} ions$/cm^2$. The thin films were characterised before and after the irradiations using scanning electron microscopy (SEM) and energy dispersive X-ray spectroscopy (EDX).

4.3. Introduction

Elements beyond the atomic number $Z = 100$ (Fm) can only be produced in single-atom quantities in accelerator-based nuclear reactions. The heaviest known elements are exclusively accessible in fusion reactions of Coulomb barrier heavy ion beams with actinide targets [152]. These superheavy elements (SHE) have very small production cross sections. These cross sections generally decrease with increasing Z, so that fewer and fewer atoms of the superheavy elements are available per unit of time. The actinide target material, deposited on a thin substrate, is distributed on the circumference of a rapidly rotating wheel to spread the ion beam across a larger surface and thus avoid overheating [206, 177, 38]. Various target-related problems restrict advances in the production of superheavy elements [38, 36, 198]. As overall detection efficiencies are already rather high in many SHE studies, production rates can be

[1]Department Chemie, Johannes Gutenberg-Universität Mainz, 55128 Mainz, Germany
[2]Helmholtz-Institut Mainz, 55128 Mainz, Germany
[3]GSI Helmholtzzentrum für Schwerionenforschung GmbH, 64291 Darmstadt, Germany
[4]Hochschule RheinMain - Ingenieurwissenschaften / Angewandte Physik & Medizintechnik, 65428 Rüsselsheim, Germany
[5]Technische Universität Darmstadt – Materialwissenschaft, 64287 Darmstadt, Germany,
[6]Max-Planck-Institut für Polymerforschung, 55099 Mainz, Germany

increased almost exclusively by using more intense ion beams and/or by using thicker targets [38]. Both options necessitate the production of actinide targets with improved properties.

4.3.1. Limits and possibilities of current target technology

Thicker targets are a promising solution to compensate the small production cross section of SHE. However, increasing the target thickness leads to scattering and thus to wider exit angles and energy distributions of the recoiling ions, which may affect the transmission through recoil separators negatively [153]. Accordingly, the usable target thickness is not necessarily only limited by the width of the excitation function but also by the target thickness dependent transmission. Earlier experiments on gas-filled separators therefore often used targets of <500 $\mu g/cm^2$, as many of the discovery experiments in Dubna in the 2000s [149]. The fact that an increase of the target thickness leads to an almost linear increase of the rate of detected reaction products has only been realised in the last ten years [38]. The transmission of gas-filled separators seems to decrease less with increasing target thickness than was assumed earlier. In addition to the development of ion beams of higher intensities [65, 181, 111], the development of thicker targets that can withstand high-intensity ion beams seems to be an approach to increase the production rate of superheavy elements. A target irradiated with an intense ion beam of 6 MeV/u ^{48}Ca ions needs to have a surface weight of about 1500 $\mu g/cm^2$ in order to cover the full-width at half maximum (FWHM) of the excitation function [38].

Currently, most actinide targets used in SHE experiments are produced by electrochemical "molecular plating" (MP), a process, which has been used essentially unchanged for several decades [162, 39]. For comparative experiments with lighter elements [112] or for the research of medical isotopes [136], as well as for target development [217], lanthanide layers prepared in the same way are used. In the MP process [206], the desired metals in the form of their nitrates or chlorides are added in dilute aqueous solutions to an organic solvent, such as isobutanol/isopropanol [177] mixtures or pure N,N-dimethylformamide (DMF) [217]. Deposition is then carried out at relatively high voltages and low current densities [107]. The deposited thin films have a characteristic morphology, and usually contain surface cracks [219]. The films are rarely completely closed in any variation [215] of the MP process, but the morphology could be improved by varying the process parameters [219]. The main advantages of the MP process are high yields and easy handling. Moreover, through the use of aqueous nitrates or chlorides, there exists a seamless connection to the usual separation methods for actinides, such as ion exchange chromatography [177], and the possibility to recover and reprocess non-deposited material as well as irradiated targets [119]. One main disadvantage of the method is that the desired metals are not deposited in pure elemental form, but impurities are co-deposited in MP thin films in considerable amounts. X-ray photoelectron spectroscopy (XPS) analyses identified carbon impurities, which were ascribed to originate from

oxidised solvents [217, 219, 215] or carbonates [142, 28]. By confocal Raman microscopy on lead MP films [132], bands ascribed to carbonates were found. Grazing incidence X-ray diffraction (GIXD) and XPS studies on the thermal post-treatment of lanthanum MP films [28] were able to detect oxocarbonates, which are the known thermal degradation products of carbonates. Other authors identified hydroxides in MP films [231, 168], which is not unexpected due to the high-pH environment at the cathode [76]. A brief summary of the current status of research on the MP process can be found in [6].

Because MP films contain many unwanted by-products, chemical reactions can occur under ion beam bombardment. Indications of this effect came from α-spectra recorded in SHE experiments [85, 20]. In the course of the ion irradiation, α-spectra of MP films of α-decaying actinides undergo significant changes. Systematic studies showed a clear change in morphology [129] and a chemical transformation of a carbonate compound into an oxide compound [132]. To better understand ion beam induced chemical transformations, well defined targets are needed. Deposition in metallic form would have the advantage that the films would contain fewer impurity atoms. However, a rapid conversion to the respective oxides [204] has to be expected unless target production and SHE experiments are carried out under inert gas atmosphere conditions.

One of the most troublesome impediments of the current MP process is the difficulty of achieving reproducible films of thicknesses >800 $\mu g/cm^2$ in one single production step, as soon as irregular geometries, like banana-shaped deposits to be mounted on target wheels [91] are required. For "simple" round targets, thicker layers have been reported [231], but not for more complicated shapes. Advances in the technically important electrochemical deposition of lanthanides [107, 115, 187, 117, 188, 60, 201] report on films grown from organic solvents [107, 115, 187, 117, 188] or ionic liquids [60, 201]. Compared to the MP process, significantly thicker lanthanide films are achieved in a single production step [115, 117, 201]. However, this improvement has not yet been transferred to actinide thin film fabrication. Comparative studies have linked the MP process to current developments in lanthanide electrochemistry [107]. In principle, a transfer to the transplutonium actinides appears possible, as very similar electrochemical behaviour is reported for these elements and the lanthanides [31]. We expect this to allow a transfer to the production of actinide targets. However, in-depth studies on the electrochemical properties [125, 126] in organic solvents have only been reported for of the early actinides so far, which are known to differ in chemical behaviour from that of the transplutonium elements [31].

4.3.2. On the way to the perfect target

To implement these new electrochemical approaches, a ligand system had to be chosen that affords a simple precursor synthesis on a milligram scale. The triflates of the lanthanides [74] and also of some

transplutonium actinides [4] are well described in literature. Lanthanide triflates are extensively used as catalysts in organic chemistry [104]. Syntheses are therefore optimized and reference spectra for analysis, e.g. Raman and infrared spectroscopy [135] and others, are sufficiently available. The triflates seem to fulfill all the requirements for a precursor. The use of triflates as precursors for electrochemical deposition has been rather limited so far [188, 60, 117, 201], a use for target preparation has not been documented to our knowledge.

A suitable solvent is also required to deposit f-elements metallically. The solvent must have a sufficiently large electrochemical window to allow reduction to the metal [117, 90]. DMF has proven itself in target production [219] and has documented good electrochemical properties for actinides [125].

In the following section (sec. 4.4), we report on the synthesis of the precursors (sec. 4.4.1), the used analytical techniques (sec. 4.4.2), the preparation of the targets (sec. 4.4.3) and the irradiation tests (sec. 4.4.4). Subsequently, the results are summarised (sec. 4.5) and discussed (sec. 4.6). A conclusion and an outlook conclude the publication (sec. 4.7).

4.4. Experimental

Our study concentrates on producing terbium and thulium targets, which serve as analogues for, e.g. americium targets. We compare target production with and without the use of inert gas atmosphere technology. The electrochemical yields were determined by neutron activation analysis (NAA). The neutron activation also made it possible to test the synthesis from radioactive materials before actinides are used. First heavy ion beam irradiation tests with thulium targets were performed at the GSI Helmholtz Centre for Heavy Ion Research in Darmstadt, Germany to test the stability of targets produced by this new method.

4.4.1. Production of radioactive Tb and Tm precursors by neutron activation

To be able to determine the partial yields of the individual steps along the entire process by means of γ-spectroscopy, radioactive tracers of the target elements (Tb and Tm) were produced. Samples of 10 mg each of terbium oxide (Tb_2O_3, CAS-No 12036-41-8, Sigma-Aldrich, 99.99 % trace metals basis) and thulium oxide (Tm_2O_3, CAS-No 12036-44-1, Sigma-Aldrich, 99.99 % trace metals basis) were neutron irradiated in polypropylene (PP) tubes in the Mainz TRIGA Mark II [44] research reactor. They were neutron irradiated in the carousel for 8 h at a power of 100 kW at a neutron flux of about $7 \times 10^{11}\,\mathrm{N/(cm^2\,s)}$ and allowed to decay for at least 15 h. By neutron activation, ^{160}Tb (half-life: 72.3 d, E_γ= 879.4 keV,

I_γ= 30.1 %) was produced from ^{159}Tb, which is the only natural terbium isotope. Thulium, which only occurs naturally as ^{169}Tm, was activated to ^{170}Tm (half-life: 128.6 d, E_γ= 84.3 keV, I_γ= 2.5 %). The produced activity was quantified by γ-spectroscopy. After activation, the activity of 10 mg terbium corresponded to 1.48(20) MBq and of 10 mg thulium to 3.20(30) MBq.

For the production of lanthanide triflate, the known synthesis methods [126, 154, 115, 74, 4] were adapted to our special conditions. Since the neutron activation was performed for metal oxide powder, the synthesis had to be carried out directly in the PP irradiation tube while maintaining radiation protection. Sixfold aliquot trifluoromethanesulfonic acid (CF_3SO_3H, CAS-No 1493-13-6, Sigma-Aldrich reagent grade, 98 %) in aqueous solution was added to the neutron-activated oxides via a cannula. The suspensions were dissolved for 8 h in an ultrasonic bath. Afterwards, the solution was concentrated to dryness in a teflon cone and the solid residue was further dried in a drying oven (100 °C, 1 h). The aqueous triflate solution dissolved the neutron-activated oxides without leaving any residue. γ-spectroscopy showed that there was no appreciable loss through sorption when switching between polypropylene or teflon vessels. The activities remained constant within the measurement error, and the conversion from oxide to triflate is therefore assumed to be quantitative. For electrochemical deposition, stock solutions were freshly prepared in DMF from dried residues. The synthesis was repeated with non-neutron activated lanthanide salts, and the triflates were characterised by nuclear magnetic resonance (NMR). The NMR data (see supplementary material) confirm the successful synthesis, but also show remaining water of crystallisation, probably due to incomplete drying.

4.4.2. Target analyses

In the following, we present analytical methods that provided clear results and were available for radioactive samples. These include radiographic imaging, scanning electron microscopy and energy dispersive X-ray spectroscopy. Additional analysis results, including Raman spectroscopy, nuclear magnetic resonance (NMR) and grazing incidence X-ray diffraction (GIXD) are presented in the supplementary material.

4.4.2.1. Radiographic imaging

Radiographic imaging (RI) [101, 70, 198, 68, 102, 67] was performed with a Typhoon™ FLA-7000 analyser from Fujifilm using imaging plates (Fujifilm, BAS IP SR 2040) to observe the relative distribution of radioactive tracers. The maximum achieved spatial resolution was 72(25) µm for weak beta-emitters; for radioisotopes with decay properties similar to those used in the present work, it was about 200 µm [70]. To avoid contamination of an exposure plate, a Mylar® film was inserted between sam-

ple and plate. The exposure time was chosen depending on the activity of the measured sample. The images were processed with the software Gwyddion 2.55 [145]. The contrast shows the relative activity of the respective areas and thus provides information about the homogeneity of the deposited thin film [101, 70, 68, 102].

4.4.2.2. Scanning electron microscopy and energy dispersive X-ray spectroscopy

Scanning electron microscopy (SEM) (Philips Inc., XL 30) was used to investigate the morphology of the deposits [68, 71]. No further preparation, such as coating with conductive materials, was performed. Images were always taken with both imaging modes, SE (secondary electrons) and BSE (back scattered electrons). The integrated nitrogen-cooled energy dispersive X-ray (EDX) detector (SphinX 133 XL40 by eumeX Instrumentebau GmbH) is equipped with an ultra-thin entrance window, allowing the detection also of light elements. EDX spectra were recorded as point spectra as well as area scans. The differences are marked in the respective spectra. The quantitative evaluation was performed with the NIST DTSA-II software [173].

4.4.3. Target production

The electrochemical deposition (circular shape, 6 mm diameter) took place in a standard cell, as shown in Ref. [43]. As substrate we used 25 µm thick titanium foils (diameter: 25 mm) from Goodfellow. Titanium foils are currently the most commonly used substrate material for the fabrication of actinide targets in SHE experiments [151, 123, 36], because they provide a good compromise between physical stability, actinide thin film adherence properties and ion beam attenuation [121, 118]. Before the deposition, the Ti foils were rinsed in isopropanol, water, acetone and again isopropanol and then dried; exceptions are explicitly mentioned. The lanthanides were deposited from the stock solutions onto titanium foils by filling 10 mL of a solution containing the desired amount of lanthanide triflates into the cell [43]. The deposition was carried out galvanostatically, i.e., at constant current. The voltage at the start and end of the reaction was recorded. The electrochemical conditions are specified individually for each case [5].

4.4.4. Irradiation experiments

The deposited films were irradiated at different target stations at the **UNI**versal **L**inear **AC**celerator (**UNILAC**) either on a fixed target station (material science M-branch beamline M3) or using a rotating target wheel [91] (TASCA beamline X8).

Table 4.1.: Parameters of different targets deposited on Ti foils, including the maximum achieved surface weight, used solvent and the inert atmosphere conditions.

sample name	element	surface weight $\mu g/cm^2$	solvent	inert gas	irradiated
Tb triflate	Tb	1890(40)	DMF	no	no
Tb MP	Tb	500(10)	IP/IB	no	no
Tb triflate 500	Tb	500(10)	DMF	no	no
Tm triflate	Tm	1960(20)	DMF	no	no
Tm inert gas	Tm	1820(20)	DMF	yes	no
TASCA GSI	Tm	1000(10)	DMF	yes	yes
CCM-10 to CCM-15	Tm	2000(200)	DMF	yes	yes

4.4.4.1. Irradiation of a TASCA target with 6.0 MeV/u ^{48}Ca ions

The finished assembled target wheel was irradiated with $^{48}Ca^{10+}$-ions of 6.0 MeV/u. The beam current was $2.5(1) \times 10^{12}$ ions/s or 400 $nA_{particle}$; the accumulated fluence was $3.9(1) \times 10^{14}$ ions/cm^2. Photographs (Fig. 4.6) and SEM images (Fig. 4.7) show changes of the surfaces due to irradiation. In the case of the irradiations at TASCA, the thin films (sample: TASCA GSI) were irradiated through the Ti foil (thickness 2.3 µm), following the usual configuration of SHE experiments [91]. In the irradiations at the M-branch, the Tm films (samples: CCM-10 - CCM-15) were irradiated directly [204].

4.4.4.2. Irradiation with 8.6 MeV/u ^{197}Au ions

Table 4.2.: Targets made from commercial thulium triflate (2000 $\mu g/cm^2$) were irradiated with 8.6 MeV/u Au^{26+} ions at different fluences.

sample name	fluence ions/cm^2
CCM-10	$3.0(3) \times 10^{11}$
CCM-11	$5.0(5) \times 10^{11}$
CCM-12	$1.0(1) \times 10^{12}$
CCM-13	$3.0(3) \times 10^{12}$
CCM-14	$5.0(5) \times 10^{12}$
CCM-15	$1.0(1) \times 10^{13}$

Irradiations were performed with 8.6 MeV/u Au^{26+} ions at the M3 beamline. To prevent heating of the samples, the ion flux was kept below ca. 2.0×10^9 ions/(cm^2 s) [204]. Six identically prepared samples (samples: CCM-10 - CCM-15) were irradiated with different fluences ranging from 3×10^{11} to 1×10^{13} ions/cm^2. The individual fluences are tabulated in Table 4.2.

4.5. Results

4.5.1. Target production

4.5.1.1. Deposition lanthanide triflates under ambient conditions

From the respective stock solution, the volume with the desired mass of terbium or thulium was taken and filled up to 10 mL with DMF. Before the galvanostatic deposition, 10 µL of the reaction solution were filled up to 500 µL with DMF and then a γ-spectrum was recorded. From the reaction solution the terbium was galvanically deposited in the cell for 1 h at $3.5(1)\,\mathrm{mA/cm^2}$. After 1 h the voltage had dropped from 600 to 400 V. After deposition, the solution was recovered and the coated titanium foil was washed with a few millilitres of isopropanol and dried in air. After deposition, 500 µL of the supernatant solution was transferred to a polypropylene tube and a γ-spectrum was recorded to determine the activity after deposition. This allowed us to determine the yield and the surface weight of the deposition indirectly, assuming that the sum of the activity in solution and the deposited activity sum up to the original activity content of the solution before plating. The deposited thin films were characterised by SEM (Fig. 4.1).

The deposited thin films show pronounced cracks, which is denoted by the community as "mudcracking". In our study the cracking became more pronounced for thicker films, deposited at ambient conditions. At higher surface weights, further material is deposited on the film in sponge-like structures, which is most evident in the case of Fig. 4.1 (b) with a surface weight of $1960(20)\,\mu\mathrm{g/cm^2}$. The morphology of the cracked films is similar to that described in detail in literature for various electrochemical methods of lanthanide deposition, [107] but especially for molecular plating. Studies on MP films [217, 219, 216, 215] showed that this characteristic breaking up of the thin film occurs during drying and thus produces the typical patterns of MP films. Using the triflate route, it was possible to reproducibly deposit terbium thin films up to $1890(40)\,\mu\mathrm{g/cm^2}$ surface weight. The deposition efficiency varied between 67-95 % for targets with more than $1500\,\mu\mathrm{g/cm^2}$ surface weight, for thinner targets the typical average deposition efficiency was >95 %. The produced thin films were as mechanically stable as MP thin films of lower surface weight, when it came to handling characteristics in target production.

The SEM image of the sample "Tm triflate" shows clear mudcracking together with sponge-like structures on top (Fig. 4.1 (b)). Compared to the deposition from terbium triflate (Fig. 4.1 (a)), the thin films of thulium triflate (Fig. 4.1 (b)) are coarser and show increased sponge formation. It can be assumed that the sponge-like structures evolve more and more with increasing duration of the deposition, since their amount increases with the surface weight of the deposits. EDX investigations provide evidence that both morphologies consist mainly of desired lanthanide. The EDX spectrum (Fig. 4.4 (a)) of the thulium sample clearly shows X-ray lines of thulium, titanium, oxygen and carbon. The spectrum shows no X-ray lines of nitrogen, sulphur or fluorine. We thus conclude that neither DMF nor triflate are con-

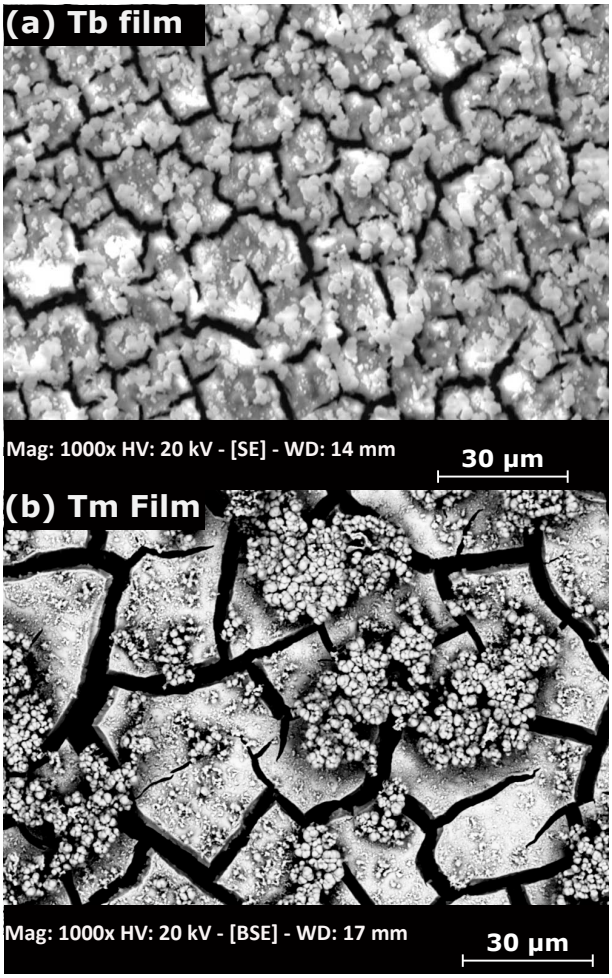

Figure 4.1.: Scanning electron microscope (SEM) images of (a) sample "Tb triflate" ($1890(40)\,\mu g/cm^2$) and (b) sample "Tm triflate" ($1960(20)\,\mu g/cm^2$) both electrochemically deposited from DMF. EDX spectra confirm that the cracked film and the sponge-like structures consist of the desired lanthanide, cf. Fig. 4.4 (a).

tained in the thin films in quantifiable amounts. This means that thulium is not deposited as triflate or fluoride. The X-ray line of carbon is probably due to organic contaminants introduced during or after the deposition. The ratio of the K_α line of oxygen and the $M_{\alpha+\beta}$ line of thulium suggests that thulium is not deposited elementally but as an oxidic species, possibly as hydroxide, oxide or as oxide hydroxide. The ratio of the $M_{\alpha+\beta}$ line of thulium and the K_α line of titanium is influenced by the sample surface and the thickness of the thulium film. On the basis of the EDX spectra, we thus cannot provide a precise value for the amount of deposited thulium and its chemical species [129]. The deposition efficiencies are $98(1)\,\%$, thus similar as those for terbium triflate.

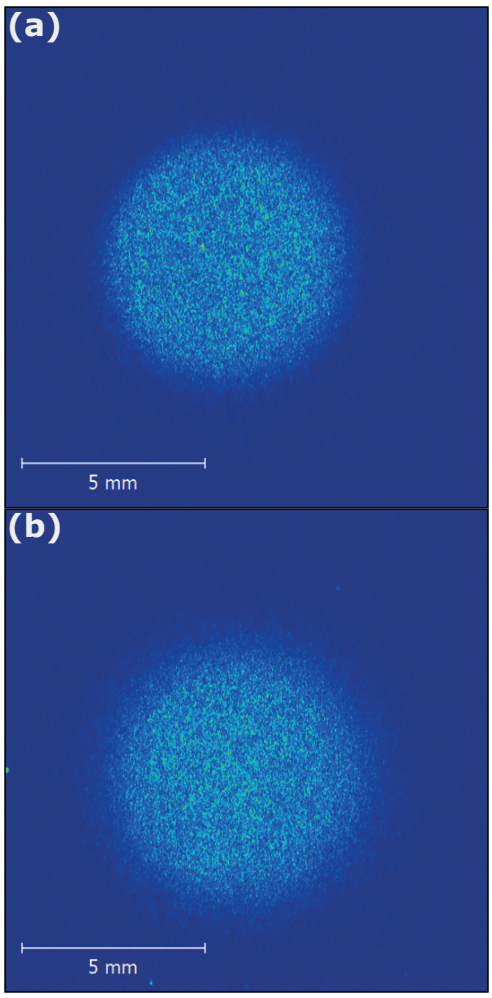

Figure 4.2.: Radiographic images of electrochemical depositions of terbium of similar surface weight ($500\,\mu g/cm^2$). Samples produced by (a) molecular plating from isoproponol/isobutanol (sample: Tb MP) and (b) triflate route from DMF (sample: Tb triflate 500). With the same layer thickness, the macroscopic distribution of the activity in both samples is almost identical; both processes coat the substrate surface uniformly.

4.5.1.2. Comparison of molecular plating samples and triflate route samples

In order to assess the morphology and deposition quality of the new method, a terbium sample was prepared by molecular plating (sample: Tb MP) according to reference [177]. A nitric acid stock solution was prepared from neutron activated terbium oxide. An aliquot of the nitric acid stock solution was taken and filled up to 10 mL with a mixture of isobutanol and isopropanol with a volume ratio of 9:1. From this solution, terbium was deposited at $0.7(1)\,mA/cm^2$ for 1.5 h resulting in a layer thickness of $500(10)\,\mu g/cm^2$. Using RI (Fig. 4.2) and SEM (Fig. 4.3), the two thin films of similar thickness were compared to contrast the MP process and the triflate route.

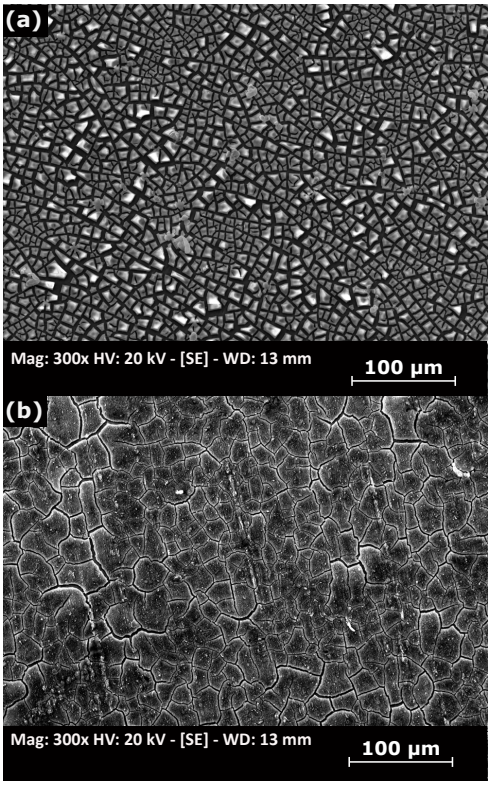

Figure 4.3.: SEM images of electrochemical depositions of terbium. Samples produced by (a) molecular plating from isoproponol/isobutanol (sample: Tb MP) and (b) triflate route from DMF (sample: Tb triflate 500). Although the film thickness is the same ($500\,\mu g/cm^2$), the surface of the MP film (a) shows finer crack structures than the film produced via the triflate route (b).

The radiographic images (Fig. 4.2) clearly show the radioactivity to be distributed homogeneously on a 200 µm resolution scale in both samples. Influences of anode shape [101, 102] are not yet visible at these intermediate surface weights ($500\,\mu g/cm^2$) for either method. In the triflate route (sample: Tb triflate 500) (Fig. 4.2 (b)), a slight corona of radioactivity is visible around the actual deposition area. We ascribe this to the lack of stability of the sealing rings against DMF, so that deposition has also taken place slightly outside the actual target area. The SEM images (Fig. 4.3) show for both deposition routes pronounced cracking of the thin films surface. The conventional MP process leads to many more cracks, compared to the surface produced via the triflate route.

4.5.1.3. Deposition from thulium triflates under inert gas conditions

By using inert atmosphere and anhydrous solvent, the influence of water and air on the deposition process should be minimised. For the tests under inert gas atmosphere, the original stock solutions were evaporated to dryness in a teflon beaker, and the solid residues were dried for 5 h at 80 °C in a drying

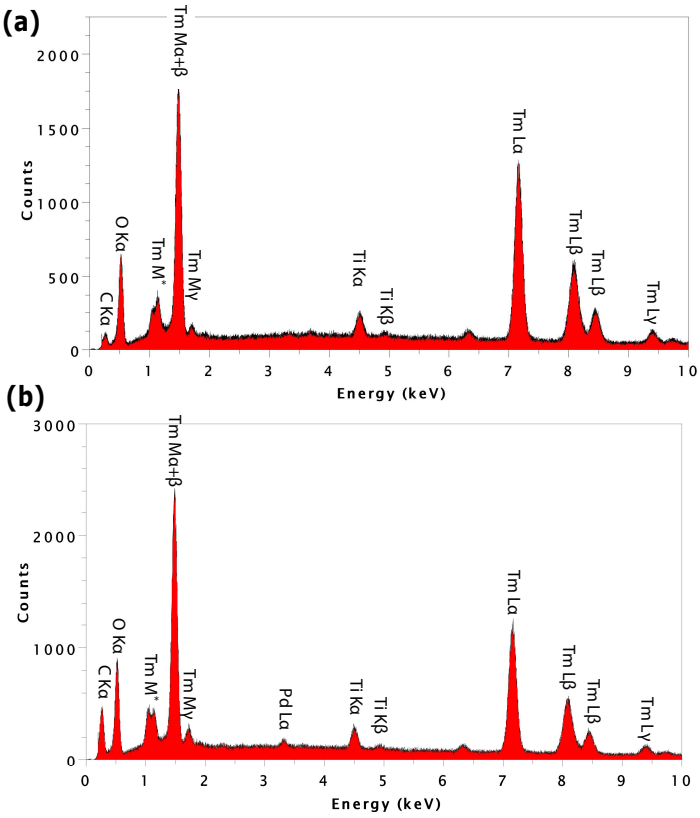

Figure 4.4.: Energy dispersive X-ray spectroscopy (EDX) spectrum of (a) electrochemically deposited thulium triflate (sample: Tm triflate, $1960(20)\,\mu g/cm^2$), produced under ambient conditions. The EDX spectrum shows only signals of thulium and titanium from the substrate, no unwanted deposition of anode material due to corrosion. (b) Tm film (sample: "Tm inert gas", $1820(20)\,\mu g/cm^2$) produced under argon atmosphere. The EDX spectrum shows first signs of anode corrosion, i.e., co-deposition of Pd anode material in the thulium thin film. The EDX data were analysed using the NIST DTSA-II software [173].

cabinet. The dried residues were then transferred to an argon glove box (MBraun UNIlab, <1 ppm water vapour, <1 ppm oxygen) where they were filled with DMF (anhydrous, 99.8 %, Sigma-Aldrich, <50 ppm residual water content) and then used for electrochemical deposition. The thulium was then galvanically deposited from this solution in the cell for 1 h at $1.8(1)\,mA/cm^2$. The yield of electrochemical deposition was $91(3)$ %. The deposits (Fig. 4.5) were initially black and appeared metallically glossy. After removal from the inert gas atmosphere of the glove box, the films turned white.

Under exclusion of water and air, the deposition leads to a clearly different morphology (Fig. 4.5 (a)). On the thin film of thulium with fine cracks (sample: Tm inert gas) a coarse sponge-like structure of thulium can be seen. From the radiographic images we conclude that they can be ascribed to particularly high activity (Fig. 4.5 (b)). The radiographic images also show that the activity decreases towards the edge of the target. Since the anode is a wire, thus having point-like geometry, the electric field lines are more

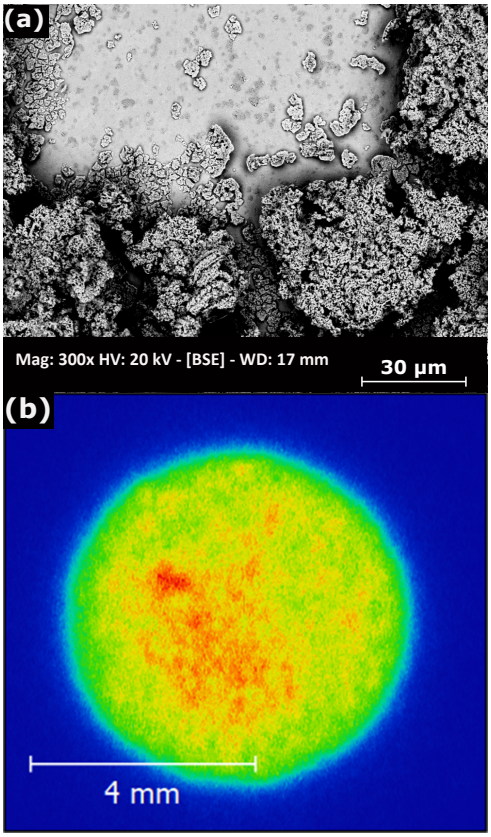

Figure 4.5.: Thulium triflate electrochemically deposited under argon atmosphere from DMF (sample: Tm inert gas, $1820(20)\,\mu g/cm^2$) (a) SEM image showing sponge-like structures, due to the exclusion of residual water hardly any mudcracking occurs. (b) radiography image revealing a heterogeneous distribution of Tm activity.

concentrated in the middle and decrease towards the outside of the sample. As a result, more thulium is deposited in the centre than at the edge, which is typical for radioactive thin films produced in similar electrochemical setups [101, 102]. The sponge-like morphology is dominating in samples prepared in an inert gas box with anhydrous DMF (99.8 %, Sigma-Aldrich, <50 ppm residual water content). The water content obviously has a strong influence on the morphology of the thulium deposits. After removal from the argon atmosphere of the glove box, we observed a tarnishing of the sample indicating an oxygen-related process. Raman spectra of the tarnished thin films (see supplementary material) revealed exclusively thulium oxide [204, 172, 209] and no other chemical species.

Under the exclusion of water and air, the achieved surface weights ($1820(20)\,\mu g/cm^2$) are above the typical values for the MP process. The EDX spectrum of the sponge-like structures (Fig. 4.4 (b)) shows only a weak Ti-K_α line from the Ti substrate, which indicates a relatively complete coverage of the substrate due to a thick deposition (Fig. 4.7 (a)). The EDX spectra also reveal a small peak due to palladium (Pd-L_α line). After a few depositions under inert gas, we see a visible anode corrosion of the

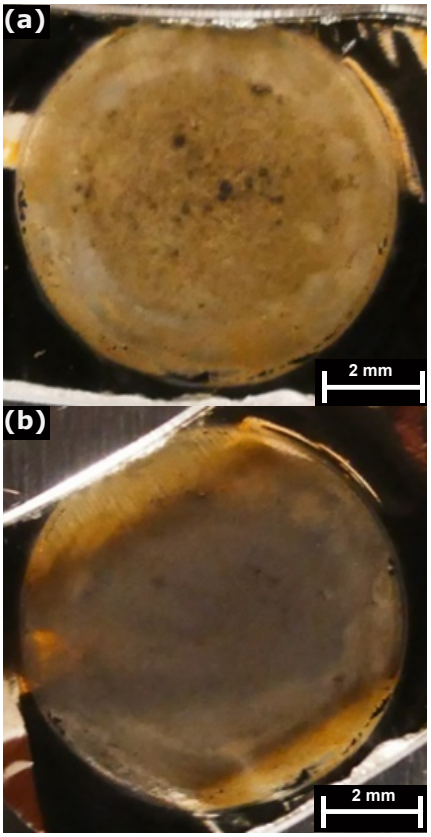

Figure 4.6.: Examples of targets deposited from thulium triflate (sample: TASCA GSI, $1000(10)\,\mu g/cm^2$) under argon atmosphere for irradiation at the TASCA-Setup, (a) unirradiated, (b) irradiated with $6.0\,MeV/u$ ^{48}Ca-beam of fluence $3.9(1) \times 10^{14}\,ions/cm^2$.

Pd electrode. This is surprising, because usually Pd remain stable in ambient atmospheres; because of this platinoids have been used in the MP process for decades [43]. Furthermore, a clear fluorine peak but no sulphur signal is visible (Fig. 4.4 (b)). The systematic fluorine contamination is probably due to the dissolution of the used Viton® sealing rings. This fluorinated polymer is not stable in DMF. If the triflate ligand were co-deposited, a clear sulphur peak would be expected. Electrochemical splitting of the carbon-fluorine bond or sulphur-carbon bond in the triflate ligand seems unlikely.

4.5.1.4. Deposition from commercial thulium triflates under inert gas conditions

Thulium triflate is also commercially available and has less water of crystallization than the precursors from the extracted oxide. Non-neutron activated targets for further irradiation experiments at GSI were produced from this ($(CF_3SO_3)_3Tm$, CAS-No 141478-68-4, Sigma-Aldrich, 98 %). To obtain a stock solution 11.4 mg $(CF_3SO_3)_3Tm$ were dissolved in 5 mL anhydrous DMF in our argon glove box. For each reaction 248 µL of the stock solution were filled up to 10 mL with DMF and then deposited on

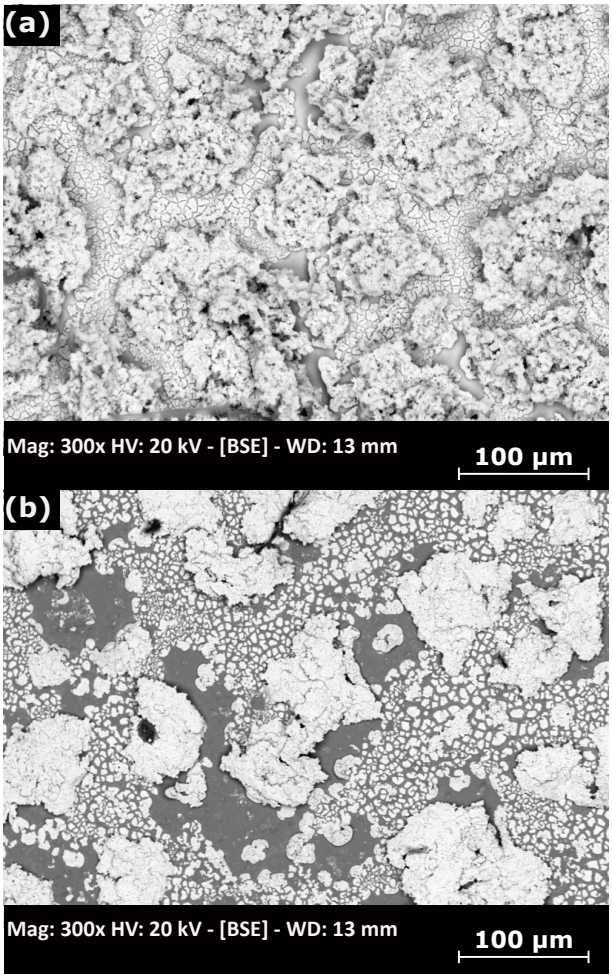

Figure 4.7.: SEM micrograph of targets deposited from thulium triflate (sample: TASCA GSI, $1000(10)\,\mu g/cm^2$) under argon atmosphere before (a) and after (b) irradiation with $6.0\,MeV/u$ ^{48}Ca-beam of 3.9×10^{14} ions/cm^2. Same sample as shown in Fig. 4.6. EDX scans identify the dark areas as titanium substrate and the sponge-like structures as thulium.

a titanium foil. The electrochemical deposition took place galvananostatically at a constant current of 0.7 mA for 2 h. The aim was to achieve a surface weight of up to $2000\,\mu g/cm^2$. Based on the experiments with activated thulium in the glovebox, an uncertainty of 10 % is assumed for the surface weight due to statistical variations in the deposition yields and to account for experimental errors.

SEM images (Fig. 4.8 (a)) show that the thulium film covers the titanium backing more completely than a typical MP film, where typically large cracks expose the titanium backing. The better coverage of the titanium substrate is supported by the EDX spectrum (Fig. 4.9), where the L_α signal of the thulium is more intense than the K_α line of titanium. The signals of the K_α lines of oxygen and fluorine are very small, but also here the L-lines of palladium are very pronounced. Obviously the anode material was co-deposited in substantial quantities on the film. In the argon glovebox clear corrosion damage became

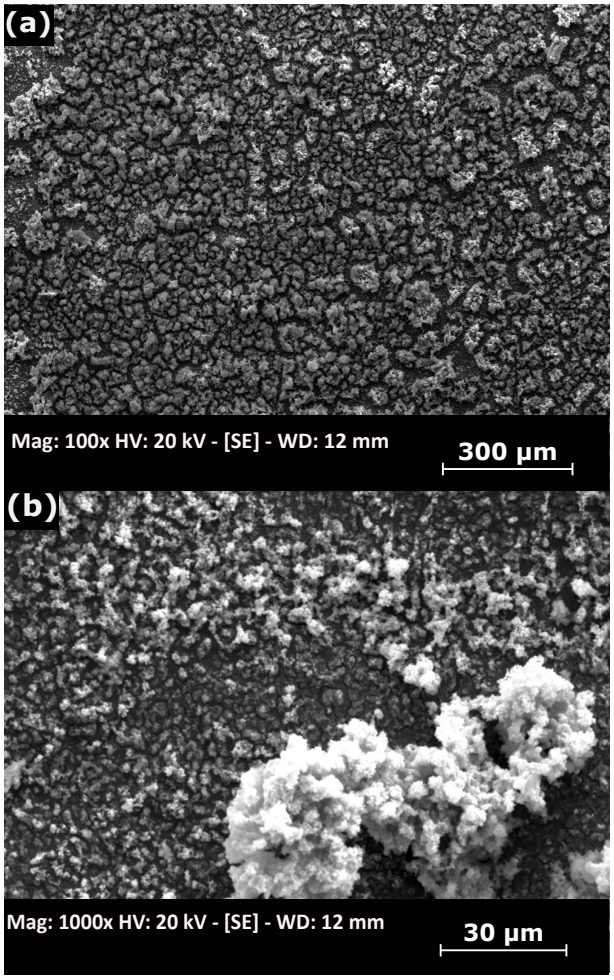

Figure 4.8.: SEM images of films deposited from commercial thulium triflate (sample: CCM-10, $2000(200)\,\mu g/cm^2$) under argon atmosphere before irradiation. (a) low and (b) high magnification. EDX scans confirm that the film consists of thulium with Pd contaminants from the electrode. When excluding residual water, obviously mudcracking is strongly suppressed.

visible on the palladium anode, a porous black precipitate was formed. In contrast to the deposition under ambient conditions, where no detectable anode corrosion occurred.

4.5.2. Target irradiation

4.5.2.1. Irradiation of a TASCA target with 6.0 MeV/u ^{48}Ca ions

For first irradiation experiments at TASCA, we used targets produced under inert gas atmosphere and water exclusion, meaning deposition in an argon glove box and using water-free DMF solvent. The morphologies of layers produced this way had less cracks and a overall better surface coverage than layers produced by classical MP process. A 2.3 µm-thick titanium substrate produced by cold rolling [118] was

used (sample: TASCA GSI) in order to come as close as possible to the experimental conditions of a real SHE experiment [91]. Eight thulium targets were produced, with surface weights of 1000 µg/cm^2 (sample: TASCA GSI). The deposition time was 2 h and the current was set to 1.2 mA/cm^2 for all depositions. After the plating process, the films were glued to the corresponding TASCA target frames [91] (Fig. 4.6 a) with a conductive two-component silver adhesive (EPO-TEK E4110 from Epoxy Technology) and then heated for 1 h at 150 °C in an oven to dry the adhesive. The resulting eight circular targets were mounted on two TASCA wheels for consecutive irradiation.

Photos of thulium samples (TASCA GSI, Fig. 4.6) before and after irradiation with a 6.0 MeV/u ^{48}Ca-beam ($3.9(1) \times 10^{14}$ ions/cm^2) show clear colour and morphological changes. The colour change of the previously white thin films at the position of the ion beam spot corresponds to observations on MP targets [85, 129, 132]. The ion beam has a circular profile [91] with Gaussian intensity distribution (FWHM $\approx$ 8 mm) in the centre. The intensity decreases towards the outside, indicating that the edges of the targets were irradiated with a smaller fluence than the centre [132]. As a result, the targets turn darker in the centre than at the edges. A comparison of the SEM images (Fig. 4.7) taken before and after irradiation clearly shows that the beam exposure results in complex changes in the morphology of the thin film [129].

4.5.2.2. Irradiation with 8.6 MeV/u ^{197}Au ions

Analysing the different samples from the fluence series, we observed that the thulium coverage of the Ti backing decreased with increasing fluence (Fig. 4.10). A quantitative analysis was not possible due to the large scattering of the morphology changes from sample area to sample area (samples: CCM-10 - CCM-15). We could not identify any changes in the Raman spectra of our irradiated lanthanide films, which is in contrast to earlier Raman studies on ion-irradiated MP lead films [132]. Only thulium oxide was detected, using confocal Raman spectroscopy (see supplementary material) [204, 172, 209]. Also in the GIXD investigations (see supplementary material), the poor signal-to-noise ratio (SNR) did not allow us to draw any conclusions about beam-induced changes in the chemical composition [132] or phase changes [204]. Again, only thulium oxide was identified, while no metallic thulium phases were detectable in any of the samples. Anode material in the form of palladium was also evidenced by GIXD, which is in agreement with the EDX results (Fig. 4.9).

4.6. Discussion

4.6.1. Precursor synthesis and influence of precursor properties on thin films

The preparation of simple organic precursors in the form of triflates from the oxides was quantitatively successful. A transfer of the synthesis protocol to the actinides seems feasible under the given laboratory conditions. Additional approaches for the synthesis actinide triflates are described in literature [4]. The NMR analysis indicates a need for improvement in the synthesis of the precursors, especially with respect to minimizing the content of water of crystallization (see supplementary material). The deposition from commercial dehydrated triflates induced a different morphology in the films produced under inert gas atmosphere. Mudcracking was almost completely absent in the films made from commercial triflates. The drying procedure after aqueous digestion plays a crucial role in suppressing the cracking process and should be optimized for further crack suppression. This in turn requires adapting established synthesis techniques [104, 103] like drying in vacuo at elevated temperatures under radiochemical safety conditions.

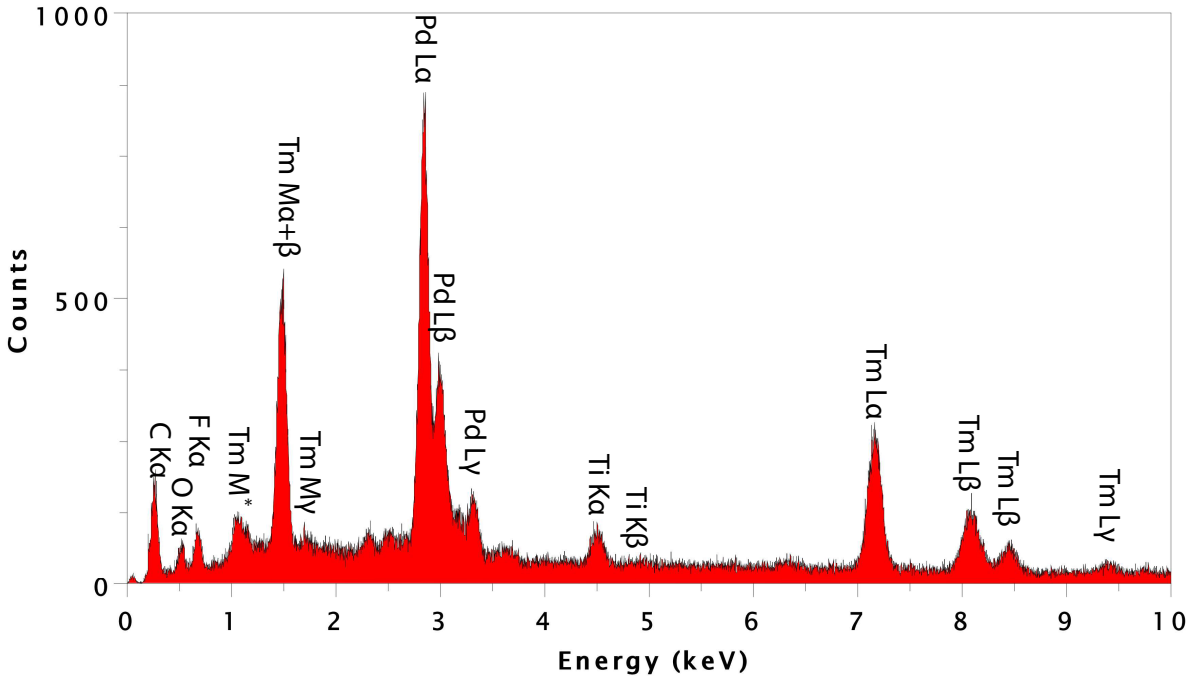

Figure 4.9.: EDX spectra of a Tm sample (CCM-10, $2000(200)\,\mu g/cm^2$) deposited from commercial thulium triflate under argon atmosphere after irradiation with 3.0×10^{11} ions/cm^2 of 8.6 MeV/u ^{197}Au ions. Ti originates from the substrate and Pd from the electrode that obviously corrodes during electro deposition.

4.6.2. Comparison of triflate route films and MP films

We demonstrated that the change from nitrates and chlorides to triflates allows a significant increase in maximum surface weight up to $1890(40)\,\mu g/cm^2$ (sample: Tb triflate), compared to conventional MP [174]. These films also showed mudcracking as dominant morphological characteristic. In addition to mudcracking, sponge-like structures are observed on the top surface for films with a surface weight above $\approx 500(10)\,\mu g/cm^2$, which is the typical thickness [38, 36] of MP films. The RI images show that the surface weight at $500(10)\,\mu g/cm^2$ and the distribution of activity of the triflate deposited from DMF (sample: Tb triflate 500) are very similar to those of the target produced by MP(sample: Tb MP) (Fig. 4.2). We thus expect that similarly homogeneous distributions can be achieved via the triflate route as by MP [107]. At higher surface weights, the influence of the anode geometry becomes more pronounced, as is also the case for films produced by MP [216] or other electrochemical deposition methods [101, 102]. An optimized anode geometry, can be expected to lead to an improvement in deposition homogeneity[117].

EDX analyses of the films show mainly thulium, but also minor other components such as carbon, which is probably due to organic contaminants introduced during or even after the chemical reaction. The EDX spectrum (Fig. 4.4 (a)) shows no indication of nitrogen, sulphur or fluorine. We thus conclude that neither DMF nor triflate are contained in the films. This means that thulium is not deposited as triflate and no solvent is intercalated into the film. The intensity ratio of the K_α line of oxygen to that of the M_α line of thulium are approximately the same for all samples produced with this method. This suggests that thulium is not deposited elementally but as an oxidic species, if no inert gas conditions are applied. It remains unclear, whether it is deposited as hydroxide, oxide or as oxide hydroxide. We cannot fully rule out deposition as metallic species, with oxidation occurring afterwards, when the thin films are removed from the deposition solution. We observed also no corrosion of the palladium anode for the samples “Tb triflate“ and “Tm triflate“. However, it should be noted that in studies using the MP method, EDX spectra showed no deposition of anode material [129], while more sensitive detection methods, such as X-ray Photoelectron Spectroscopy (XPS), demonstrated co-deposition of anode material in analogous experiments [217]. A deposition of traces of anode material can therefore not be ruled out. In other electrochemical methods for the production of actinide thin films, sponge- or moss-like structures were explained by a co-deposition of platinoids, which were used as anode material [10]. This explanation does not hold for the present samples, since no significant anode corrosion is measurable when working under ambient conditions.

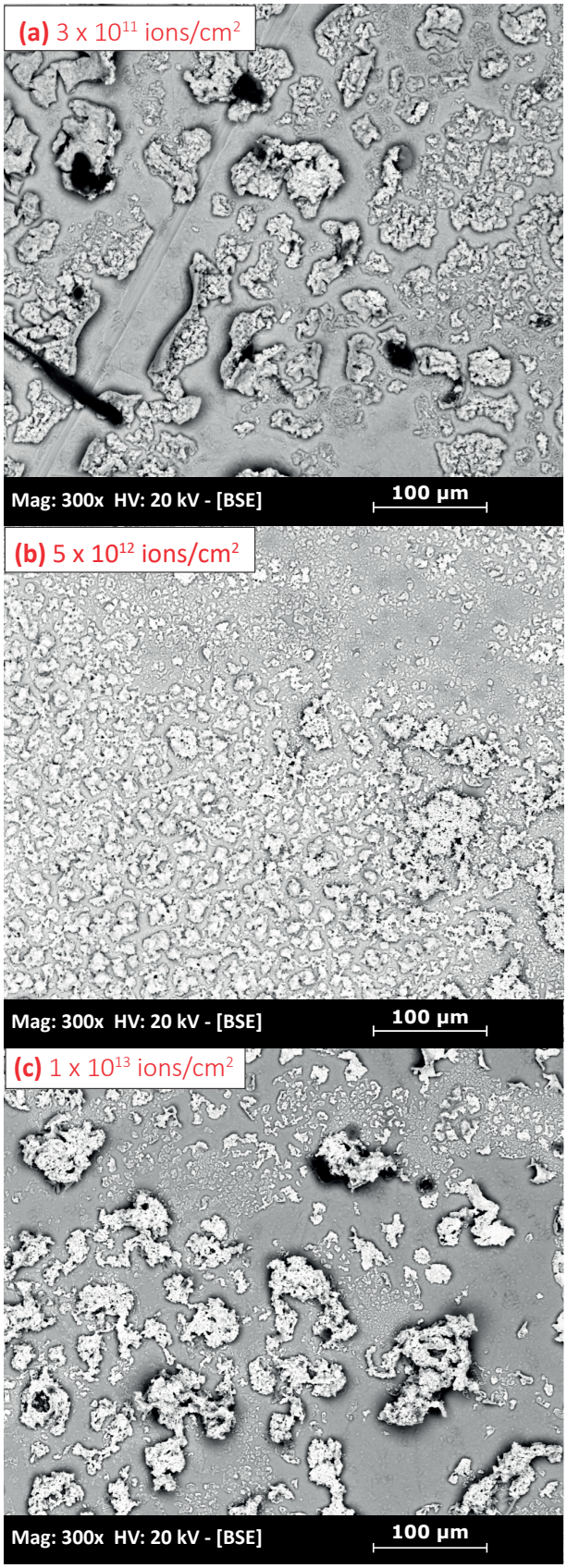

Figure 4.10.: SEM images of films deposited from commercial thulium triflate under argon atmosphere after irradiation with 8.6 MeV/u ^{197}Au ions at fluences of (a) 3.0×10^{11} ions/cm^2, (sample: CCM-10); (b) 5.0×10^{12} ions/cm^2, (sample: CCM-14); (c) 1.0×10^{13} ions/cm^2, (sample: CCM-15).

4.6.3. Inert atmosphere conditions - the influence of residual water

Switching to inert atmosphere conditions results in clear changes in the film morphology. Mudcracking is significantly reduced and most of the thulium is deposited with a sponge-like morphology (Fig. 4.5). The achieved surface weights are far above those of conventional molecular plating. However, the samples showed significant air sensitivity. This could be an indication of at least partially metallic deposition, but definitive analytical proof is still lacking. Films electrochemically deposited from commercial thulium triflate showed no mudcracking, but sponge-like structures on a closed film (Fig. 4.8). Exclusion of residual water thus almost completely eliminates the surface cracking ("mudcracking") in the thin films.

Under inert gas atmosphere conditions, co-deposition of anode material increases significantly as evidenced in the EDX spectrum (Fig. 4.4 (b)). Reactions with atmospheric oxygen and residual water would probably prevent corrosion of the anode, since in ambient conditions, platinoids appear to be stable anode materials. Additionally, dry DMF attacks the Viton® sealing rings of our electrochemical molecular plating cells and the adhesive silver glue between the titanium foils and the TASCA frames. In consequence, new cell designs are being developed. Ethylene propylene diene monomer rubber (EPDM) sealing rings are under consideration as DMF stable seal for the new cell design. Moreover, alternative anode materials need to be tested to avoid corrosion of the anode and incorporation into the thin film. Instead of the established platinoids, modern anode materials such as glassy carbon and boron-doped diamond could be used. Heavy elements have to be avoided as they lead to undesirable α-emitters in the interaction with swift heavy ions [38].

Samples produced via the triflate route on a Ti backing (sample: TASCA GSI) showed beam-induced changes in the photos (Fig. 4.6) and SEM images (Fig. 4.7). The films discolour under ion irradiation. As revealed by electron microscopy, the deposited material no longer completely covers the titanium backing. This is an undesirable effect for SHE experiments, as the ion beam now passes without the possibility of interacting with the desired actinide target material. Similar changes in the continuous coverage of MP target material observed with SEM and α-spectroscopy have been described qualitatively [85, 129, 25]. Since the ions deposit substantial amounts of energy in the targets, high temperatures occur along the ion path, which can lead to thermal spikes, with localized melting [129] or shrinking [25] of the films. Sputtering [203] could also play a role, but has hardly been described in the literature for the investigation of target materials in SHE research. Irradiation also causes changes in the titanium foils. After irradiation they typically expand and sag in the frames of the target wheel [38, 132], which exerts further mechanical stress on the thin films.

4.7. Conclusion and outlook

For the production of the heaviest elements in ^{48}Ca-induced reactions with actinides, thicker targets would be advantageous [38]. With the aim to establish a method that holds the promise of producing thicker actinide targets, lanthanide analoges were electrochemically deposited from triflate precursors in DMF. The lanthanides were neutron activated before target production, to allow for electrochemical yield determination and radiographic imaging.

We demonstrated that the digestion of the oxides of terbium and thulium and the conversion into triflates proceed with high yields. A milligram-scale preparation with actinides seems feasible [4, 50, 14]. The preparation of anhydrous triflates [74, 128, 228] needs to be optimized, including a continuous analytical monitoring. In particular the exclusion of water and air will provide better reaction control, both in the preparation of the triflate precursors and in the deposition of the thin films. With electrochemical deposition from thulium and terbium triflates in DMF, layer thicknesses exceeding those regularly achievable with MP were produced that are similarly stable and homogeneous as the films from MP (Fig. 4.8).

For the first test of their radiation hardness, these targets were exposed to intense Ca and Au beams at Coulomb barrier energies, however at fluences that were substantially below those required in SHE experiments. These first tests indicate a basic suitability as a target material and promise to overcome the present thickness limitations of MP produced films [36, 38].

4.8. Acknowledgements

We would like to thank our colleagues from the research reactor TRIGA Mainz for carrying out the neutron activation of the lanthanide standards. Special thanks for the support with Raman spectroscopy and sample irradiation go to the colleagues from the GSI Materials Research department. We also acknowledge the local support of the mechanical workshop at the Mainz TRIGA reactor site. The results presented here are based on the experiment U308, which was performed at the beam line X8/TASCA and on irradiations at the M3-beamline of the UNILAC at the GSI Helmholtzzentrum für Schwerionenforschung, Darmstadt (Germany) in the frame of FAIR Phase-0. There are no ethical objections to the research presented here. The authors have accepted responsibility for the entire content of this manuscript and approved its submission. This research was supported by the German BMBF (grant No 05P21NMFN2) and by the Helmholtz Institute Mainz. The raw data can be obtained on request from the corresponding author.

5. Conclusions and Outlook

The present study has yielded four novel insights into the molecular plating process and its application in the production of targets for superheavy element research. Firstly, the formation of carbonate and formate in the MP thin films was investigated. Secondly, the chemical changes in the MP thin film triggered by ion irradiation were examined. Thirdly, initial approaches to replacing the established MP method were explored. And fourthly, which analytical methods provide the most reliable insights into the complex system of MP thin films and thin target backings was investigated.

5.1. Carbonate and formate in MP thin films

The analytical methods employed in this study did not reveal the presence of decomposition products from the solvents used, oxides, or hydroxides. This finding contradicts the previously established doctrine regarding the chemical composition of MP thin films. Previous studies have indicated the presence of carbonates in MP films [28, 29], as initially reported in the lead system (Ch. 2). The current study has also detected formates as a second carbon species in MP thin films. A more comprehensive understanding of these findings can be attained by referencing the relevant Pourbaix diagram (Fig. 5.1). The findings of *Bumroongsakulsawat et al.* [22] and *König et al.* [105] demonstrate that, under the electrochemical conditions of the MP process in the employed humid organic solvents, dissolved carbon dioxide can be converted into both carbonates and formates.

Furthermore, the solubilities of carbon dioxide for the most common MP solvents tabulated at *Izutsu* [90] should also be considered. At room temperature and normal pressure, the solubility of carbon dioxide in water is 0.033 $\frac{\text{mol}}{\text{L}}$, 0.15 $\frac{\text{mol}}{\text{L}}$ to 0.17 $\frac{\text{mol}}{\text{L}}$ for short-chain alcohols and 0.18 $\frac{\text{mol}}{\text{L}}$ for DMF [90].

From the tabulated values and diagrams, as well as the analysis results of the present work, it can be deduced that the moisture and carbon dioxide content of the solvents used should have an influence on the MP process. Since no publication on the MP process has been found that addresses drying or degassing steps for the solvents used, studies that exclude water and carbon dioxide would certainly be a promising approach.

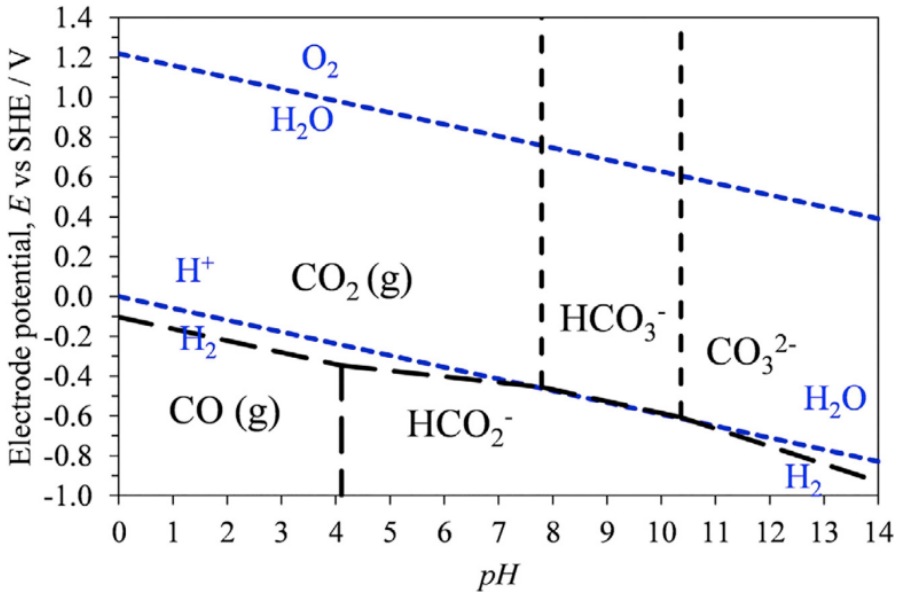

Figure 5.1.: The following is a metastable potential-pH (Pourbaix) diagram for a C-H_2O system at 298 K and 1 bar. The diagram illustrates how changes in acidity and electrode potential of the system can affect its speciation [105].

The Pourbaix diagram (Fig. 5.1) provides a clear explanation as to why only carbonates and not formates could be detected in the MP lead system (Ch. 2). The half-cell potential for lead in the electrochemical series is still at -0.126 V, while the half-cell potentials for f-metals, i.e. lanthanides or actinides, are between -1.66 V for uranium and -2.379 V for lanthanum [31], well outside the y-axis of the diagram shown. However, it can be assumed that if the formate range were extended, the f-metals would be located well within that range.

In addition, the contemporary literature on the electrochemistry of the f-metals and the Pourbaix diagram shown (Fig. 5.1), advocate the exploration of electrochemical process control with the incorporation of a reference electrode. Initial endeavours were unsuccessful due to the unavailability of systems that met the stipulated performance criteria. Initial attempts to network with established institutions in the field of electrochemistry to address the problem also remained fruitless due to the ongoing restrictions imposed by the Coronavirus pandemic, and any results that could have been incorporated into this work were also not forthcoming.

5.2. Chemical changes due to ion irradiation

As outlined in the introduction, observations from heavy ion experiments revealed alterations in the alpha spectra of actinide targets produced via the MP process when exposed to ion irradiation [85, 20].

Initial studies primarily documented morphological changes [129]; however, the analytical methods employed precluded a comprehensive understanding of the underlying chemical changes. The present study employs confocal Raman spectroscopy, a vibrational spectroscopy method with high spatial resolution (Ch. 2 and 3), to address this knowledge gap. Initial studies with MP lead targets indicated a conversion of carbonates into oxides [71], suggesting that the targets may have lost volatile components such as carbon and oxygen during the irradiation process. Research on thulium targets has revealed a conversion of a mixture of carbonates and formates to thin films that contain less volatile components, such as carbon and oxygen. However, analysis of both unirradiated and irradiated MP thin films was more complicated than in the lead system, since the thin films are chemically more complex.

Lanthanide MP thin films are chemically complex amorphous systems, so the radiation-induced changes observed in this study were less clearly defined than in comparable studies on highly pure and highly crystalline compounds [204, 205]. The analysis results obtained could not be directly incorporated into theoretical descriptions of irradiation damage [200]. However, the loss of volatile components and the associated shrinkage of the films were detectable for all irradiation experiments. The shrinkage of the MP films presents an experimental obstacle for SHE experiments, since less material is optimally exposed to the ion beams [119]. Furthermore, the present experiments could only map the first few minutes of a full SHE campaign, and real SHE targets receive significantly higher radiation doses than those that could be reproduced in this work. Thus, further chemical changes in the MP thin films under irradiation are to be expected. The available irradiation times at the accelerator, as well as access to radiologically certified laboratories, are the limiting factor for such studies.

5.3. Alternatives to the MP process

In the present work, two fundamentally new methods for target production were examined with regard to their irradiation behaviour. Initially, lead targets produced by the drop-on-demand method were irradiated (Ch. 2), and a new electrochemical method was also trialled (Ch. 4). These targets were then examined for their irradiation behaviour.

In the DoD process [70], aqueous lead nitrate is simply applied to a target foil and thermally treated. The lead oxides produced in this way showed hardly any chemical changes at the applied radiation doses. Repeated experiments with lanthanides were not included in the study. Prior to irradiation, the DoD targets exhibited incomplete coverage of the target foil and poor adhesion of the thin films, which could hinder the effectiveness of a subsequent SHE production campaign. Notwithstanding these limitations, the method demonstrates considerable untapped potential, as evidenced by earlier studies with other target systems in fundamental physical research [68]. The method exhibits a high degree of flexibility in terms

of form. The potential for producing chemically well-defined compounds prior to irradiation would enhance the predictability of their irradiation behaviour, as evidenced by the literature on lanthanide [204] and actinide [205] oxides. Moreover, less complex, better defined starting systems would streamline the post-irradiation analysis. However, the necessary development work was beyond the scope of this thesis and would undoubtedly be a significant undertaking for numerous further theses. Instead, the current work focused on enhancing an electrochemical process to complement or replace the MP process.

In contrast to the actinides, the electrochemical production of lanthanide thin films is of current technological importance and has been the subject of numerous publications [107, 117, 201]. Despite the known chemical similarities [31] of the post-plutonium actinides to the lanthanides and the importance of the latter for SHE research, no attempts have been made to use modern electrochemical techniques for target fabrication. The first attempts to deposit target wheel segments in dry and degassed dimethylformamide (DMF) under an argon atmosphere, using triflate as the counteranion (Ch. 4), were characterised by laborious development work which is hardly mentioned in this publication. Numerous prototypes of a modified electrochemical cell had to be tested before successful deposition was achieved. This was because dry and degassed DMF in an argon atmosphere attacked the existing sealing [177] and bonding systems [118] of the electrochemical cell and the target wheel [91] segments in a previously unknown way.

However, further development work is required before its application in an actinide system can be considered. The platinum-group anode systems utilised to date also appear to be unsuitable, as they are prone to corrosion under new reaction conditions. The incorporation of foreign metals into the target thin film is unacceptable for SHE campaigns. In this regard, the establishment of a setup common in electrochemistry, employing a reference electrode, would be advisable. The unavailability of turnkey systems in the market during the period when this research was being conducted has thus far impeded the advancement of experiments in this direction.

Initial experiments demonstrated that, despite the aforementioned challenges in development and the time constraints associated with meeting the irradiation deadline, it was feasible to produce targets of greater thickness in a single step than was typically achievable using the MP process. The composition of these thin films was not fully elucidated before and after irradiation using the appropriate methods. However, GIXD measurements indicated the presence of an oxidic form, which could be attributed to the installation of the targets in ambient air within the experimental stations. It is evident that methods that deviate from the conventional pathways of the MP process retain the capacity to yield target systems that have the potential to unveil novel avenues for SHE research [36, 38].

5.4. Lessons from MP thin film analysis

The present work constitutes a further example of trial and error in determining which analytical methods provide the most reliable analytical results in the complex system of MP thin films on thin, flexible titanium foils. Without summarising all three publications, it can be concluded that methods with a spatial resolution that made it possible to analyse individual tiles and, preferably, without the need to touch the sample surface, since target foils tend to tear, have almost exclusively proven successful.

Confocal Raman microscopy has yielded the most results, but the interpretation of the measurements is not always straightforward due to the necessity of reference spectra. The scarcity of reference spectra for lanthanide compounds and their virtual absence for actinide compounds poses a significant challenge, yet it also presents a substantial opportunity, particularly if a device is permanently available in a radiologically certified laboratory. An extension using spatially resolved IR spectroscopy would be preferable, as bulk IR spectroscopy has been shown to complement the Raman data well, despite the presence of experimental difficulties.

X-ray diffraction methods provided significant contributions to this research, particularly in understanding the formate composition in thin films. There are also enough reference diffraction patterns given here for both lanthanides and actinides. However, the morphology of the samples posed a substantial challenge. Access to diffraction methods with high spatial resolution was not attained; nevertheless, based on the analysis results, it was anticipated that methods such as coherent diffractive imaging (CDI) [134] could surmount the challenges posed by sample morphology. However, access to such methods is only possible after a sometimes lengthy application process at the relevant research facilities.

For measurements at a specialized research facility such as the Helmholtz-Zentrum Dresden-Rossendorf (HZDR), Rutherford backscattering spectrometry (RBS) with high spatial resolution has also proven to be the method of choice. Here, too, a lot of trial and error was necessary, which took up the majority of the requested measuring time. However, observations made using other methods could be reproduced well, while other methods of ion beam analysis failed due to the lack of spatial resolution of the morphology of the MP films. For future measuring campaigns, it is now clear which measuring methods should be given preference when applying.

A completely different approach could not be published in the present work, since only experiments could be carried out within the scope of manufacturer demonstrations, which prohibit a publication of the analysis results obtained in this way. However, 3D laser scanning microscopy not only confirmed the results of scanning electron microscopy (SEM) and atomic force microscopy (AFM), but it did so

without vacuum conditions and without the need for contact or further preparation steps. The 3D laser scanning microscopy uses three different measuring principles combined in one device. Depending on the application, a confocal laser, focus variation and white light interferometry can be used. This enables highly precise measurements and analyses of various measurement objects with a maximum resolution in the sub-nanometre range. It is possible to quickly capture measuring areas in the square centimetre range with large differences in height, which would enable the characterisation of entire target segments. This enables a quick analysis of both the overall shape and specific areas. Even difficult materials, such as those with transparent and reflective surfaces, can be measured quickly, with high accuracy and over a large area. 3D laser scanning microscopy can measure objects independently of magnification, surface roughness and composition. Particularly impressive was the rapid possibility to statistically determine siginificant data about the thin films. While AFM and SEM only provide information about the thickness, roughness and percentage coverage of the MP thin films when viewed through a keyhole, 3D laser scanning microscopy provides an overall picture of the manufactured target. This would enable the research group's permanent staff technicians and chemists to better quantify the daily target production statistically using such a method. This would certainly not be basic research in the strict sense of the word, but it would be a common method of quality control and quality development, as is common in the chemical industry. The fact that modern devices using this measuring principle allow the integration of confocal Raman or IR microscopy brings us back to the analysis results of this work.

A. Appendix

A.1. Appendix for chapter 4

A.2. Abstract

In this appendix analytical results are shown in detail, including data from nuclear magnetic resonance (NMR) spectroscopy of the precursors, diffraction images under grazing incidence (GIXD), Raman spectroscopy and energy dispersive X-ray spectroscopy (EDX) mappings.

A.3. NMR

As discussed in the main body of the publication, neutron-activated sesquioxides (Tm_2O_3, Tb_2O_3) was reacted with highly concentrated trifluoromethanesulfonic acid (CF_3SO_3H, CAS-No 1493-13-6, Sigma-Aldrich reagent grade, 98 %) in closed polypropylene tubes and completely dissolved [74]. By means of gamma spectroscopy, it was possible to prove that all the activity was now indeed in solution, i.e. that the acidic digestion was complete. By means of nuclear magnetic resonance spectroscopy (NMR), the chemical structure was now to be clarified; in particular, the remaining water of crystallisation was of particular interest. The precursor protocol was repeated for non-neutron activated thulium oxide (Tm_2O_3), as access to appropriate measuring equipment in a radioactive controlled area was not available.

NMR experiments were performed at a Bruker Avance III 700 MHz NMR spectrometer equipped with a QXI probe head with z-gradient. ^{1}H spectra were acquired by accumulating 64 scans and a relaxation delay of 8 s at a transmitter frequency of 700.36 MHz. ^{19}F spectra were acquired in direct excitation with 256 scans and a relaxation delay of 2 s at a transmitter frequency of 658.95 MHz. The ppm values were referenced to tetramethylsilane (TMS) in the case of ^{1}H NMR and to fluorobenzene in the case of ^{19}F NMR. $Tm(OTf)_3$ was used as prepared below and all other chemicals were obtained from Sigma Aldrich and used without further purification.

For the preparation of the NMR stock solution, a sample of $Tm(OTf)_3$ (6 mg, 10^{-2} mmol) was dissolved in D_2O (1 mL). The reference solution was prepared by adding trifluoromethanesulfonic acid (2.5 µL, 3×10^{-2} mmol) to D_2O (1 mL). As a measurement vial, an NMR tube (company Deutero) with coax-

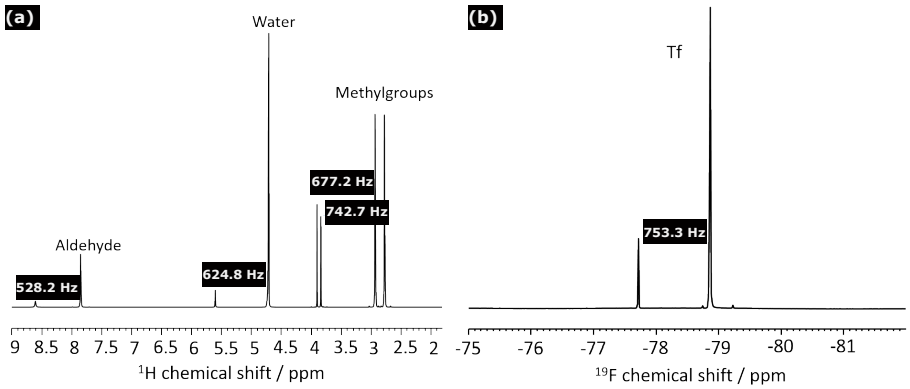

Figure A.1.: NMR spectra of ^{1}H (left) and ^{19}F (right) of $Tm(Tf)_3$ in D_2O/DMF mixture acquired at room temperature.

ial insert was used. The outer vial was filled with the reference and the inner one with the analyte. In addition, N,N-dimethylformamide (20 µL) was added to both, the inner and the outer tube, to identify a possible complex formation between the paramagnetic metal centre and the DMF solvent.

The ^{1}H and ^{19}F NMR spectra are displayed in Fig A.1. Aldehyde, methyl, and water proton NMR signals were assigned due to their characteristic chemical shift values. Note that all signals for the paramagnetic shifts are time averaged signals between the different states of different proximity to the paramagnetic centers. In the case of the fluorine spectra, only two signals (one of reference OTf and the other of the paramagnetic sample) were obtained, indicating that no fluoride products were formed due to decomposition reactions during the synthesis. For complex formation with DMF, the differences for the frequencies in the proton spectra were determined and are compiled in table A.1. The values for the paramagnetic susceptibility are calculated with the following formula and are given in table A.1.

$$\chi_M^p = \frac{\delta \upsilon^p M^p}{\upsilon_0 S_f m^p} - \chi_M^{dia} \tag{A.1}$$

Here, χ_M^p is the molar paramagnetic susceptibility, $\delta\upsilon^p$ is the difference in the frequencies of the paramagnetic and the reference sample, υ_0 is the operating frequency of the spectrometer, S_f the shape factor of the used magnet ($\frac{4\pi}{3}$) and M^p and m^p are the molar mass and the mass of the paramagnetic substance. χ_M^{dia} is the diamagnetic correction term, which can be neglected for small molecules [166] and therefore was ignored here.

Table A.1.: Chemical shift values, frequency differences $\Delta\nu$ and molar paramagnetic susceptibility χ_M^p for $Tm(OTf)_3$ in D_2O/DMF mixture, measured at room temperature.

		$\Delta\nu$ Hz	χ_M^p mol^{-1}
DMF	^1H (H-1, 8.61/7.86 ppm)	528.2	1.85×10^{-2}
	^1H (H-2, 3.91/2.95 ppm)	677.2	2.37×10^{-2}
	^1H (H-3, 3.83/2.77 ppm)	742.7	2.60×10^{-2}
Water	^1H (5.59/4.72 ppm)	624.8	2.19×10^{-2}
OTf	^{19}F	753.3	2.81×10^{-2}

The values show that the aldehyde protons experience the lowest paramagnetic shift of all protons in DMF and that the paramagnetic shifts of the methyl protons are larger. This observation indicates a shorter average distance of the methyl groups to the paramagnetic center. All results suggest that the $Tm(OTf)_3$ complex dissociates in water, being in an equilibrium with the hydrated form $[Tm(H_2O)_x]OTf_3$. We conclude that upon crystallization, the complex still carries water molecules in the coordination shell because of incomplete drying.

A.4. Grazing incidence X-ray diffraction

In grazing incidence X-ray diffraction(GIXD), a very small angle of incidence (ω) is chosen to limit the penetration depth of the photons to a thin surface layer of the film. The X-ray beam and sample are fixed to ensure a small angle of incidence ($\omega \approx 0.1$ - 5°) while the detector moves at an angle of 2Θ to collect diffraction signals. The structural information thus originates predominantly from the near-surface region (<400 nm). For the GIXD measurements, a PTS 3003 device from the Seifert company with a rotating anode was used with CuK_α radiation (λ = 1.5406 Å).

We identified two reflections than can be asigned to thulium(III)oxide, at 27.8° and 82.1°. The peak at 27.8° is rather broad and decreases with increasing fluence. The peak at 82.1° was only sporadically detected. No other thulium compound could otherwise be fitted to these reflexes, yet the GIXD data alone are not a reliable identification. However, since EDX and Raman point to the same compound, thulium(III) oxide is the most obvious explanation.

A.5. EDX mapping

Scanning electron microscopy (SEM) images in combination with EDX mappings were recorded to determine the local distribution of the specific elements in the irradiated (sample CCM-14, irradiated with 5.0×10^{12} ions/cm^2, cf. main manuscript) thin films (Fig. A.3). Panel (a) is a secondary electron (SE)

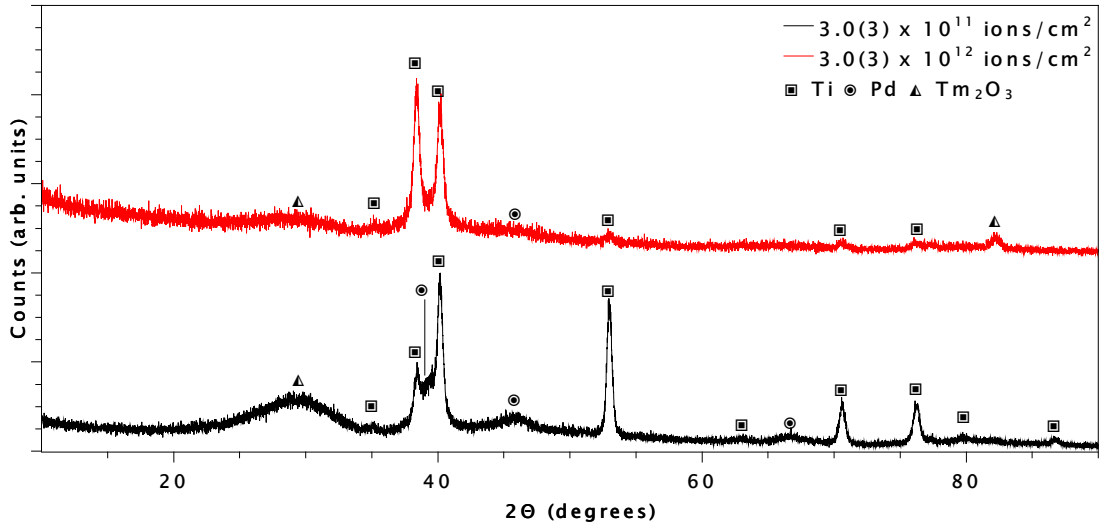

Figure A.2.: X-ray diffraction patterns of two ion-irradiated thulium thin films made by electrodepositon from triflate on Ti backings (50 µm). GIXD patterns recorded after irradiation with 8.6 MeV/u ^{197}Au ions at fluences of 3.0×10^{11} ions/cm^2 (black) and 3.0×10^{12} ions/cm^2 (red).

image of the sample surface. The inhomogeneous morphology is clearly visible: Bright areas show deposited thulium and palladium, the darker areas the titanium backing. Panel (b) is the signal of the TiK$_\alpha$ line. Dark areas indicate a thicker coverage with deposited thulium and palladium. Since those heavier elements dampen the TiK$_\alpha$ signal, they appear darker in the elemental mapping. Panel (c) shows the distribution of the PdL$_\alpha$ line in the thin film; palladium was used as the anode material. A large local concentration of palladium can be seen in the right half of the image. Panel (d) shows the distribution of thulium in the thin film. This image representation of the TmL$_\alpha$ signal largely reproduces the SE image, except for the areas of high palladium concentration.

Local islands of anode material (Fig. A.3) were detected for thin films produced from commercial thulium triflates under inert atmosphere conditions. In layers produced by other methods, such islands of anode material were not observed, as indicated by the EDX spectra in the main manuscript (Fig. 4 a).

A.5.0.1. Raman spectroscopy

Raman spectra from 50 to 4000 cm^{-1} were collected with a Jobin Yvon (Horiba) LabRam HR 800 spectrometer equipped with an Olympus BX41 optical microscope and a Si-based charge-coupled device (CCD) detector [132, 71, 167]. The instrumentation used a grating with 1800 $\frac{\text{grooves}}{\text{mm}}$ and a slit width of 100 mm. Excitation wavelengths of 633 nm and 488 nm were used. These parameters and the optical path length of the spectrometer led to a spectral resolution of 0.8 cm^{-1}. The spectral acquisition time

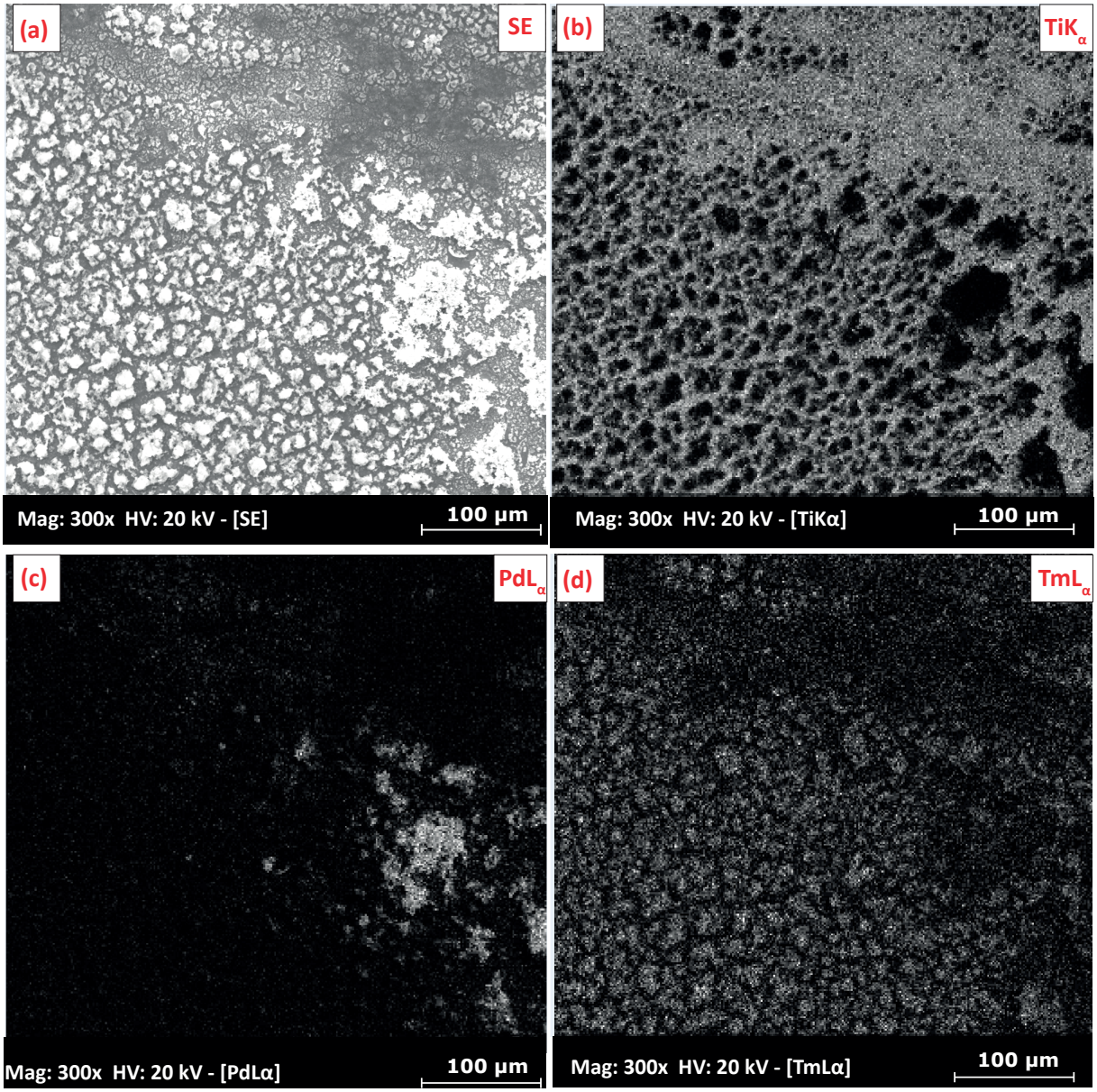

Figure A.3.: Scanning electron micrographs and EDX maps of thin films deposited from commercial thulium triflate under argon atmosphere (sample: CCM-15, 2000 µg/cm^2) after irradiation with a 8.6 MeV/u ^{197}Au ions (1.0×10^{13} ions/cm^2). (a) SE (b) TiK$_\alpha$ (c) PdL$_\alpha$ (d) TmL$_\alpha$ maps.

was set to 40 s for all measurements. In order to exclude modifications due to laser irradiation, long-term measurements were carried out analogous to [23]. The Raman spectra were assessed using the software packages Fityk [224] and Spectragryph [130].

The Raman spectra of all investigated samples were characterised by a high background noise and a poor signal-to-noise ratio. Therefore, only a few peaks could be identified above the background. These however, could be clearly assigned to thulium(III) oxide [204, 172, 209]. The Raman bands of other thulium compounds in question, e.g. carbonates [132, 221] or triflates [74], would lie in a different range.

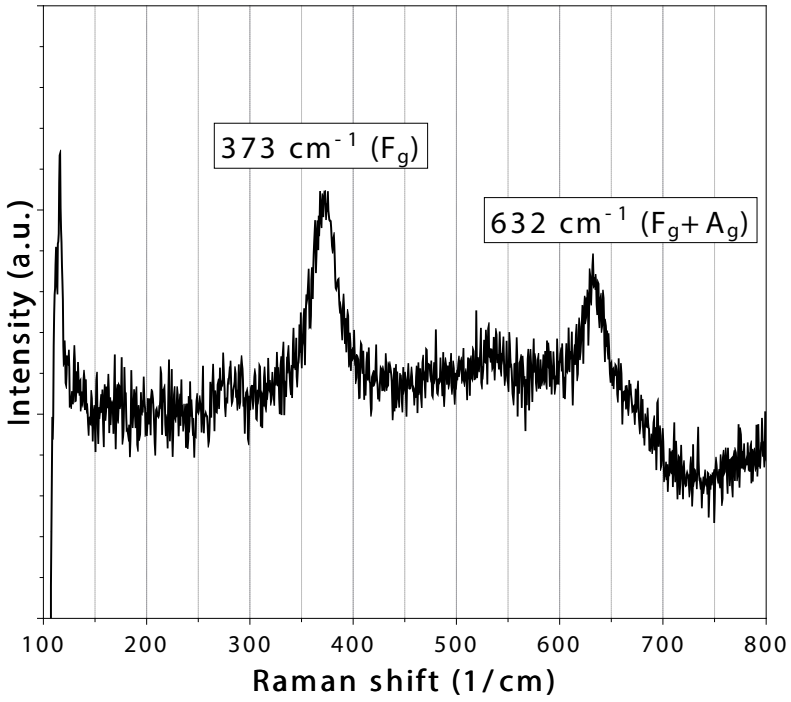

Figure A.4.: Raman spectrum of deposits from thulium triflate under argon atmosphere (Tm inert gas, $1820(20)\,\mu g/cm^2$). The two prominent peaks $373\,cm^{-1}$ (F_g) and $632\,cm^{-1}$ (F_g+A_g) correspond to the literature values [204, 172, 209] for Tm_2O_3. Further peaks could not be clearly assigned due to the poor signal-to-noise ratio and a high background.

Nuclear Inst. and Methods in Physics Research, A 957 (2020) 163366

Contents lists available at ScienceDirect

Nuclear Inst. and Methods in Physics Research, A

journal homepage: www.elsevier.com/locate/nima

ODIn — A setup for Off-line Deposit Irradiations of thin layers for nuclear physics applications

R. Haas [a,b,c,*], C.-C. Meyer [a,b], S. Böhland [a], Ch. E. Düllmann [a,b,c], J. Mäder [c], K. Tinschert [c]

[a] Department Chemie, Johannes Gutenberg-Universität Mainz, Fritz-Strassmann-Weg 2, 55128 Mainz, Germany
[b] Helmholtz-Institut Mainz, Staudingerweg 18, 55128 Mainz, Germany
[c] GSI Helmholtzzentrum für Schwerionenforschung GmbH, Planckstraße 1, 64291 Darmstadt, Germany

ARTICLE INFO

Keywords:
Off-line irradiation
Ion beams
Electron beams
Targets
Thin layer deposits

ABSTRACT

A table top setup was developed for the irradiation of thin layers with low-energy electrons and ions of gaseous species. This serves to gain a better understanding of the chemical microprocesses involved during irradiations. The gained insights will complement the understanding of heavy-ion beam induced transformations at on-line facilities and will be used to develop an accelerator-independent method to transform freshly produced targets into a long-term stable form. The pilot experiment for these Off-line Deposit Irradiations (ODIn) is installed at the Helmholtz Institute Mainz. The setup, beam characterization and first commissioning are described.

1. Introduction

Thin films of radionuclides are a key element in many nuclear physics applications. These include applications as nuclear targets in accelerator-based experiments, e.g., in the production of superheavy elements in heavy-ion fusion reactions. With ever increasing beam intensities of new and more powerful accelerators, the targets have to withstand ever more intense heavy-ion bombardments over long time periods. For the synthesis of the heaviest elements, actinide targets are used, which are frequently produced using the well established "Molecular Plating" technique [1,2]. This method is also applied for the production of radionuclide samples, e.g., serving as recoil ion sources providing α-decay daughters [3] or fission fragments. A. Vascon et al. characterized this method in more detail for lanthanides [4], which served as homologs of actinides, and found ideal parameters to produce crack-free large area targets [5]. The performance as α-particle source was characterized as well [6]. An important finding was the additional deposition of organic solvent material as well as the speciation of the deposited lanthanide on the produced targets. The latter indicated that the material is deposited as hydroxides and carboxylates, but not in the originally provided chemical form, e.g, the nitrate [5]. The deposits are known to often be quite sensitive to moisture and oxygen and deteriorate during long storage time periods at air. Furthermore, the deposit was found to be covered by a thin layer of organic solvent material. Other target fabrication methods include Pulsed Laser Deposition (PLD) [7], Polymer-Assisted Deposition (PAD) [8] and Drop-on-Demand inkjet printing (DoD) which was recently developed and characterized [9]. The Drop-on-Demand technique has some advantages when compared to the Molecular Plating technique in regard to the chemical purity and amount of the deposited material and is not limited to deposition on electrically conductive substrates. Several different targets and sources have recently been produced by this technique [10,11]. Also with this technique, the final deposits are hygroscopic and may deteriorate at air.

To prevent such aging processes of freshly produced targets, they are usually converted into a long-term stable form. For this, the state-of-the-art relies on a well established on-line baking-in procedure with heavy-ion beams. During these irradiations, organic impurities are largely destroyed and the actinide species can be converted into the oxide [12]. To give just one recent example, we refer to [13], where ^{248}Cm targets were conditioned with a 5.6 MeV/u ^{48}Ca-beam on-line at the Separator for Heavy Ion reaction Products (SHIP). Alpha-spectra of the ^{248}Cm layer recorded before and after the baking-in procedure reveal a narrowing of the lines, indicating a loss of material in the layer while the activity stayed constant. It is already known that such transformations cannot be reproduced by heating up to 700 °C in an oxidizing or reducing gaseous atmosphere [14] and are not just caused by induced heat in the target layer during irradiation [15]. The field of the induced effects of such beams on target materials is well investigated by several groups. Some exemplary findings are phase transformations in cubic C-type lanthanide sesquioxides by electronic excitation [16] or beam induced electronic sputtering [17]. To date, though, it is still not well known, if similar effects of target conditioning can be achieved with ion or electron beams of substantially lower energies.

* Corresponding author at: Department Chemie, Johannes Gutenberg-Universität Mainz, Fritz-Strassmann-Weg 2, 55128 Mainz, Germany.
E-mail address: raphhaas@uni-mainz.de (R. Haas).

https://doi.org/10.1016/j.nima.2019.163366
Received 30 September 2019; Received in revised form 12 December 2019; Accepted 23 December 2019
Available online 26 December 2019

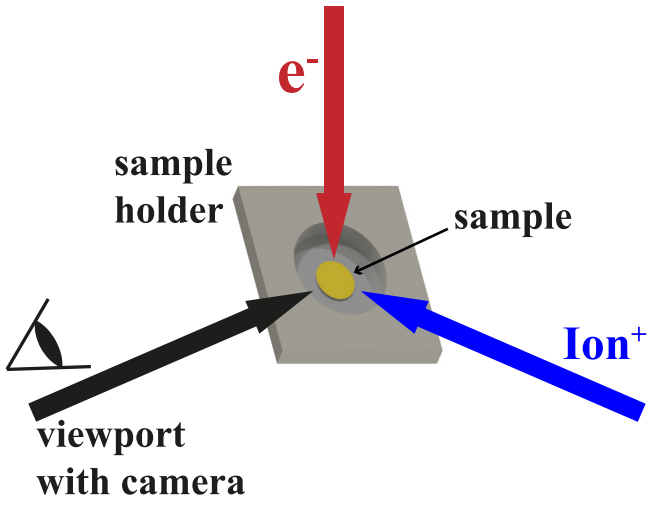

Fig. 1. General sketch of the ODIn working principle.

2. ODIn — a setup for Off-line Deposit Irradiation

As a new approach for investigations on the chemical and physical microprocesses during irradiations of target material with low-energy ion and electron beams, a new setup for Off-line Deposit Irradition (ODIn) was constructed at the Helmholtz Institute Mainz. This serves as a test bench and pilot facility for the development of a method to condition freshly produced actinide targets independently of on-line accelerator beam availability. ODIn provides electron beams up to 1.5 keV as well as ion beams of gaseous species up to 5 keV with currents of hundreds of μA. A general sketch is depicted in Fig. 1. The beam currents can be measured via a Faraday cup or by direct measurement of the current induced in the sample holder. Additionally, the irradiated samples as well as phosphor screens can be monitored by a camera through a viewport flange. A LabVIEW based remote control system was developed for the experiment and the beam profiles were measured with phosphor screens for several irradiation parameters. For commissioning, lead samples were produced on gold plated Kapton foil by Molecular Plating and were irradiated with electron beams.

2.1. Vacuum system and general setup

The technical drawing of the ODIn setup is given in Fig. 2. The setup comprises an electron gun (Kimball Physics, EFG-7 with EGPS-1017 power supply) and a sputter ion gun (tectra, IonEtch Sputter gun GenII) described in the following sections.

The irradiation chamber comprises both the electron gun and the ion gun as well as a viewport flange to monitor the sample, a cluster-flange with a Faraday cup (Kimball Physics Inc., FC-70, 0.063” aperture) mounted in the middle of a flange opposite to the ion gun and a turbo pump (Pfeiffer Vacuum, HiCube 300 H, 260 L/min for nitrogen, ultimate pressure at below 1×10^{-10} mbar). It takes one minute to reach a pressure of 1×10^{-5} mbar in the irradiation chamber after opening the gate valve to the airlock and 10 min more to reach a pressure below 1×10^{-6} mbar. This is ideal for the irradiation of many samples in one day without any heating of the vacuum parts and to keep a safe environment for the gun systems. Furthermore, the manually driven gate valve grants a slow release of the residual pressure of the airlock after it was pumped down to 1.5 mbar. An ultimate pressure of 2.5×10^{-8} mbar can be reached in the complete experiment if the gate valve is open. If the gate valve is closed, an ultimate pressure below 6×10^{-9} mbar can easily be reached without heating.

To allow sample changes without breaking vacuum in the irradiation chamber, a second chamber serving as an airlock is separated by a manually operated UHV gate valve. One small chamber (sample chamber) consists of a quick access door to enable easier sample changes and a rotary feedthrough to move the mounted sample or phosphor screen between both chambers and to arrange it towards a specific source by a turn of 90°. The airlock can be evacuated by a membrane pump (Pfeiffer Vacuum, MVP 030-3 diaphragm pump, 30 L/min, ultimate pressure: below 2 mbar) in about 80 s to a pressure of 1.5 mbar and can be vented with nitrogen by a manual valve to avoid moisture from the air entering the airlock. The nitrogen gas is passed through a tube filled with dried $CaCl_2$ to remove residual moisture in the gas before entering ODIn.

2.2. Beam sources

The electron gun system (Kimball Physics, EFG-7 with EGPS-1017 power supply) is a commercially available, complete subsystem with included deflection electrodes. A simple scheme of the electron gun is given in Fig. 3 including all elements and their applied voltages. The beam energy, current and focus are adjustable over wide ranges. The gun system is able to produce electron beams within an energy range of 10 eV up to 1.5 keV at specified beam currents in the range of 1 nA up to 100 μA. At a working distance between 25 mm and 200 mm, spot diameters of 1 mm up to 100 mm can be achieved with Gaussian or uniform beam profile. In the used system a standard tantalum disk is used as a cathode and serves as the electron source. It is built inside a tubular structure with an aperture fixed to one end which is called Wehnelt or grid. By applying a negative voltage to this structure, the electric field between the cathode and Wehnelt suppresses electron emission from the cathode perimeter, leaving only the center of the cathode to emit. By varying this voltage, a selection of either of the two previously mentioned beam profiles can be made. It can also be used to pulse the electron beam by adjusting a sufficiently high negative potential to cut off the beam. An aperture plate downstream of the Wehnelt acts as anode and is at ground potential. The potential difference between the cathode and anode determines the energy and trajectory of the electrons. The focusing lens is an Einzel lens with the first and third element at ground potential and the second element at negative focusing potential. At a given electron energy and working distance, the spot diameter is a function of focus voltage. The minimum spot diameter varies for different electron energies and is found by scanning the focus voltage as discussed in Section 3.1. The last part of optics consists of two pairs of curved deflection plates for X- and Y-deflection, which allows scanning a specific area with a beam focused on the target and to correct the shape of the beam. To minimize the distortion of the beam, a small deflection can be applied, which results in a more circular spot shape. The gun system can be operated at pressures in the range of 1×10^{-11} mbar up to 1×10^{-5} mbar with manually driven source voltage and current or emission current control (ECC). With ECC the electron source is heated up slowly and the source voltage and current are continuously adjusted to deliver a specific emission current. The beam current is in general about half of the emission current. The gun system is mounted on a port aligner for linear and angular adjustments at the irradiation chamber and the distance between the gun’s aperture and the sample holder is about 80 mm.

The ion gun system (tectra, IonEtch Sputter gun GenII) is a commercially available filamentless ion source based on microwave plasma discharge. The principle of the source is coupling of microwave energy at 2.45 GHz into a coaxial waveguide and from there via evanescent wave coupling into a plasma chamber made of alumina. The intense oscillating electric fields produce a plasma discharge of the used gas. Using microwaves to produce and sustain the plasma has some advantages, e.g., the ions can be extracted at very low energies down to 25 eV without the plasma collapsing and also the use of reactive gases such as oxygen and hydrogen is permitted, since there are no hot metal electrodes in the plasma. This allows the possibility to produce proton

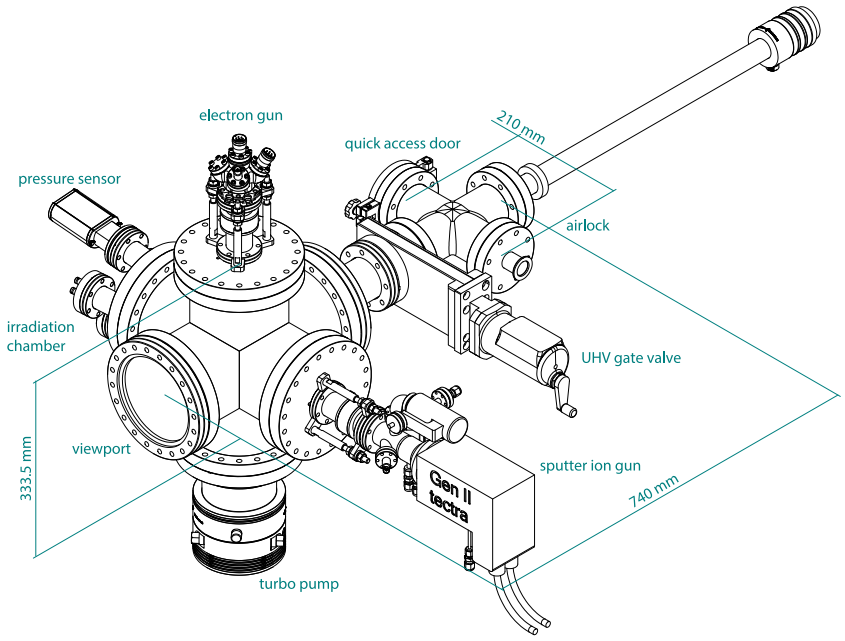

Fig. 2. Technical drawing of the ODIn experiment.

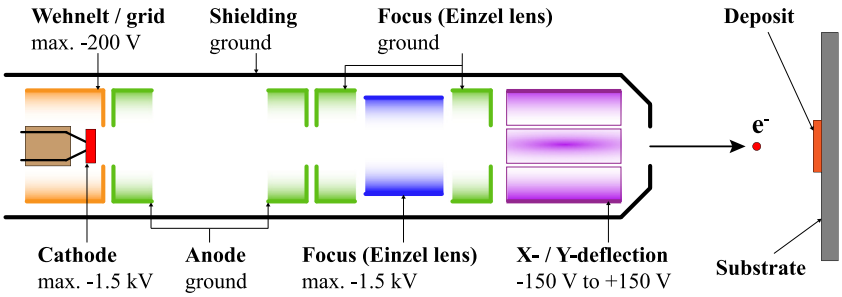

Fig. 3. Scheme of the electron gun system including a simple illustration of all elements with their applied voltages.

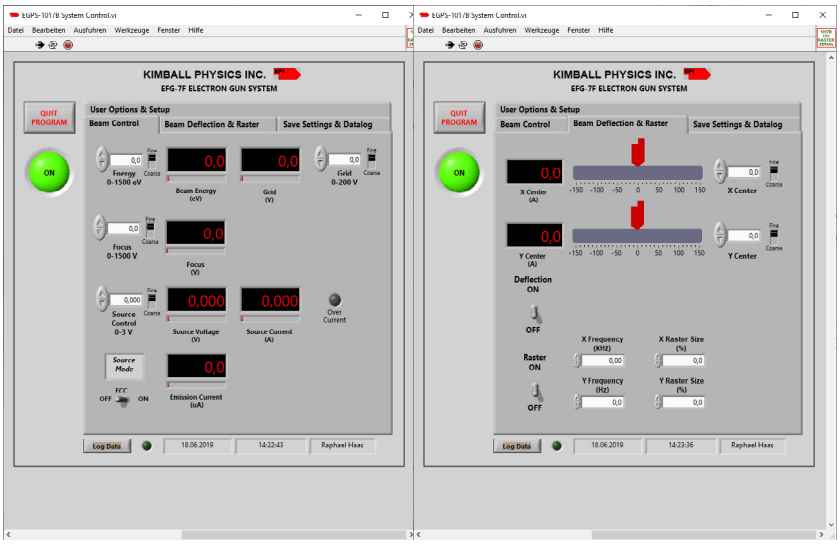

Fig. 4. LabVIEW remote control user interface of the electron gun system delivered by Kimball Physics. (left) General beam control, setting and readout: Energy, grid, focus, source voltage and Emission Current Control (ECC) switch. (right) Deflection and area scan control.

beams. The produced ions are extracted from the plasma using two single-hole extraction apertures and beam energies of up to 5 keV with a maximum beam current of 2 mA can be produced. The gun system is watercooled by an external chiller (Huber, HTS1, 650 W cooling capacity) and magnetron current, beam energy and extraction voltage can be controlled by its power supply. Furthermore, the magnetron

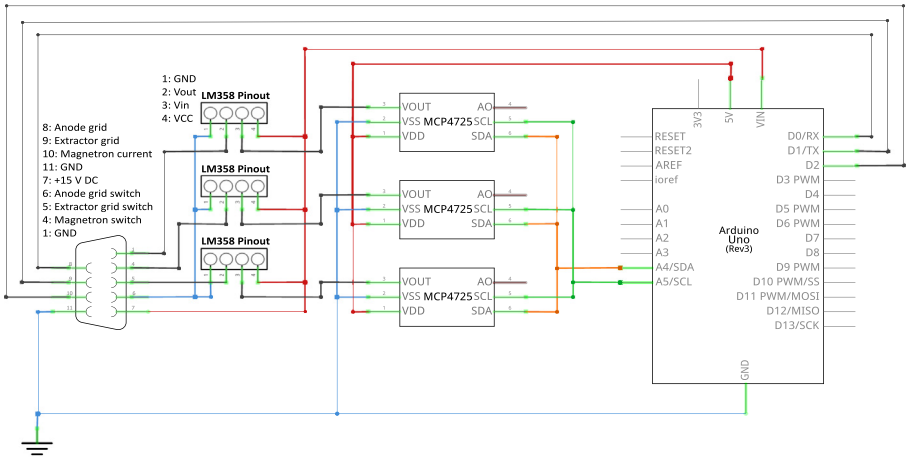

Fig. 5. Simplified circuit diagram of the remote control for the ion gun power supply.

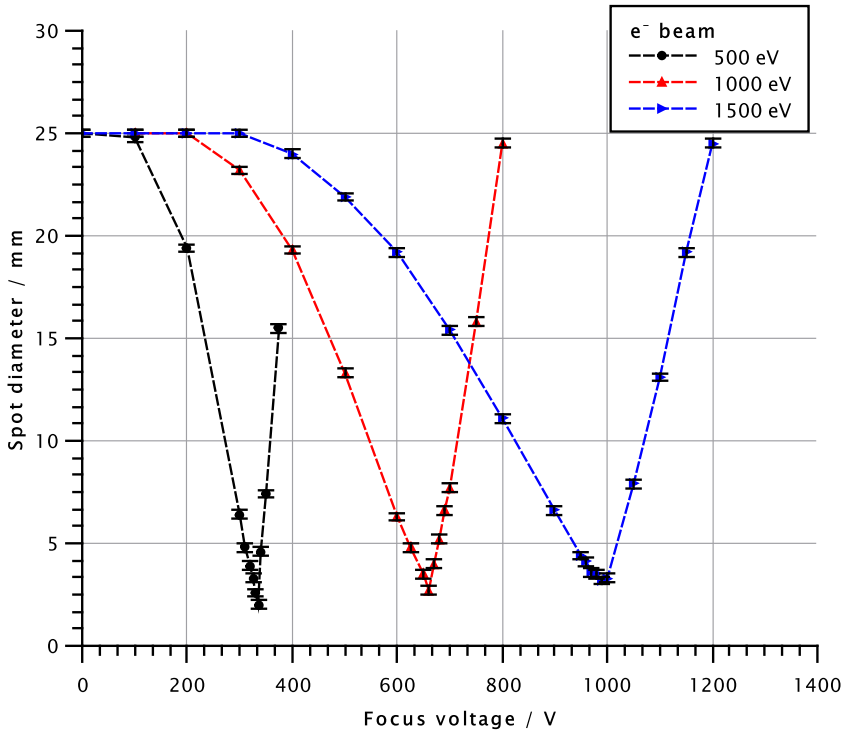

Fig. 6. The effect of focus voltage on spot diameter at three different energies, showing minimum spots at focus/energy = 0.66.

current, beam current and voltages on the ion optics can be read out on the power supply. The investigated influence of the controllable parameters on the produced beam profiles and currents is discussed in Section 3.2. Similar to the electron gun, also the ion gun is mounted on a port aligner at the irradiation chamber and the working distance is about 115 mm.

2.3. Sample introduction and monitoring

Either a target or a phosphor screen (e.g. GIDS, SCR-25-ITO-P43) is fixed between two titanium frames and can quickly be exchanged since it is just fixed with one screw in the sample holder. The maximum diameter of a target is restricted to 25 mm by the titanium frames. The holder itself is a single piece of titanium with an insertion slot for the titanium frames and is tilted at a 45° angle towards both the gun systems and the viewport in the irradiation chamber. Thus, phosphor screens or targets can be monitored with a camera (Rauscher, Basler piA1000-60gc with camera lens MVL25M23 from Thorlabs) through the viewport in the irradiation chamber.

2.4. Control system

The power supplies of both gun systems as well as the camera system and the pressure readout can be controlled remotely. The user interface of the LabVIEW VI provided by Kimball Physics used for electron gun control is shown in Fig. 4. It provides control of all adjustable gun parameters (anode, grid and focus potentials, cathode voltage, deflection and scanning) and data logging. Additionally, the Emission Current Control (ECC) can be switched on, so the source voltage is adjusted automatically to deliver a steady emission current. The cathode temperature is also monitored in a third window, which is not shown in the figure.

The power supply of the sputter ion gun provides a D-Sub 9 pin connector for analog input remote control of the adjustable parameters

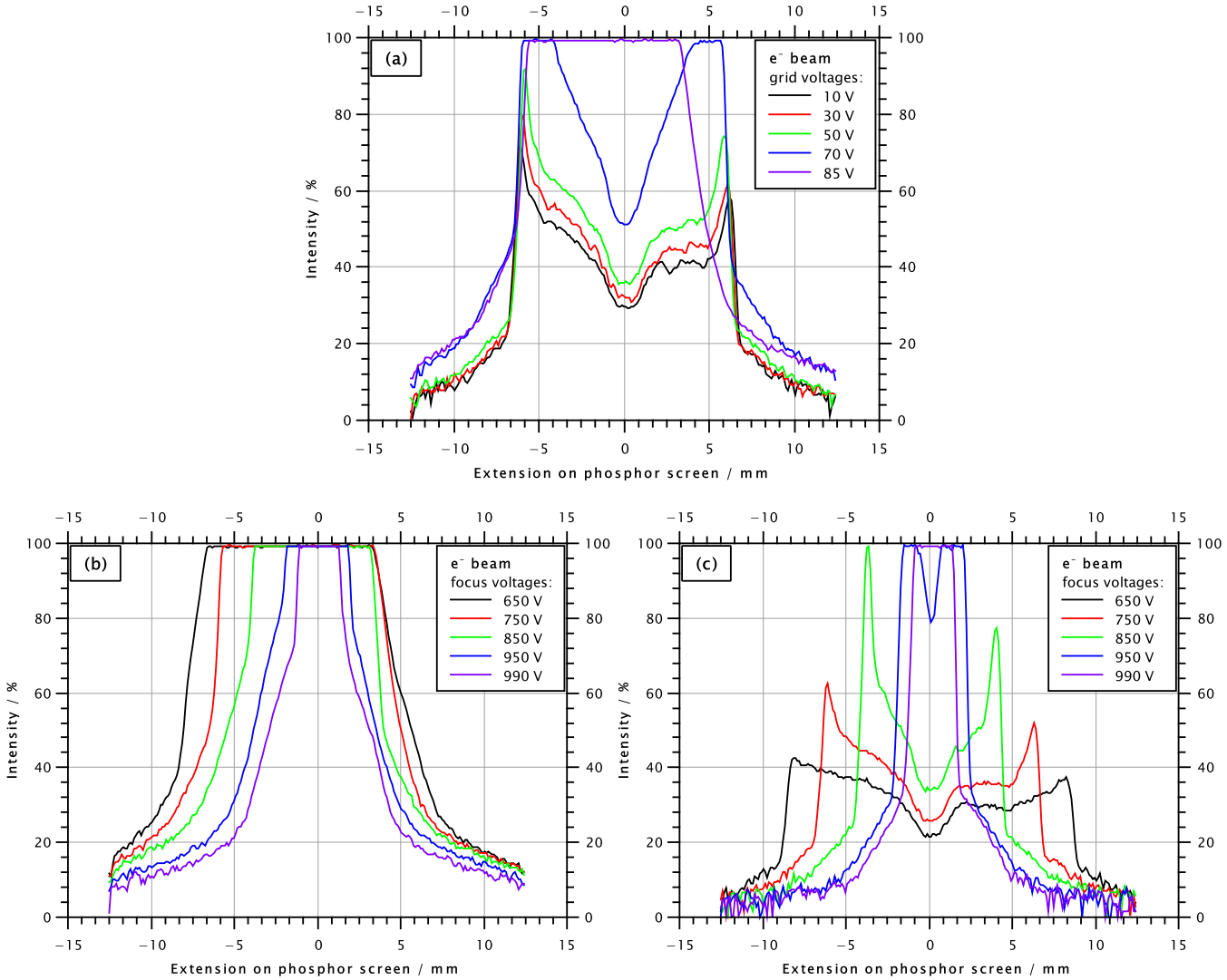

Fig. 7. Beam profiles taken with different electron gun parameters at beam energy of 1500 eV: (a) variation of grid voltage between 10 V and 85 V at focus voltage of 750 V, (b) variation of focus voltage between 650 V and 990 V at grid voltage of 83 V and (c) variation of focus voltage between 650 V and 990 V at grid voltage of 0 V.

of the ion gun. Three pins enable the remote control of a single gun parameter by applying a voltage of 5 V. Another three pins are used for metering by an applied voltage between 0 V and 10 V. One pin provides a voltage of 15 V with an internal resistance of 1.5 kΩ and the residual pins are ground. For this connector, a remote control was developed using a commercially available microcontroller (Arduino Uno), three MCP4725 digital-analog-converters (Adafruit, 12 bit, maximum 5 V output, controlled via I^2C) and three LM358 amplifier modules (LC Technology, working voltage 5 V to 12 V, 10 kΩ adjustable resistor for gain adjustment) for covering a metering region between 0 V to 10 V. The simplified circuit diagram is illustrated in Fig. 5. The remote control was also written in LabVIEW with a design matching that of the user interface shown in Fig. 4.

The readout of the dual gauge (Pfeiffer Vacuum, PT G28 290) is done in a separate LabVIEW VI. Both the pressure in front of the membrane pump as well as the pressure inside the irradiation chamber are monitored. The interlock for both gun systems is provided by the relay of the dual gauge and is not included in the LabVIEW remote control to avoid communication errors.

The camera is controlled by ethernet with a software provided from Basler. The camera can be operated in continous or single shot mode and its software provides several options for image enhancements.

The pumps as well as the valves are all manually driven.

3. Characterization of the available beams

3.1. Electron beams

The beam profiles of the electron beam were investigated with a phosphor screen (GIDS, SCR-25-ITO-P43) monitored by a camera. The green channel of the taken pictures was used for the evaluation of the beam profiles with Gwyddion 2.5. A constant emission current of 10 μA was used for all beam tests. First, the beam spot diameter was investigated for different energies at 500 eV, 1000 eV and 1500 eV against different focus voltages with grid voltage fixed at 0 V. For instance, Fig. 7(c) displays the beam spot shape observed on the phosphor screen at the energy 1500 eV. Due to the size of the phosphor screen, spot diameters above 25 mm are not measurable. The phosphor screen was fixed at the position of a target in the sample holder. The resulting spot diameters are illustrated in Fig. 6. The minimum spot diameter is reached for focus/energy = 0.66. It corresponds to the specification data sheet of the electron gun [18].

Then the influence of the grid voltage on the beam profile was investigated in different measurements for an energy of 1500 eV. At first, the grid voltage was varied between 10 V and 85 V and a focus voltage of 750 V. In a second measurement, the grid voltage was fixed at 83 V and the measurement of the spot diameter was repeated at focus voltages between 650 V and 990 V. The resulting beam profiles

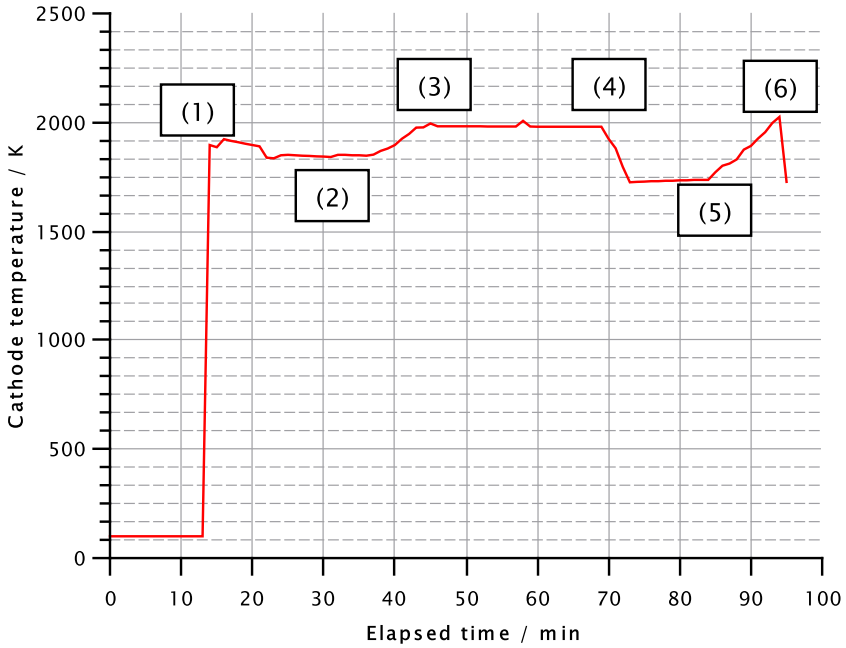

Fig. 8. Cathode temperature of the electron gun during the measurements shown in Fig. 7. At (1), the source voltage is applied slowly to deliver an emission current of 10 μA. The cathode warms up and cathode temperature decreases a bit at (2). Then the grid voltage is slowly increased to 85 V at (3). At (4) grid voltage is turned off again and the cathode temperature decreases again from 2000 K to about 1700 K. At (5), grid voltage is increased to 83 V again and the cathode temperature rises to 2000 K. At (6), the source voltage is turned off.

are illustrated in Fig. 7(a) and (b). Space charge effects are responsible for the donut-shaped profile. Depressions in central intensity are at least partially due to radiation damage at this position on the phosphor screen and are thus unrelated to the true beam profile.

During these measurements, the cathode temperature reaches a maximum of about 2000 K with the Grid voltage turned on and cools down after a warm up and with Grid voltage turned off to about 1700 K. An example graph of the evolution of the cathode temperature during operation of the electron gun is given in Fig. 8.

3.2. Ion beams

The ion gun was characterized in a comparable setup with the same camera system as in ODIn and the same dimensions of the vacuum chamber and working distance. The beam profiles were measured with a CsI phosphor screen (125 mm x 95 mm x 2 mm alumina plate coated with CsI) in a working distance of about 115 mm and the beam currents were measured with a Faraday cup (fabricated at GSI, 6 cm in diameter) on the opposite site of the ion gun in a working distance of about 317 mm.

In general, the beam current was measured against the variation of magnetron current, anode potential and extraction potential. At specific parameters, the phosphor screen was moved in front of the Faraday cup into the ion beam to measure the beam profile. Nitrogen gas was used to operate the ion gun. The gas flow was increased first for enough molecules to ignite the plasma and the chamber pressure was kept fixed at 3×10^{-4} mbar. The Faraday cup was polarized to suppress secondary electrons. For the measurement of the beam current against the magnetron current, the anode potential was adjusted to 3.3 kV and the extraction voltage was adjusted to −0.9 kV. The current on the cup was limited to a maximum of 175 μA. A diagram of the measured current against the magnetron current is illustrated in Fig. 9(a). Beam profiles were taken at magnetron currents of 6 mA, 12 mA and 20 mA as shown in Fig. 9(b). The beam profiles were evaluated in the non-tilted axis after subtraction of the background fluorescence of the phosphor screen.

In another measurement the magnetron current was adjusted to 20 mA and extraction potential was kept at −0.9 kV. The anode potential was varied between 0.1 kV and 4 kV. The current on the cup was limited to a maximum of 163 μA. For a measurement of currents against even higher anode potentials, the extraction potential was increased to −1.1 kV and current on the cup was limited to a maximum of 109 μA. Then the anode potential was varied between 0.2 kV and 5 kV. Beam profiles were taken in the first measurement at 1.5 kV, 3 kV, 3.4 kV and 4 kV and in the second measurement at 1.4 kV, 2.6 kV, 3.6 kV, 4.5 kV and 5 kV. The diagram of the measured current against anode potential for different extraction potentials is given in Fig. 10(a). The corresponding beam profiles are shown in Fig. 10(b) for extraction potential of −0.9 kV and in Fig. 10(c) for extraction potential of −1.1 kV.

In the last measurement the magnetron current was kept at 20 mA and the anode potential was adjusted to 3.7 kV. The extraction potential was varied between 0 kV and 2 kV. The current on the cup was limited to a maximum of 164 μA. Beam profiles were taken at extraction potentials of 0.3 kV, 0.8 kV, 1.1 kV and 1.9 kV. The diagram of the measured current against extraction potential is given in Fig. 11(a). The corresponding beam profiles are shown in Fig. 11(b).

3.3. Discussion on beam parameters

3.3.1. Electron beams

Electron beam spot diameters of 2 mm to 4 mm can be achieved with electrons in an energy range of 500 keV to 1500 keV. A small spot size is ideal to obtain a maximum of deposited energy and flux per unit area and time. The scanning function of the electron gun allows irradiating areas that are larger than the spot diameter. The beam spot size and profile can be altered by varying the grid voltage (see Fig. 7(b) and (c)). In this way, the profile can be smoothed, and the influence of space charge effects can be reduced. For 1500 keV electrons, the ideal grid voltage was found to be 83 V. At voltages above 90 V, the beam is completely suppressed.

3.3.2. Ion beams

The effects of (i) magnetron current, (ii) anode potential, and (iii) extraction potential on ion current and beam profile were studied for nitrogen ions. The beam current varies proportionally to the magnetron

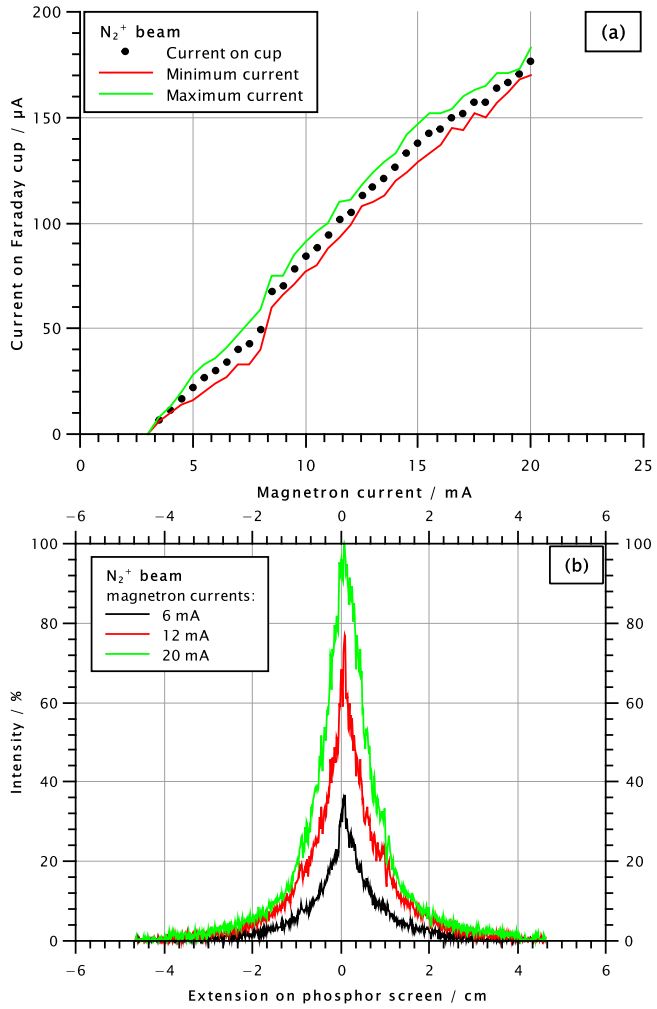

Fig. 9. The measured current on Faraday cup against magnetron current of the ion gun with the anode potential at 3.3 kV and extraction voltage of −0.9 kV is shown in (a). The red and green line represent the lowest and highest measured currents, respectively. The evaluated beam profiles are shown in (b). They are presented as a function of the fluorescence intensity against the extension to the center of the screen. (For interpretation of the references to color in this figure legend, the reader is referred to the web version of this article.)

current (see Fig. 9(a)). The beam current intensity depends on the anode and extraction potentials; the maximum current is obtained at 3.7 kV anode potential and 1 kV extraction potential. The corresponding beam spot diameter is about 1 cm. In contrast to the electron beam, the ion beam cannot be scanned across the target area. Therefore, a variation of the beam spot size is the only option to change the irradiated area. To this end, the potential can be set to lower values than 3.7 kV and 1 kV, which will increase the beam spot size, at the expense of a reduced intensity.

4. First commission and irradiation of samples

4.1. Theoretical stopping powers and ranges of projectiles in matter

With the given electron and ion energies provided by the gun systems in ODIn, the different stopping powers and ranges in matter can be estimated. The software SRIM-2013 [21,22] provides stopping powers and ranges for ions and target materials up to uranium. For stopping powers and ranges of electrons in matter, the National Institute of Standards and Technology (NIST) provides a database [19,20] for many different pure element as well as common target materials like

Table 1
Theoretical total stopping powers of different beams provided by the ODIn setup in three exemplary target materials. The values are given for the maximum beam energies which can be provided at ODIn. Data for electron and proton beams are taken from the NIST database [19,20]. The data for Xe beams were calculated with SRIM-2013 [21,22].

Target material	Total stopping powers for different beams (MeV cm^2 g^{-1})		
	Electron beam (1.5 keV)	H^+ beam (5 keV)	Xe^+ beam (5 keV)
Carbon (amorphous)	80.6	308.6	5773
Lead (metal)	15.6	35.26	978.1
Uranium (metal)	13.7	41.77	830.3

Table 2
Theoretical ranges in matter of different beams provided by the ODIn setup in three exemplary target materials. The values are given for the maximum beam energies which can be provided at ODIn. Data for the electron and proton beams are taken from the NIST database [19,20]. The data for Xe beams were calculated with SRIM-2013 [21,22].

Target material	CSDA (continuous-slowing-down approximation) ranges in matter for different beams (mg cm^{-2})		
	Electron beam (1.5 keV)	H^+ beam (5 keV)	Xe^+ beam (5 keV)
Carbon (amorphous)	<0.28	0.025	0.0016
Lead (metal)	<0.83	0.26	0.0041
Uranium (metal)	<0.89	0.22	0.0044

lead oxide or uranium oxide. Tables 1 and 2 give some total stopping powers and ranges of electron beams, light ion (hydrogen) and heavy ion (xenon) beams, which can be produced at ODIn, in exemplary target materials like amorphous carbon, metallic lead and uranium. The stopping powers and ranges in matter are given for the maximum beam energies which can be produced at ODIn.

The given values indicate that only deposits with a thickness lower than 100 µg/cm^2 can be irradiated completely with the electron and ion beams provided by ODIn. With H^+ beams, the CSDA range is at its maximum with 260 µg/cm^2 for metallic lead and at 220 µg/cm^2 for metallic uranium. Therefore, H^+ beams seem to be most promising with respect to the ranges in matter. For ion beams of heavier gasous species, the stopping powers rise and the ion beams will probably induce more sputtering than transformations on the chemical species and will destroy the deposit. Sputtering could be used to remove organic impurities on the surface of the deposits.

4.2. Irradiation tests of Pb samples

In a first irradiation test performed to commission the setup, molecular plated lead samples were irradiated with electron beams at 1.5 keV and 100 µA emission current. This section is meant to give a short report of the first irradiation with ODIn. Further analytical investigations of the sample will be described elsewhere.

4.2.1. Reagents and materials

145.7 mg of lead nitrate (Sigma-Aldrich, ≥99.0%) were dissolved in 10 mL of 0.1 M nitric acid, to give a concentration of 44 mmol/L. An aliquot of 20 µL was filled into the plating cell and was mixed with 1 mL of isopropanole and 9 mL of isobutanole. A round Kapton foil (Goodfellow, Polyimid - Film DuPont™ Kapton®, 25 µm thickness) with a diameter of 25 mm was cleaned with isopropanole, dried at air and then sputter coated with about 34 nm of gold on both sides. It was used as cathode. A palladium wire (Goodfellow, 99.99+%, 1 mm thickness) was used as anode.

4.2.2. Instrumentation and methods

Molecular Plating was performed in an upright cylindrical cell with 1.15 kV and 0.6 mA for 45 min. The contact area on the substrate (Kapton foil with gold coating) was 0.5 cm^2. After the plating process,

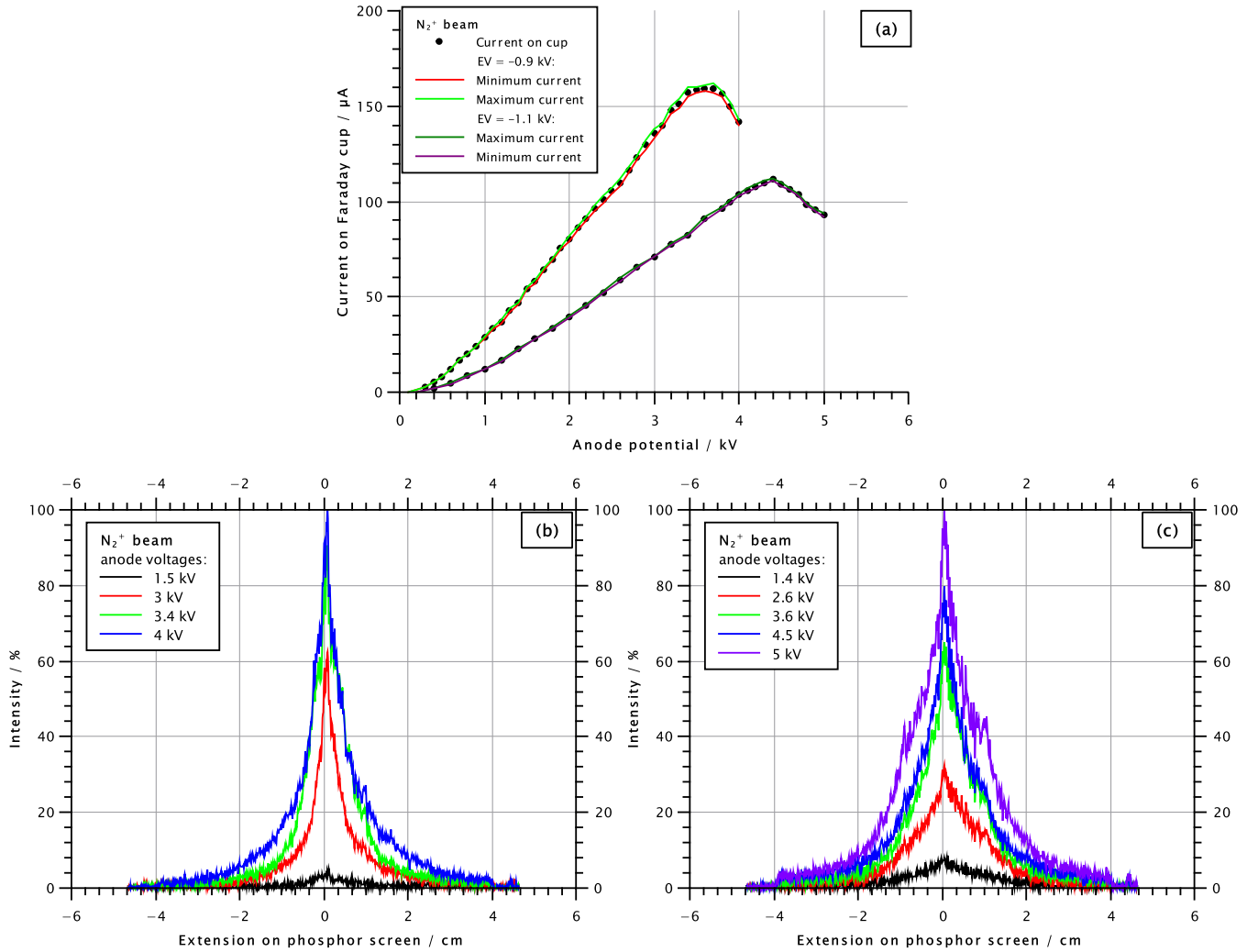

Fig. 10. (a) Measured current on Faraday cup against anode voltage of the ion gun is shown for a magnetron current of 20 mA and extraction voltages (EV) of −0.9 kV and −1.1 kV. The lines represent the lowest and highest measured currents, respectively. The evaluated beam profiles as a function of the fluorescence intensity against the extension to the center of the screen are shown for extraction voltages of −0.9 kV in (b) and −1.1 kV in (c).

the sample was dried at air in the fume hood for 24 h. Two identical samples were prepared by this method to have one sample for comparison after irradiation of the other one. In case of a 100% yield in the molecular plating process, the deposit thickness is about 365 µg/cm^2 which is about 59.4 µm.

The sample was carefully fixed on the sample holder in ODIn with conductive tape. It was irradiated with 1.5 keV electron beam and emission current of 100 µA with focus on the surface of the deposit. The focus voltage was at 990 V and grid voltage at 0 V. The spot diameter was about 3 mm. Due to a voltage on the deflection electrodes during scanning and the angle of 45° on the sample surface, the beam spot shape was slightly deformed to a triangle. After a short moment, the surface turned dark at the spot where the focused beam impacted. The beam was then scanned slowly over the complete deposit surface until it turned completely dark by visual observation. The whole irradiation with an irradiance or flux density of about 2.1 W/cm^2 took about an hour with an approximated deposited energy of 4.74×10^{16} MeV/cm^2. For electron gun power $\dot{Q}$ of 0.15 W, a thermal conductivity λ of the Kapton foil of 0.4 W/(m K), a beam spot radius r of 1.5 mm and the thickness of the Kapton foil d of 25 µm, the difference of temperature ΔT between the irradiated deposit and the sample holder can be calculated with Fourier's law

$$\dot{Q} = \lambda \cdot \pi \cdot r^2 \cdot \frac{\Delta T}{d}$$

and is about 1.3 K considering thermal conduction.

126

4.2.3. Results and discussion

Both the non-irradiated and the irradiated sample were investigated with a light microscope (VHX-7000, Keyence). The surface of the irradiated deposit turned black during the irradiation with the 1.5 keV electron beam. The range of the electron beam into the deposit should be about 14 µm with respect to a stopping power of 17.43 MeV cm^2/g (in lead oxide) [19]. Therefore, the beam was completely stopped in the deposit. The change in color indicates that a chemical or a crystal transformation occurred. The induced structural changes were investigated by confocal Raman spectroscopy (HR800 system, Horbia Jobin Yvon, λ_0 : 633 nm). The spectrometer was calibrated with a silicon sample. The microscopic pictures with three magnifications and the Raman spectra of both samples are shown in Fig. 12. The spectra indicate a chemical transformation from lead carbonate [23] to lead(II) oxide [24]. The observed changes in color agree well with coulomb barrier irradiations of similar produced lead targets at UNILAC. A detailed follow-up spectroscopic investigation and comparison of lead targets irradiated off-line at ODIn and on-line at UNILAC is on its way. The investigation will show if it is possible to investigate the radiation-induced chemical reactions in target materials even without beam time at particle accelerators.

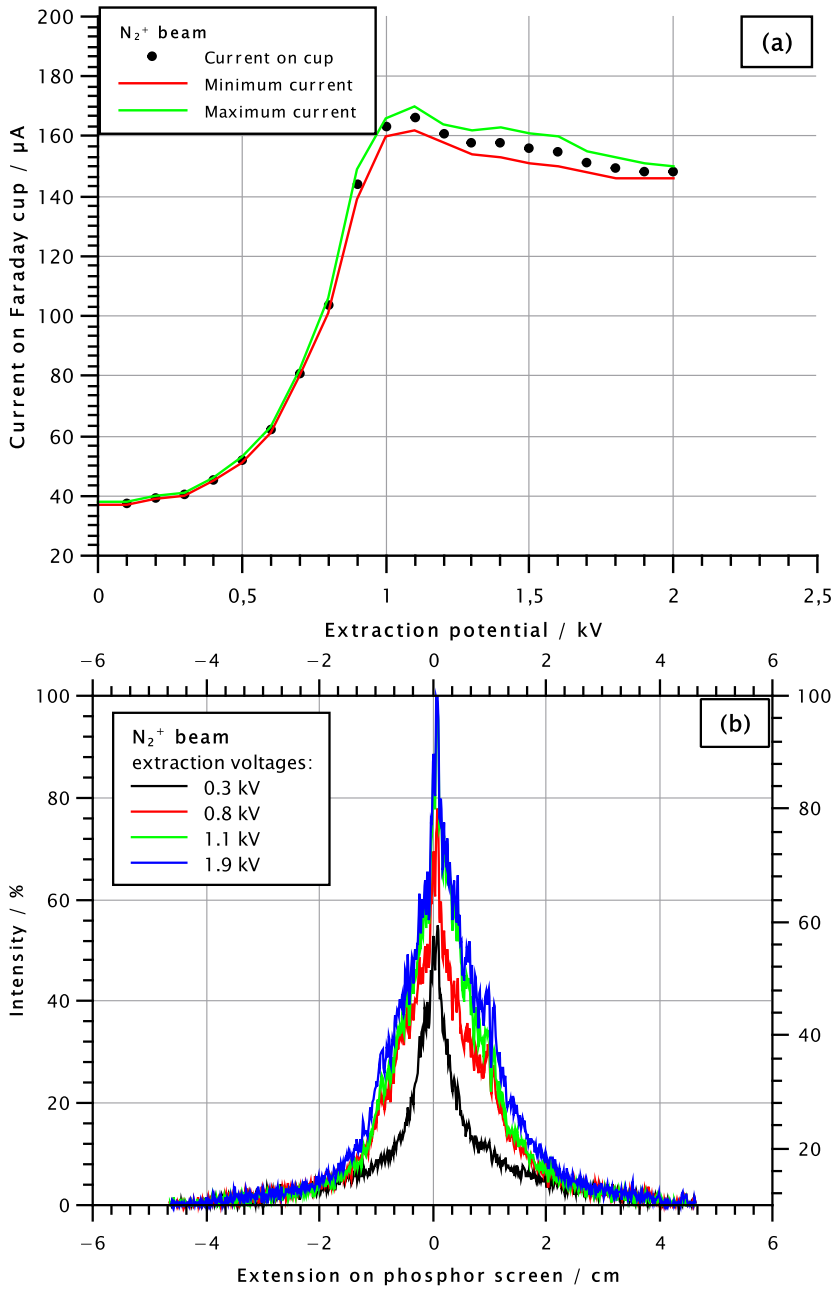

Fig. 11. (a) Measured current on Faraday cup against extraction voltage of the ion gun is shown for a magnetron current of 20 mA and anode potential of 3.7 kV. The lines represent the lowest and highest measured currents, respectively. The evaluated beam profiles as a function of the fluorescence intensity against the extension to the center of the screen are shown for an anode potential of 3.7 kV in (b).

5. Conclusion and outlook

A new setup, named ODIn, was successfully constructed for the irradiation of samples with low energy electron and ion beams, characterized with regard to the electron gun and ion gun and tested for the first time with a molecular plated lead sample. The electron gun can generate up to 1.5 keV electron beams with up to 100 µA beam current. The spot diameters of the electron beam and beam profiles of the electron gun were investigated with a phosphor screen. Minimum spot diameters of 2 mm to 4 mm in diameter can be produced depending on the electron energy. The beam profile can be adjusted with the grid voltage from a nearly uniform to a Gaussian profile. Furthermore, the ion gun was characterized and the dependency of the beam current on different magnetron currents, anode voltages and extraction voltages was investigated. Also the beam profiles were investigated with a phosphor screen and they are more lorentzian shaped with a FWHM of about 2 mm to 3 mm. The complete setup can be controlled by remote with a delivered LabVIEW software for the electron gun and an Arduino-based remote control for the ion gun. The first irradiation of a lead sample with 1.5 keV electron beams showed a visible change on the deposit surface indicated by a change of color from orange to black. Raman analysis showed a chemical transformation of lead carbonate to lead(II) oxide. In future experiments, the irradiated samples of ODIn will be compared with samples irradiated with Coulomb-barrier heavy-ion beams at the UNILAC accelerator at GSI in Darmstadt and with samples irradiated with proton beams of tens of MeV energy at the IGISOL facility in Jyväskylä. Investigations of the chemical and crystal transformations on the surface of irradiated samples are currently ongoing, using analytical methods like Raman spectroscopy, scanning electron microscopy (SEM) as well as atomic force microscopy (AFM).

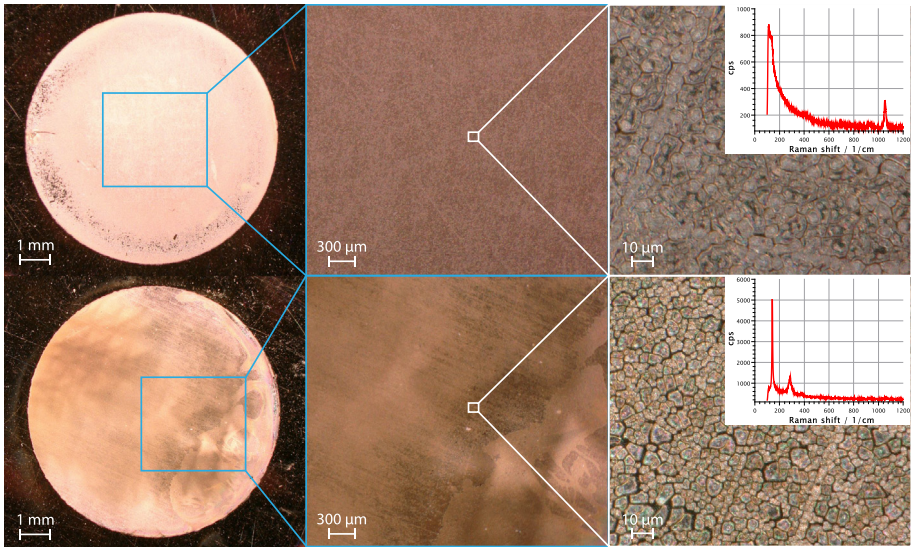

Fig. 12. Optical microscope pictures of the non-irradiated lead sample (top) and of the electron-irradiated sample (bottom). The inset in the right-most pictures displays Raman spectra of the samples. These were recorded with a 633 nm excitation wavelength at 16 mW, using spectral autofocus. The change in the spectra indicates a chemical transformation of lead carbonate [23] to lead(II) oxide [24]. (For interpretation of the references to color in this figure legend, the reader is referred to the web version of this article.)

These studies will help shedding light on the processes taking place in thin films irradiated with low energy particles. New insights into the chemical behavior of conventional target materials in the particle beam could be an important intermediate step in the development of new targets for the future generation of accelerators.

Declaration of competing interest

The authors declare that they have no known competing financial interests or personal relationships that could have appeared to influence the work reported in this paper.

CRediT authorship contribution statement

R. Haas: Conceptualization, Software, Investigation, Data curation, Writing - original draft, Writing - review & editing, Visualization, Project administration. **C.-C. Meyer:** Validation, Investigation, Writing - review & editing, Visualization. **S. Böhland:** Investigation. **Ch. E. Düllmann:** Conception and supervision of the Project. **J. Mäder:** Investigation, Resources. **K. Tinschert:** Investigation, Resources.

Acknowledgments

The authors acknowledge the support of the staff of the target laboratory at GSI in Darmstadt for investigations of our samples with their optical microscope. The authors acknowledge the help of C. Trautmann, M. Tomut, A. Prosvetov and P. Simon for their assistance with the Raman measurements. We also acknowledge the local support of the mechanical workshop at the Institute of Nuclear Chemistry and the financial support from the Helmholtz Institute Mainz, Germany.

References

[1] W. Parker, R. Falk, Nucl. Instrum. Methods 16 (1962) 355–357.
[2] N. Trautmann, H. Folger, Nucl. Instrum. Methods Phys. Res. A 282 (1989) 102–106.
[3] L. von der Wense, B. Seiferle, M. Laatiaoui, J.B. Neumayr, H.-J. Maier, H.-F. Wirth, C. Mokry, J. Runke, K. Eberhardt, Ch.E. Düllmann, N.G. Trautmann, P.G. Thirolf, Nature 533 (2016) 47–51.
[4] A. Vascon, S. Santi, A. Isse, T. Reich, J. Drebert, H. Christ, Ch.E. Düllmann, K. Eberhardt, Nucl. Instrum. Methods Phys. Res. A 696 (2012) 180–191.
[5] A. Vascon, S. Santi, A. Isse, A. Kühnle, T. Reich, J. Drebert, K. Eberhardt, Ch.E. Düllmann, Nucl. Instrum. Methods Phys. Res. A 714 (2013) 163–175.
[6] A. Vascon, N. Wiehl, T. Reich, J. Drebert, K. Eberhardt, Ch.E. Düllmann, Nucl. Instrum. Methods Phys. Res. A 721 (2013) 35–44.
[7] A. Mitu, M. Dumitru, R. Suvăilă, A. Oprea, I. Gheorghe, P. Mereută, S. Brajnicov, I. Burducea, N.M. Florea, N. Mărginean, T. Glodariu, M. Dinescu, G.C.–. Danil, Vacuum 161 (2019) 162–167.
[8] M.A. Garcia, M.N. Ali, N.N. Chang, T. Parsons-Moss, P.D. Ashby, J.M. Gates, L. Stavsetra, K.E. Gregorich, H. Nitsche, Nucl. Instrum. Methods Phys. Res. A 613 (2010) 396–400.
[9] R. Haas, S. Lohse, Ch.E. Düllmann, K. Eberhardt, C. Mokry, J. Runke, Nucl. Instrum. Methods Phys. Res. A 874 (2017) 43–49.
[10] M. Weigand, T. Heftrich, Ch.E. Düllmann, K. Eberhardt, S. Fiebiger, J. Glorius, K. Göbel, R. Haas, C. Langer, S. Lohse, Phys. Rev. C 97 (2018) 035803.
[11] K. Eberhardt, Ch.E. Düllmann, R. Haas, C. Mokry, J. Runke, P. Thörle-Pospiech, N. Trautmann, AIP Conf. Proc. 1962 (2018) 030009.
[12] P.R. Watson, W. Loveland, P.M. Zielinski, K.E. Gregorich, H. Nitsche, Nucl. Instrum. Methods Phys. Res. B 226 (2004) 543–548.
[13] S. Hofmann, S. Heinz, R. Mann, J. Maurer, J. Khuyagbaatar, D. Ackermann, S. Antalic, W. Barth, M. Block, H. Burkhard, Eur. Phys. J. A 48 (2012) 62.
[14] J.D. Burns, K.G. Myhre, N.J. Sims, D.W. Stracener, R.A. Boll, Nucl. Instrum. Methods Phys. Res. A 830 (2016) 95–101.
[15] D. Mayorov, E. Tereshatov, T. Werke, M. Frey, C. Folden, Nucl. Instrum. Methods Phys. Res. B 407 (2017) 256–264.
[16] C.L. Tracy, M. Lang, F. Zhang, C. Trautmann, R.C. Ewing, Phys. Rev. B 92 (2015) 174101.
[17] L. Breuer, P. Ernst, M. Herder, F. Meinerzhagen, M. Bender, D. Severin, A. Wucher, Nucl. Instrum. Methods Phys. Res. B 435 (2018) 101–110.
[18] Kimball Physics Inc., EFG-7 / EGPS-1017 datasheet, 2016, https://www.kimballphysics.com/electron-gun-specs-efg-7-egps-1017 [Online; accessed 25-October-2019].
[19] M.J. Berger, J.S. Coursey, M.A. Zucker, J. Chang, Stopping-power & range tables for electrons, 2017, https://physics.nist.gov/PhysRefData/Star/Text/ESTAR.html [Online; accessed 25-October-2019].
[20] M.J. Berger, J.S. Coursey, M.A. Zucker, J. Chang, Stopping-power & range tables for protons, 2017, https://physics.nist.gov/PhysRefData/Star/Text/PSTAR.html [Online; accessed 25-October-2019].
[21] J.F. Ziegler, M. Ziegler, J. Biersack, Nucl. Instrum. Methods Phys. Res. B 268 (2010) 1818–1823.
[22] J.F. Ziegler, SRIM - The stopping and range of ions in matter, 2013, https://www.srim.org/ [Online; accessed 25-October-2019].
[23] L. Burgio, R.J.H. Clark, Spectrochim. Acta Part A 57 (2001) 1491–1521.
[24] L. Burgio, R.J.H. Clark, S. Firth, Analyst 126 (2001) 222–227.

B. Bibliography

[1] W. Aaron, M. Petek, L. Zevenbergen, and J. Gibson. Development and preparation of thin, supported targets and stripper foils. *Nucl. Instrum. Methods Phys. Res. A*, 282(1):147–152, 1989.

[2] F. A. Andersen, L. Brecevic, et al. Infrared spectra of amorphous and crystalline calcium carbonate. *Acta Chem. Scand*, 45(10):1018–1024, 1991.

[3] S. Antalic, P. Cagarda, D. Ackermann, H.-G. Burkhard, F.-P. Heßberger, S. Hofmann, B. Kindler, J. Kojouharova, B. Lommel, R. Mann, et al. Target cooling for high-current experiments at SHIP. *Nucl. Instrum. Methods. Phys. Res. A*, 530(3):185–193, 2004.

[4] C. Apostolidis, B. Schimmelpfennig, N. Magnani, P. Lindqvist-Reis, O. Walter, R. Sykora, A. Morgenstern, E. Colineau, R. Caciuffo, R. Klenze, et al. $[An(H_2O)_9](CF_3SO_3)_3$ (An = U-Cm, Cf): Exploring Their Stability, Structural Chemistry, and Magnetic Behavior by Experiment and Theory. *Angew. Chem. Int. Ed.*, 49(36):6343, 2010.

[5] E. Artes. Herstellung von f-Element Targets mit hohen Flächengewichten. Master's thesis, Johannes Gutenberg University Mainz, Germany, 2020.

[6] E. Artes, Ch. E. Düllmann, C.-C. Meyer, and D. Renisch. The process of molecular plating and the characteristics of the produced thin films–what we have learned in 60 years and what is still unknown. In *EPJ Web of Conferences*, volume 285, page 03001. EDP Sciences, 2023.

[7] D. R. Baer, K. Artyushkova, H. Cohen, C. D. Easton, M. Engelhard, T. R. Gengenbach, G. Greczynski, P. Mack, D. J. Morgan, and A. Roberts. XPS guide: Charge neutralization and binding energy referencing for insulating samples. *J. Vac. Sci. Technol. A*, 38(3):031204, 2020.

[8] N. Barradas, C. Jeynes, and R. Webb. Simulated annealing analysis of Rutherford backscattering data. *Applied Physics Letters*, 71(2):291–293, 1997.

[9] W. Barth, K. Aulenbacher, M. Basten, M. Busch, F. Dziuba, V. Gettmann, M. Heilmann, T. Kürzeder, M. Miski-Oglu, H. Podlech, et al. First heavy ion beam tests with a superconducting multigap CH cavity. *Phys. Rev. Accel. Beams*, 21:020102, 2018.

[10] A. Beesley, M. Crespo, N. Weiher, N. Tsapatsaris, J. Cózar, H. Esparza, C. Méndez, P. Hill, S. Schroeder, and M. Montero-Cabrera. Evolution of chemical species during electrodeposition

of uranium for alpha spectrometry by the Hallstadius method. *Appl. Radiat. Isot.*, 67:1559–1569, 2009.

[11] S. Belaya, V. Bakovets, A. Boronin, S. Koshcheev, M. Lobzareva, I. Korolkov, and P. Stabnikov. Terbium oxide films grown by chemical vapor deposition from terbium (III) dipivaloylmethanate. *Inorg. Mater.*, 50(4):379–386, 2014.

[12] L. Benedik, G. Sibbens, A. Moens, R. Eykens, M. Nečemer, S. Škapin, and P. Kump. Preparation of thick uranium layers on aluminium and stainless steel backings. *Appl. Radiat. Isot.*, 87:238–241, 2014.

[13] S. Bernal, G. Blanco, J. Gatica, J. Pérez-Omil, J. Pintado, and H. Vidal. Chemical reactivity of binary rare earth oxides. In *Binary rare earth oxides*, pages 9–55. Springer, 2004.

[14] J. C. Berthet, M. Lance, M. Nierlich, and M. Ephritikhine. Simple Preparations of the Anhydrous and Solvent-Free Uranyl and Cerium (IV) Triflates $UO_2(OTf)_2$ and $Ce(OTf)_4$- Crystal Structures of $UO_2(OTf)_2(py)_3$ and $[\{UO_2\ (py)_4\}_2\ (\mu\text{-}O)][OTf]_2$. *Eur. J. Inorg. Chem.*, 2000(9):1969, 2000.

[15] H. A. Bethe and R. F. Bacher. Nuclear physics A. Stationary states of nuclei. *Rev. Mod. Phys.*, 8(2):82, 1936.

[16] K. Binnemans. Lanthanides and actinides in ionic liquids. *Chem. Rev.*, 107(6):2592–2614, 2007.

[17] M. Block, F. Giacoppo, F.-P. Heßberger, and S. Raeder. Recent progress in experiments on the heaviest nuclides at SHIP. *Riv. del Nuovo Cim.*, pages 1–45, 2022.

[18] R. Bolotovsky, A. Bulkin, G. Krutov, V. Kudryashev, V. Trunov, V. Ul'yanov, O. Antson, P. Hiismäki, H. Pöyry, A. Tiitta, et al. Neutron diffraction study of the crystal structure of rare-earth and yttrium anhydrous deuterated formates. *Solid State Commun.*, 76(8):1045–1049, 1990.

[19] E. M. Bond, W. A. Moody, and T. A. Bredeweg. Production of double-sided targets by electrodeposition: initial evaluation and optimization of performance. *J. Radioanal. Nucl. Chem.*, 296(2):847–851, 2013.

[20] N. Brewer, V. Utyonkov, K. Rykaczewski, Y. T. Oganessian, F. S. Abdullin, R. Boll, D. Dean, S. Dmitriev, J. Ezold, L. Felker, et al. Search for the heaviest atomic nuclei among the products from reactions of mixed-Cf with a ^{48}Ca beam. *Phys. Rev. C: Nucl. Phys.*, 98(2):024317, 2018.

[21] M. H. Brooker, S. Sunder, P. Taylor, and V. J. Lopata. Infrared and Raman spectra and X-ray diffraction studies of solid lead (II) carbonates. *Can. J. Chem.*, 61:494–502, 1983.

[22] P. Bumroongsakulsawat and G. Kelsall. Effect of solution ph on co: formate formation rates during electrochemical reduction of aqueous co2 at sn cathodes. *Electrochimica Acta*, 141:216–225, 2014.

[23] L. Burgio and R. J. Clark. Library of FT-Raman spectra of pigments, minerals, pigment media and varnishes, and supplement to existing library of Raman spectra of pigments with visible excitation. *Spectrochim. Acta, Part A*, 57:1491–1521, 2001.

[24] L. Burgio, R. J. Clark, and S. Firth. Raman spectroscopy as a means for the identification of plattnerite (PbO_2), of lead pigments and of their degradation products. *Analyst*, 126:222–227, 2001.

[25] J. Burns, K. Myhre, N. Sims, D. Stracener, and R. Boll. Effects of annealing temperature on morphology and thickness of samarium electrodeposited thin films. *Nucl. Instrum. Methods Phys. Res., Sect. A*, 830:95–101, 2016.

[26] P. Caro, J. Sawyer, and L. Evning. The infrared spectra of rare earth carbonates. *Spectrochim. Acta A Mol. Biomol. Spectrosc.*, 28(6):1167–1173, 1972.

[27] J. Cazaux. Mechanisms of charging in electron spectroscopy. *J. Electron Spectrosc. Relat. Phenom.*, 105(2-3):155–185, 1999.

[28] J. Choi and Y. H. Chung. Preparation of lanthanum oxide and lanthanum oxycarbonate layers on titanium by electrodeposition with organic solution. *J. Nanomater.*, 2016, 2016.

[29] J. Choi and Y. H. Chung. Preparation of Lanthanum and Cerium Targets for Nuclear Reactions. In *6^{th} Asia-Pacific Symposium on Radiochemistry*, pages 1–2. Korea Atomic Energy Research Institute (KAERI), 2017.

[30] D. A. Ciomartan, R. J. H. Clark, L. J. McDonald, and M. Odlyha. Studies on the thermal decomposition of basic lead (II) carbonate by Fourier-transform Raman spectroscopy, X-ray diffraction and thermal analysis. *J. Chem. Soc., Dalton Trans.*, pages 3639–3645, 1996.

[31] S. Cotton. *Lanthanide and actinide chemistry*. John Wiley & Sons, Ltd, 2013.

[32] D. Cox, A. Såmark-Roth, D. Rudolph, L. Sarmiento, C. Fahlander, U. Forsberg, P. Golubev, J. Heery, A. Yakushev, H. Albers, et al. Spectroscopic tools applied to flerovium decay chains. In *J. Phys. Conf. Ser.*, volume 1643, page 012125. IOP Publishing, 2020.

[33] D. M. Cox, A. Såmark-Roth, D. Rudolph, L. G. Sarmiento, R. M. Clark, J. L. Egido, P. Golubev, J. Heery, A. Yakushev, S. Åberg, H. M. Albers, M. Albertsson, M. Block, H. Brand, T. Calverley, R. Cantemir, B. G. Carlsson, Ch. E. Düllmann, J. Eberth, C. Fahlander, U. Forsberg, J. M.

Gates, F. Giacoppo, M. Götz, S. Götz, R.-D. Herzberg, Y. Hrabar, E. Jäger, D. Judson, J. Khuyagbaatar, B. Kindler, I. Kojouharov, J. V. Kratz, J. Krier, N. Kurz, L. Lens, J. Ljungberg, B. Lommel, J. Louko, C.-C. Meyer, A. Mistry, C. Mokry, P. Papadakis, E. Parr, J. L. Pore, I. Ragnarsson, J. Runke, M. Schädel, H. Schaffner, B. Schausten, D. A. Shaughnessy, P. Thörle-Pospiech, N. Trautmann, and J. Uusitalo. Spectroscopy along flerovium decay chains. II. Fine structure in odd-*A* ^{289}Fl. *Phys. Rev. C: Nucl. Phys.*, 107:L021301, Feb 2023.

[34] M. Crespo. A review of electrodeposition methods for the preparation of alpha-radiation sources. *Appl. Radiat. Isot.*, 70(1):210–215, 2012.

[35] S. Dmitriev, M. Itkis, and Y. Ts. Oganessian. Status and perspectives of the Dubna superheavy element factory. In *EPJ Web of Conferences*, volume 131, page 08001. EDP Sciences, 2016.

[36] S. Dmitriev and A. Popeko. High-power radioactive targets as one of the key problems in further development of the research program on synthesis of new superheavy elements. *J. Radioanal. Nucl. Chem.*, 305:927–933, 2015.

[37] Ch. E. Düllmann. Radioelements: Transactinides. In *Nuclear-and Radiochemistry - Volume 2: Modern Applications*, pages 293–330. de Gruyter, 2016.

[38] Ch. E. Düllmann, E. Artes, A. Dragoun, R. Haas, E. Jäger, B. Kindler, K.-M. Mangold, C.-C. Meyer, et al. Advancements in the fabrication and characterization of actinide targets for superheavy element production. *J. Radioanal. Nucl. Chem.*, 332(5):1505–1514, 2022.

[39] Ch. E. Düllmann, M. Block, F. P. Heßberger, J. Khuyagbaatar, B. Kindler, J. V. Kratz, B. Lommel, G. Münzenberg, V. Pershina, D. Renisch, et al. Five decades of gsi superheavy element discoveries and chemical investigation. *Radiochim. Acta*, 110(6-9):417–439, 2022.

[40] Ch. E. Düllmann, M. Schädel, A. Yakushev, A. Türler, K. Eberhardt, J. Kratz, D. Ackermann, L.-L. Andersson, M. Block, W. Brüchle, et al. Production and Decay of Element 114: High Cross Sections and the New Nucleus ^{277}Hs . *Phys. Rev. Lett.*, 104(25):252701, 2010.

[41] C. D. Easton, C. Kinnear, S. L. McArthur, and T. R. Gengenbach. Practical guides for x-ray photoelectron spectroscopy: Analysis of polymers. *J. Vac. Sci. Technol. A*, 38(2):023207, 2020.

[42] K. Eberhardt, W. Brüchle, Ch. E. Düllmann, K. Gregorich, W. Hartmann, A. Hübner, E. Jäger, B. Kindler, J. Kratz, D. Liebe, et al. Preparation of targets for the gas-filled recoil separator TASCA by electrochemical deposition and design of the TASCA target wheel assembly. *Nucl. Instrum. Methods Phys. Res., Sect. A*, 590:134–140, 2008.

[43] K. Eberhardt, Ch. E. Düllmann, R. Haas, C. Mokry, J. Runke, P. Thörle-Pospiech, and N. Trautmann. Actinide targets for fundamental research in nuclear physics. In *AIP Conference Proceedings*, volume 1962, page 030009. AIP Publishing LLC, 2018.

[44] K. Eberhardt and C. Geppert. The research reactor triga mainz–a strong and versatile neutron source for science and education. *Radiochim. Acta*, 107(7):535–546, 2019.

[45] K. Eberhardt, M. Schädel, E. Schimpf, P. Thörle, and N. Trautmann. Preparation of targets by electrodeposition for heavy element studies. *Nucl. Instrum. Methods Phys. Res. A*, 521(1):208–213, 2004.

[46] K. Eberhardt, P. Thörle, A. Nähler, and N. Trautmann. Preparation of actinide targets by electrodeposition for heavy-ion studies and laserspectroscopic investigations. In *AIP Conference Proceedings*, volume 576, pages 1144–1147. American Institute of Physics, 2001.

[47] H. G. Edwards, P. Vandenabeele, J. Jehlicka, and T. J. Benoy. An analytical Raman spectroscopic study of an important English oil painting of the 18th Century. *Spectrochim. Acta, Part A*, 118:598–602, 2014.

[48] N. Fairley. Casaxps vamas processing software. *http://www. casaxps. com*, 2010.

[49] A. C. Ferrari and J. Robertson. Interpretation of Raman spectra of disordered and amorphous carbon. *Phys. Rev. B*, 61(20):14095, 2000.

[50] M. G. Ferrier, E. R. Batista, J. M. Berg, E. R. Birnbaum, J. N. Cross, J. W. Engle, H. S. La Pierre, S. A. Kozimor, J. S. L. Pacheco, B. W. Stein, et al. Spectroscopic and computational investigation of actinium coordination chemistry. *Nat. Commun*, 7(1):1, 2016.

[51] J. FitzPatrick, E. Bond, A. Slemmons, and D. Vieira. Preparation of americium targets for nuclear chemistry experiments at dance. *J. Radioanal. Nucl. Chem.*, 276(2):561–566, 2008.

[52] H. Folger, W. Hartmann, F. Heßberger, S. Hofmann, J. Klemm, G. Münzenberg, V. Ninov, W. Thalheimer, and P. Armbruster. Developments of ^{170}Er, ^{204,206,207,208}Pb and ^{209}Bi target wheels for reaction studies and synthesis of heaviest elements. *Nucl. Instrum. Methods. Phys. Res. A*, 362(1):64–69, 1995.

[53] R. L. Frost, W. Martens, J. T. Kloprogge, and Z. Ding. Raman spectroscopy of selected lead minerals of environmental significance. *Spectrochim. Acta, Part A*, 59:2705–2711, 2003.

[54] H. Gäggeler, D. Jost, A. Türler, P. Armbruster, W. Brüchle, H. Folger, F. Heßberger, S. Hofmann, G. Münzenberg, V. Ninov, et al. Cold fusion reactions with 48Ca. *Nucl. Phys. A*, 502:561–570, 1989.

[55] M. A. Garcia, M. N. Ali, N. N. Chang, T. Parsons-Moss, P. D. Ashby, J. M. Gates, L. Stavsetra, K. E. Gregorich, and H. Nitsche. Metal oxide targets produced by the polymer-assisted deposition method. *Nucl. Instrum. Methods Phys. Res., Sect. A*, 613:396–400, 2010.

[56] M. A. Garcia, M. N. Ali, T. Parsons-Moss, P. D. Ashby, and H. Nitsche. Metal oxide films produced by polymer-assisted deposition (PAD) for nuclear science applications. *Thin Solid Films*, 516:6261–6265, 2008.

[57] Geffcken, Gustav. Beiträge zur kenntnis der löslichkeitsbeeinflussung. *Z. Phys. Chem.*, 49(1):257–302, 1904.

[58] K. Glover. Target preparation past and present in the united kingdom. *Nuclear Instruments and Methods in Physics Research Section A: Accelerators, Spectrometers, Detectors and Associated Equipment*, 236(3):435–446, 1985.

[59] K. Glover, F. Rogers, and T. Tuplin. Techniques used at harwell in the preparation of stable and active nuclide targets. *Nuclear Instruments and Methods*, 102(3):443–450, 1972.

[60] L. Glukhov, A. Greish, and L. Kustov. Electrodeposition of rare earth metals Y, Gd, Yb in ionic liquids. *Russ. J. Phys. Chem. A*, 84(1):104, 2010.

[61] G. Greczynski and L. Hultman. The same chemical state of carbon gives rise to two peaks in X-ray photoelectron spectroscopy. *Sci. Rep.*, 11(1):1–5, 2021.

[62] J. P. Greene, A. Heinz, J. Falout, and R. V. Janssens. Rotating target wheel system for super-heavy element production at atlas. *Nucl. Instrum. Methods. Phys. Res. A*, 521(1):214–221, 2004.

[63] J. P. Greene, R. V. Janssens, and I. Ahmad. Preparation of actinide targets by molecular plating for coulomb excitation studies at ATLAS. *Nucl. Instrum. Methods. Phys. Res. A*, 438(1):119–123, 1999.

[64] J.-C. Grivel. Thermal decomposition of $Ln(C_2H_5CO_2)$ $3\cdot$ H_2O (Ln= Ho, Er, Tm and Yb). *J. Therm. Anal. Calorim.*, 109(1):81–88, 2012.

[65] G. Gulbekian, S. Dmitriev, M. Itkis, Yu. Ts. Oganessyan, B. Gikal, I. Kalagin, V. Semin, S. Bogomolov, V. Buzmakov, I. Ivanenko, et al. Start-Up of the DC-280 Cyclotron, the Basic Facility of the Factory of Superheavy Elements of the Laboratory of Nuclear Reactions at the Joint Institute for Nuclear Research. *Phys. Part. Nucl. Lett.*, 16(6):866, 2019.

[66] A. Gurbich. SigmaCalc recent development and present status of the evaluated cross-sections for IBA. *Nucl. Instrum. Methods Phys. Res. B*, 371:27–32, 2016.

[67] R. Haas. *Tailor-made thin radionuclide layers for targets and recoil ion sources in nuclear applications*. PhD thesis, Johannes Gutenberg-Universität Mainz, Germany, 2020.

[68] R. Haas, M. Hufnagel, R. Abrosimov, Ch. E. Düllmann, D. Krupp, C. Mokry, D. Renisch, J. Runke, and U. W. Scherer. Alpha spectrometric characterization of thin ^{233}U sources for $^{229(m)}$Th production. *Radiochim. Acta*, 108(12):923–941, 2020.

[69] R. Haas, M. Hufnagel, R. Abrosimov, Ch. E. Düllmann, D. Krupp, C. Mokry, D. Renisch, J. Runke, and U. W. Scherer. Towards ^{233}U recoil ion sources providing ^{229}Th ions with minimum energy spread. *Radiochim. Acta*, 108(12):923 – 941, 2020.

[70] R. Haas, S. Lohse, Ch. E. Düllmann, K. Eberhardt, C. Mokry, and J. Runke. Development and characterization of a Drop-on-Demand inkjet printing system for nuclear target fabrication. *Nucl. Instrum. Methods Phys. Res., Sect. A*, 874:43–49, 2017.

[71] R. Haas, C.-C. Meyer, S. Böhland, Ch. E. Düllmann, J. Mäder, and K. Tinschert. ODIn - A setup for Off-line Deposit Irradiations of thin layers for nuclear physics applications. *Nucl. Instrum. Methods Phys. Res., Sect. A*, 957:163366, 2020.

[72] H. Haba. A new period in superheavy-element hunting. *Nat. Chem.*, 11:10–13, 2019.

[73] R. A. Haefer. *Oberflächen-und Dünnschicht-Technologie: Teil I: Beschichtungen von Oberflächen*, volume 5. Springer-Verlag, 2013.

[74] M. E. M. Hamidi and J.-L. Pascal. Synthesis and structural characterization of some anhydrous $Ln(OTf)_3$ complexes (Ln = Sc, La, Nd, Sm, Gd and Er; OTf = CF_3SO_3). *Polyhedron*, 13(11):1787, 1994.

[75] M. Hämmer and H. A. Höppe. Crystalline orthorhombic Ln $[CO_3][OH]$(Ln= La, Pr, Nd, Sm, Eu, Gd) compounds hydrothermally synthesised with CO_2 from air as carbonate source. *Z. Naturforsch. B*, 74(1):59–70, 2019.

[76] P. G. Hansen. The conditions for electrodeposition of insoluble hydroxides at a cathode surface: a theoretical investigation. *J. Inorg. Nucl. Chem.*, 12:30–37, 1959.

[77] Y. He, L. Han, C. Wang, Q. Chen, M. M. Sartin, G. Li, R. Hu, J. Tu, X. Xie, Y. Yang, et al. Molecular plating of actinide compounds on wafer-scale aluminum substrate. *J. Alloys Compd.*, 878:160393, 2021.

[78] G. Herrmann. Historical reminiscences: the pioneering years of superheavy element research. In *The chemistry of superheavy elements*, pages 485–511. Springer, 2014.

[79] G. Herzberg. *Molecular spectra and molecular structure*. D. van Nostrand, 1945.

[80] R.-D. Herzberg. Nuclear structure of superheavy elements. In *The chemistry of superheavy elements*, pages 83–133. Springer, 2014.

[81] J. Hodkiewicz. Characterizing graphene with raman spectroscopy. *Thermo Fisher Scientific*, page 51946, 2010.

[82] J. Hoffmann. Änderungen der Bleioxyde durch Licht und Druck. *Z. Anorg. Allg. Chem.*, 228:160–168, 1936.

[83] S. Hofmann. Synthesis of superheavy elements by cold fusion. *Radiochim. Acta*, 99(7-8):405–428, 2011.

[84] S. Hofmann. Synthesis and properties of isotopes of the transactinides. *Radiochim. Acta*, 107(9-11):879–915, 2019.

[85] S. Hofmann, S. Heinz, R. Mann, J. Maurer, J. Khuyagbaatar, D. Ackermann, S. Antalic, W. Barth, M. Block, H. Burkhard, et al. The reaction ^{48}Ca + ^{248}Cm $\rightarrow$ $^{296}116^{*}$ studied at the GSI-SHIP. *Eur. Phys. J.*, 48:62, 2012.

[86] Y. I. Hori. Electrochemical CO_2 reduction on metal electrodes. In *Modern aspects of electrochemistry*, pages 89–189. Springer, 2008.

[87] L. T.-T. Huong, T. Häger, W. Hofmeister, et al. Confocal micro-Raman spectroscopy: a powerful tool to identify natural and synthetic emeralds. *Gems Gemol.*, 46:36–41, 2010.

[88] G. A. Hussein, G. A. Mekhemer, and B. A. Balboul. Formation and surface characterization of thulium oxide catalysts. *Phys. Chem. Chem. Phys.*, 2(9):2033–2038, 2000.

[89] C. Ingelbrecht, A. Moens, R. Eykens, and A. Dean. Improved electrodeposited actinide layers. *Nucl. Instrum. Methods Phys. Res. A*, 397(1):34–38, 1997.

[90] K. Izutsu, editor. *Electrochemistry in nonaqueous solutions*. John Wiley & Sons, Professor Dr. K. Izutsu, 3-8-23 Motomachi, Matsumoto 390-0803, Japan, 2nd edition, 2009.

[91] E. Jäger, H. Brand, Ch. E. Düllmann, J. Khuyagbaatar, J. Krier, M. Schädel, T. Torres, and A. Yakushev. High intensity target wheel at TASCA: target wheel control system and target monitoring. *J. Radioanal. Nucl. Chem.*, 299(2):1073–1079, 2014.

[92] L. Jin. *Préparation de cibles d'uranium: compréhension du procédé d'électroprécipitation pour optimiser les conditions opératoires*. PhD thesis, Université Paris-Saclay, 2021.

[93] A. M. Kaczmarek, K. Van Hecke, and R. Van Deun. Nano-and micro-sized rare-earth carbonates and their use as precursors and sacrificial templates for the synthesis of new innovative materials. *Chem. Soc. Rev.*, 44:2032–2059, 2015.

[94] J. Kallunkathariyil, C. Stodel, C. Marry, G. Frémont, B. Bastin, J. Piot, E. Clément, S. Le Moal, V. Morel, J.-C. Thomas, et al. S3 targets monitoring with an electron gun. In *AIP Conference Proceedings*, volume 1962, page 030019. AIP Publishing LLC, 2018.

[95] V. Kartha and S. Venkateswaran. Vibrational spectra and normal vibrations of rare earth formates. *Spectrochim. Acta A Mol. Biomol. Spectrosc.*, 37(11):927–934, 1981.

[96] J. Kayser and M. Scherschel. Molecular plating of cobalt and neodymium on thin aluminium foils. *Nucl. Instrum. Methods. Phys. Res. A*, 268(1):19–23, 1988.

[97] J. Khuyagbaatar, A. Yakushev, Ch. E. Düllmann, D. Ackermann, L.-L. Andersson, M. Asai, M. Block, R. Boll, H. Brand, D. Cox, et al. ^{48}Ca + ^{249}Bk fusion reaction leading to element Z= 117: Long-lived α-decaying ^{270}Db and discovery of ^{266}Lr. *Phys. Rev. Lett.*, 112(17):172501, 2014.

[98] P. Kim, A. Anderko, A. Navrotsky, and R. E. Riman. Trends in structure and thermodynamic properties of normal rare earth carbonates and rare earth hydroxycarbonates. *Minerals*, 8:106, 2018.

[99] B. Kindler, D. Ackermann, D. Gembalies-Datz, W. Hartmann, F. Heßberger, S. Hofmann, J. Klemm, B. Lommel, R. Mann, and J. Steiner. Chemical Compound Targets for SHIP-Production, Properties, and Application. In *AIP Conference Proceedings*, volume 680, pages 781–784. American Institute of Physics, 2003.

[100] B. Kindler, D. Ackermann, W. Hartmann, F. P. Heßberger, S. Hofmann, B. Lommel, R. Mann, and J. Steiner. Chemical compound targets for SHIP on heated carbon backings. *Nucl. Instrum. Methods. Phys. Res. A*, 561(1):107–111, 2006.

[101] H. Klemenčič and L. Benedik. Alpha-spectrometric thin source preparation with emphasis on homogeneity. *Appl. Radiat. Isot.*, 68(7-8):1247, 2010.

[102] Y. G. Ko. Preparation and characterization of electrodeposited layers as alpha sources for alpha-particle spectrometry. *J. Radioanal. Nucl. Chem.*, 326:861, 2020.

[103] S. Kobayashi and I. Hachiya. Lanthanide triflates as water-tolerant lewis acids. activation of commercial formaldehyde solution and use in the aldol reaction of silyl enol ethers with aldehydes in aqueous media. *J. Org. Chem.*, 59(13):3590, 1994.

[104] S. Kobayashi, M. Sugiura, H. Kitagawa, and W. W.-L. Lam. Rare-earth metal triflates in organic synthesis. *Chem. Rev.*, 102(6):2227, 2002.

[105] M. König, J. Vaes, E. Klemm, and D. Pant. Solvents and supporting electrolytes in the electrocatalytic reduction of CO_2. *iScience*, 19:135–160, 2019.

[106] I. Krossing and I. Raabe. Noncoordinating anions—fact or fiction? a survey of likely candidates. *Angewandte Chemie International Edition*, 43(16):2066–2090, 2004.

[107] F. Kurth, J. Froemel, S. Tanaka, M. Esashi, and T. Gessner. Electroplating of neodymium iron alloys. In *2016 IEEE 11th Annual International Conference on Nano/Micro Engineered and Molecular Systems (NEMS)*, pages 405–408. IEEE, 2016.

[108] T. Kutty, I. Mohamed, and J. Tareen. Hydrothermal phase equilibria in Ln_2O_3-H_2O-CO_2 systems for Tm, Yb and Lu. *Mater. Chem. Phys.*, 10(5):425–441, 1984.

[109] C. Lars, B. Seiferle, C. Schneider, J. Jeet, I. Amersdorffer, N. Arlt, F. Zacherl, R. Haas, D. Renisch, P. Mosel, et al. The concept of laser-based conversion electron Mössbauer spectroscopy for a precise energy determination of ^{229m}Th. *Hyperfine Interact.*, 240:23, 2019.

[110] P. E. Larson and M. A. Kelly. Surface charge neutralization of insulating samples in X-ray photoemission spectroscopy. *J. Vac. Sci. Technol. A*, 16(6):3483–3489, 1998.

[111] S. Lauber, S. Yaramyshev, M. Basten, K. Aulenbacher, W. Barth, C. Burandt, M. Droba, F. Dziuba, P. Forck, V. Gettmann, et al. An alternating phase focusing injector for heavy ion acceleration. *Nucl. Instrum. Methods Phys. Res., Sect. A*, 1040:167099, 2022.

[112] L. Lens, A. Yakushev, Ch. E. Düllmann, M. Asai, J. Ballof, M. Block, H. M. David, J. Despotopulos, A. Di Nitto, K. Eberhardt, et al. Online chemical adsorption studies of hg, tl, and pb on sio2 and au surfaces in preparation for chemical investigations on cn, nh, and fl at tasca. *Radiochim. Acta*, 106(12):949, 2018.

[113] D. Liebe, K. Eberhardt, W. Hartmann, T. Häger, A. Hübner, J. Kratz, B. Kindler, B. Lommel, P. Thörle, M. Schädel, et al. The application of neutron activation analysis, scanning electron microscope, and radiographic imaging for the characterization of electrochemically deposited layers of lanthanide and actinide elements. *Nucl. Instrum. Methods. Phys. Res. A*, 590(1-3):145–150, 2008.

[114] D. Liebe, K. Eberhardt, W. Hartmann, A. Hübner, B. Kindler, J. Kratz, B. Lommel, J. Steiner, and P. Thörle. Molecular plating of uranium on thin aluminum backings. Technical report, Institute of Nuclear Chemistry - Johannes Gutenberg University Mainz, 2006.

[115] P. Liu, Q. Yang, Y. Tong, and Y. Yang. Electrodeposition of Gd-Co film in organic bath. *Electrochim. Acta*, 45(13):2147, 2000.

[116] Y. V. Lobanov, G. Buklanov, F. S. Abdullin, A. Polyakov, I. Shirokovsky, Y. S. Tsyganov, and V. Utyonkov. Targets of uranium, plutonium, and curium for heavy-element research. *Nucl. Instrum. Methods Phys. Res., Sect. A*, 397(1):26–29, 1997.

[117] J. Lodermeyer, M. Multerer, M. Zistler, S. Jordan, H. J. Gores, W. Kipferl, E. Diaconu, M. Sperl, and G. Bayreuther. Electroplating of dysprosium, electrochemical investigations, and study of magnetic properties. *J. Electrochem. Soc.*, 153(4):C242, 2006.

[118] B. Lommel, W. Brüchle, K. Eberhardt, W. Hartmann, A. Hübner, B. Kindler, J. V. Kratz, D. Liebe, M. Schädel, and J. Steiner. Backings and targets for chemical and nuclear studies of transactinides with TASCA. *Nucl. Instrum. Methods Phys. Res., Sect. A*, 590:141–144, 2008.

[119] B. Lommel, Ch. E. Düllmann, B. Kindler, and D. Renisch. Status and developments of target production for research on heavy and superheavy nuclei and elements. *Eur. Phys. J.*, 59(2):14, 2023.

[120] B. Lommel, D. Gembalies-Datz, W. Hartmann, S. Hofmann, B. Kindler, J. Klemm, J. Kojouharova, and J. Steiner. Improvement of the target durability for heavy-element production. *Nucl. Instrum. Methods. Phys. Res. A*, 480(1):16–21, 2002.

[121] B. Lommel and B. Kindler. *Targets for Particle Accelerators*, chapter 20, page 619. John Wiley Sons, Ltd, 2009.

[122] W. Loveland. High quality actinide targets. *J. Radioanal. Nucl. Chem.*, 307(3):1591–1594, 2016.

[123] W. Loveland, L. Yao, D. M. Asner, R. Baker, J. Bundgaard, E. Burgett, M. Cunningham, J. Deaven, D. Duke, U. Greife, et al. Targets for precision measurements. *Nucl. Data Sheets*, 119:383, 2014.

[124] R. Mann, D. Ackermann, S. Antalic, H. Burkhard, P. Cagarda, D. Gembalies-Datz, W. Hartmann, F. Heßberger, S. Hofmann, B. Kindler, et al. On-line target control. *GSI report*, page 224, 2003.

[125] L. Martinot, D. Laeckmann, T. Materne, and V. Müller. Contribution to the knowledge of the electrochemical properties of actinides in non-aqueous media. I: The reduction of tetravalent uranium in various organic solvents. *J. Less-Common Met.*, 163(1):185, 1990.

[126] L. Martinot, L. Lopes, J. Marien, and C. Jérôme. Electrochemistry of lanthanum and uranium chlorides in organic media: Deposition of lanthanum and uranium. *J. Radioanal. Nucl. Chem.*, 253(3):407, 2002.

[127] D. Marx, F. Nickel, G. Münzenberg, K. Güttner, H. Ewald, W. Faust, S. Hofmann, H. Schött, and W. Thalheimer. A rotating target wheel with thin targets for heavy ion beams of high current densities. *Nuclear Instruments and Methods*, 163(1):15–20, 1979.

[128] J. Massaux and G. Duyckaerts. Méthode de préparation de sels anhydres de lanthanides pour la polarographie en solvants non aqueux aprotiques. *Anal. Chim. Acta*, 73(2):416, 1974.

[129] D. Mayorov, E. Tereshatov, T. Werke, M. Frey, and C. Folden III. Heavy-ion beam induced effects in enriched gadolinium target films prepared by molecular plating. *Nucl. Instrum. Methods Phys. Res., Sect. B*, 407:256–264, 2017.

[130] F. Menges. Spectragryph-optical spectroscopy software, Version 1.2. 14, 2020, 2020.

[131] C.-C. Meyer, E. Artes, M. Bender, J. Brötz, Ch. E. Düllmann, C. Haese, E. Jäger, B. Kindler, B. Lommel, M. Major, M. Rapps, D. Renisch, C. Trautmann, and A. Yakushev. Fabrication, swift heavy ion irradiation, and damage analysis of lanthanide targets. *Radiochim. Acta*, 111(11):801–815, 2023.

[132] C.-C. Meyer, A. Dragoun, Ch. E. Düllmann, R. Haas, E. Jäger, B. Kindler, B. Lommel, A. Prosvetov, M. Rapps, D. Renisch, et al. Chemical conversions in lead thin films induced by heavy-ion beams at Coulomb barrier energies. *Nucl. Instrum. Methods. Phys. Res. A*, page 166365, 2022.

[133] G. Meyer and L. R. Morss. *Synthesis of lanthanide and actinide compounds*, volume 2. Springer Science & Business Media, 1990.

[134] J. Miao. Computational microscopy with coherent diffractive imaging and ptychography. *Nature*, 637(8045):281–295, 2025.

[135] J. Mink, M. Y. Skripkin, L. Hajba, C. Németh, A. Abbasi, and M. Sandström. Infrared and raman spectroscopic and theoretical studies of nonaaqua complexes of trivalent rare earth metal ions. *Spectrochim. Acta, Part A*, 61(7):1639, 2005.

[136] A. Moiseeva, R. Aliev, V. Unezhev, V. Zagryadskiy, S. Latushkin, N. Aksenov, N. Gustova, M. Voronuk, G. Y. Starodub, and A. Ogloblin. Cross section measurements of ^{151}eu (^{3}he, ^{5}n) reaction: new opportunities for medical alpha emitter ^{149}tb production. *Scientific reports*, 10(1):1, 2020.

[137] K. J. Moody. Synthesis of superheavy elements. In *The chemistry of superheavy elements*, pages 1–81. Springer, 2014.

[138] K. Morita. SHE research at RIKEN/GARIS. *Nucl. Phys. A*, 944:30–61, 2015.

[139] M. Moura, A. Ayala, J. Mendes Filho, I. Guedes, C. Paschoal, A. Leyva, G. Polla, D. Vega, P. De Perazzo, and H. Lanza. Thermal behavior in $Pr(HCOO)_3$ crystals. *J. Raman Spectrosc.*, 35(2):159–164, 2004.

[140] K. Myhre, J. Burns, H. Meyer, N. Sims, and R. Boll. Samarium electrodeposited acetate and oxide thin films on stainless steel substrate characterized by XPS. *Surface Science Spectra*, 23(1):70–81, 2016.

[141] K. G. Myhre, J. D. Burns, N. J. Sims, D. W. Stracener, and R. A. Boll. Effects of annealing on fission fragment release from electrodeposited Cf-252 thin-films. *Nucl. Instrum. Methods Phys. Res., Sect. A*, 955:163282, 2020.

[142] K. G. Myhre, J. C. Delashmitt, N. J. Sims, S. M. Van Cleve, and R. A. Boll. Samarium thin films molecular plated from N, N-dimethylformamide characterized by XPS. *Surf. Sci. Spectra*, 25(2):024003, 2018.

[143] K. G. Myhre, J. C. Delashmitt, N. J. Sims, S. M. Van Cleve, and R. A. Boll. Samarium thin films molecular plated from N,N-dimethylformamide characterized by XPS. *Surf. Sci. Spectra*, 25:024003, 2018.

[144] Y. Nagame and M. Hirata. Production and properties of transuranium elements. *Radiochim. Acta*, 99(7-8):377–393, 2011.

[145] D. Nečas and P. Klapetek. Gwyddion: an open-source software for SPM data analysis. *Open Phys.*, 10(1):181, 2012.

[146] D. E. Newbury and N. W. Ritchie. Performing elemental microanalysis with high accuracy and high precision by scanning electron microscopy/silicon drift detector energy-dispersive X-ray spectrometry (SEM/SDD-EDS). *J. Mater. Sci.*, 50(2):493–518, 2015.

[147] S. G. Nilsson. Binding states of individual nucleons in strongly deformed nuclei. *Dan. Mat. Fys. Medd.*, 29(CERN-55-30):1–69, 1955.

[148] Y. Ts. Oganessian and S. N. Dmitriev. Synthesis and study of properties of superheavy atoms. Factory of Superheavy Elements. *Russ. Chem. Rev.*, 85:901, 2016.

[149] Yu. Ts. Oganessian. Heaviest nuclei from ^{48}ca-induced reactions. *J Phys G Nucl Part Phys*, 34(4):R165, 2007.

[150] Yu. Ts. Oganessian, F. S. Abdullin, C. Alexander, J. Binder, R. A. Boll, S. Dmitriev, J. Ezold, K. Felker, J. Gostic, R. K. Grzywacz, et al. Experimental studies of the ^{249}Bk+ ^{48}Ca reaction including decay properties and excitation function for isotopes of element 117, and discovery of the new isotope ^{277}Mt. *Physical Review C—Nuclear Physics*, 87(5):054621, 2013.

[151] Yu. Ts. Oganessian, F. S. Abdullin, S. Dmitriev, J. Gostic, J. Hamilton, R. Henderson, M. Itkis, K. Moody, A. Polyakov, A. Ramayya, et al. Investigation of the ^{243}Am + ^{48}Ca reaction prod-

ucts previously observed in the experiments on elements 113, 115, and 117. *Phys. Rev. C*, 87(1):014302, 2013.

[152] Yu. Ts. Oganessian and V. Utyonkov. Superheavy nuclei from ^{48}Ca -induced reactions. *Nucl. Phys. A*, 944:62–98, 2015.

[153] Yu. Ts. Oganessian, V. Utyonkov, A. Popeko, D. Solovyev, F. Sh. Abdullin, S. Dmitriev, D. Ibadullayev, M. Itkis, N. Kovrizhnykh, D. Kuznetsov, et al. Dgfrs-2—a gas-filled recoil separator for the dubna super heavy element factory. *Nucl. Instrum. Methods Phys. Res., Sect. A*, 1033:166640, 2022.

[154] Y. Ohki, Y. Suzuki, T. Takeuchi, and A. Ouchi. The Crystal and Molecular Structure of Scandium(III), Yttrium(III), and Some Lanthanoid(III) p-Toluenesulfonates, $[Sc(C_7H_7SO_3)_2(H_2O)_4](C_7H_7SO_3)\cdot 2H_2O$ and $[M(C_7H_7SO_3)_2(H_2O)_6](C_7H_7SO_3)\cdot 3H_2O$ (M = Y, Sm, Gd, Dy, Ho, Er, Yb); and Yttrium(III) and Dysprosium(III) 2-Naphthalenesulfonates, $[M(C_{10}H_7SO_3)_2(H_2O)_6](C_{10}H_7SO_3)\cdot 3H_2O$ (M = Y, Dy) . *Bull. Chem. Soc. Jpn.*, 61(2):393, 1988.

[155] A. Ölcer, J. Drebert, and T. Reich. XPS-Oberflächenanalyse von elektrochemisch hergestellten Urantargets. Technical report, Institut für Kernchemie, Johannes Gutenberg-Universität Mainz (Germany), 2007.

[156] A. Orera, G. Larraz, and M. Sanjuán. Spectroscopic study of the competition between dehydration and carbonation effects in La_2O_3-based materials. *J. Eur. Ceram. Soc.*, 33(11):2103–2110, 2013.

[157] W. Parker, H. Bildstein, and N. Getoff. Molecular plating I, a rapid and quantitative method for the electrodeposition of thorium and uranium. *Nucl. Instr. Methods*, 26:55–60, 1964.

[158] W. Parker, H. Bildstein, and N. Getoff. Molecular plating I, a rapid and quantitative method for the electrodeposition of thorium and uranium. *Nucl. Instrum. Methods*, 26:55–60, 1964.

[159] W. Parker, H. Bildstein, and N. Getoff. Molecular plating III the rapid preparation of radioactive reference samples. *Nucl. Instr. Methods*, 26:314–316, 1964.

[160] W. Parker, H. Bildstein, N. Getoff, H. Fischer-Colbrie, and H. Regal. Molecular plating II a rapid and quantitative method for the electrodeposition of the rare-earth elements. *Nucl. Instr. Methods*, 26:61–65, 1964.

[161] W. Parker and M. Colonomos. Preparation of thin layers of ^{237}Np for absolute counting and fission detectors. *Nucl. Instr. Methods*, 66(1):137–140, 1968.

[162] W. Parker and R. Falk. Molecular plating: a method for the electrolytic formation of thin inorganic films. *Nucl. Instr. Methods*, 16, 1962.

[163] W. Parker and W. Gullholmer. Molecular plating: preparation of self-supporting films. Technical report, Chalmers Tekniska Hogskola, Goteborg (Sweden), 1966.

[164] D. L. Perry and T. Wilkinson. Synthesis of high-purity α-and β-PbO and possible applications to synthesis and processing of other lead oxide materials. *Appl. Phys. A*, 89(1):77–80, 2007.

[165] I. Petermann, K. Langanke, G. Martínez-Pinedo, I. Panov, P.-G. Reinhard, and F.-K. Thielemann. Have superheavy elements been produced in nature? *Eur. Phys. J.*, 48(9):1–11, 2012.

[166] C. Piguet. Paramagnetic susceptibility by NMR: theßolvent correctionrremoved for large paramagnetic molecules. *J. Chem. Educ.*, 74(7):815, 1997.

[167] A. Prosvetov, G. Hamaoui, N. Horny, M. Chirtoc, F. Yang, C. Trautmann, and M. Tomut. Degradation of thermal transport properties in fine-grained isotropic graphite exposed to swift heavy ion beams. *Acta Mater.*, 184:187–198, 2020.

[168] Z. Qin, H. Fan, Y. Xu, J. He, X. , Lei, H. Liu, and G. Jin. Preparation of thick americium targets and synthesis of ^{259}db. *J. Nucl. Radiochem. Sci.*, 3(1):183, 2002.

[169] M. Ramaniah, R. Singh, S. Awasthi, and S. Prakash. Studies on electrodeposition of actinide elements from non-aqueous medium. *Appl. Radiat. Isot.*, 26(11):648–650, 1975.

[170] S. Rau, F. Heiße, F. Köhler-Langes, S. Sasidharan, R. Haas, D. Renisch, Ch. E. Düllmann, W. Quint, S. Sturm, and K. Blaum. Penning trap mass measurements of the deuteron and the HD^+ molecular ion. *Nature*, 585(7823):43–47, 2020.

[171] M. S. Refat and K. M. Elsabawy. Infrared spectra, Raman laser, XRD, DSC/TGA and SEM investigations on the preparations of selenium metal, (Sb_2O_3, Ga_2O_3, SnO and HgO) oxides and lead carbonate with pure grade using acetamide precursors. *Bull. Mater. Sci.*, 34:873, 2011.

[172] Y. Repelin, C. Proust, E. Husson, and J. Beny. Vibrational spectroscopy of the c-form of yttrium sesquioxide. *J. Solid State Chem.*, 118(1):163, 1995.

[173] N. W. Ritchie. Getting Started with NIST* DTSA-II. *Microscopy Today*, 19(1):26, 2011.

[174] J. Roberto, C. W. Alexander, R. A. Boll, J. Burns, J. Ezold, L. Felker, S. L. Hogle, and K. Rykaczewski. Actinide targets for the synthesis of super-heavy elements. *Nucl. Phys. A*, 944:99–116, 2015.

[175] J. B. Roberto, M. Du, J. G. Ezold, S. L. Hogle, J. Moon, K. Myhre, and K. P. Rykaczewski. Actinide targets for the synthesis of superheavy nuclei. *The European Physical Journal A*, 59(12):304, 2023.

[176] D. Rudolph, U. Forsberg, P. Golubev, L. Sarmiento, A. Yakushev, L.-L. Andersson, A. Di Nitto, Ch. E. Düllmann, J. Gates, K. Gregorich, et al. Spectroscopy of element 115 decay chains. *Phys. Rev. Lett.*, 111(11):112502, 2013.

[177] J. Runke, Ch. E. Düllmann, K. Eberhardt, P. Ellison, K. Gregorich, S. Hofmann, E. Jäger, B. Kindler, J. Kratz, J. Krier, et al. Preparation of actinide targets for the synthesis of the heaviest elements. *J. Radioanal. Nucl. Chem.*, 299(2):1081–1084, 2014.

[178] S. Sadi, A. Paulenova, W. Loveland, P. Watson, J. Greene, S. Zhu, and G. Zinkann. Surface morphology and phase stability of titanium foils irradiated with 136 MeV ^{136}Xe. *Nucl. Instrum. Methods Phys. Res. B*, 328:78–83, 2014.

[179] S. Sadi, A. Paulenova, P. Watson, and W. Loveland. Growth and surface morphology of uranium films during molecular plating. *Nucl. Instrum. Methods. Phys. Res. A*, 655(1):80–84, 2011.

[180] R. Sagaidak. Effects of beam wobbling and target rotation on the target temperature in experiments with intense heavy ion beams. *Phys. Rev. Accel. Beams*, 24(8):083001, 2021.

[181] H. Sakai, H. Haba, K. Morimoto, and N. Sakamoto. Facility upgrade for superheavy-element research at riken. *Eur. Phys. J. A*, 58(12):238, 2022.

[182] A. Såmark-Roth, D. Cox, D. Rudolph, L. Sarmiento, B. Carlsson, J. Egido, P. Golubev, J. Heery, A. Yakushev, S. Åberg, et al. Spectroscopy along Flerovium Decay Chains: Discovery of ^{280}Ds and an Excited State in ^{282}Cn. *Phys. Rev. Lett.*, 126(3):032503, 2021.

[183] M. San Andrés, J. De la Roja, S. Dornheim, and V. Baonza. Litharge and massicot: Thermal decomposition synthetic route for basic lead (II) carbonate and Raman spectroscopy analysis. In *Lasers in the Conservation of Artworks: Proceedings of the International Conference Lacona VII, Madrid, Spain, 17-21 September 2007*, page 89. CRC Press, 2008.

[184] L. Sanchez-Cupido, J. M. Pringle, A. L. Siriwardana, A. Unzurrunzaga, M. Hilder, M. Forsyth, and C. Pozo-Gonzalo. Water-Facilitated electrodeposition of neodymium in a phosphonium-based ionic liquid. *J. Phys. Chem. Lett.*, 10(2):289–294, 2019.

[185] M. Schädel. Chemistry of superheavy elements. *Angew. Chem. Int. Ed.*, 45(3):368–401, 2006.

[186] A. Seminara and E. Rizzarelli. Trifluoromethanesulfonate as non-coordinating anion in lanthanide complexes. *Inorganica Chimica Acta*, 40:249–256, 1980.

[187] K. Shirasaki, T. Yamamura, T. Herai, and Y. Shiokawa. Electrodeposition of uranium in dimethyl sulfoxide and its inhibition by acetylacetone as studied by EQCM. *J. Alloys Compd.*, 418(1-2):217, 2006.

[188] K. Shirasaki, T. Yamamura, T. Herai, Y. Shiokawa, I. Satoh, and M. Oku. Electrodeposition of Lanthanum in Aprotic Solvents Studied by HMDE, EQCM and XPS. *ECS Meeting Abstracts*, 18:849, 2007.

[189] G. Sibbens, M. Ernstberger, T. Gouder, M. Marouli, A. Moens, A. Seibert, D. Vanleeuw, M. V. Zúñiga, T. Wiss, M. Zampella, et al. Morphological and compositional study of ^{238}U thin film targets for nuclear experiments. In *AIP Conference Proceedings*, volume 1962, page 030007. AIP Publishing LLC, 2018.

[190] E. Silva, M. Moura, A. Ayala, I. Guedes, G. Polla, D. Vega, D. Tobia, and M. Saleta. Vibrational modes of rare-earth formates. *J. Raman Spectrosc.*, 40(8):954–957, 2009.

[191] T. Smirnova, V. Volodin, M. Lebedev, and V. Belyi. Raman scattering spectroscopy of inclusions of carbon in Al_2O_3 films and its solid solutions with HfO_2. *Opt. Spectrosc.*, 110(1):55–59, 2011.

[192] G. D. Smith and R. J. Clark. Raman microscopy in archaeological science. *J. Archaeol. Sci.*, 31:1137–1160, 2004.

[193] O. R. Smits, Ch. E. Düllmann, P. Indelicato, W. Nazarewicz, and P. Schwerdtfeger. The quest for superheavy elements and the limit of the periodic table. *Nature Reviews Physics*, 6(2):86–98, 2024.

[194] L. Song and M. Rong-jun. IR of Hydrated Rare Earth Carbonates. *Sci. Tech. Eng. J. (STEJ)*, 7(7):36, 2007.

[195] L. Spiridigliozzi, M. Bortolotti, G. Accardo, A. Vergara, D. Frattini, C. Ferone, R. Cioffi, and G. DellAgli. An in-depth multi-technique characterization of rare earth carbonates–$RE_2(CO_3)_3 \cdot 2\,H_2O$ –owning tengerite-type structure. *J. Rare Earths*, 2021.

[196] L. Spiridigliozzi, C. Ferone, R. Cioffi, M. Bortolotti, and G. Dell'Agli. New Insights in the Hydrothermal Synthesis of Rare-Earth Carbonates. *Materials*, 12:2062, 2019.

[197] P. Steinegger. Open questions on chemistry in the synthesis and characterization of superheavy elements. *Commun. Chem.*, 4(1):1–4, 2021.

[198] C. Stodel. Methods of targets characterization. In *EPJ Web of Conferences*, volume 229, page 02001. EDP Sciences, 2020.

[199] C. Stodel, J.-F. Libin, C. Marry, F. Lutton, M.-G. Saint-Laurent, B. Bastin, J. Piot, E. Clement, S. Le Moal, V. Morel, et al. High intensity targets stations for S 3. *J. Radioanal. Nucl. Chem.*, 305:761–767, 2015.

[200] C. Stodel, M. Toulemonde, C. Fransen, B. Jacquot, E. Clément, G. Fremont, M. Michel, and C. Dufour. "Thermal Spike" model applied to thin targets irradiated with swift heavy ion beams at few MeV/u. In *EPJ Web of Conferences*, volume 229, page 05001. EDP Sciences, 2020.

[201] G. Suppan. *Electroplating dysprosium from ionic liquid-based solutions-A promising electrochemical step to produce stronger high performance Nd (Dy)-Fe-B sintered magnets*. PhD thesis, University of Regensburg, Germany, 2016.

[202] M. N. Torrico, R. A. Boll, and M. Matos. Electrodeposition of actinide compounds from an aqueous ammonium acetate matrix: Experimental development and optimization. *Nucl. Instrum. Methods. Phys. Res. A*, 790:64–69, 2015.

[203] M. Toulemonde, W. Assmann, C. Trautmann, F. Grüner, H. Mieskes, H. Kucal, and Z. Wang. Electronic sputtering of metals and insulators by swift heavy ions. *Nucl. Instrum. Methods Phys. Res., Sect. B*, 212:346, 2003.

[204] C. Tracy, M. Lang, F. Zhang, C. Trautmann, and R. Ewing. Phase transformations in Ln_2O_3 materials irradiated with swift heavy ions. *Phys. Rev. B: Condens. Matter*, 92:174101, 2015.

[205] C. L. Tracy, M. Lang, J. M. Pray, F. Zhang, D. Popov, C. Park, C. Trautmann, M. Bender, D. Severin, V. A. Skuratov, et al. Redox response of actinide materials to highly ionizing radiation. *Nat. Commun.*, 6(1):1–9, 2015.

[206] N. Trautmann and H. Folger. Preparation of actinide targets by electrodeposition. *Nucl. Instrum. Methods Phys. Res., Sect. A*, 282:102–106, 1989.

[207] V. K. Tripathi and R. Nagarajan. Sol–Gel Synthesis of High-Purity Actinide Oxide ThO_2 and Its Solid Solutions with Technologically Important Tin and Zinc Ions. *Inorg. Chem.*, 55:12798–12806, 2016.

[208] A. Türler and V. Pershina. Advances in the production and chemistry of the heaviest elements. *Chem. Rev.*, 113(2):1237–1312, 2013.

[209] A. Ubaldini and M. M. Carnasciali. Raman characterisation of powder of cubic RE_2O_3 (RE= Nd, Gd, Dy, Tm, and Lu), Sc_2O_3 and Y_2O_3. *J. Alloys Compd.*, 454(1-2):374, 2008.

[210] I. Usoltsev, R. Eichler, G. Vostokin, A. Sabel'nikov, N. Aksenov, Y. Albin, G. Bozhikov, V. Chepigin, S. Dmitriev, V. Y. Lebedev, et al. Preparation and high intensity heavy ion irradiation tests of intermetallic ^{243}Am/Pd targets. *Nucl. Instrum. Methods Phys. Res. B*, 318:297–305, 2014.

[211] Ustinov, O and Schadrin, A and Shmidt, O and Shudegova, O . Study of carbon dioxide solubility in nitric acid and metal nitrates solutions for estimation of carbon-14 distribution between gas

phase and solution during dissolution of spent nuclear fuel. *17. radiochemical conference. Booklet of abstracts*, NFC-P11(Id: 98), 2014.

[212] W. Van der Eijk, W. Oldenof, and W. Zehner. Preparatio of thin sources, a review. *Nuclear Instruments and Methods*, 112(1-2):343–351, 1973.

[213] P. Vandenabeele, H. Edwards, and J. Jehlička. The role of mobile instrumentation in novel applications of Raman spectroscopy: archaeometry, geosciences, and forensics. *Chem. Soc. Rev.*, 43:2628–2649, 2014.

[214] A. Vascon. *Molecular plating of thin lanthanide layers with improved material properties for nuclear applications*. PhD thesis, Johannes Gutenberg University Mainz, 2013.

[215] A. Vascon, J. Runke, N. Trautmann, B. Cremer, K. Eberhardt, and Ch. E. Düllmann. Quantitative molecular plating of large-area ^{242}Pu targets with improved layer properties. *Appl. Radiat. Isot.*, 95:36–43, 2015.

[216] A. Vascon, S. Santi, A. Isse, A. Kühnle, T. Reich, J. Drebert, K. Eberhardt, and Ch. E. Düllmann. Smooth crack-free targets for nuclear applications produced by molecular plating. *Nucl. Instrum. Methods Phys. Res., Sect. A*, 714:163–175, 2013.

[217] A. Vascon, S. Santi, A. Isse, T. Reich, J. Drebert, H. Christ, Ch. E. Düllmann, and K. Eberhardt. Elucidation of constant current density molecular plating. *Nucl. Instrum. Methods Phys. Res., Sect. A*, 696:180–191, 2012.

[218] A. Vascon, S. Santi, A. Isse, T. Reich, J. Drebert, H. Christ, K. Eberhardt, and Ch. E. Düllmann. Fundamental aspects of molecular plating and production of smooth crack-free Nd targets. *J. Radioanal. Nucl. Chem.*, 299:1085–1091, 2014.

[219] A. Vascon, N. Wiehl, T. Reich, J. Drebert, K. Eberhardt, and Ch. E. Düllmann. The performance of thin layers produced by molecular plating as α-particle sources. *Nucl. Instrum. Methods Phys. Res., Sect. A*, 721:35–44, 2013.

[220] P. Watson, W. Loveland, P. Zielinski, K. Gregorich, and H. Nitsche. Changes in surface composition and morphology of UF_4 targets during heavy ion irradiation. *Nucl. Instrum. Methods Phys. Res., Sect. B*, 226:543–548, 2004.

[221] U. Wehrmeister, A. L. Soldati, D. Jacob, T. Häger, and W. Hofmeister. Raman spectroscopy of synthetic, geological and biological vaterite: a Raman spectroscopic study. *J. Raman Spectrosc.*, 41(2):193–201, 2010.

[222] M. Weigand, T. Heftrich, Ch. E. Düllmann, K. Eberhardt, S. Fiebiger, J. Glorius, K. Göbel, R. Haas, C. Langer, S. Lohse, et al. 66.7-keV γ-line intensity of Tm-171 determined via neutron activation. *Phys. Rev. C: Nucl. Phys.*, 97:035803, 2018.

[223] C. v. Weizsäcker. Zur Theorie der Kernmassen. *Z. Phys.*, 96(7):431–458, 1935.

[224] M. Wojdyr. Fityk: a general-purpose peak fitting program. *J. Appl. Crystallogr.*, 43(5-1):1126–1128, 2010.

[225] A. Yakushev, J. M. Gates, A. Türler, M. Schädel, Ch. E. Düllmann, D. Ackermann, L.-L. Andersson, M. Block, W. Brüchle, J. Dvorak, et al. Superheavy element flerovium (element 114) is a volatile metal. *Inorg. Chem.*, 53(3):1624–1629, 2014.

[226] A. Yakushev, J. Khuyagbaatar, Ch. E. Düllmann, M. Block, R. Cantemir, D. Cox, D. Dietzel, F. Giacoppo, Y. Hrabar, M. Iliaš, et al. Manifestation of relativistic effects in the chemical properties of nihonium and moscovium revealed by gas chromatography studies. *Frontiers in Chemistry*, 12:1474820, 2024.

[227] A. Yakushev, L. Lens, Ch. E. Düllmann, J. Khuyagbaatar, E. Jäger, J. Krier, J. Runke, H. Albers, M. Asai, M. Block, et al. On the adsorption and reactivity of element 114, flerovium. *Frontiers in chemistry*, 10:976635, 2022.

[228] N. Yanagihara, S. Nakamura, and M. Nakayama. A thermal study of several lanthanide triflates. *Polyhedron*, 17(20):3625, 1998.

[229] M. M. Yang, D. A. Crerar, and D. E. Irish. A Raman spectroscopic study of lead and zinc acetate complexes in hydrothermal solutions. *Geochim. Cosmochim. Acta*, 53:319–326, 1989.

[230] D. Zagorac, H. Müller, S. Ruehl, J. Zagorac, and S. Rehme. Recent developments in the inorganic crystal structure database: theoretical crystal structure data and related features. *J. Appl. Crystallogr.*, 52(5):918–925, 2019.

[231] Q. Zhi, G. Junsheng, and G. Zaiguo. Preparation of the thicker americium targets by molecular plating. *Appl. Radiat. Isot.*, 54(5):741–744, 2001.

[232] J. F. Ziegler, M. D. Ziegler, and J. P. Biersack. SRIM–The stopping and range of ions in matter (2010). *Nucl. Instrum. Methods Phys. Res. B*, 268(11-12):1818–1823, 2010.

C. List of Figures

D. List of Tables

E. Acknowledgments

Ich möchte Christoph E. Düllmann meinen aufrichtigen Dank aussprechen, da er mich in seiner Forschungsgruppe aufgenommen und über einen langen Zeitraum hinweg meine Dissertation betreut hat. Ein besonderer Dank gebührt Dennis Renisch, dessen Unterstützung für die Realisierung mancher Experimente unabdingbar war. Jacque van de Laar möchte ich für die zahlreichen humorvollen Anekdoten sowie die mustergültige Übergabe der Organisation der Vorlesung meinen Dank aussprechen. Des Weiteren danke ich meinen Kollegen aus den Superheavies, Jonas Stricker, Steffen Lohse, Elisabeth Rickert, Sebastian Berndt, Dominik Dietzel, Lotte Lens, Lauren Reed und Yuki Ishikawa, für ihre hervorragende Zusammenarbeit bei Konferenzen, in der Lehre und im Labor. Es war mir eine besondere Ehre, die Abschlussarbeiten von Roman Abrosimov, Andreas Dragoun, Maximilian Rapps und natürlich Ernst Artes zu betreuen. Des Weiteren möchte ich Tom Kieck und Raphael Haas-van den Heuvel für die detaillierte Einarbeitung in die Strukturen des Helmholtz-Instituts Mainz sowie für die angenehme Arbeitsatmosphäre in unserem gemeinsamen Büro danken. Ernst Artes gebührt mein besonderer Dank für die konstruktive Zusammenarbeit bei einer Vielzahl externer Messkampagnen und die transparente Aufteilung der gemeinsam erzielten Forschungsergebnisse.

Ich möchte Christina Trautmann meinen aufrichtigen Dank aussprechen. Sie hat die Zweitbetreuung meiner Doktorarbeit übernommen, mir Zugang zu ihren Laboren gewährt und mich zu Konferenzen und Workshops mitgenommen. Die gesamte Trautmann-Forschungsgruppe war fast meine zweite Forschungsgruppe. Des Weiteren möchte ich Alexander Prosvetov, Marilena Tomut, Pascal Simon und Markus Bender meinen Dank aussprechen, die sich mit meinen anfänglichen Schwierigkeiten mit dem Raman-Mikroskop auseinandersetzen mussten.

Michael Block sei für die Begutachtung meiner Dissertation gedankt. Seiner gesamten Arbeitsgruppe sei für die gute Kameradschaft auf der gemeinsamen zweiten Etage des Helmholtz-Instituts Mainz gedankt. Insbesondere für die meist reibungslose Nutzung der gemeinsamen Labore. Mustapha Laatiaoui sei für leckeren Tee und manchen guten Rat gedankt.

Ohne die festangestellten Mitarbeiter der Mainzer Kernchemie und des Helmholtz-Instituts Mainz wäre diese Arbeit nicht möglich gewesen. Ohne das Organisationstalent von Petra Sach-Muth und Miriam Jäger hätte es weder erfolgreiche Messkampagnen noch andere schöne Dienstreisen gegeben. Jörg Runke,

Christoph Mokry und Petra Thörle sei für die geduldige Unterstützung bei der Herstellung meiner Targets gedankt. Prof. Norbert Trautmann danke ich für so manchen guten Rat und viel notwendige Kritik in den monatlichen Target-Besprechungen. Ulrich Krille und seinem Team von der mechanischen Werkstatt sei für Anfertigung meiner zahlreichen Projekte besonders gedankt.

Ohne den Forschungsreaktor TRIGA Mainz wäre diese Arbeit nicht möglich gewesen. Ich möchte mich an dieser Stelle bei Christopher Geppert und insbesondere bei Klaus Eberhardt für ihre Unterstützung bedanken. Mein Dank gilt auch dem Strahlenschutzteam für seine Geduld. Der Strahlenpass und die erforderlichen Transportpapiere wurden immer vorbereitet, auch zu ungünstigen Zeiten.Außerdem danke ich Christian Gorges, Jessica Riemer, Agathe Heiser, Ines Mittelstedt, Andrea Nähler und Sabrina Samer für ihre Unterstützung.

Ich möchte Samer Amayri meinen Dank aussprechen, da er sich stets als ein guter Nachbar erwiesen hat. Ebenso gilt mein Dank Felix Berg und Markus Breckheimer für ihre Unterstützung während unserer gemeinsamen Zeit als Diplomanden und Doktoranden.

Ich möchte an dieser Stelle Herrn Constantin Haese vom Max-Planck-Institut für Polymerforschung in Mainz meinen aufrichtigen Dank aussprechen, der die Messung der NMR-Spektren durchgeführt hat. Ebenso gilt mein Dank Herrn Tobias Häger vom Institut für Geowissenschaften, der mir großzügigerweise den Zugang zu seinem Ramam-Mikroskop ermöglicht hat. Mein aufrichtiger Dank gebührt den Kollegen der GSI Darmstadt, Egon Jäger, Alexander Yakushev, Brigitta Schausten, Birgit Kindler und Bettina Lommel, die mir großzügigerweise viel Strahlzeit und Targetfolien zur Verfügung gestellt haben. Es gebührt dem Ion Beam Center des Helmholtz-Zentrums Dresden-Rossendorf, insbesondere Franz Munnik, großer Dank für die mustergültige Durchführung meiner Ionenstrahlanalytik.

Es sei mir gestattet, an dieser Stelle dem Joint Research Centre – Institute for Transuranium Elements Karlsruhe sowie insbesondere den Kollegen Alice Seibert, Thomas Gouder und Olaf Walter meinen aufrichtigen Dank für die Durchführung einer äußerst erfolgreichen Messzeit unter den besonderen Schwierigkeiten der COVD19-Pandemie auszusprechen. Ich bedanke mich bei Joachim Brötz und Martin Major vom Institut für Materialwissenschaften der TU Darmstadt für die Durchführung der GIXD-Messungen. Ich möchte mich bei Ulrich W. Scherer und Dominik Krupp von der Hochschule Mannheim für die kurzfristige Bereitstellung ihrer Laboratorien bedanken.

Ich möchte mich bei unseren Kollegen von der Universität Jyväskylä und der DECHEMA Gesellschaft für Chemische Technik und Biotechnologie e.V. Frankfurt für die Organisation von Forschungsaufent-

halten bedanken, die aufgrund der Corona-Pandemie nicht mehr von mir durchgeführt werden konnten.

Abschließend möchte ich meiner Familie und meinen langjährigen Mitbewohnern in meiner Mainzer Wohngemeinschaft meinen Dank aussprechen. Ohne Ihre Unterstützung wäre das Chemiestudium und die anschließende Promotion nicht möglich gewesen. Zudem möchte ich meiner Frau Anne für ihre Unterstützung bei der Fertigstellung dieser Arbeit danken.

Vielen herzlichen Dank!